UNIVERSITÀ DELLA CALABRIA

UNIVERSITA' DELLA CALABRIA

Dipartimento di Fisica

Dottorato di Ricerca in

Scienze e Tecnologie Fisiche, Chimiche e dei Materiali in convenzione con il CNR

CICLO XXXIII

Nanostructured materials for energy: synthesis and chemical-physical characterization for gas adsorption applications

Settore Scientifico Disciplinare: FIS/01

Coordinatore: Ch.ma Prof.ssa Gabriella Cipparrone

Firma ___ Firma oscurata in base alle linee guida del Garante della privacy

Supervisore: Ch.mo Prof. Raffaele Giuseppe Agostino

Firma Firma oscurata in base alle linee guida del Garante della privacy

Co-Supervisore: Dott. Alfonso Policicchio

Firma Firma oscurata in base alle linee guida del Garante della privacy

Dottorando: Dott. Giuseppe Conte

Firma Firma oscurata in base alle linee guida del Garante della privacy

A coloro che amo…e muovono la mia vita…

Index

3.4 Assessment of activated carbon fibers from commercial Kevlar® as nanostructured material for gas storage: effect of activation procedure and adsorption of CO_2 and CH_4

3.4.1 State of the art

3.4.2 Experimental section

3.4.2.1 Materials

3.4.2.2 Synthesis of ACFs from commercial Kevlar® (AKFs)

3.4.2.3 Characterization techniques and analysis

3.4.3 Results and discussion

3.4.3.1 Bulk and Surface characterization

3.4.3.2 Gas adsorption analysis

3.4.4 Conclusions

3.4.5 Supporting Information

3.5 Hydrogen storage performances for mesoporous silica synthesized with mixed tetraethoxysilane and methyltriethoxysilane precursors in acidic condition

3.5.1 State of the art

3.5.2 Experimental

3.5.2.1 Sample synthesis

3.5.2.2 Sample characterization

3.5.2.3 Hydrogen storage capacity

3.5.3 Results and discussion

3.5.3.1 FT-IR measurements

3.5.3.2 Nitrogen adsorption measurements

3.5.3.3 X-ray diffraction

3.5.3.4 Electron microscopy investigation

3.5.3.5 Hydrogen adsorption capacity

3.5.4 Conclusions

3.6 CO_2 Adsorption Investigation on an Innovative Nanocomposite Material with Hierarchical Porosity

3.6.1 State of the art

3.6.2 Materials

3.6.3 Methods

5. Conclusions

Abstract

Il termine nanoscienze definisce lo studio di fenomeni e tecniche di manipolazione dei materiali su scala atomica e molecolare, dove le proprietà differiscono notevolmente da quelle osservate su scale maggiori. Attualmente la ricerca scientifica dedica grandi sforzi alla comprensione degli effetti nanometrici sulle proprietà fisico-chimiche della materia, in quanto possono essere utilizzate anche su scala diversa per sviluppare processi e prodotti caratterizzati da nuove funzioni e prestazioni, applicabili in vari settori tra cui salute, società dell'informazione, energia, trasporti, sicurezza e spazio. Relativamente alle nanoscienze, la progettazione, lo sviluppo e la creazione di materiali, sistemi e dispositivi attraverso il controllo della materia su scala nanometrica sono definite come nanotecnologie. Tra di esse, esistono tecniche e processi di preparazione in grado di ottenere materiali nanoporosi per applicazioni nel settore chimico, energetico o dei trasporti.

Proprio in tale ambito si inquadra questo lavoro di tesi che è focalizzato sullo sviluppo e la caratterizzazione di nanostrutture porose per l'adsorbimento gas. In settori strategici come quello dell'energia e dei trasporti "verdi", immagazzinare e distribuire alcune tipologie di gas in maniera ecosostenibile ed innovativa, riducendo al contempo i costi energetici, è diventata una sfida tecnologica significativa. Ad esempio, l'aumento dell'uso di combustibili puliti e alternativi a quelli tradizionali (es. idrogeno, gas naturale, bio-metano) nell'industria automobilistica dipende molto dallo sviluppo di soluzioni di stoccaggio avanzate. In particolare, l'idrogeno può anche svolgere un ruolo fondamentale nei processi power to gas (PtG), ovvero di conversione dell'energia in eccesso proveniente da fonti rinnovabili (FER), rispondendo al problema dell'intermittenza di alcune di esse (solare ed eolico). In questo caso, la sfida è lo stoccaggio di idrogeno. Le forme tradizionali di stoccaggio come la compressione e liquefazione sono opzioni costose, mentre lo stoccaggio con materiali allo stato solido potrebbe rappresentare una soluzione interessante.

Allo stesso tempo, il continuo aumento dei gas serra in atmosfera, ha portato a porre la necessità di implementare soluzioni finalizzate alla cattura o stoccaggio/utilizzo dell'anidride carbonica (CCS/U) per la mitigazione dei cambiamenti climatici. Anche se esistono già metodi di stoccaggio della CO_2 (assorbimento in solventi, assorbimenti chimici, etc.), alcuni problemi come l'elevata volatilità o degradabilità hanno reso necessario trovare metodi alternativi più efficaci.

Pertanto, la crescente necessità di immagazzinare alcune tipologie di gas con maggiore efficienza e sicurezza ha spinto la ricerca scientifica verso lo sviluppo di materiali adsorbenti

nanostrutturati che siano in grado di migliorare questi requisiti, avere costi di produzione ridotti e capacità di rilasciare le specie assorbite senza dispendio di energia.

La necessità di ottenere un addensamento del gas in condizioni termodinamiche distanti da quelle di liquefazione ha spinto la comunità scientifica ad approfondire lo studio del fenomeno della condensazione per fisisorbimento di strati molecolari sulle superfici dei materiali ad alta superficie specifica. Combinando la bassa entalpia di condensazione del gas, dovuto agli effetti dei deboli potenziali dispersivi e di interazioni che non prevedono la formazione di legame chimico, con lo sviluppo di materiali costituiti essenzialmente da superfici (materiali nano porosi) si possono sviluppare sistemi per ottenere la condensazione reversibile di grandi quantità di gas in condizioni di pressione e temperature vicini a quelle ambiente.

A tal fine, una serie di materiali solidi porosi dalla struttura opportunamente ingegnerizzata (ad esempio zeoliti, strutture metallo-organiche, polimeri, carboni attivati, etc.), sono stati sviluppati e investigati durante il lavoro di ricerca focalizzando l'attenzione sulla reversibilità dei processi di adsorbimento.

Tra gli adsorbenti studiati, i materiali a base di carbonio hanno mostrato una buona efficacia nella separazione e nello stoccaggio di varie specie gassose evidenziando anche vantaggi nei metodi di produzione semplici e a basso costo. Attraverso il loro utilizzo, inoltre, è possibile sviluppare una tecnologia di stoccaggio del gas reversibile e sostenibile basata sul metodo del fisisorbimento. Carboni attivati con struttura nanoporosa sono stati sviluppati e preparati in laboratorio studiando ed analizzando in dettaglio i processi di formazione della porosità e, successivamente, caratterizzando il loro comportamento all'adsorbimento dei vari gas. Allo stesso tempo, al fine di effettuare un confronto, sono state testate altre tipologie di materiali porosi sviluppate e preparate in collaborazione con gruppi di ricerca di altri dipartimenti, università o istituti. Tutti i materiali analizzati, sono stati caratterizzati con tecniche di porosimetria a 77 K e testati per l'adsorbimento delle principali specie gassose di interesse energetico, ossia CO_2, CH_4 e H_2. Le condizioni termodinamiche (pressione e temperatura) utilizzate nelle misurazioni sono state variate in base alla tipologia di gas e agli studi effettuati. Particolare attenzione è stata posta allo studio ed analisi della struttura porosa, che insieme al parametro area di superficie specifica (SSA), influenza fortemente le proprietà chimico-fisiche dei materiali e i meccanismi di interazione all'interfaccia solido-gas. Pertanto, nella valutazione delle capacità di stoccaggio per i diversi gas, la dimensione e distribuzione dei pori si è dimostrata una variabile significativa da considerare nello studio di un materiale.

Per comprendere a fondo questi sistemi e il loro comportamento è stato, quindi, necessario l'utilizzo di diverse tecniche e metodi di analisi tra cui: Microscopia elettronica a scansione (SEM) e Microscopia elettronica a trasmissione (TEM), Diffrazione a raggi X (XRD), Analisi

a raggi X a dispersione energetica (EDX), Spettroscopia a infrarossi in trasformata di Fourier (FTIR), tecniche volumetriche di tipo Sievert.

Il lavoro di ricerca effettuato, quindi, ha portato allo sviluppo di varie metodologie per la preparazione e la sintesi di materiali con elevata superficie specifica. Quest'ultime consentono di controllare i processi di formazione della porosità permettendo di ottenere strutture nano porose omogenee adatte per l'adsorbimento di diverse specie gassose. Le nanostrutture sintetizzate hanno mostrato elevate capacità di stoccaggio, processi ciclici e alta reversibilità che, uniti al basso costo dei precursori utilizzati, rappresentano un'ottima base di partenza per l'implementazione di soluzione tecnologiche alternative a problematiche e/o esigenze del settore energetico e dei trasporti, in particolare, nella gestione ed utilizzo dell'idrogeno.

I risultati raggiunti durante le attività sperimentali, svolte anche in collaborazione con altri dipartimenti, istituti di ricerca ed università, hanno portato alla redazione di una serie di lavori scientifici presentati a conferenze e pubblicati su riviste internazionali peer-reviewed.

1. Introduction

1.1 Preface

The term Nanoscience defines the study of phenomena and techniques of manipulation of the materials on the atomic and molecular scale, where the properties differ considerably from those observed on larger scales. Currently, scientific research dedicates great efforts to understanding the nanometric effects on the physico-chemical properties of matter, as they can also be used on a different scale in order to develop processes and products characterized by new functions and performances, applicable in various sectors including health, information society, energy, transport, security and space.

Related to nanoscience, the design, development and synthesis of materials, systems and devices through the control of matter at the nanoscale are currently defined as Nanotechnologies [1]. For example, in the biomedical field devices are built on a molecular scale, by transferring the synthesis laboratory to the nanometer scale. Other nanostructures constitute the frontier of miniaturization, with applications mainly in the electronic field. Nanostructured materials are developed through the introduction of particles with few nanometers size in products such as ceramics or steel, in order to improve their characteristics. Furthermore, there are preparation processes and techniques capable of obtaining nanoporous materials for applications in chemical and energy sector.

At the nanometer level, the wavelike properties of the electron within matter and the atomic interactions are affected by the size of the material [2]. As a result, changes in thermodynamical properties as well as magnetic, optical and/or electronic properties can be observed when the material assumes nano-dimensions. Moreover, due to the high surface-to-volume ratio associated with nano-sized materials, an enormous improvement in chemical properties can also be achieved through size reduction [2]. Small-scale interactions favor phenomena such as the adsorption into porous solid materials that are characterized, owing to the absence of activation energy, by fast kinetics, reversibility, non-destruction of material structure [3,4]. By creating nanostructures, therefore, it is possible to control the fundamental properties of a given material even without changing its chemical composition. This should, in principle, allow us to develop new materials with useful properties and tunable features according to the need and kind of application.

In strategic sectors such as energy and transport, the innovation of gas storing and distribution has become a significant technological challenge in order to minimize the energy waste and

the costs if compared to current methods [5-7]. For example, the increase in the use of cleaner and alternative fuels (e.g. hydrogen, natural gas, bio-methane) in the automotive industry strongly depends on the development of advanced storage solutions [8-11]. In particular, hydrogen can also play a fundamental role in power to gas (PtG) processes, i.e. the conversion and storage of the excess energy from renewable energy sources (RES), resolving the problem of their intermittency (solar and wind) [12].

In this framework, a challenge is the H_2 storage considering that compressed and liquid forms are expensive options, while storage using solid-state materials could represent an interesting solution [13,14]. Furthermore, the continous increase of greenhouse gases in the atmosphere has led to the need of solutions aimed at Carbon Capture and Storage/Utilization (CCS/U) [15,16] for the mitigation of the climate changes. Even though there are already CO_2 storage methods (solvent absorption, chemical absorption, etc.), some problems such as high volatility or degradability have made it necessary to find more effective alternative methods. Therefore, the increasing need to store gases with greater efficiency and safety has prompted scientific research towards the development of nanostructured adsorbent materials capable of improving these requirements, together with low-cost manufacture and the ability to release the sorbed species without wasting energy [10,17].

The need to obtain a gas condensation in thermodynamic conditions far from those of liquefaction has prompted the scientific community to investigate the phenomenon of condensation by physisorption. Molecular layers can be packed in this way on the surfaces of materials with a high specific surface area. By combining the low enthalpy of condensation of the gas due to the effects of interactions not involving the formation of a chemical bond and/or weak dispersive potentials, with the development of materials that essentially consist of surfaces (nanoporous materials), we can obtain systems enabling reversible condensation of large quantities of gas under pressure and temperatures conditions close to the ambient ones.

Over the past few decades, a number of novel structured porous solid physical adsorbents (e.g. zeolites, metal-organic frameworks, covalent organic frameworks etc.) have been investigated as active materials for energy-related applications [18,19]. Among the investigated adsorbents, carbon-based materials appear to be the most effective in separation and storage [8, 20-22]. Through their use, in fact, it is possible to develop reversible and sustainable gas storage technology based on the physisorption method [23] since the weak interaction forces through adsorbate and adsorbent allow to produce a dense molecules film at the gas-solid interface and to release gas changing thermodynamic conditions. Activated carbons (ACs) with nanoporous structure are considered a very interesting material for CCS [24-26] and gas

and energy storage [14, 27-29] due to their characteristics such as good structural stability, high cyclability, tunable porosity and easy regeneration of the material [30,31]. In nanostructured carbon-based materials, the physico-chemical properties are influenced by the pore dimension, surface morphology [32] and the inclusion of dopant atoms or nanoparticles. It has been shown that the incorporation of metallic atoms or clusters can be used to modify the porosity and morphology material. However, the different parameters affecting the synthesis process makes very difficult the identification of methods allowing independent control of the content and distribution of a specific metallic species in the carbon structure. A parameter that can influence the choice of material is the Specific Surface Area (SSA), which determines the number of available adsorption sites and, therefore, the ability to increase gas storage. The SSA, i.e. the adsorbent surface accessible to the adsorbate per unit of mass of the material, depends on the size and distribution of the pores, which influences the access of the various gaseous species on the base of the dynamic radius of their molecules [33,34]. Therefore, in evaluating the storage capacities for different gases, the pore size distribution is a significant variable to be considered when investigating a material [35]. For this reason, during the research work also other types of porous materials have been studied.

Therefore, the gas storage into porous materials by physisorption process is one of the most promising and energetically sustainable methods thanks to reversible process [36,37] and fast kinetics of adsorption/desorption without damage the absorbent material [38, 39]. In order to improve the performance of materials, this research has focused its interest on understanding the basic mechanisms in the interaction between gaseous species and the surfaces of porous materials. Furthermore, a series of materials have been developed and produced in the laboratory, investigating in detail the porosity formation processes through the study and analysis of synthesis/pyrolysis key parameters.

To achieve a deep understanding of these systems and their behavior towards gas adsorption, it has needed a cross-linked study performed by means of different techniques and analysis methods with the final target to perform a complete and systematic characterization (chemical, structural and morphological) of the materials. Generally, our studies involved: Scanning Electron Microscopy (SEM) and Transmission Electron Microscopy (TEM), X-Ray Diffraction (XRD), Energy Dispersive X-ray Analysis (EDX), Fourier-Transform Infrared Spectroscopy (FTIR), volumetric techniques/methods.

References

1. Springer Handbook of Nanotechnology Editors: Bhushan, Bharat (Ed. 2004).

2. A. N. Goldstein - Handobook of Nanophase Materials, Marcel Dekker, Inc., New York, 1997.

3. Lim KL, Kazemian H, Yaakob Z, Daud WRW. Solid-state materials and methods for hydrogen storage: A critical review. Chem Eng Technol 2010;33:213–26. doi:10.1002/ceat.200900376.

4. Schlichtenmayer M, Hirscher M. Nanosponges for hydrogen storage. J Mater Chem 2012;22:10134. doi:10.1039/c2jm15890f.

5. H. Blanco, A. Faaij, A review at the role of storage in energy systems with a focus on Power to Gas and long-term storage, Renew. Sustain. Energy Rev. 81 (2018) 1049–1086.

6. J. Speirs, et al., A greener gas grid: what are the options, Energy Policy 118 (2018) 291–297.

7. M.A. Meysam Qadrdan, et al., The Future of Gas Networks, 1, Springer International Publishing, 2020, p. 69, p. VIII.

8. P.-S. Choi, et al., A review: methane capture by nanoporous carbon materials for automobiles, Carbon Lett. 17 (2016).

9. M. Hirscher, et al., Materials for hydrogen-based energy storage – past, recent progress and future outlook, J. Alloys. Compd. 827 (2020) 153548.

10. S. Alhasan, R. Carriveau, D.S.K. Ting, A review of adsorbed natural gas storage technologies, Int. J. Environ. Stud. 73 (3) (2016) 343–356.

11. S. Stelitano, et al., Low pressure methane storage in pinecone-derived activated carbons, Energy Fuels 32 (10) (2018) 10891–10897.

12. Götz, M.; Kolb, T.; Reimert, R. Renewable Power-to-Gas: Atechnological and economic review. Renew. Energy 2016, 85, 1371–1390.

13. Niaz, S.; Manzoor, T.; Pandith, H.A. Hydrogen storage: Materials, methods and perspectives. Renew. Sustain. Energy Rev. 2015, 50, 457–469.

14. Ren, J.; Nicholas, M.; Shijun, L. Current research trends and perspectives on materials-based hydrogen storage solutions: A critical review. Int. J. Hydrogen Energy 2017, 42, 289–311.

15. M.E. Boot-Handford, et al., Carbon capture and storage update, Energy Environ. Sci. 7 (1) (2014) 130–189.

16. A. Policicchio, et al., Assessment of commercial poly(ε-caprolactone) as a renewable candidate for carbon capture and utilization, J. Co2 Util. 19 (2017) 185–193.

17. Z. Nie, Y. Lin, X. Jin, Research on the theory and application of adsorbed natural gas used in new energy vehicles: a review, Front. Mech. Eng. 11 (3) (2016) 258–274.

18. Q. Zhang, et al., Nanomaterials for energy conversion and storage, Chem. Soc. Rev. 42 (7) (2013) 3127–3171.

19. K.E. Hurst, J.M. Luther, C. Ban, S.T. Christensen, Nanomaterials for energy applications. Metrology and Standardization of Nanotechnology, 2017, pp. 505–518.

20. T.D. Burchell, in: T.D. Burchell (Ed.), Carbon Materials for Advanced Technologies, Elsevier Science Ltd, Oxford, 1999 p. xv-xviii.

21. Q. Ma, et al., Carbon-based functional materials derived from waste for water remediation and energy storage, Adv. Mater. 29 (13) (2017) 1605361.

22. H. Zhao, et al., Carbon-based adsorbents for post-combustion capture: a review, Greenh. Gases Sci. Technol. 8 (1) (2018) 11–36.

23. K.A. Cychosz, M. Thommes, Progress in the physisorption characterization of nanoporous gas storage materials, Engineering 4 (4) (2018) 559–566.

24. A.-H. Lu, G.-P. Hao, X.-Q. Zhang, Porous carbons for carbon dioxide capture, in: A.- H. Lu, S. Dai (Eds.), Porous Materials for Carbon Dioxide Capture, Springer Berlin Heidelberg, Berlin, Heidelberg, 2014, pp. 15–77.

25. Y. Zhao, X. Liu, Y. Han, Microporous carbonaceous adsorbents for CO2 separation via selective adsorption, RSC Adv. 5 (38) (2015) 30310–30330.

26. Yang, J.; Yue, L.; Hu, X.; Zhao, Y.; Lin, Y. E_cient CO2 Capture by Porous Carbons Derived from Coconut Shell. Energy Fuels 2017, 31, 4287–4293.

27. Peng, S.; Li, L.; Tian, L.L.; Adams, S. Electrospun carbon nanofibers and their hybrid composites as advanced materials for energy conversion and storage. Nano Energy 2016, 22, 361–395.

28. Policicchio, A.; Maccallini, E.; Ciuchi, F.; Giordano, G. Higher methane storage at low pressure and room temperature in new easily scalable large-scale production activated carbon for static and vehicular applications. Fuel 2013, 104, 813–821.

29. F.D. Minuto at al., Liquid-like hydrogen in the micropores of commercial activated carbons. International journal of hydrogen energy 40 (2015) 14562-14572.

30. K.K.F. Rodrí guez-Reinoso, Nanoporous Materials for Gas Storage, 1st ed. 2019 ed, Green Energy and Technology. 2019, Singapore Springer, 2019.

31. G. Conte, et al., Assessment of activated carbon fibers from commercial Kevlar as nanostructured material for gas storage: effect of activation procedure and adsorption of CO2 and CH4. Journal of Analytical and Applied Pyrolysis 152 (2020) 104974.

32. C. Di Valentin, A. Tilocca, A. Selloni, T. J. Beck, A. Klust, M. Batzill, Y. Losovyj, and U. Diebold, J. Am. Chem. Soc. 127, 9895 (2005).

33. Bhatia, S. K.; Myers, A. L. Langmuir, 2006, 22, 1688-1700.

34. Yushin, G., Dash, R., et al. Advanced Functional Materials, 2006, 16, 2288-2293.

35. Gogotsi Y, Portet C, Osswald S, Simmons JM, Yildirim T, Laudisio G, et al. Importance of pore size in high-pressure hydrogen storage by porous carbons. Int J Hydrogen Energy 2009;34:6314–9.

36. L. Zhou, Progress and problems in hydrogen storage methods, Renew. Sustain. Energy Rev. 9 (4) (2005) 395–408.

37. M. Fichtner, Nanotechnological aspects in materials for hydrogen storage, Adv. Eng. Mater. 7 (6) (2005) 443–455.

38. M. Schlichtenmayer, M. Hirscher, Nanosponges for hydrogen storage, J. Mater. Chem. 22 (20) (2012) 10134–10143.

39. H. Oh, et al., Experimental assessment of physical upper limit for hydrogen storage capacity at 20 K in densified MIL-101 monoliths, RSC Adv. 4 (6) (2014) 2648–2651.

1.2 Collaborations

Development, analysis and characterization of nanostructured materials for energy-related applications reported in this PhD work were performed in collaboration with:

Universities and Research Organizations

Dipartimento di Ingegneria Meccanica, Energetica e Gestionale - DIMEG, Università della Calabria, Arcavacata di Rende (CS), Italy - *Eng. S. Candamano.*

Dipartimento di Ingegneria dell'Ambiente - DIAm, Università della Calabria, Arcavacata di Rende (CS), Italy - *Prof. G. Giordano, Prof. M. Migliori, Prof. A. Macario, Prof. G. Golemme and Eng. A. Aloise.*

CNR - ITAE, Institute for Advanced Energy Technologies "Nicola Giordano", Messina, Italy - *Dr. R. Pedicini, Dr. S. Maisano and Dr. V. Chiodo.*

CNR - NANOTEC, Institute of Nanotechnology, c/o University of Calabria, Arcavacata di Rende (CS), Italy - *Dr. Giovanni Desiderio.*

CNR - ITM, Institute on Membrane Technology, c/o University of Calabria, Arcavacata di Rende (CS), Italy - *Prof. Alberto Figoli and Dr. Francesco Galiano.*

"Coriolan Drăgulescu" Institute of Chemistry, Timisoara, Romania - *Dr. Ana-Maria Putz and Dr. Cătălin Ianăşi.*

Centro de Investigaciones Energéticas, Medioambientales y Tecnológicas (CIEMAT), Madrid, España - *Prof. Isabel Rucandio and Dr. Maria Belen Gómez-Mancebo.*

University of Groningen, Faculty of Science and Engineering - Units: Surfaces and Thin Films, Groningen, Netherlands - *Prof. Petra Rudolf and Dr. Oreste De Luca.*

Private Companies

Rina Consulting - Centro Sviluppo Materiali S.P.A, Roma, Italy - *Eng. Emanuele Bertelli, Eng. Sara Stelitano, Eng. Elisabetta Mecozzi.*

DeltaE s.r.l., Quattromiglia (CS), Italy - *Dr. Giovanni Desiderio and Eng. Andrea Perrone.*

2. Investigated systems and experimental approaches

2.1 Nanostructured materials

The dimensionality of a system has a profound influence on its physical behaviour, more specifically for nanostructured materials in which the typical size is comparable to the size of the fundamental physical quantities. In particular, the method of adsorbing gaseous species using porous nanostructured materials represents an important alternative to compression, liquefaction or the use of solid materials for chemisorption.

When hydrogen gas is concerned, the limiting factors are safety concerns in the first two cases while the chemisorption process is affected by non-negligible energy inefficiencies as it requires heat supply to release the absorbed gases (typical example is the hydrogen storage by means of metal hydrides) [1].

Even in the traditional processes of carbon capture and storage (CCS) through chemical solvents (i.e., amines, ionic liquids) [2], although their efficiency, are not sustainable due to the current environmental constraints. Furthermore, the increasingly frequent CO2 reuse (Carbon Capture and Utilization - CCU) in the food or beverage industry as a carbonating agent as well as in the pharmaceutical industry, requires high levels of CO2 purity and reversibility of absorption processes [3,4].

Consequently, research efforts are directed towards the development of porous materials capable of adsorbing various gaseous species in a reversible manner, at temperatures and pressure conditions close to environmental or operating ones and with a large storage capacity. Possible candidates, among porous and microporous materials, which can potentially satisfy these characteristics are zeolites, porous polymers, metal-organic frameworks (MOFs) and activated carbons (ACs).

Zeolites are a family of minerals with a regular and microporous crystalline structure characterized by an enormous amount of empty volumes inside the crystals in shape of pores and channels of sub-nanometric dimensions and internal surfaces of almost 1000 m^2/g. Their general formula of this type of material is:

$$(M^{n+})_{x/n}[(AlO_2)_x(SiO_2)_y]^{x-}\ wH_2O$$

in which the cations M of valence n balance the anionic charge of the framework, resulting from the presence of trivalent aluminum and x, y and z are integer. The ratio of silicon to aluminum atoms becomes important in determining their chemical properties, usually a ratio

greater than or equal to one is chosen. The cations with the purpose of balancing the charge, of natural zeolites, are usually alkaline metals or alkaline-earth metal ions such as: Na^+, K^+, Ca^{2+} and Ba^{2+}. In the case of synthetic zeolites, it is tried to use both inorganic and organic cations. Zeolites appear as a regular complex of cages (internal cavities) of different shapes and sizes connected to each other and to the outside through a network of channels with diameters between 0.3 and 1.0 nm [5]. Consequently, the channels carry out a selection of the incoming gas molecules with respect to the dimensions, thus attributing to the zeolites the function of molecular sieves.

Porous polymers are a new class of materials that lend themselves well to gas or vapour separation applications by taking advantage of high permeability combined with good separation factors. These materials have an intrinsic microporosity, that is, billions of microscopic cavities that allow the passage of small gas molecules in a selective manner. Starting from these characteristics, the polymers can be modified through simple techniques to obtain nanofibers characterized by low cost, high porosity and high specific surface per unit of mass. At the same time, these characteristics must be associated with an ease release of the gas molecules when thay have to be extracted from the polymer, therefore, optimizing both the adsorption and desorption processes [6].

Another example of porous materials are MOFs, a class of hybrid, organic and inorganic microporous materials, composed of agglomerates of metal ions connected to each other by organic binders that form two/three-dimensional crosslinks, which have recently been included as one of the possible materials for hydrogen storage [7]. These materials are of particular interest due to their large specific surface area (1000 - 6000 m^2/g) and their cage structure which allows them to have a very low skeletal density ($\cong$ 0.59 g/cc) [8]. The pore diameter can be adjusted by changing the type of organic molecule used for the synthesis and thus creating various types of MOFs with different structural characteristics. They, therefore, appear to be suitable for storing gas, in particular hydrogen and methane, but also useful for various other types of applications. To produce these structures, a transition metal is suitably mixed with organic compounds that have more or less long organic chains (appropriately chosen) which will determine the size of the porous cells. The synthesis conditions depend on the used metal and the organic part to be bound. The main property of MOFs consists in the possibility of designing the cage, thus modulating the nanoporosity, and therefore the gas adsorption capacity, by choosing the metal centres with different coordination and the organic ligands. The research results suggest that new MOFs with larger organic ligands may have higher performance [8].

Among the porous materials owing the aforementioned characteristics, we have the active carbons (ACs). These materials can be easily synthesized [9,10] by means of environmentally friendly processes often using precursor materials such as biomass, wood, bamboo, cellulose, organic residues, etc. Furthermore, it is possible to optimize their porosity so that they are more effective in the selective adsorption of a particular gas species. Various types of commercial activated carbon can also be suitable for gas adsorption, as they often have microporous and mesoporous structures. They can exist in various forms including powders, granules, small extruded cylinders, spherical beads, fibers (figure 1), whose porosity is induced by physical or chemical activation processes [9,10].

Figure 1. Different forms of Activated Carbons (ACs).

The process of producing activated carbon begins with the selection of a source of raw carbon which is selected based on the properties that are to be obtained in the material, such as the structure of the pores. For example, the result could be a porous nanostructured carbon containing crystallized graphite and/or amorphous carbon with a high specific surface area. The preparation includes the sequence of a series of steps: dehydration, carbonization, and activation. The first two steps involve slow heating of the material in an inert atmosphere, while the activation step requires exposure to additional chemicals or other oxidizing agents in form of gas flow. In general, raw materials are carbonized at temperatures up to about 1000 K to remove volatile substances and increase the carbon content while, in the activation phase, temperatures up to 1173 K are applied to develop porosity and SSA [11]. The type of activation, the relative used oxidizing elements, and the process temperature are the main parameters that influence the structure of the pores of the final product. Physical activation in the gaseous phase with oxygen is very aggressive compared to those with carbon dioxide or steam. Therefore, the latter molecules are more frequently used to obtain a mild activation and the development of a uniform porous structure [9,12]. Chemical activation, on the other hand, often requires the addition of inorganic species in solution, which react with the precursor materials before or during carbonization. In fact, a commonly used activation technique is the

use of alkaline hydroxide (KOH, NaOH) in solid form during carbonization. In this way, the process develops a large porous structure with high specific surfaces areas even up to 3000 m^2/g, leading to the formation of carbons classified as "superactive" [13]. Compared to physical activation, the chemical activation method involves lower process temperatures, shorter times to develop a high porosity even though sometimes characterized by the prevalence of mesopores. In fact, the chemical species aggressiveness causes the erosion of the material at the expense of microporosity [12].

Therefore, characteristics such as organic chemical structure, high porosity, flexible and low-cost production processes give to ACs a relevant role among the most promising materials for gas storage.

In conclusion, the aforementioned nanostructured materials were investigated during the PhD research project, paying particular attention to their physisorption properties.

2.2 Experimental methods and techniques

As previously mentioned, different techniques have been used to characterize the analyzed systems and, consequently, different experimental apparata. The latter are described in the following section.

Scanning Electron Microscopy (SEM) is the best known and most widely-used of the surface analytical techniques [14]. SEM, accompanied by X-ray analysis, is considered a relatively rapid, inexpensive, and basically non-destructive approach to surface analysis. It is often used to survey surface analytical problems before proceeding to techniques that are more surface-sensitive and more specialized. High-resolution images of surface topography, with excellent depth of field, are produced using a highly-focused scanning (primary) electron beam. The primary electrons enter a surface with an energy of 0.5 - 30 keV and generate many low energy secondary electrons. The intensity of these secondary electrons is largely governed by the surface topography of the sample.

An image of the sample surface can thus be constructed by measuring secondary electron intensity as a function of the position of the scanning primary electron beam. High spatial resolution is possible because the primary electron beam can be focused to a very small spot (< 10 nm). High sensitivity to topographic features on the outermost surface (< 5 nm) is achieved when using a primary electron beam with an energy of <1 keV. In addition to low

energy secondary electrons, backscattered electrons and X-rays are also generated by primary electron bombardment. The intensity of backscattered electrons can be correlated to the atomic number of the element within the sampling volume. Hence, some qualitative elemental information can be obtained. The analysis of characteristic X-rays emitted from the sample gives more quantitative elemental information. Such X-ray analysis can be confined to analytical volumes as small as 1 cubic micron.

- **e-SEM:** The Scanning Electron Microscope used (Quanta FEG 400 (FEI)) operates in the e-SEM mode, that is environmental-SEM, and allows to operate in very low vacuum conditions (≤ 20 Torr) with the possibility to collect secondary electron with an appropriate detector (GSED). The gas ionization process on the sample allows the compensation of the charge product by the electron beam on the surface. In this way it is possible to analyze also non-conductive sample without a pre-metallization. Moreover, operating in a relative high pressure permits to study sample with a high content of volatile substances, like water, polymer and etc. Cooling the sample close to or below 0°C is possible to work in a condition of 100% relative humidity.

Figure 2. SEM microscope supplied to the Physics Department - University of Calabria.

Transmission Electron Microscopes (TEM) allows to obtain high resolution images (Δx = 2 Å). It has some similarities with the ordinary optical microscope: an incident electron beam passes through a very thin sample and projects an image on a fluorescent screen or a CCD sensor.

The electrons are generated by a tungsten filament or a Lanthanum Hexaboride (LaB6) source and accelerated up to several hundreds keV and focuses on a submicrometric region by a complex series of electromagnetic lenses, usually from six to eight, consisting of electromagnetic windings arranged symmetrically compared to the incident beam. The electron beam is produced and shaped in Ultra High Vacuum (UHV) conditions generated by both turbomolecular and ion pumps.

The beam passing through the sample is focused by an objective lens on a fluorescent screen (or CCD detector), giving rise to a much larger image. By using this apparatus, it is possible to obtain a morphological and electronic characterization in the nanometer scale.

X-Ray Diffraction (XRD) is a non-destructive technique used for the qualitative and quantitative analysis of crystalline materials, in powder or solid-state [15]. The used instrumentation consists of a Bruker-axs D8 discover thin film diffractometer, adapted to work on powders in the Bragg-Brentano configuration. The copper doublet K_α was used as the source (weighted average λ(Cu K_α) = 1.5418 Å), and where necessary the radiation was reduced to $K_{\alpha1}$ (1.54056 Å), removing the contribution of $K_{\alpha2}$ (1.54439 Å) by means of a beam compressor that acts as a monochromator crystal. The powder holder is made up of glass capillaries (diameter 0.8 mm, wall thickness 10 μm) inserted in a specially made diaphragm sample holder. Finally, the X-ray detector is connected to a suitable acquisition system. Furthermore, the system is equipped with various slits with the possibility of changing the position of the sample with respect to the X-ray source by varying six degrees of freedom (x, y, z, χ, θ and 2θ). No vacuum equipment is provided as the measurements are carried out in air: the radiation used is highly energetic and the diffusion due to air simply implies a negligible widening of the peaks compared to the experimental resolution.

X-rays originate both from the braking of electrons (Breemstrahlung) in metal targets, and from the inelastic excitation of internal electrons of the atoms constituting the target. The first process results in continuous and extensive emission; the second provides narrow lines. The experimental apparata exploit the variation of the wavelength of the incident radiation, or by keeping the latter fixed (monochromatic beam), the angle of incidence is varied by rotating either the emitter around the sample or the polar angle and azimuth of the sample in a sample holder equipped with goniometers.

With the use of the XRD technique, it is possible to obtain information about the size of the fundamental cell, the positions of the nuclei in the cell, the distribution of electrons. The physical phenomenon of diffraction can in fact be described by Bragg's law through which the grazing angle β of diffraction, the wavelength λ of the radiation X and the distance d between parallel reticular planes (i.e. planes which intersect points of the crystal lattice where the atoms of the species under examination are located). If we suppose we have two of these planes, on each of which X-ray impacts at a reticular point, the rays are diffracted by an angle β.

In order for the radiation to be detected, the interference between the two waves must be constructive and this occurs if the difference in the path (AB + BC) between the two rays are equal to an integer multiple of the incident wavelength.

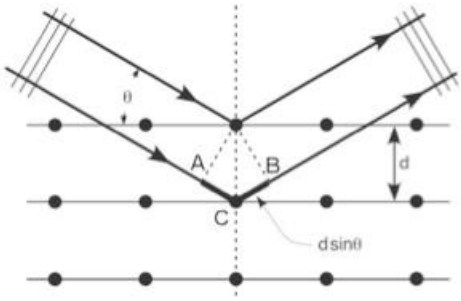

Figure 3. Illustrative scheme of Bragg diffraction.

Therefore, by the equation:

$$AB + BC = 2d\sin(\theta) = n\lambda \qquad \textit{Eq. 1}$$

we have

$$d = n\lambda/2\sin(\theta) \qquad \textit{Eq. 2}$$

Using the following relation, the values of the lattice parameters can be obtained:

$$1/d^2 = h^2/a^2 + k^2/b^2 + l^2/c^2 \qquad \textit{Eq. 3}$$

where (h, k, l) are the Miller indices.

From the analysis of the scattered radiation spectrum, it is, therefore, possible to evaluate the crystallinity of the sample. In fact, if peaks appear at certain angles, it means that the radiation has been diffused in a constructive way by the atoms arranged according to a precise crystalline configuration on parallel planes (h, k, l). Therefore, it can be concluded that the sample has a certain crystallinity. If, on the other hand, a signal without peaks is detected, it means that the species under examination is amorphous.

In addition to an analysis on the crystallinity of the samples, through X-ray diffraction from powders, it is possible to perform a qualitative analysis of the components of the species. This exam is based on two considerations:

- each chemical element or compound capable of assuming a crystalline form gives rise to a diffraction pattern different from that of other substances;
- in a mixture of different crystalline components, each component gives rise, independently from the others, to its own diffraction pattern.

The advantages of this technique are the speed of measurement and the small amount of the required sample. To recognize the presence of a given substance in the sample, after

interpolation of the spectrum at the peaks, the angles at which they appear are extrapolated, and these data are compared with the databases in which the spectra of the various elements are catalogued and molecules, provide the required information.

Energy Dispersive X-ray Analysis (EDX) is a method that exploits the emission of X-rays generated by an accelerated electron beam incident on the sample and allows us to obtain the qualitative characterization and centesimal analysis of solid materials [14]. The qualitative characterization allows to identify a certain element, while the centesimal analysis provides the percentage quantity of species present in the sample. The instrument outputs a discrete spectrum in which the peaks correspond to the energy levels from which the X radiation comes. The higher the peak, the higher the concentration of the elements to which they correspond. The software with which the system is managed takes into account the so-called ZAF matrix effects, with respect to which the various peaks are weighted and normalized. The abbreviation indicates that corrections are made due to the atomic number (Z), absorption (A) and fluorescence (F). The Z correction is due to the strict dependence between the backscatter, in which there is no release of X radiation, and the atomic number of the element on which the phenomenon occurs, therefore it is also linked to the density of the species. Furthermore, the phenomenon of stopping-power which corrects the energy absorbed by atoms with a specific atomic number. Correction A is due to the phenomenon of reabsorption of X radiation in the material and if the analysis were not made it would be affected by an underestimation of the quantity of elements present in the sample. Correction F instead takes into account the fluorescence produced by the secondary electrons. Furthermore, in the EDX analysis, the detection of a noisy background signal due to the braking radiation (Bremsstrahlung) that the electrons undergo when they are in motion in an electromagnetic field appears. This signal is automatically subtracted in the spectral analysis returned by the instrument.

Fourier-Transform Infrared Spectroscopy (FTIR) is an analysis technique that is based on the absorption of infrared radiation (IR), i.e. with a wavelength between 0.78 and 100 μm, by molecule and solids. This phenomenon is due to the ability of IR radiations to cause variations in the vibrations of the bonds, entering into resonance with them and making the atoms vibrate; this occurs when the radiation has a frequency equal to or multiple of the natural one of the bond. The vibrations of the bonds can be classified as follows:

- *stretching:* variation in the length of the bonds; it can be symmetrical (if the bonds shorten or lengthen at the same time) or asymmetrical (if one bond lengthens while the other shortens);
- *bending:* variation of the bond angles; it can be in the plane or out of the plane, depending on whether the vibrations of the bonds occur in the same plane or not. The bending in the piano can be scissoring or rocking; that out of a plane can be twisting or wagging.

Furthermore, for an IR radiation to be absorbed, it must cause a variation of the dipole moment, that is, of the polarity of the molecule. The interaction with electromagnetic radiation causes vibrational transitions: the energy of the vibration of two or more bonded atoms changes. Only the vibrations that cause a dipole moment variation of the bond cause absorption of infrared radiation (IR active).

The stretching frequency of a particular functional group can be calculated approximately using Hooke's law of the simple harmonic oscillator:

$$v = \frac{1}{2\pi c}\sqrt{k/m} \qquad \textit{Eq. 4}$$

with v wavelength expressed in numbers [cm^{-1}]

c light speed

k bond strength constant [dine cm^{-1}]

m reduced mass of the atoms involved [$m_a m_b/(m_a+m_b)$]

As is well known, in fact, the following relation holds:

$$E = hv \qquad \textit{Eq. 5}$$

where *E* is the energy associated with the radiation, h is Planck's constant ($6.626 \cdot 10^{-34}$ J·s) and *v* is the frequency of the radiation.

Therefore, if the radiation hitting the molecule has a frequency such that the energy associated with it is equal to energy distance between roto-vibrational levels, then this radiation is absorbed and consequently, there is an increase in the amplitude of the oscillations of the system itself. Since each bond absorbs radiation at characteristic frequencies, it is possible to obtain information on the presence of different functional groups in a compound and therefore on the chemical nature of a substance.

The Fourier transform spectrophotometer (FT-IR), unlike the dispersion ones, does not have a monochromator but uses a mechanical device called Michelson's interferometer. This is made up of three mirrors: a semi-transparent central one (SS), a fixed one (SF) and a mobile

one (SM). The analysis is carried out with an instrument called a spectrophotometer and consists in sending infrared radiation of variable frequencies, usually between 4000 and 400 cm^{-1}, to the substance under examination, and identifying which of them are absorbed. To reduce the error due to background noise, FT-IR instrumentation is used.

The ray coming out from the IR source is divided into two parts by means of a semi-transparent mirror (splitter): the two rays obtained are then out of phase with each other, as they reflect one on a fixed mirror and the other on mobile mirror. The rays coming from the two mirrors are then recombined with each other and, crossing the sample, they generate the interferogram, which is subjected to anti-Fourier transform, according to a process called anodization. Since the position of the moving mirror, and therefore the optical path of one of the radiations, varies over time, the interference between the radiations and the transmittance of the sample will also vary over time. The graph showing the transmittance of the sample as a function of time is called an interferogram, but since it is difficult to interpret, a mathematical operator is used, the Fourier transform, which transforms it into a spectrum, obtaining the transmittance as a function of the wave number (the reciprocal of the wavelength).

Then we proceed to the interpretation of the spectrum obtained, going back to the functional groups present in the molecule and its possible structural formula.

Volumetric techniques/methods. Physisorption processes on porous and non-porous materials are investigated determining the adsorption isotherms and the enthalpies of adsorption by the mean of thermodynamic measurements. The physical quantities in which the gas uptake is determined are pressure, mass or gas flow. The volumetric method makes use of gas handling apparatus (known as a Sieverts' apparatus), that for historical and practical reasons, is the most common method for this purpose. The amount of the adsorbed gas is evaluated by monitoring the change of pressure which follows the exposition of the gas to the adsorbent. Thus, the adsorption isotherm is made by determining the adsorptive concentration in a step-by-step procedure, at different equilibrium pressures. The operational scheme of a Sievert's type apparatus is shown below in figure 4 [16-18].

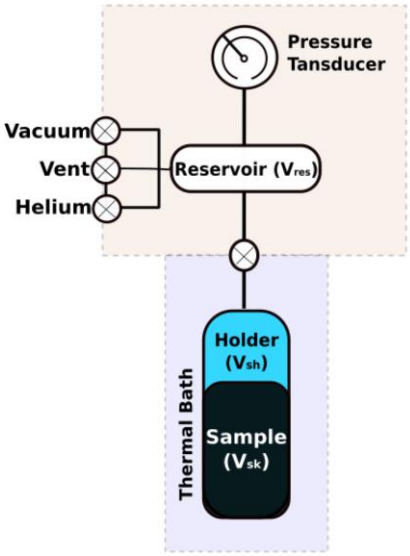

Figure 4. Schematic view of Sievert's type apparatus

A known quantity of gas expands between two calibrated volumes, the reservoir (V_{res}) and the sample holder (V_{sh}), containing the adsorbent with a known skeletal volume (V_{sk}). It is possible to evaluate the excess adsorbed moles n_{exc}, using the real gas law, from the pressure drop after the expansion. In the simplified case, where the system is at the same temperature, and considering the compressibility factor for each pressure-temperature state, the excess adsorption can be expressed as:

$$n_{exc} = a \cdot (P_{res} \cdot V_{res} - P_{exp} \cdot V_{exp}) \qquad Eq.\ 6$$

where $a = 1/Z \cdot R \cdot T$ *and* $V_{exp} = V_{res} + V_{sh} - V_{sk}$.

For this calculation, it is crucial to determine the sample skeletal volume. The latter is usually measured by helium (He) pycnometry assuming that it is not adsorbed at high temperatures and low pressures [19,20]. The gas uptake is expressed in terms of weight percent (wt.%), which allows the comparison of samples with different masses, and is expressed as the weight ratio between the adsorbed gas (m_{ads}) and the sum of the sample (m_s) and the adsorptive:

$$wt.\% = \frac{m_{ads}}{m_{ads}+m_s} \cdot 100 \qquad Eq.\ 7$$

The experimentally measured quantity is the excess adsorption n_{exc}, which is a good approximation of the absolute adsorption n_{ads} in low pressure (LP) ranges. On the other hand, for high pressure apparatus (HP), the correction is needed to take into account the displacement of n_{exc} from n_{ads} because of increasing of the gas phase concentration. Measuring the adsorption at different temperature requires further volume calibration, when the sample

holder and the reservoir volumes are not at the same temperature. Indeed, each apparatus has its own procedure for the cold volume calibration.

- **fast Pressure concentration Temperature (fPcT):** the fPcT is a home-made Sievert's type apparatus developed and optimized by the academic spin-off DeltaE s.r.l. [21]. It performs high pressure measurements in a range from 1 mbar up to 80 bar, supplied by ultra-pure (99.9999%) gas lines: hydrogen, methane, carbon dioxide, nitrogen and helium. The apparatus was designed to measure at 77 K (liquid nitrogen bath) and at room temperature, but through the development of an adequate temperature control system on the sample holder, the apparatus is able to measure at 196 K and on a wide range of temperatures around room temperature. The same apparatus allows the skeletal volume evaluation by helium pycnometry, which is performed at 1 bar and at room temperature (≅ 298 K). Each measurement is preceded by a sample heating treatment (473 K) in ultra-high vacuum (UHV) chamber (10^{-6} mbar) for 12 hours to remove moisture and pre-adsorbed molecules.

  The fPcT apparatus consists of a gas manifold with a series of tubes and valves connecting the sample holder void volume to the gas reservoirs void volume and pressure transducers, which is schematically represented in figure 5 and shown in figure 6.

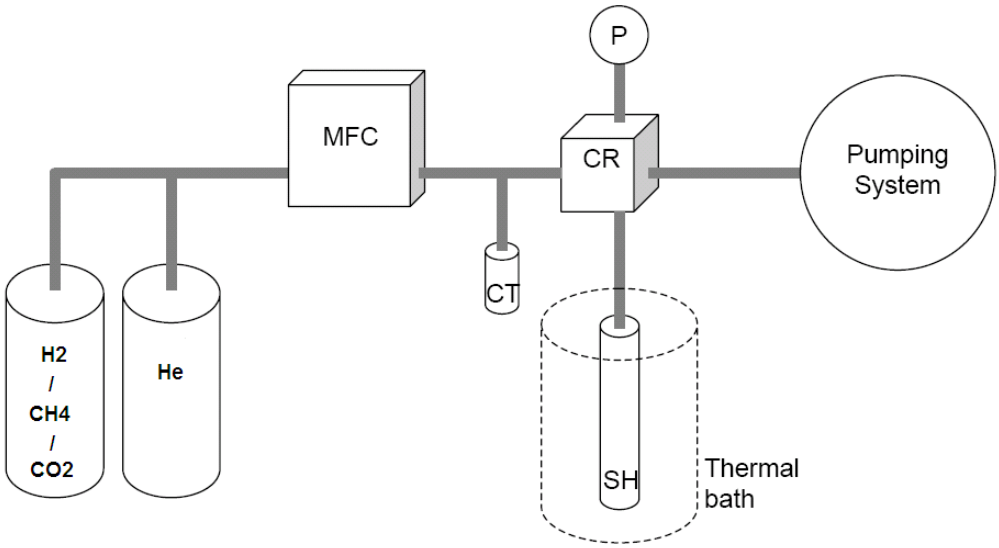

Figure 5. Schematic representation of the f-PcT apparatus. MFC (Mass Flow Controller), CR (Calibrated Reservoir), CT (Cryogenic Trap), SH (Sample Holder), P (Pressure Transducer).

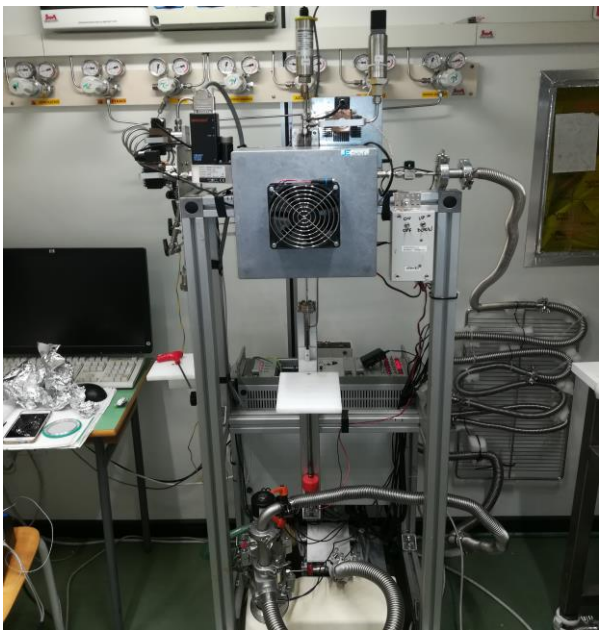

Figure 6. Image of the f-PcT apparatus in the Surface and Energy laboratory of Physics Department - University of Calabria.

A mass flow controller (MFC) is inserted to control the admittance gas in the reservoir. Two pressure transducers with end scale of 1 bar (P1) and 100 bar (P100) are mounted in the reservoir volume to measure the lower and higher pressures ranges respectively. Errors of 1×10^{-5} bar and 1×10^{-3} bar are made in the pressure measurements respectively. The principal system void volumes are divided by electro-valves.

The sample holder is thermalized with a specific bath at different temperatures (depending the gas used, hydrogen, methane, carbon dioxide etc.). The temperature of the reservoir is measured by a probe with a precision of ca. 0.015 K while the SH temperature is measured by k-type thermocouple which takes in account the A probe measurements as reference temperature. The temperatures of the reservoir and SH is monitored at different points checking his uniformity within the error of 0.1%. The vacuum has been obtained by pumping system consisting of membrane and turbo molecular pump achieving pressures less than 1.3×10^{-3} mbar. The fPcT can measure small amounts of sample, up to a few hundred mg, with high reproducibility and accuracy. To diminish the experimental error, measurements are performed with 200 to 500 mg of sample.

All the equipment (pressure and temperature measurements, valves, pumping system, time settings and data acquisition and analysis) is controlled by home-made software (in Lab-View) which manages the apparatus by an acquisition card.

- **ASAP 2460** is a Micromeritics volumetric apparatus for low pressure N_2 adsorption measurements at liquid nitrogen temperature (77 K). It works in normal operative mode designed by the manufacturer. Measurements are performed in the pressure range of 10^{-10} bar up to 1 bar using 4 transducers and by 99.9999% purity gas. Procedures and details about the apparatus can be found on the company web site (www.micromeritics.com). The samples are heated at about 473 K for 12 hours in UHV before adsorption measurements.

2.3 Adsorption isotherms

The description of a physical adsorption process of a gas by a solid material occurs through the construction of characteristic curves which report, at constant temperatures, the quantity of gas adsorbed by the surface as a function of the equilibrium pressure of the physical process. The typical curves utilized to investigate the samples' storage capacity are the isotherm plots.

Generally, the grade of adsorption is determined from the surface coverage coefficient θ:

$$\theta = \frac{number\ of\ sites\ occupied\ by\ the\ adsorbate\ (N_s)}{total\ number\ of\ sites\ available\ on\ the\ adsorbent\ (N)} \qquad Eq.\ 8$$

when θ is equal to 1, then the adsorbate ensemble is called a monolayer [22].

The trend of the isotherms varies according to the type of adsorbate, adsorbent and gas-surface intermolecular forces involved in the process. In literature, different shapes (types) of isotherms for each particular gas-solid system are presented. The majority of them are divided based on the extended IUPAC classification into nine main groups [23]. The information deriving from the isotherms is very useful since the isotherm shape reveals information about the pore structure of the material. For example, one of the most common isotherm shapes is the Type Ia that is associated with the adsorption of molecules into microporous materials Figure 7. In this isotherm, the slope rises steeply at low pressures and it reaches a plateau at higher pressures and is fully reversible.

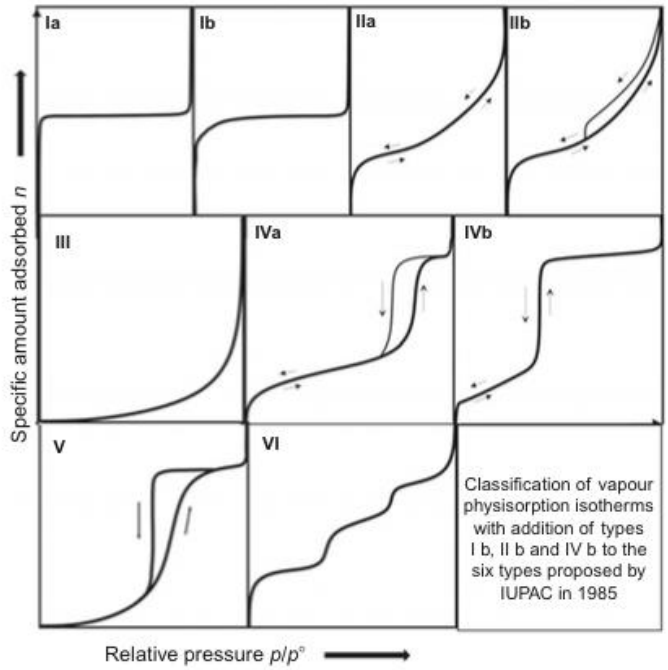

Figure 7. IUPAC classification of gas adsorption isotherm [24].

In addition to material porous properties, the isotherm shape analysis and the trend can estimate either the energy bonds involved in the adsorption mechanism by using selected theoretical models. Moreover, information concerning the enthalpy of adsorption and material heterogeneity it is possible to extract from the analysis of some models.
The thermodynamic models used during the experimental work are described below.

2.4 Thermodynamic models

In the following section, different models describing physisorption process in sub- and supercritical temperature are presented. It is tried to start from the simplest models following by more sophisticated ones describing the adsorption process in heterogeneous porous materials. Moreover, it is explained how to extract useful structural information such as pore size distribution, specific surface area, and adsorption enthalpy.

2.4.1 Henry's law

Henry's law is the simplest physisorption model initially formulated for gas-liquid solutions by William Henry in 1803, and it describes the gas uptake at low pressure. It assumes that in an adsorption system, the molecules interact with the surface independently from each other and that the amount of the molecules adsorbed at a certain temperature is proportional to pressure.

Thus, Henry's law [25] is expressed as:

$$n(T) = k_H(T) \cdot P \qquad \textit{Eq. 9}$$

where P is the thermodynamic equilibrium pressure, k_H is a constant showing the adsorption strength and it depends on the temperature in accordance with the Boltzman distribution (function).

This model is valid only for very low adsorption concentrations; therefore, it is limited to a small range of pressures called "Henry's region". Nevertheless, in the case of micropore filling or when the adsorptive-adsorbent interaction is strong, the isotherm exhibits a deviation from the linearity even at very low pressures.

2.4.2 Langmuir model

The adsorption model introduced by Langmuir in 1916 revolutionized surface science [26]. The basic idea behind this formulation is the assumption that the number of available adsorption sites is limited. The adsorption system, in which this model is based on, is a flat and homogeneous surface with equivalent adsorption sites where only one molecule is adsorbed without dissociation for each ad-site; and when all the available adsorption sites are occupied, the formation of a monomolecular layer (monolayer) completes. The amount of the adsorbed molecule is expressed in terms of the fractional coverage θ (see Eq. 8), where at θ=1 the monolayer formation is completed.

The molecular adsorption rate (R_{ads}) is proportional to the pressure (P) and to the number of available adsorption sites (1-θ), according to the:

$$R_{ads} = k_a \cdot P \cdot (1 - \theta) \qquad \textit{Eq. 10}$$

where k_a is the adsorption constant rate which depends on the number of collisions weighted by the probability of sticking. Instead, the probability of molecule desorption depends on the adsorptive-adsorbent interaction strength with respect to the temperature according to the Arrhenius distribution; thus, the rate of desorption (R_{des}) is expressed as:

$$R_{des} = k_d \cdot \theta \qquad \textit{Eq. 11}$$

where $k_d = k_{d0} \cdot \exp(-\Delta H/R \cdot T)$, ΔH is the adsorption enthalpy, and the inverse of k_d is the residence time of a molecule on the surface.

At the equilibrium state, the number of desorbed molecules is equal to the adsorbed molecules; indeed, the Langmuir equation is obtained from equaling Eq. 10 and Eq. 11:

$$\theta = \frac{K \cdot P}{1 + K \cdot P} \qquad \textit{Eq. 12}$$

where *K* is:

$$K = \frac{k_a}{k_b} = k_0 \cdot e^{(-\frac{\Delta H}{R \cdot T})} \qquad \textit{Eq. 13}$$

Moreover, the Langmuir equation at very low pressures reduces to the linear form of Henry's law. Even though the importance of the Langmuir model lies in its simplicity, many isotherms even with a similar shape, rarely obey this equation over a great range of concentrations. Of course, Langmuir himself pointed out that in real materials, there are other adsorption mechanisms that can take place, for example when adsorption occurs in materials with more than one kind of adsorption site, or when the multimolecular adsorption occurs [26-28].

2.4.3 Brunauer Emmett Teller (BET) equation

The first formulation of multimolecular gas adsorption theory, referred to as "BET", was introduced in 1938 by Brunauer Emmett Teller [29] on the basis of Langmuir model.

The introduced innovation was the possibility that a gas molecule could accommodate on top a pre-adsorbed molecule. Besides, since each adsorptive molecule is independent of each other, the formation of a new layer does not require the completion of the previous layer. Moreover, at the saturation pressure P_0, an infinite number of monomolecular layers is adsorbed.

As discussed before, the multi-layer adsorption mechanism is due to adsorptive-adsorbent interaction, instead of the monolayer adsorption which is based on adsorptive-surface interaction. Monolayer adsorption is governed by the characteristic adsorption enthalpy (ΔH_{ads}), whereas for multi-layer adsorption, the interaction energy between the layers is assumed to be equal to the condensation enthalpy of a pure bulk material (ΔH_{liq}).

The BET model is able to reproduce the Type II s-shape isotherm. At low P/P_0, it increases like Type I isotherm, and then after the knee formation, there is a near-linear region followed by multilayer adsorption until it reaches the transition phase at $P=P_0$. The region that corresponds to the monolayer completion was empirically identified as "B point", which is at the beginning of the near-linear region [30].

The most common form of the BET equation used to fit the Type II isotherms, is the linear expression:

$$\frac{P}{n \cdot (P_0 - P)} = \frac{1}{n_m \cdot C} + \frac{C-1}{n_m \cdot C} \cdot \frac{P}{P_0} \qquad \textit{Eq. 14}$$

where *P* is the equilibrium pressure, P_0 is the saturation vapor pressure, *n* is the total number of adsorbed molecules, n_m is the number of molecules within the monolayer film, and $C \cong exp$

$(\Delta H_1 - \Delta H_{liq}/R \cdot T)$, where ΔH_1 is attributed to the average adsorption enthalpy of less active ad-site on the adsorbing surface.

Since the shape of the isotherm depends on *C* parameter, $C>2$ shows the characteristic knee similar to what we have in Type I isotherm, whereas $C<2$ shows a curvature with no inflexion point representing the Type III isotherm; taken into account that *C* in this model is always positive.

2.4.4 Tóth model

The majority of the adsorption models are based on the severe restriction of adsorption sites homogeneity so they are not able to represent the real materials adequate enough such as, for example, the activated carbons. The solution proposed by Tóth was based on an empirical modification of the Langmuir model, rising from the observation that at the same pressure, a heterogeneous surface uptakes more adsorptive than a homogeneous one with the same accessible surface [31].

The energetic heterogeneity of the adsorption sites is introduced by further parameter t; thus, the Langmuir equation is modified in:

$$\frac{n}{n_m} = \frac{K \cdot P}{(1+(K \cdot P)^t)^{1/t}} \qquad \textit{Eq. 15}$$

For $t = 1$, the equation reverts to the original Langmuir equation; if $0 < t < 1$, it shows that the surface is heterogeneous and the adsorptive-adsorbent interactions overcomes the adsorptive-adsorptive lateral interaction. If $t > 1$, the situation is vice versa which means that the adsorptive-adsorptive interactions are the stronger ones. Moreover, it was found out that *t* not only depends on the heterogeneity of ad-sites, but also on the adsorptive molecules' mobility and their interaction with the adsorbent [32].

2.4.5 Pore size distribution: Density Functional Theory (DFT)

Another approach to model the adsorption in porous materials is based on mathematical and computational methods. Indeed, it is possible to construct a digital microscopic representation of complex adsorption systems to simulate the adsorption capacities, enthalpies or selectivities of different gases. This computational strategy was implemented first to help and guide the interpretation of experimental data; however, it is proved that this methodology is predictive in well-defined and characterized systems [33].

One of the goals of the computational modelling is the calculation of the pore size distribution (PSD), which is determined from the inversion of the generalized adsorption isotherm (GAI):

$$N(T,P) = \int_0^\infty \rho(w,T,P) \cdot f(w) dw \qquad \textit{Eq. 15}$$

where the pore size distribution function, $f(w)$ is computed experimentally from the adsorption isotherm data $N(T,P)$ and the kernel $\rho(w,T,P)$.

The kernel function is a series of single pore isotherms (SPIs) generated by simulating the density of gas molecule within a determinate shaped pore, at a given temperature T and pressure P, varying the specific pore dimension (w). The molecular modelling of the SPIs has two steps: constructing the realistic atomic digital representation of the adsorbent, followed by choosing an appropriate "force field" function which reproduces, as realistic as possible, the adsorptive-adsorbent potential energy [34].

The inversion of GAI is independent of the method used to generate the SPIs. Thus, basically, it is common to refer to PSD with the name of the implemented computational method. For example, molecular dynamics (MD), Monte Carlo (MC), or Density Functional Theory (DFT).

DFT methods (e.g. DFT, local DFT, non-local DFT, quenched solid DFT) are widely used in literature for PDS determination because its computation is less time consuming than MD or MC with the same results. Furthermore, NLDFT is accepted as a reference characterization method by the International Standard Organization (ISO) [35].

The main difference between QSDFT and NLDFT is that QSDFT takes into account the surface roughness, whereas NLDFT assumes homogeneous adsorbent surface, and it fails in simulating the systems with very narrow pores due to a molecular layering effect. On the other hand, NLDFT is better than QSDFT and GCMC in modelling the capillary condensation [33]. Recently, Jagiello et. Al. [36] has developed the NLDFT for carbon slit-shaped pores with energetically heterogeneous surface proving the applicability of this model even in narrow pores.

Usually, PDS is determined from nitrogen (N_2) adsorption at the temperature of 77 K; recently many authors have suggested that using other probe molecules such as argon (Ar) at 87 K, or carbon dioxide (CO_2) at 300 K can produce more reliable results [37]. It is also important not to forget the relation between the porosity and the probe molecules, which intimately influence the probed accessible surface.

2.4.6 Specific Surface Area (SSA) evaluation

The accessible surface area (SA) is an important characteristic of a porous material for its implication on adsorption proprieties. As already discussed during the material description section, the amount of gas uptake depends on the extension of the solid interfaces [16,38]. This quantity is not directly measurable, but it is possible to be determined by some geometrical assumption, from monolayer capacity n_m:

$$SA = n_m \cdot N_a \cdot \sigma \qquad \textit{Eq. 16}$$

where n_m is the number of molecules within the monolayer film, N_a is the Avogadro number and σ is the average area occupied by each probe molecule defined as:

$$\sigma = f \cdot \left(\frac{M}{\rho_{liq} \cdot N_a}\right)^{2/3} \qquad \textit{Eq. 17}$$

where f is the packing factor, M is the adsorptive molar mass and ρ_{liq} the density of the adsorptive in the liquid phase at the operating temperature.

Since the surface area is an extensive quantity, to compare different materials, it is common to refer to the specific surface area (SSA), calculated by dividing the SA to the mass of the sample, so its unit will be [m^2g^{-1}].

The monolayer capacity nm is determined from the adsorption isotherms, analyzing them with an appropriate model such as BET equation. Indeed, even if n_m could be derived from the linearization of the Langmuir equation, this model still could not be used because of its limited range of applicability, especially in the presence of micropores [39].

Usually, the most common gas to be used for SSA determination [30] is nitrogen (N_2) measured at its critical temperature (77 K). However, as stated before, recent experiments show that by using Ar, CO_2 [40] or hydrogen (H_2), it is possible to probe higher surface area in the presence of microporosity and ultramicroporosity [41].

The adsorption isotherm is plotted in BET coordinates, $(P/P_0) / [n \cdot (1- P/P_0)]$ versus P/P_0 and it could be fitted by a straight line with a slope $s = (C-1)/n_m$ and an intercept $i = 1/ n_m \cdot C$, from which it is possible to obtain the value of the monolayer concentration n_m and the C parameter. It is known that in Type II isotherm, the approximate range of linearity for the BET plot is between 0.05 and 0.35 P/P_0, but many porous materials show a deviation from linearity even before 0.2 P/P_0. That is why two consistency criteria are proposed: 1) non negative value of the C parameter; 2) the pressure range of BET applicability have to show a continuous increase of the $n \cdot (P/P_0)$ versus P/P_0; the pressure corresponding to n_m, calculated as $P/P_0 = 1/(\sqrt{C} + 1)$, should be within the selected pressure range.

2.4.7 Enthalpy determination

The affinity between the adsorptive and a certain material depends on the adsorptive-surface interaction strength, and it is one of the most important factors of the whole adsorption processes. The energy is released when the gas molecule is adsorbed on the surface since it loses a degree of freedom during the transition from a free gas to a bi-dimensional adsorbate layer.

It is possible to measure the strength of the interaction in terms of the isosteric enthalpy of adsorption from the adsorption isotherms taken at different temperatures. If the adsorption process is reversible, which is the case when adsorption and desorption branch coincide, the thermodynamic equilibrium is reached ($\mu_a=\mu_g$), on the reference pressure ranges. Moreover, assuming the temperature *T*, the constant volume *V*, and neglecting the structural modification of the sample which changes the accessible area *A*, it is possible to
define the isosteric adsorption enthalpy as:

$$\Delta H_{\mathrm{ads}}\big|_{\mathrm{T},\theta\mathrm{i}} = R \cdot \left.\frac{\partial \ln(P)}{\partial(1/T)}\right|_{\theta\mathrm{i}} \qquad \textit{Eq. 18}$$

which is equivalent to the Clausius-Clapeyron equation.

The enthalpy at a given surface coverage θi is calculated from the Van't Hoff plot fitting with a straight line the logarithm of the pressure versus the inverse of the temperature Van't Hoff plot. This method is very sensitive to the equilibrium pressure measurement. Thus, it is not always reliable especially in the case of high measurement errors or at low pressures if the equilibrium pressure is not well established [42,43].

2.5 Examined systems

Different kind of nanostructured systems has been characterized in order to evaluate the efficiency in the adsorption processes and compare their morphological/structural properties for a deeper understanding of the porosity formation processes and mechanisms of interaction at the solid-gas interface. The analyzed systems are:

- ✓ Activated Carbons (ACs) samples from Pinecones (*Pinus pinea*), produced at Surface and Energy Laboratory of Physics Department, University of Calabria, Italy.

- ✓ Activated Carbons (ACs) samples from Posidonia Oceanica and Wood chips, produced at CNR - ITAE, Institute for Advanced Energy Technologies "Nicola Giordano", Messina, Italy.

- ✓ Activated Carbon Fibers (ACFs) samples from commercial Kevlar®, produced at Surface and Energy Laboratory of Physics Department, University of Calabria, Italy.

- ✓ Ordered Mesoporous Silica samples prepared with different ratios of functionalized precursors, produced at "Coriolan Drăgulescu" Institute of Chemistry, Timisoara, Romania.

- ✓ NaX nanozeolite-geopolymermonolith using metakaolin as aluminosilicate source and sodium silicate solution as activator, produced at DIMEG Department, University of Calabria, Italy.

- ✓ Poly(L-lactide) (PLA) in form of commercial pellets, powder, and flakes, purchased from Galatea Biotech Srl.

- ✓ Activated Carbons (ACs) samples from commercial amorphous cellulose purchased from Sigma-Aldrich, produced at Surface and Energy Laboratory of Physics Department, University of Calabria, Italy.

- ✓ Cu-Impregneted Activated Carbons (ACs) samples from commercial amorphous cellulose purchased from Sigma-Aldrich, produced at Surface and Energy Laboratory of Physics Department, University of Calabria, Italy.

Particular attention was dedicated to the development of nanostructured materials from biomass or low-cost raw materials, for potential industrial application in the energy or automotive sector, in addition to the eco-sustainability of the synthesis processes used.

The activated carbons (ACs) analyzed were produced in the laboratory through chemical or physical activation. According to the type of precursor, also the preparation and the activation parameters selected have been varied, as the structural characteristics of the raw materials are different.

For the ACs production at Surface and Energy Laboratory of Physics Department - University of Calabria, it was used a prototype apparatus for pyrolysis suitably modified and adapted during the experimentation. The apparatus consists of an electric furnace equipped with a stainless-steel reactor, acts as a sample holder, linked to a pipeline for the inlet/outlet gas. Process parameters (temperature, heating rates, gas flow) setting and monitoring were performed in real-time on computers through a home-made software developed in the LabView environment (National Instrument).

Other materials were prepared in collaboration with national and foreign research departments or institutes, as well as the execution of some investigation techniques, while the main activities of analysis and chemical-physical characterization of the materials were carried out mainly in the laboratories and facilities of the University of Calabria.

The detailed description of the developed nanostructures and analyzed, with synthesis/preparation processes and the various experimental techniques used will be shown below in the section dedicated to the results of the research work.

References

1. N.A.A. Rusman, M. Dahari. A review on the current progress of metal hydrides material for solid-state hydrogen storage applications. International Journal of Hydrogen Energy Volume 41, Issue 28, 27 July 2016, Pages 12108-12126

2. S. Zeng, X. Zhang, L. Bai, X. Zhang, H. Wang, J. Wang, D. Bao, M. Li, X. Liu, S. Zhang, Chem. Rev. 2017, 117, 9625.

3. R. M. Cuéllar-Franca, A. Azapagic, J. CO_2 Util. 2015, 9, 82.

4. K. Armstrong, P. Styring, E. A. Quadrelli Eds., Carbon Dioxide Utilisation: Closing the Carbon Cycle, 1st ed., Elsevier, London, UK 2015, p. 336.

5. Ying Ma, Wei Tong, Hua Zhou, Steven L Suib. A review of zeolite-like porous materials. Microporous and Mesoporous Materials, Volume 37, Issues 1–2, May 2000, Pages 243-252.

6. A. Thomas, P. Kuhn, J. Weber, M-M. Titirici, M. Antonietti. Porous Polymers: Enabling Solutions for Energy Applications. Macromolecular Rapid Communications, 06 February 2009, https://doi.org/10.1002/marc.200800642.

7. H. W. Langmi, J. Ren, B. North, M. Mathe, D. Bessarabov. Hydrogen Storage in Metal-Organic Frameworks: A Review. Electrochimica Acta, Volume 128, 10 May 2014, Pages 368-392.

8. M. Alhamani, H. Doan and C-H. Cheng. A Review on Breathing Behaviors of Metal-Organic-Frameworks (MOFs) for Gas Adsorption. Materials 2014, 7(4), 3198-3250; https://doi.org/10.3390/ma7043198.

9. H. Marsh and F. Rodríguez-Reinoso. Book: Activated carbon. Elsevier 2006.

10. Almansa C, Molina-Sabio M, Rodríguez-Reinoso F. Adsorption of methane into ZnCl2-activated carbon derived discs. Microporous Mesoporous Mater 2004;76:185–91. doi:10.1016/j.micromeso.2004.08.010.

11. K. Inomata, K. Kanazawa, et al., Carbon 40, 87, 2002.

12. P. T. Williams, A. R. Reed. Development of activated carbon pore structure via physical and chemical activation of biomass fibre waste. Biomass and Bioenergy, Volume 30, Issue 2, February 2006, Pages 144-152.

13. J. Wang and S. Kaskel. KOH activation of carbon-based materials for energy storage. J. Mater. Chem., 2012, 22, 23710-23725.

14. Joseph I. Goldstein, Harvey Yakowitz – *Practical scanning electron microscopy, Electron and Ion Microprobe Analysis* – Plenum Press, New York and London 1975.

15. C. Kittel (1971), "Introduzione alla fisica dello stato solido", Boringhieri editore, cap. I e II.

16. Badalyan a., Pendleton P. Analysis of uncertainties in manometric gas-adsorption measurements. II. Uncertainty in αS-analyses and pore volumes. J Colloid Interface Sci 2008;326:1–7. doi:10.1016/j.jcis.2008.07.001.

17. Lee YW, Clemens BM, Gross KJ. Novel Sieverts' type volumetric measurements of hydrogen storage properties for very small sample quantities. J Alloys Compd 2008;452:410–3. doi:10.1016/j.jallcom.2006.11.014.

18. Rouquerol J, Rouquerol F. Methodology of Gas Adsorption. Adsorpt. by Powders Porous Solids, Elsevier; 2014, p. 57–104. doi:10.1016/B978-0-08-097035-6.00003-6.

19. Sircar S. Measurement of Gibbsian Surface Excess. AIChE J 2001;47:1169–76. doi:10.1002/aic.690470522.

20. Rouquerol J, Avnir D, Fairbridge CW, Everett DH, Haynes JM, Pernicone N, et al. Recommendations for the characterization of porous solids (Technical Report). Pure Appl Chem 1994;66:1739–58. doi:10.1351/pac199466081739.

21. Policicchio A, Maccallini E, Kalantzopoulos GN, Cataldi U, Abate S, Desiderio G, et al. Volumetric apparatus for hydrogen adsorption and diffusion measurements: Sources of systematic error and impact of their experimental resolutions. Rev Sci Instrum 2013;84:103907. doi:10.1063/1.4824485.

22. Gary Attard, Colin Barnes, Surfaces, Oxford University Press, 1998

23. Sing KSW. Reporting physisorption data for gas/solid systems with special reference to the determination of surface area and porosity (Recommendations 1984). Pure Appl Chem 1985;57:603–19. doi:10.1351/pac198557040603.

24. Rouquerol F, Rouquerol J, Sing KSW, Maurin G, Llewellyn P. Introduction. Adsorpt. By Powders Porous Solids, Elsevier; 2014, p. 1–24. doi:10.1016/B978-0-08-097035-6.00001-2.

25. Sing KSW, Everett DH, Haul RAW, Moscou L, Pierotti RA, Rouquerol J, et al. Reporting Physisorption Data for Gas/Solid Systems. Handb. Heterog. Catal., vol. 57, Weinheim, Germany: Wiley-VCH Verlag GmbH & Co. KGaA; 2008, p. 603–19. doi:10.1002/9783527610044.hetcat0065.

26. Langmuir I. THE CONSTITUTION AND FUNDAMENTAL PROPERTIES OF SOLIDS AND LIQUIDS. PART I. SOLIDS. J Am Chem Soc 1916;38:2221–95. doi:10.1021/ja02268a002.

27. Langmuir I. THE CONSTITUTION AND FUNDAMENTAL PROPERTIES OF SOLIDS AND LIQUIDS. II. LIQUIDS. 1. J Am Chem Soc 1917;39:1848–906. doi:10.1021/ja02254a006.

28. Langmuir I. The Adsorption of Gases on Plane Surfaces of Glass, Mica and Platinum. J Am Chem Soc 1918;40:1361–403. doi:10.1021/ja02242a004.

29. Brunauer S, Emmett PH, Teller E. Adsorption of Gases in Multimolecular Layers. J Am Chem Soc 1938;60:309–19. doi:10.1021/ja01269a023.

30. Sing KSW. Assessment of Surface Area by Gas Adsorption. Adsorpt. by Powders Porous Solids, Elsevier; 2014, p. 237–68. doi:10.1016/B978-0-08-097035-6.00007-3.

31. Tóth J. Calculation of the BET-Compatible Surface Area from Any Type I Isotherms Measured above the Critical Temperature. J Colloid Interface Sci 2000;225:378–83. doi:10.1006/jcis.2000.6723.

32. TOTH J. Adsorption. CRC Press; 2002.

33. Maurin G. Modelling of Physisorption in Porous Solids. In: Elsevier, editor. Adsorpt. By Powders Porous Solids, Elsevier; 2014, p. 191–235. doi:10.1016/B978-0-08-097035-6.00006-1.

34. Jagiello J, Ansón A, Teresa Martínez M. DFT-based prediction of high-pressure H_2 adsorption on porous carbons at ambient temperatures from low-pressure adsorption data measured at 77 K. J Phys Chem B 2006;110:4531–4. doi:10.1021/jp057340x.

35. Madani SH, Diaz LH, Biggs MJ, Pendleton P. Uncertainty in pore size distribution derived from adsorption isotherms: II. Adsorption integral approach. Microporous Mesoporous Mater 2015;214:217–23. doi:10.1016/j.micromeso.2015.04.030.

36. Jagiello J, Olivier JP. 2D-NLDFT adsorption models for carbon slit-shaped pores with surface energetical heterogeneity and geometrical corrugation. Carbon N Y 2013;55:70-80. doi:10.1016/j.carbon.2012.12.011.

37. Jagiello J, Ania CO, Parra JB, Jagiello L, Pis JJ. Using DFT analysis of adsorption data of multiple gases including H2 for the comprehensive characterization of microporous carbons. Carbon N Y 2007;45:1066–71. doi:10.1016/j.carbon.2006.12.011.

38. Salvador F, Montero J, Sánchez-Montero MJ, Izquierdo C. Mechanism of heterogeneous adsorption in the storage of hydrogen in carbon fibers activated with supercritical water and steam. Int J Hydrogen Energy 2011;36:7567–79. doi:10.1016/j.ijhydene.2011.03.079.

39. Broom DP. The accuracy of hydrogen sorption measurements on potential storage materials. Int J Hydrogen Energy 2007;32:4871–88. doi:10.1016/j.ijhydene.2007.07.056.

40. Ravikovitch P, Vishnyakov a, Russo R, Neimark A. Unified Approach to Pore Size Characterization of Microporous Carbonaceous Materials from N2,Ar,and CO2 Adsorption Isotherms. Langmuir 2000;16:2311–20.

41. Oh H, Gennett T, Atanassov P, Kurttepeli M, Bals S, Hurst KE, et al. Hydrogen adsorption properties of platinum decorated hierarchically structured templated carbons. Microporous Mesoporous Mater 2013;177:66–74. doi:10.1016/j.micromeso.2013.04.020.

42. Shen D, Bülow M. Isosteric study of sorption thermodynamics of single gases and multicomponent mixtures on microporous materials. Microporous Mesoporous Mater 1998;22:237–49. doi:10.1016/S1387-1811(98)00090-0.

43. Beckner M, Dailly A. Adsorption Enthalpy Calculations of Hydrogen Adsorption at Ambient Temperature and Pressures Exceeding 300 bar. Am J Anal Chem 2013;04:8–16. doi:10.4236/ajac.2013.410A3002.

3. Research results

3.1 Pinecone-Derived Activated Carbons as an Effective Medium for Hydrogen Storage

3.1.1 State of the art

The European Commission's Directive 2009/28/EC (renewable energy sources (RES) directive) has established that at least 20% of energy consumption must come from RES by 2020, and EU countries have agreed to a target of 27% by 2030 [1].

Thus RES, such as solar or wind, will play a significant role in electric power generation. The most prominent disadvantage of RES is their variability, which needs to be balanced for electric grid stability purposes. Consequently, long-term and large-capacity electricity storage is required, as well as reserve production capacity. Current storage systems present low energy densities or limited storage potential. There are different paths for the conversion of energy produced from RES into gaseous or liquid fuels. The power to gas (PtG) processes represent one of the aforementioned alternatives. A PtG process connects the electrical network to the gas network by converting excess energy into gas through the

conversion and storage of hydrogen (H_2) [2]. The challenge for PtG systems is the momentary H_2 storage. Compressed and liquid forms are not considered economically viable options for H_2 storage, while storage using solid-state materials could represent an interesting third solution [3,4].

Among different solid materials, carbon-based materials have attracted interest for their unique features (excellent stability, adjustable porosity, good electronic conductivity, etc.) that allow them to assume key functions in various technologies [5], such as gas and energy storage [4,6-12], water treatment [13], and/or carbon dioxide (CO_2) capture [14].

However, these carbon materials are generally products of fossil-fuel-based precursors (e.g., methane (CH_4), phenol, and pitch) that are created using methods that are dangerous and expensive for the natural environment. Biomass-derived carbon-based materials represent an efficient, greener, and low-cost alternative [15-18]. These display physicochemical characteristics [19], such as being suitable for obtaining carbon-based materials with desired properties for different applications [20-22].

Consequently, natural, organic, and agricultural wastes, such as corncob [23], wood [24],

rice husks [25], olive stones [26], sucrose [27], and jute [28], have been explored as biomass sources for the production of activated carbons (ACs) [29] with high specific surface areas

(SSAs) that are connected to a very determined porosity, both of which are basic parameters for H_2 storage [30].

Generally, ACs are the result of a gradual process in which a pulverization phase is followed by the carbonization of the material in an inert gas atmosphere with an appropriate temperature trend. Subsequently, chemical or physical activation is performed [31]. The chemical activation process consists of the mixing of the carbon source with a chemically active agent. Among several chemically active agents [32], potassium hydroxide (KOH) has been extensively utilized to activate the carbon as it allows for obtaining porous carbon with a well-defined micropore size distribution and a high SSA (≤ 3000 m^2/g), which give rise to excellent storage properties [12,33-35].

It is commonly thought that ACs' porous structure is the crucial characteristic for H_2 adsorption capacity. More specifically, a high SSA and a large volume of micropores, with diameters in the range of 6-8 Å, are necessary for an efficient performance as an H_2 storage material. In this field, the strategy is now dedicated to going beyond the so-called Chahine rule: the maximum adsorption capacity scales with the specific surface area at a rate of 1 wt% per 500 m^2/g, i.e., 6 H_2 molecules/nm^2 of the pore surface [36-38].

Pinecones, a widely available biomass, are mostly composed of cellulose and lignin [39,40], which means that it represents an interesting carbon source. Once pulverized, it has a porous structure that represents an excellent platform that can interact with and capture several chemical species, leading to an optimization of the structure in the final products. To date, as a porous carbon source, pinecones have been largely investigated as electrodes for supercapacitors and lithium-ion batteries [41] and for water treatment [42]; however, no reports on their use as an adsorbent for hydrogen storage has been reported. Toward this aim, new motivation was recently provided by the report of Blankenship et al. [43] on cellulose-acetate-derived microporous carbons with high SSAs and pore volumes, according to which, a high oxygen content noticeably improves the H_2 adsorption capacity. Based on the above, the objective of this work was to demonstrate that the modification of the morphology and textural properties of biomass-based porous carbons from pinecones synthesized using a chemical activation procedure represents a useful and convenient method for obtaining high-performance hydrogen storage materials. In particular, the focus of the study was on the effects of different KOH/pinecone powder weight ratios used during the synthesis procedure on the sample's porosity. Furthermore, detailed microstructure analysis using density function theory (DFT) and an evaluation of the hydrogen storage performance using a Sievert's type apparatus, as well as their correlation, was investigated and is reported herein.

3.1.2 Material and Sample Preparation

Pinecones from stone pine (Pinus pinea) (Figure 1), collected from the local area of Sila, Italy, were used as raw materials. Distilled water was used to repeatedly wash all the cones to remove soluble impurities; they were then dried for 12 h at 353 K. After drying, the cleaned cones were milled using a blender. The obtained pinecone powder (PC) was heated at 453 K for 5 h to remove the unwanted moisture [42] and the resultant powder was denoted as dehydrated pinecone powder (DPC). Then, the DPC was dissolved in 100 mL of demineralized water with KOH/DPC ratios equal to 0.5, 1, and 3. After stirring for 24 h at 353 K, the black-colored mixture was dried at 373 K until the moisture was removed; then, using a ceramic crucible, it was transferred to a tubular furnace under a 100 mL/min helium flow (99.999% purity Helium). The sample was slowly heated to 1173 K at a heating rate of 5 K/min and remained at this temperature for 2 hours. The steps of the transformation process of PC into porous carbons are schematically reported below in Figure 1.

Figure 1. Schematic procedure for the preparation of the activated porous carbons from pinecones.

In the final step, distilled water was once again used to wash the resulting dark solid material until a pH = 7 condition was reached; then, the material was kept at 353 K for drying in an electric oven in air. The resultant powder was labeled ADPCx (activated carbonized pinecone), where "x" denotes the KOH/DPC ratio, as shown in Table 1.

Table 1. Textural properties and H_2 adsorption properties of the samples.

Sample	KOH/ DPC	[a] S_{BET} (m^2/g)	[b] V_T (cm^3/g)	[c] V_{micro} (cm^3/g)	DFT Cumulative Pore Volume (cm^3/g)		[f] V_{meso} (cm^3/g)	[g] V_{macro} (cm^3/g)	[h] F_{micro} (%)	[i] H_2 (wt%)	[l] H_2 (wt%)
					[d] Ultra-Micropores	[e] Super-Micropores					
DPC	0	0.42	0.003	0.0001	0	0.0001	0.0001	0.0028	3	0.00	0.00
ADPC0.5	0.5	441	0.1633	0.1506	0.0993	0.0513	0.0087	0.0041	92	0.73	1.79
ADPC1	1	1173	0.4513	0.3836	0.1854	0.1982	0.0630	0.0048	85	1.57	5.25
ADPC3	3	1050	0.4487	0.3254	0.1479	0.1775	0.1204	0.0030	73	1.28	3.40

[a] SBET: Specific surface area (SSA) as a result of the Brunauer–Emmett–Teller (BET) method applied in the 0.05–0.15 relative pressure range. [b] V_T: Estimated total pore volume with a relative pressure of $P/P_0 = 0.99$. [c] V_{micro}: Micropore volume extracted from the cumulative volume. [d] Ultramipores: Volume of pores with less than a 7 Å width. [e] Supermicropores: Volume of pores with less than a 20 Å width. [f] V_{meso}: Pore volume with a diameter lower than 500 Å in width. [g] V_{macro}: Macropore volume as the rest of the total pore volume once the micropore and mesopore volumes were subtracted. [h] F_{micro}: Micropore volume fraction = (micropore volume/total pore volume) × 100. [i] H_2 uptake: Hydrogen storage capacity at 77 K and 1 bar. [l] H_2 uptake: Hydrogen storage capacity at 77 K and 80 bar. DPC: Dehydrated pinecone powder, ADPC: Activated carbonized pinecone, DFT: Density function theory.

3.1.3 Characterization

Morphological scanning electron microscope (SEM) images were recorded using an FEI Quanta 200 FEG, a field emission SEM, using an electron beam of 20 keV to track any change in the morphology of the samples after the activation process. A chemical composition estimation was obtained using a JEOL JXA-8230 electron probe micro-analyzer (EPMA) equipped with five wavelength-dispersive spectrometers (WDS).

The phase structure of the samples was examined using X-ray powder diffraction (XRD) patterns acquired in reflection mode on a Philips PW 1830 diffractometer equipped with Cu Kα (40 kV, 40 mA) filtered radiation. All patterns were recorded in the 2θ range from 2° to 70°, with steps of 0.02° and a counting time of 1 s per step, at room temperature (RT ≅ 298 K); the sample stage effect was taken into consideration.

A Micromeritics ASAP 2460 apparatus was used to measure the N_2 adsorption isotherms at 77 K to evaluate the sample's textural properties. All samples were subjected to a thermal treatment at 473 K for 12 h in a vacuum before each adsorption test. The Brunauer-Emmett-Teller (BET) method [44] was applied in the 0.05-0.15 relative pressure range to extrapolate the specific surface area of each sample, while V_T, the total pore volume, was assessed by recording the N_2 uptake at a relative pressure P/P_0 of 0.995. Density functional theory (DFT), considering slit-shaped pores [45], was used to calculate the total micropore volume (V_{micro}) and the pore size distributions (PSDs) to estimate the trends in the porosity changes. The H_2 adsorption capacity at 77 K was evaluated for different pressure ranges, in particular from 0 to 1 bar and from 0 to 80 bar, using the Micromeritics ASAP 2460 instrument and a Sieverts' type apparatus (fPcT) [46], respectively. Before each adsorption/desorption measurements, all investigated materials were treated at high temperature (≅ 473 K) overnight. The gas storage uptake (wt%-weight percent of adsorbed gas per gram of adsorbent) was established through an analysis of the adsorption isotherms.

3.1.4 Results and discussion

3.1.4.1 Surface and Structure Analysis

SEM images of the DPC and ADPC samples are shown below in Figure 2. Figure 2a clearly shows the smooth surface of the carbonized sample containing few micropores, while a sponge-like morphology with a heterogeneous distribution of pores was present for the activated ones (Figure 2b-d). The pores were larger for higher KOH/DPC ratios, leading to the presence of a microporous structure on the walls separating the macropores, which is shown in the insets. Here, we confirm that the formation of porous cavities in the material was produced by the KOH activation process [33-35].

In Figure 3, the XRD patterns in the 15-35° 2θ range of all samples are reported. The DPC sample showed a broad peak centered at 2θ = 23° (002), denoting the typical amorphous graphite structure [24,31,47]. The (002) peak disappeared in the activated samples, confirming the amorphous and non-graphitic nature of the ADPCs samples. The pore network was an outcome of the activation process, i.e., a series of redox reactions between the carbon material and the potassium compounds, as well as at the temperature evolution timing during the next carbonization process, led to the selective dissolution of the species on the carbon framework surface, [24,25,27,34].

WDS analysis (Supplementary Table S1) showed that the samples mainly consisted of carbon and oxygen, with 81.3 at% and 17.7 at%, respectively, and 1 at% of other elements. The O/C atomic ratios were comparable with those recently obtained by Blankenship et al. [43].

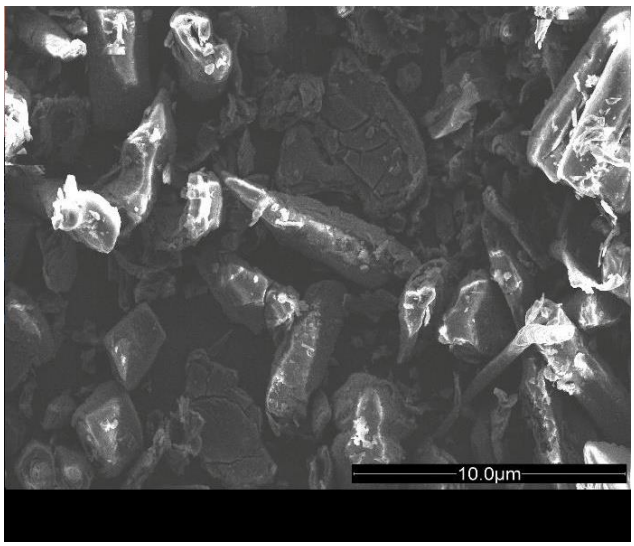

(a)

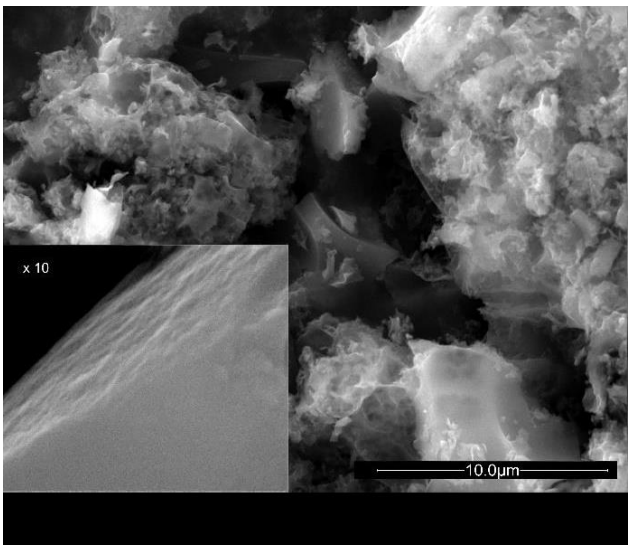

(b)

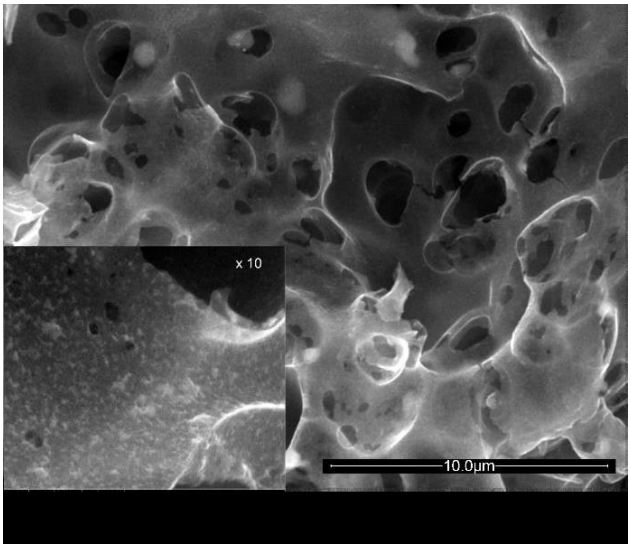

(c)

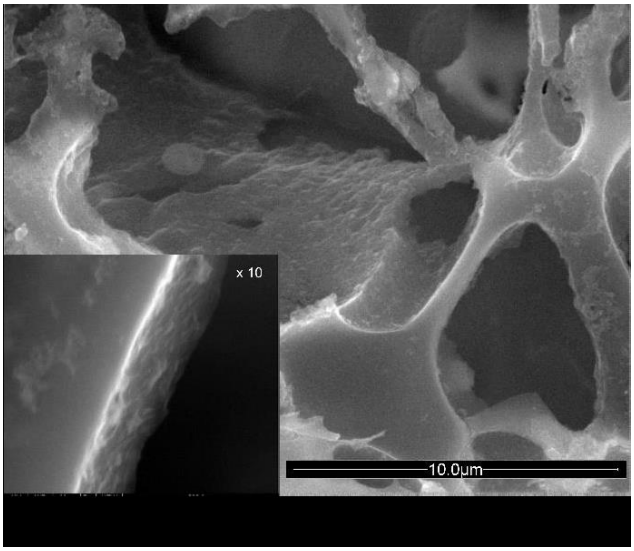

(d)

Figure 2. SEM images of (a) DPC, (b) ADPC0.5, (c) ADPC1, and (d) ADPC3. The inset in (a), (b), (c) and (d) show further magnified images.

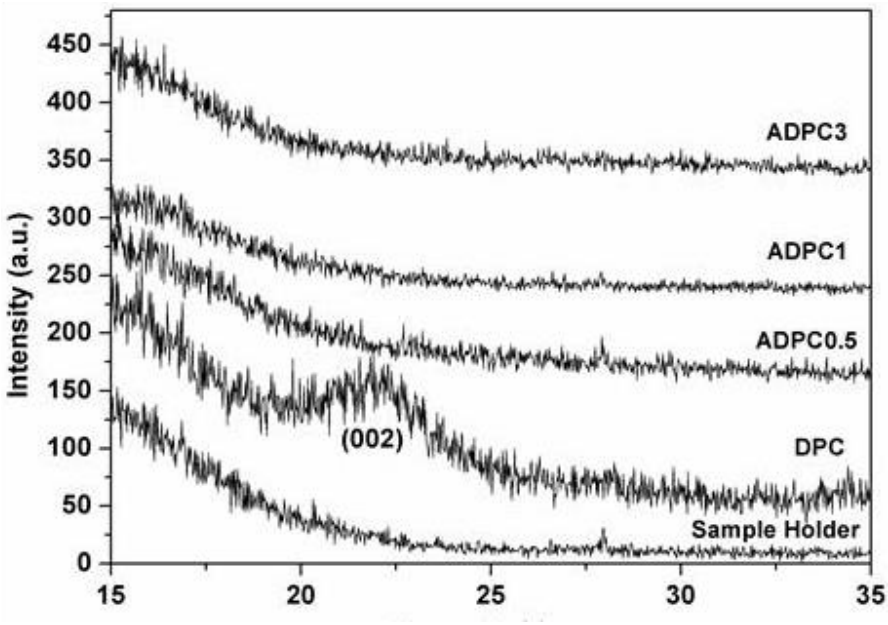

Figure 3. XRD pattern of samples between 2θ = 15° and 37°. The complete spectrum is shown in Figure S1.

3.1.4.2 Textural Properties Analysis

Figure 4 shows the nitrogen adsorption/desorption isotherms as measured at the liquid nitrogen temperature. Here, as later, for the sake of clarity, only the curves of the most significant samples are shown. As expected, the DPC sample did not show an appreciable N_2 uptake (here not shown), indicating that the sample had a very low porosity and confirming the SEM analysis results.

According to the IUPAC classification [48], the shapes of the isotherms were of types I and IV. This was related to a developed mesopore structure coexisting with a microporous framework. The N_2 uptake rapidly increased at a very low relative pressure ($P/P_0 < 0.01$) for all the measured isotherms, which is as an indication of their microporous character; an indication of their micropore capacity was connected to the quasi-horizontal plateau in the range $P/P_0 > 0.1$, and a hysteresis loop at the relative pressure range of 0.4-1.0, which was associated with the capillary condensation that occurred in mesopores.

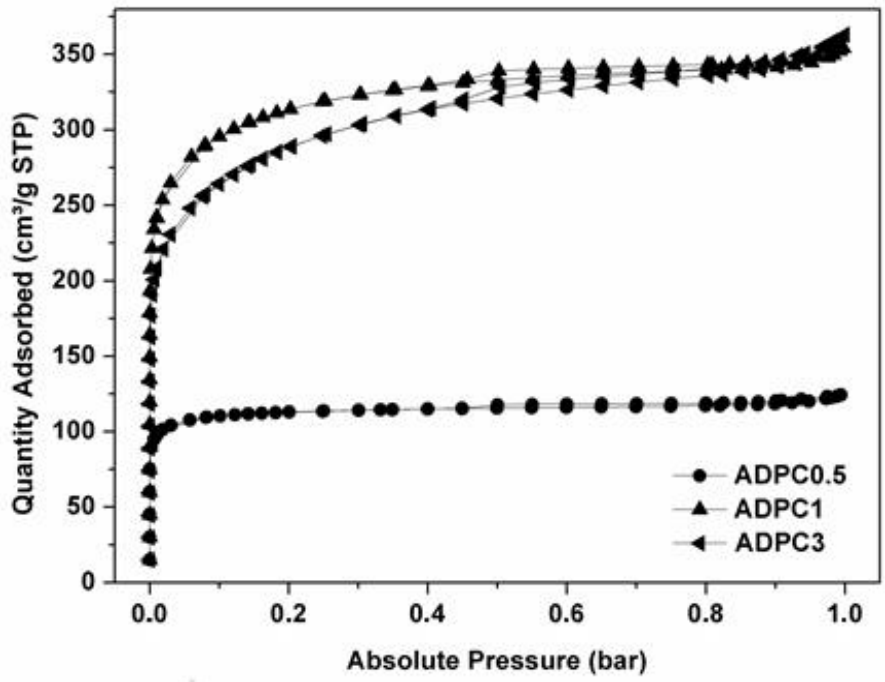

Figure 4. N_2 adsorption-desorption isotherms at 77 K.

By looking at the curves' details, it can be noted that the ADPC0.5 sample had a narrower isothermal knee and a less extensive hysteresis loop than the other samples, indicating mainly microporous structures with a lower mesoporosity. On the contrary, the other samples showed a much more considerable amount of adsorbed N_2 at low pressures, which is symptomatic of a higher microporosity; furthermore, the more extensive broadening of the isotherm flection point, as well as of the hysteresis loop, was representative of both an increase of the micropore width and the development of mesoporosity, as already shown in the SEM investigation. In particular, the ADPC3 sample exhibited the greatest knee widening, which was indicative of a greater mesoporosity (Table 1). This can be linked to the micropores removal and the development of the mesopores due to the excessive KOH content [33-35]. The examination of the adsorption isotherms and PSDs allowed us to quantify these structural differences, as reported in Table 1.

The PSDs were evaluated using DFT and the cumulative volume, as shown in Figure 5, clearly shows that the activation process increased the size of the micropores and generated mesopores. All the PSD plots (Figure S2) exhibited a significant peak in the ultra-microporous region centered around 0.5 nm and series of peaks in the microporous region, whereas the pore size range extended into the mesoporous area only for the samples with a KOH/DPC ratio higher than 0.5. The porosity was therefore homogenous and concentrated in a narrow range (<1 nm), which is a crucial feature for effective H_2 adsorption. All these observations point out that KOH/PC ratio was a critical factor in the development of porosity during the

activation process. More specifically, increasing the impregnation ratio increased the microporosity (Figure 6), which reached its highest value when the KOH/DPC ratio was equal to 1. At higher KOH/DPC ratios, we observed the development of the mesoporosity of ACs in the 20-200 Å range, which is an essential characteristic for their application in different fields [49].

Furthermore, when comparing the cumulative volume curve for the ADPC3 and ADPC1 samples, a rigid shift was evident showing that while the latter had a dominant microporous character (pore dimensions were essentially confined below 30 Å), the former developed a mesoporous character. In fact, calculating the difference between the cumulative volume of ADPC1 and that of ADPC3 (Figure S3), it is noted that this tended to increase up to a maximum of around 15 Å and then decreased, thus highlighting the greater microporous character of the first sample relative to the second, as well as the ability of this process to finely tune the material porosity. Furthermore, the probed pinecone AC samples presented a higher micropore fraction relative to other biomass activated carbons [7,23,25,27,33].

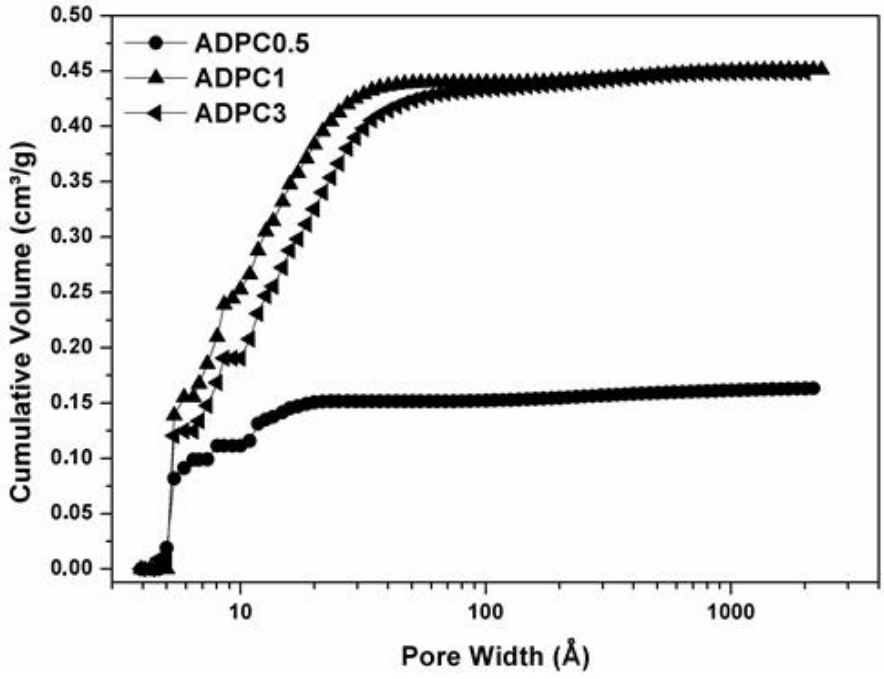

Figure 5. Cumulative pore volume of the analyzed samples.

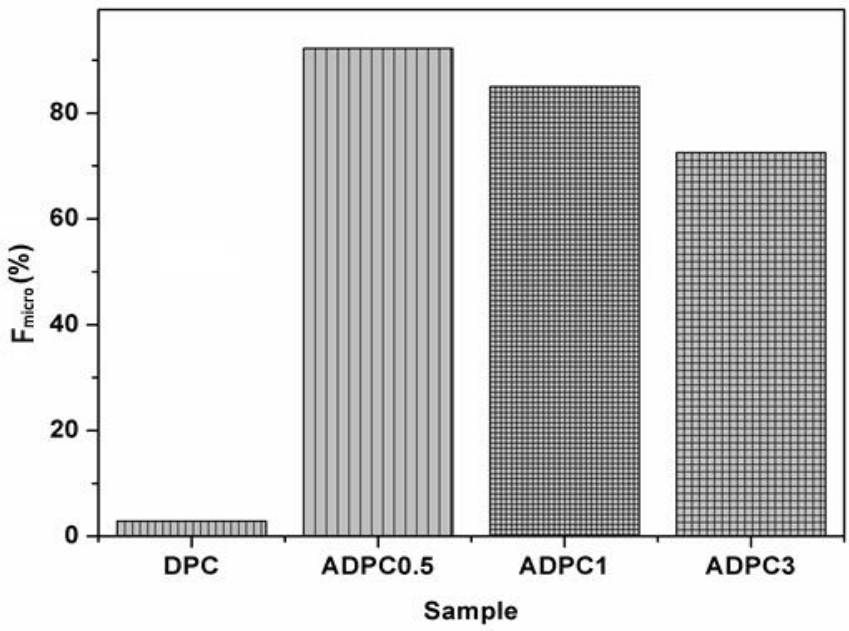

Figure 6. Micropore volume fractions (see Table 1 for the acronym definitions).

The textural properties, as recovered via the analysis of the N_2 adsorption isotherms, are summarized in Table 1, where the fractions of ultra-micropores, super-micropores, and mesopores were evaluated in accordance with the pore classification given by IUPAC [48]. As seen, the KOH/PC ratio influenced the textural properties (Figure S4), in particular the microporous fraction (F_{micro}), which decreased as the KOH/PC ratio increased. The increase of the KOH/PC ratio involved damage to the structure, which reduced F_{micro}, and at the same time, increased the mesoporous fraction. By increasing the KOH/DPC ratio, more KOH was retained into the raw material; this is an advantage because the activation reaction proceeded more effectively with more micropores being created in the raw material. On the other hand, as a drawback, the same process produced damage in the already produced porous structure.

ADPC0.5 showed the highest microporous fraction, confirming the microporous nature of this sample, although the total micropore volume was very low. ADPC1 presented the highest micropore volume (0.383 cm^3/g) and BET surface area (1173 m^2/g). These parameters decreased when the KOH/DPC ratio increased above 1.

Comparing the obtained results with the literature [23-25,27,28,33,43], while the PSD was similar and both the V_T and SSA showed lower values, the ADPCs had both a higher oxygen content and microporous fraction, showing that the synthesis of highly microporous carbon for H_2 uptake can take advantage of the use of pinecones as biomass precursors, while the optimization of the activation procedure parameters could further improve this feature.

3.1.4.3 Hydrogen Adsorption

To have a preliminary estimation and comparison of the H2 storage capacity of all the analyzed samples, hydrogen adsorption/desorption measurements (see Figure 7) were undertaken at liquid nitrogen temperature (77 K) in the 0-1 bar range.

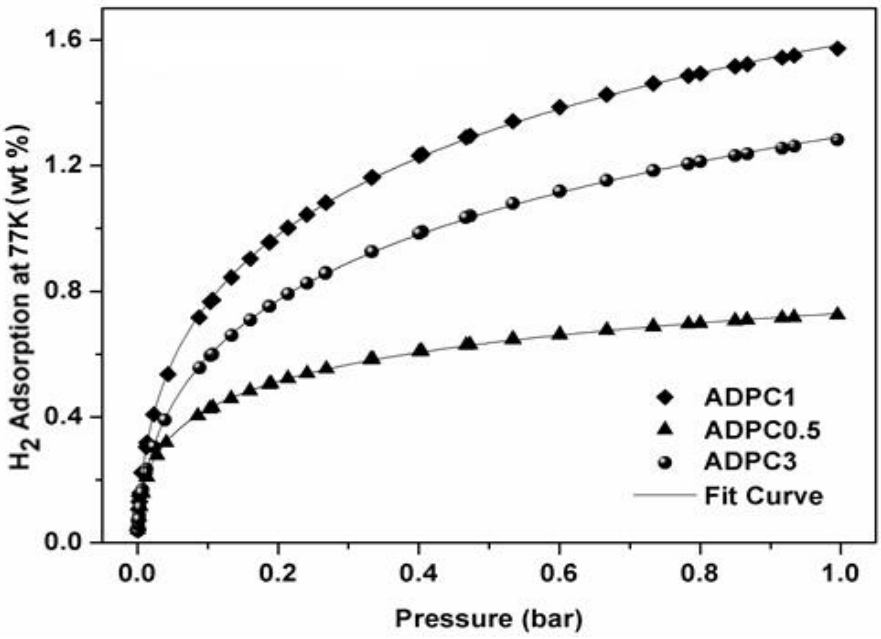

Figure 7. H_2 adsorption isotherms at 77 K up to 1 bar.

The H_2 uptake was as low as 0.38 wt% in the DPC sample, while higher storage capacities were observed for the activated samples. This trend was expected [23,30,33], as we have reported that a larger SSA and micropore volume boosts the H_2 absorption [35].

To illustrate this, Figure 8, using the data of Table 1, shows the trend of absorption as a function of the micropore volume and the SSA for the different samples. It is evident from Figure 8 that the H_2 uptake increased with the increase of the aforementioned textural properties. This behavior occurred because carbon materials with a high micropore volume maximize the interaction potential between the hydrogen molecules and the carbon surface due to the overlap between potential fields, leading to the pore filling and therefore higher H_2 adsorption.

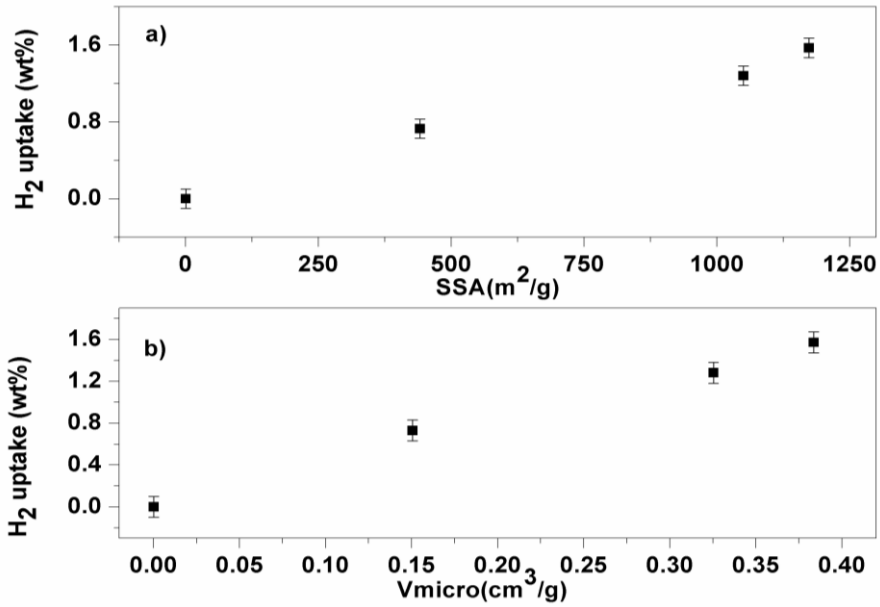

Figure 8. (a) H_2 uptake at 1 bar and 77 K vs. SSA. (b) H_2 uptake at 1 bar and 77 K vs. V_{micro}.

The highest H_2 uptake was obtained for the ADPC1 sample (1.6 wt%) and it was comparable to the literature data [33], taking into account the differences in the textural parameters and their compensation effects. The ADPC3 sample showed a similar absorption capacity at 1 bar, as expected due to their textural properties. To estimate the trend of the samples' adsorption properties, the experimental data were fitted using the Töth equation [50]:

$$wt\% = \frac{wt\%_{\max}\,(K \cdot P_{eq})}{(1 + (K \cdot P_{eq})^{t})^{1/t}}$$

where *t* is the Töth parameter, which is a measure of the degree of homogeneity of the pore surface; $wt\%_{max}$ is the absorption capacity of H_2 that is asymptotically reached at high pressures; and *K* is the kinetic equilibrium constant that represents the energy interaction between gas molecules and pore surfaces. The latter takes into account the affinity of the samples toward the binding of hydrogen molecules on the surface, as well as the occupancy rate of the adsorption sites. The values of these parameters are given in Table 2.

Table 2. Töth equation fitting parameters for the activated samples.

Sample	$wt\%_{max} \pm \Delta wt\%$	$t \pm \Delta t$	$K \pm \Delta K$
ADPC0.5	1.634 ± 0.2	0.254 ± 0.005	4.401 ± 0.03
ADPC1	5.435 ± 0.2	0.244 ± 0.005	2.858 ± 0.03
ADPC3	4.980 ± 0.2	0.242 ± 0.005	2.587 ± 0.03

The *t* parameter was similar, within the error, for all the analyzed samples, which indicated an equal and low homogeneity ($t \cong 0.25$) of the surface adsorption sites. Notably, the *K* values of ADPC1 and ADPC3 samples were very close, indicating their similar adsorption sites and adsorption mechanism (Table 2). This is also clearly visible by examining the curvature of the isotherms (Figure 7). Exceptionally, the ADPC0.5 sample showed higher *K* values compared to the other samples, indicating a much quicker saturation at the adsorption sites.

From the analysis reported in Figure 7, it is quite evident that the adsorption isotherms of the different samples did not approach saturation, which suggests that a higher uptake was possible by increasing the pressure. Consequently, the H_2 adsorption measurements were performed at liquid nitrogen temperatures (77 K) up to 80 bar.

The 77 K isotherms showed a maximum storage capacity at 80 bar (Figure 9) that moved from a minimum value of ≅ 1.8 wt% for the ADPC0.5 sample to a maximum value of ≅ 5.5 wt% for ADPC1. Cycles following the first cycle led to a slight lowering of the maximum adsorption capacity that could be quickly recovered using a mild thermal treatment at 473 K for 12 h (Figure S5). The faint trapping of the H_2 molecules by the ADPCs pores suggested that a weak physisorption process was involved in the interaction between the sorbent and adsorbate, allowing for a completely reversible isotherm, which is different from ultra-microporous commercial ACs [51].

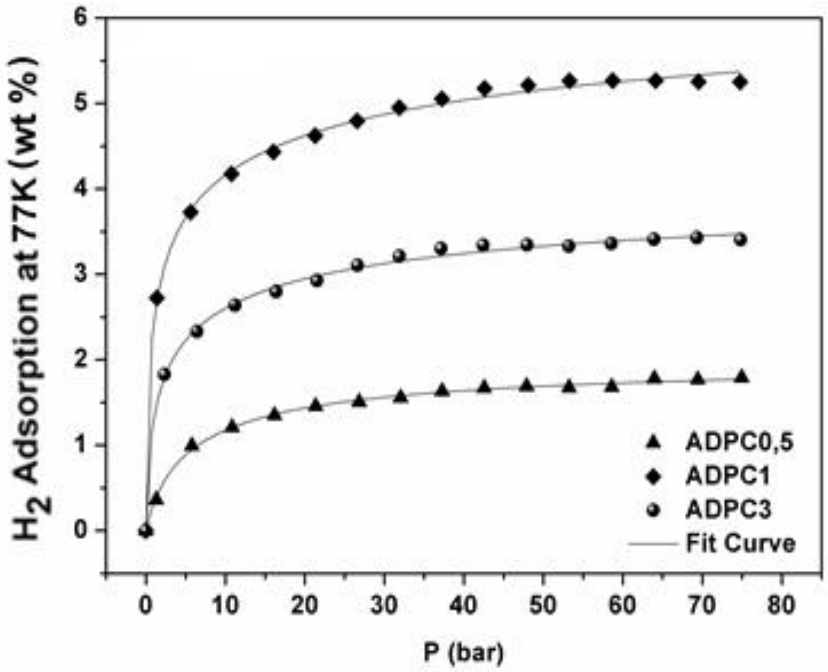

Figure 9. H_2 adsorption isotherms at 77 K up to 80 bar. The magnitude of the error is the size of the symbol itself. Solid lines represent fits to the Töth equation.

It is important to highlight that the H_2 uptake trend when moving to a higher pressure (see Figure 10) was the same as that observed at 1 bar (Figure 8), confirming the relationship between absorption and the textural properties. Our results show the non-universality of the Chahine rule [30,36,37] for the ultra-microporous samples with a high oxygen content. In fact, the ADPC1 sample, whose SSA was equal to 1173 m^2/g, showed an asymptotic uptake (Figure 10a) close to 5.5 wt%, i.e., 14 H_2 molecules/nm^2, which was more than double that of the expected value. Similar results were found for all the analyzed samples. Furthermore, we note that the H_2 uptake was also proportional to the micropore volume (Figure 10 b). Consequently, although the SSA of the analyzed sample was not very large compared to that of similar ACs [26,39], the H_2 uptake of the analyzed samples attained high and remarkable values.

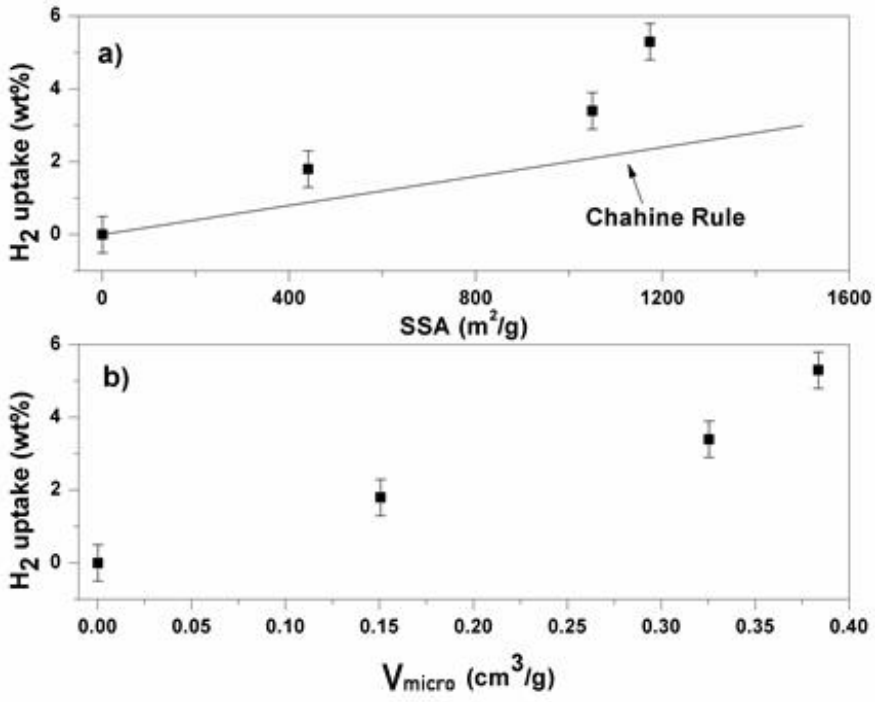

Figure 10. (a) H_2 uptake at 80 bar and 77 K vs. SSA. (b) H_2 uptake at 80 bar and 77 K vs. V_{micro}.

3.1.5 Conclusions

Activated microporous carbon suitable for H_2 storage applications were successfully prepared from stone pine (Pinus pinea) collected from the local area of Sila, Calabria, Italy, using KOH activation processes. All samples showed a pore size distribution centered around 0.5 nm, a fraction micropore volume higher than 50%, and an atomic O/C ratio close to 20%. The highest micropore volume, 0.383 $cm^3 \cdot g^{-1}$, was obtained when the ratio between the dehydrated pinecones biomass and KOH was 1:1. This sample showed the best H_2 storage capacity values

at 77 K: 1.6 wt% at 1 bar 5.25 wt% at 80 bar. These results went well beyond the Chahine rule with an increase of more than 150% relative to the expected values. In conclusion, this work demonstrated that by using pinecone biomass as raw material, together with a small amount of KOH and a simple process, it was possible to produce activated carbon with a high microporosity and a residual oxygen content. Furthermore, we showed that the activated carbon's porosity could be tuned by modifying
the production parameters, allowing for tailoring it for several uses, such as adsorbed natural gas applications, gas separation through molecular sieving, and CO_2 capture.

3.1.6 Supporting Information

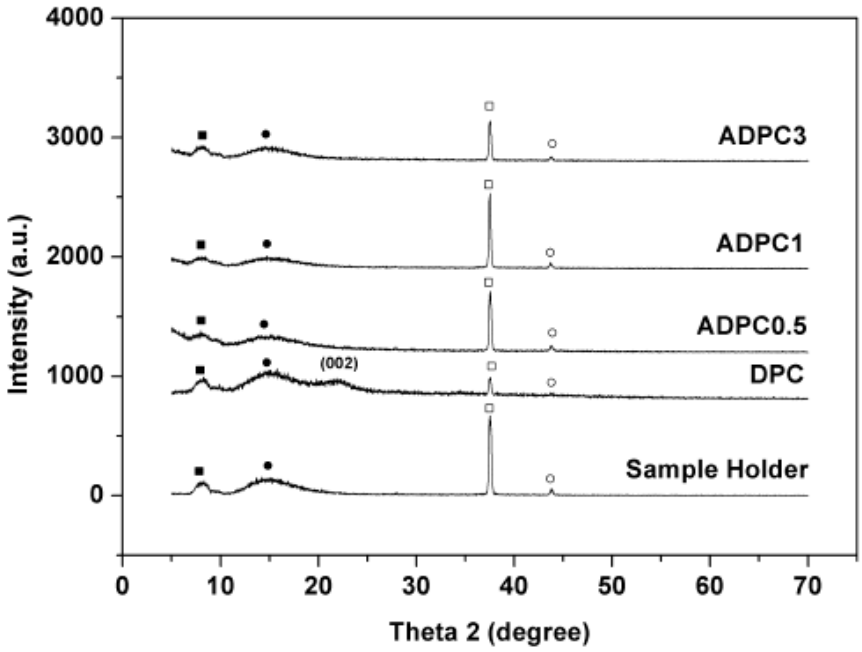

Figure S1: XRD pattern

Table S1: Percentual Chemical Composition of ADPC samples

	C	O	Na	Si	Mg	Al	S	K	Ca	Ti
ADPC1	81,898	17,366	0,007	0,080	0,124	0,016	0,012	0,476	0,018	0,002
ADPC3	80,767	18,059	0,004	0,261	0,127	0,233	0,023	0,460	0,056	0,009

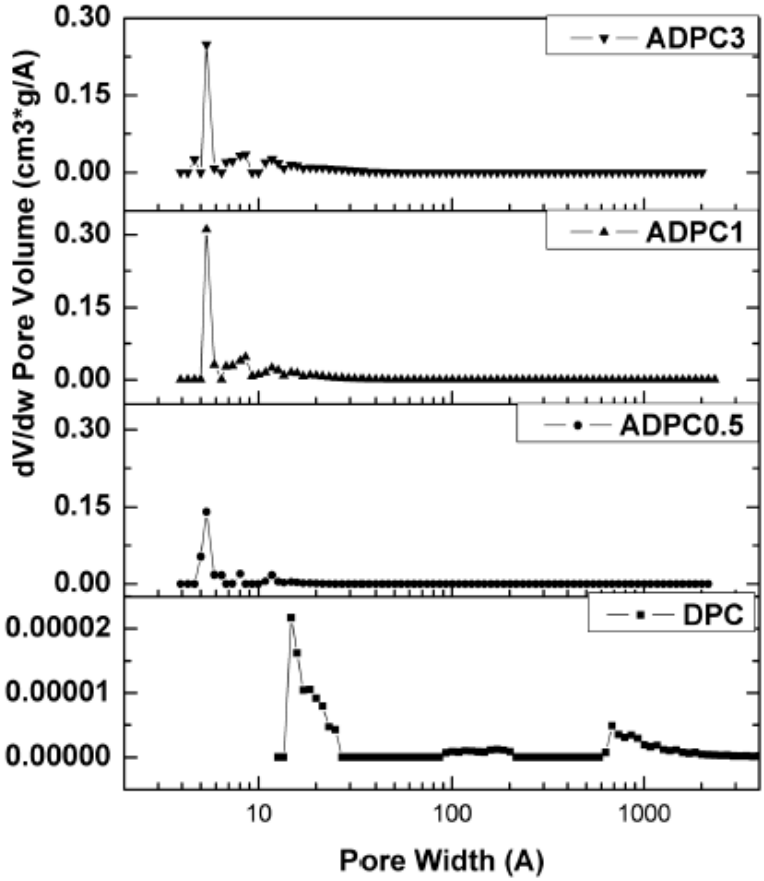

Figure S2: PSD of all samples

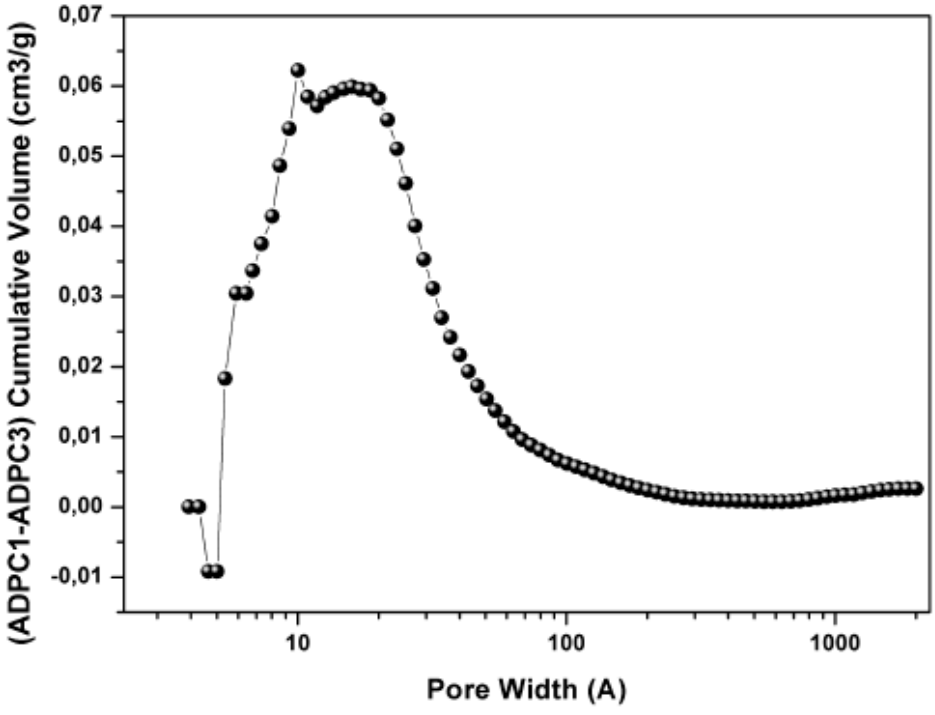

Figure S3: Difference between ADPC1 and ADPC3 Cumulative Volume

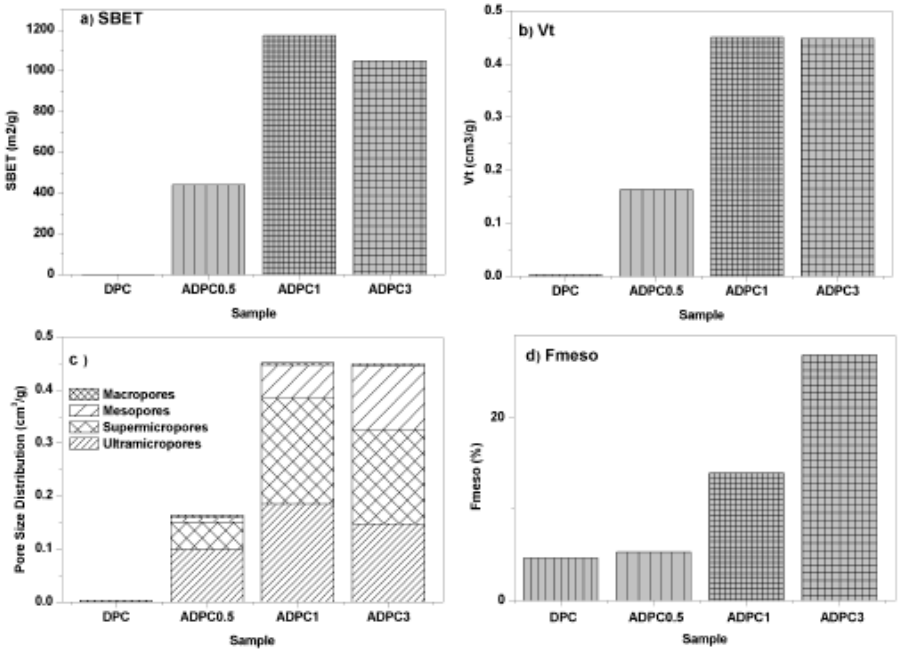

Figure S4: Textural properties vs KOH/PC Ratio a) SBET; b) VT; c) PSD and d) Fraction of mesopore volume. See table 1 for acronyms.

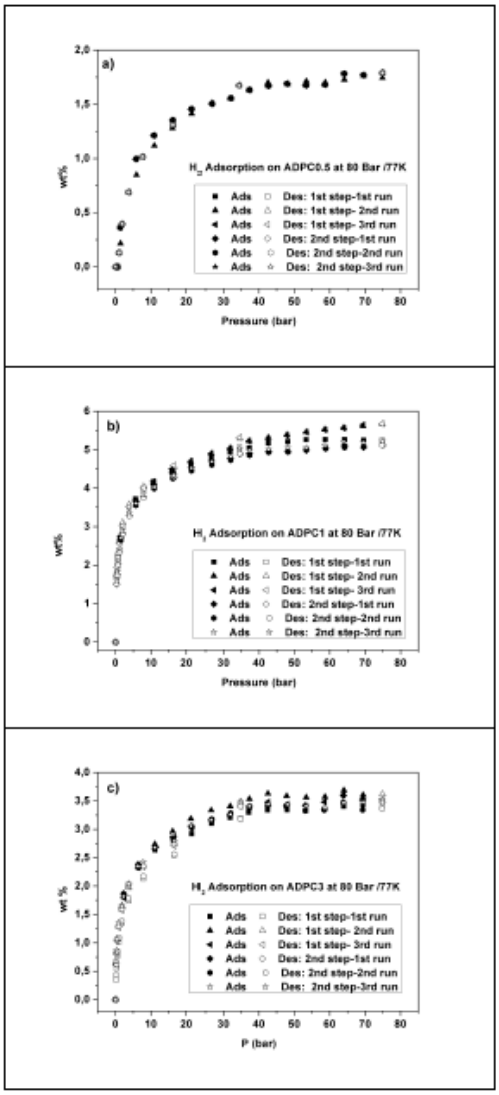

Figure S5: H_2 uptake as function of equilibrium pressure at 77K in a) ADPC0.5 b) ADPC1 and c) ADPC3

References

1. Zervos, A.; Boer, C.L.; Tesniere, L. Mapping Renewable Energy Pathways towards 2020—EU Roadmap; European Renewable Energy Council: Brussels, Belgium, 2011.

2. Götz, M.; Kolb, T.; Reimert, R. Renewable Power-to-Gas: A technological and economic review. Renew. Energy 2016, 85, 1371–1390.

3. Niaz, S.; Manzoor, T.; Pandith, H.A. Hydrogen storage: Materials, methods and perspectives. Renew. Sustain. Energy Rev. 2015, 50, 457–469.

4. Ren, J.; Nicholas, M.; Shijun, L. Current research trends and perspectives on materials-based hydrogen storage solutions: A critical review. Int. J. Hydrogen Energy 2017, 42, 289–311.

5. Burchell, T.D. Carbon Materials for Advanced Technologies; Elsevier Science Ltd: Oxford, UK, 1999.

6. Peng, S.; Li, L.; Tian, L.L.; Adams, S. Electrospun carbon nanofibers and their hybrid composites as advanced materials for energy conversion and storage. Nano Energy 2016, 22, 361–395.

7. Policicchio, A.; Maccallini, E.; Ciuchi, F.; Giordano, G. Higher methane storage at low pressure and room temperature in new easily scalable large-scale production activated carbon for static and vehicular applications. Fuel 2013, 104, 813–821.

8. Pantò, F. Electrospun C/GeO2 paper-like electrodes for flexible Li-ion batteries. Int. J. Hydrogen Energy 2017, 42, 28102–28112.

9. Faye, O.; Szpunar, J.A. An Efficient Way To Suppress the Competition between Adsorption of H2 and Desorption of nH2–Nb Complex from Graphene Sheet: A Promising Approach to H2 Storage. J. Phys. Chem. C 2018, 122, 28506–28517.

10. Faye, O.; Tanveer, H.; Amir, K.; Jerzy, S. Tailoring the capability of carbon nitride (C3N) nanosheets toward hydrogen storage upon light transition metal decoration. Nanotechnology 2018, 30, 075404.

11. Gajdics, M.S.T.; Kovács Kis, V.; Béke, F.; Novák, Z.; Schafler, E.; Révész, Á. Microstructural Investigation of Nanocrystalline Hydrogen-Storing Mg-Titanate Nanotube Composites Processed by High-Pressure Torsion. Energy 2020, 13, 563.

12. Gadipelli, S. Superior Multifunctional Activity of Nanoporous Carbons with Widely Tunable Porosity: Enhanced Storage Capacities for Carbon-Dioxide, Hydrogen, Water, and Electric Charge. Adv. Energy Mater. 2020, 10, 1903649.

13. Belaustegui, Y.; Zorita, S.; AntonuccI, P.; Panto, F. Electro-spun graphene-enriched carbon fibres with high nitrogen-contents for electrochemical water desalination. Desalination 2018, 428, 40–49.

14. Yang, J.; Yue, L.; Hu, X.; Zhao, Y.; Lin, Y. Efficient CO2 Capture by Porous Carbons Derived from Coconut Shell. Energy Fuels 2017, 31, 4287–4293.

15. Titirici, M.-M.; White, R.J.; Brun, N. Sustainable carbon materials. Chem. Soc. Rev. 2015, 44, 250–290.

16. Wang, J.; Ding, B.; Dong, S.Y.; Hao, X.D. Biomass derived carbon for energy storage devices. J. Mater. Chem. A 2017, 5, 2411–2428.

17. Schröder, E.; Oechsler, K.T.B.; Herberger, S. Activated Carbon from Waste Biomass. In Progress in Biomass and Bioenergy Production; Shaukat, S.S., Ed. IntechOpen, University of Karachi: Karachi,Sindh,Pakistan, 2011.

18. Khalil, H.P.S.A.; Jawaid, M. Activated Carbon from Various Agricultural Wastes by Chemical Activation with KOH: Preparation and Characterization. J. Biobased Mater. Bioenergy 2013, 7, 708–714.

19. Zhang, F.; Li, G.-D.; Chen, J.-S. Effects of raw material texture and activation manner on surface area of porous carbons derived from biomass resources. J. Colloid Interface Sci. 2008, 327, 108–114.

20. Deng, J.; Li, M.; Wang, Y. Biomass-derived carbon: Synthesis and applications in energy storage and conversion. Green Chem. 2016, 18, 4824–4854.

21. Gao, Z. Biomass-derived renewable carbon materials for electrochemical energy storage. Mater. Res. Lett. 2017, 5, 69–88.

22. Wang, H.; Yu, W.; Shi, J.; Mao, N. Biomass derived hierarchical porous carbons as high-performance anodes for sodium-ion batteries. Electrochim. Acta 2016, 188, 103–110.

23. Zhang, C.; Geng, Z.; Cai, M.; Zhang, J. Microstructure regulation of super activated carbon from biomass source corncob with enhanced hydrogen uptake. Int. J. Hydrogen Energy 2013, 38, 9243–9250.

24. Xiao, Y.; Dong, H.; Long, C.; Zheng, M.T. Melaleuca bark based porous carbons for hydrogen storage. Int. J. Hydrogen Energy 2014, 39, 11661–11667.

25. Heo, Y.-J.; Park, S.-J. Synthesis of activated carbon derived from rice husks for improving hydrogen storage capacity. J. Ind. Eng. Chem. 2015, 31, 330–334.

26. Bader, N.; Ouederni, A. Optimization of biomass-based carbon materials for hydrogen storage. J. Energy Storage 2016, 5, 77–84.

27. Choi, Y.-K.; Park, S.-J. Preparation and characterization of sucrose-based microporous carbons for increasing hydrogen storage. J. Ind. Eng. Chem. 2015, 28, 32–36.

28. Ramesh, T.; Rajalakshmi, N.; Dhathathreyan, K.S. Synthesis and characterization of activated carbon from jute fibers for hydrogen storage. Renew. Energy Environ. Sustain. 2017, 2, 4.

29. Manocha, S. Activated carbon from biomass. AIP Conf. Proc. 2013, 1538, 120–123.

30. Jiménez, V.; Paula, S. Hydrogen storage in different carbon materials: Influence of the porosity development by chemical activation. Appl. Surf. Sci. 2012, 258, 2498–2509.

31. Min, S.; Bao, S.; Jin, R.; Xiao, L.; Wu, Y.; Zhong, Z.;Huang, Y.J. The comparison of two activation techniques to prepare activated carbon from corn cob. Biomass Bioenergy 2013, 48, 250–256.

32. Härmas, M. Microporous–mesoporous carbons for energy storage synthesized by activation of carbonaceous material by zinc chloride, potassium hydroxide or mixture of them. J. Power Sources 2016, 326, 624–634.

33. Sethia, G.; Sayari, A. Activated carbon with optimum pore size distribution for hydrogen storage. Carbon 2016, 99, 289–294.

34. Wang, J.; Kaskel, S. KOH activation of carbon-based materials for energy storage. J. Mater. Chem. 2012, 22, 23710–23725.

35. Minoda, A. Synthesis of KOH-activated porous carbon materials and study of hydrogen adsorption. J. Alloy. Compd. 2013, 580, S301–S304.

36. Masika, E.; Mokaya, R. Hydrogen Storage in High Surface Area Carbons with Identical Surface Areas but Different Pore Sizes: Direct Demonstration of the Effects of Pore Size. J. Phys. Chem. C 2012, 116, 25734–25740.

37. Gogotsi, Y. Importance of pore size in high-pressure hydrogen storage by porous carbons. Int. J. Hydrogen Energy 2009, 34, 6314–6319.

38. Cabria, I.; López, M.J.; Alonso, J.A. The optimum average nanopore size for hydrogen storage in carbon nanoporous materials. Carbon 2007, 45, 2649–2658.

39. Sangchoom, W.; Mokaya, R. Valorization of Lignin Waste: Carbons from Hydrothermal Carbonization of Renewable Lignin as Superior Sorbents for CO2 and Hydrogen Storage. ACS Sustain. Chem. Eng. 2015, 3, 1658–1667.

40. Yang, H.; Yan, R.; Chen, H. Characteristics of hemicellulose, cellulose and lignin pyrolysis. Fuel 2007, 86, 1781–1788.

41. Bello, A. Renewable pine cone biomass derived carbon materials for supercapacitor application. RSC Adv. 2016, 6, 1800–1809.

42. Duman, G. Production of Activated Carbon from Pine Cone and Evaluation of Its Physical, Chemical, and Adsorption Properties. Energy Fuels 2009, 23, 2197–2204.

43. Blankenship Ii, T.S.; Balahmar, N.; Mokaya, R. Oxygen-rich microporous carbons with exceptional hydrogen storage capacity. Nat. Commun. 2017, 8,. 1545.

44. Brunauer, S.; Emmett, P.H.; Teller, E. Adsorption of Gases in Multimolecular Layers. J. Am. Chem. Soc. 1938, 60, 309–319.

45. Seaton, N.A.; Walton, J.P.R.B.; Quirke, N. A new analysis method for the determination of the pore size distribution of porous carbons from nitrogen adsorption measurements. Carbon 1989, 27, 853–861.

46. Policicchio, A. Volumetric apparatus for hydrogen adsorption and diffusion measurements: Sources of systematic error and impact of their experimental resolutions. Rev. Sci. Instrum. 2013, 84, 103907.

47. Qu, D. Investigation of Hydrogen Physisorption Active Sites on the Surface of Porous Carbonaceous Materials. Chem. Eur. J. 2008, 14, 1040–1046.

48. Sing, K.S.W.; Haul, D.H.E.L.; Pierotti, R.A.; Rouquerol, J.; Siemieniewska, T. Reporting Physisorption Data for Gas/Solid Systems. In Handbook of Heterogeneous Catalysis; Wiley-VCH Verlag GmbH & Co. KGaA, Weinheim, Germania, 2008; pp. 1217–1230.

49. Xin, W.; Song, Y. Mesoporous carbons: Recent advances in synthesis and typical applications. RSC Adv. 2015, 5, 83239–83285.

50. Toth, J. Adsorption Theory, Modeling and Analysis; Marcel Dekker: New York, NY,USA, 2020.

51. Minuto, F.D.; Aloise, A.; Policicchio, A. Liquid-like hydrogen in the micropores of commercial activated carbons. Int. J. Hydrogen Energy 2015, 40, 14562–14572.

3.2 Low Pressure Methane Storage in Pinecone-Derived Activated Carbons

3.2.1 State of the art

In the last 10 years, the growing energy demand and the need to decrease the environmental effects from the use of fossil fuels have led to the study of new clean fuels. In particular, attention is paid to those who show lower atmospheric emissions and higher availability than conventional petroleum. Among these we find hydrogen and natural gas (NG), two alternative fuels which have many similarities: both are gaseous at room temperature and can be stored as cryogenic liquid or compressed gases [1].

Natural gas is composed of chiefly methane (CH_4) and, compared to gasoline, has a higher energy per mass of fuel, a higher combustion efficiency, a lower cost, and a much cleaner burning, as it contains less carbon per unit of energy of any fossil fuel. The main NG drawback is its low energy density, which can be improved using two different techniques: the first named compressed natural gas (CNG) in which NG is stored at high pressure and room temperature (actually used for mobile applications), with an energy density of 9.2 MJ/L; the second is the liquefied natural gas (LNG) in which NG is stored as a liquid at 112 K and atmospheric pressure (actually used for long-distance gas transportation), with an energy density of 22.2 MJ/L [2].

A more recent and less-demanding solution in terms of pressure and temperature concerns CH_4 storage in porous materials (adsorbed natural gas, ANG). This technology allows, under 500 psi (~35 bar), 80% of volumetric energy density of CNG under 3000 psi (~207 bar), with an acceptable gas density (3-8 MJ/L) [3-5].

To date, a variety of microporous solid materials [6-8], such as zeolites [9] and activated carbons [10], have been used for gas storage applications above all thanks to their microporosity. Previous studies, in fact, have evaluated the effect of pore size and geometry in gas storage capacities demonstrating that in microporous materials there is an overlap of pore wall potentials, which allows the confinement of high quantities of gas molecules and therefore a high adsorption capacity [11].

Among the different materials, the carbon-based ones have unique characteristics (good electronic conductivity, adjustable porosity/morphology, and excellent stability) that allow them to play important roles in various technologies [12], from the energy and gas storage [10,13,2] to the water treatment [14].

The turning point for a greener economy is not only the use of new clean fuels, but also the technology that revolves around their application. In this regard, many carbon materials for

ANG are generally produced from precursors based on fossil fuels [15] with harmful and costly methods for the environment. To overcome this problem, the research is turning its attention increasingly to the biomass that is an excellent precursor for the production of activated carbons (ACs) with chemical-physical properties such as to be applied advantageously in different sectors [16-19]. Up to now, to our knowledge, only a few articles have been published concerning the use of biomass ACs for CH_4 storage and none having pinecones as a precursor [20-23].

Pinecones are widely available biomass and a carbon source over their entire parts, being essentially composed of cellulose and lignin [24]. Powdered pinecones show a porous nature able to absorb several chemical active agents, thus providing an excellent platform to optimize the morphology of the final products. As a porous carbon source, they have been extensively studied as a biosorbent for water treatment [25], electrodes for supercapacitors and lithium-ion batteries [26] and gas storage [27], but there are no reports on the use of pinecone-derived carbons for CH_4 storage.

Generally, the ACs were prepared by subsequent pulverization and carbonization of raw materials in an inert gas atmosphere at an appropriate temperature followed by chemical or physical activation [28]. Among the latter, the chemical activation in KOH is the one that allows the acquisition of porous coals with ultrahigh specific surface area (SSA) and well-defined porosity which give rise to excellent properties in energy storage and conversion [29]. This experimental work deals with the synthesis of ACs from pinecone and the modification of their morphology via KOH activation to enhance textural properties and CH_4 storage capacity. The ACs samples were then synthesized using different KOH/pinecone powder weight ratios investigating how the latter influences the sample's features such as microstructure and CH_4 storage capacity and how they are connected to each other.

3.2.2 Experimental section

3.2.2.1 Materials

The ACs were prepared starting from pinecones from Stone Pine (Pinus pinea). The cones were washed repeatedly with distilled water (DW) to remove soluble impurities, dried at 353 K for 12 h and then pulverized using a blender to obtain a pinecone powder (PC). The latter was dehydrated at 453 K for 5 h (DPC) and then it was placed in a solution (100 mL) of DW with a weight-ratios of KOH/DPC (0.5, 1, and 3) and stirred for 24 h at 353 K.

After the moisture was removed, the black colored mixture was then transferred to a ceramic crucible in a tubular furnace under He (He, 99.999% purity) flow of 100 mL/min and heated at 1173 K for 2 h with a heating rate of 5 K/min to complete the activation process. Finally, the resulting dark solid material (ADPCx, activated dehydrated-carbonized pinecone in which x denote the KOH/DPC ratio) was washed with distilled water until the neutral pH was obtained and dried at 353 K in an electric oven in air.

3.2.2.2 Characterization

To investigate in depth the synthesized systems and correlate their chemical, structural, and morphological features with the adsorption/desorption ones, different techniques were used. In particular, we performed systematic scanning electron microscopy (SEM), X-ray diffraction (XRD), and nitrogen adsorption-desorption characterizations to investigate chemical, structural, and morphological properties, while the volumetric technique (f-PcT isotherms) was performed to evaluate CH_4 adsorption/desorption properties.

A FEI Quanta FEG 200 field emission scanning electron microscopes (ESEM) with an electron beam of 20 keV was employed to record scanning electron images in order to observe morphology changes in the samples subjected to the activation process.

The phase structure of the samples was examined through XRD patterns measured on a Philips PW 1830 diffractometer using Cu Ka (40 kV, 40 mA) filtered radiation. Measurements were performed in reflection mode placing the sample powder on the special homemade sample holder. All analyses were acquired at room temperature (RT $\cong$ 298 K) and the patterns recorded in the 2-theta (2θ) range from 2° to 70°, in steps of 0.02° and counting time 1 s per step. The effect related to the sample stage has been taken into account.

Structural properties of the samples were carried out by physical adsorption of N_2 at 77 K using a Micromeritics ASAP 2460 apparatus. Before each adsorption measurement, the activated samples were dried under vacuum at 473 K for 12 h. The SSA was calculated according to the Brunauer-Emmett-Teller (BET) method [30] within a relative pressure range of 0.005-0.11. The total pore volume V_T was calculated from the N_2 uptake at relative pressure P/P_0 of 0.995; the total micropore volume V_{micro} and the pore size distributions (PSD) were calculated by Density Functional Theory (DFT) considering slit-shaped pores [31].

The CH_4 adsorption measurements, at room temperature (RT), were carried out from 0 to 35 bar with a Sieverts' apparatus (f-PcT) realized by DeltaE S.r.l. [32]. The gas storage capacity, as weight percent of gas adsorbed per gram of adsorbent (wt%), was determined from

adsorption isotherms. Before starting any adsorption/desorption test, all samples were outgassed at 473 K overnight.

3.2.3 Results and discussion

3.2.3.1 Surface and Structural Analysis

Scanning electron microscopy analysis (see Supporting Information Figure S1) performed on the DPC and ADPC samples reveals that the dehydrated sample exhibits a smooth surface, while the activated ones show a sponge-like morphology with heterogeneous pores. Increasing KOH/DPC ratio leads to an enlargement of the pores and to the presence of a microporous structure on the surfaces separating the macropores. Therefore, it could be confirmed that the KOH activation process is the maker of the formation of porous cavities into the material [29]. In fact, the activation mechanism involves a series of redox reactions between the potassium compounds and carbon producing an etching of the carbon framework generating the amorphous non graphitic pore network [29,28], such as confirmed by XRD analysis (see Figure S2).

3.2.3.2 Textural Properties Analysis

N_2 adsorption/desorption tests performed on the DPC sample does not show any appreciable uptake and consequently any porosity, while, according to the IUPAC classification [33], the activated samples show Type I and Type IV isotherms with a decreasing adsorption and extensive widening of the isotherm knee and of the hysteresis loop as the ratio KOH/DPC increases (see Figure S3). This behavior can be attributed to the destruction of micropores and the development of mesopores that takes place due to excessive KOH content [29].

As reported in Figure S4, a further evidence of the activation process effects is obtained clearly by the PSD of the investigated samples calculated by using the DFT; the results show a homogeneous porosity concentrated below 10 Å, which is a relevant feature for an effective absorption of CH_4. In fact, the requirements for a material to exhibit a high CH_4 storage capacity are first a large volume of micropores, where CH_4 molecules can be strongly adsorbed; second a narrow pore size distribution, centered around 8-12 Å, which is the optimal size required to accommodate two/three CH4 molecules [15].

With this in mind, it is possible to state that the KOH/DPC ratio is a fundamental parameter in the development of porosity and, in particular, the microporosity increases as the impregnation ratio increases, showing the highest value for the KOH/DPC ratio equal to 1. A

further increase in the KOH/DPC ratio leads to the development of the mesoporosity of the ACs in the range 20-200 Å.

The textural properties, deduced from the N_2 adsorption isotherms are reported in Table 1.

Table 1. Textural properties of ADPCx Samples.

Sample	KOH/ DPC	[a] S_{BET} (m^2/g)	[b] V_T (cm^3/g)	[c] V_{micro} (cm^3/g)	DFT Cumulative Pore Volume (cm^3/g)		[f] V_{meso} (cm^3/g)	[g] V_{macro} (cm^3/g)	[h] F_{micro} (%)	[h] $F_{ultra-m}$ (%)	[h] $F_{super-m}$ (%)	[h] F_{meso} (%)
					[d] Ultra-Micro	[e] Super-Micro						
DPC	0	0.42	0.003	0.0001	0	0.0001	0.0001	0.0028	3	0	3	4
ADPC0.5	0.5	441	0.1633	0.1506	0.0993	0.0513	0.0087	0.0041	92	61	31	5
ADPC1	1	1173	0.4513	0.3836	0.1854	0.1982	0.0630	0.0048	85	41	44	14
ADPC3	3	1050	0.4487	0.3254	0.1479	0.1775	0.1204	0.0030	73	33	40	27

[a] S_{BET}: specific surface area computed using BET equation in the relative pressure range of 0.005-0.1. [b] V_T: total pore volume estimated at a relative pressure $P/P_0 = 0.99$. [c] V_{micro}: micropore volume determined from cumulative volume. [d] Ultramicropores: volume of pores with less than 7 Å width. [e] Supermicropores: volume of pores with less than 20 Å width. [f] V_{meso}: volume of pores with less than 50 nm width. [g] V_{macro}: macropore volume determined from subtraction of micropore and mesopore volume from total pore volume. [h] F_{micro}: fraction of (microultra-supermeso)pore volume = ((microultra-supermeso) pore volume/total pore volume) × 100.

Here the proportion of ultramicropores, supermicropores, and mesopores is evaluated following the IUPAC classification [33]. As seen in Figure 1, the microporous fraction (F_{micro}) changes with the KOH/DPC ratio such as the other textural properties. In particular, the F_{micro} decreases as the KOH increases in favor of an increase in the mesoporous fraction that can be attributed to the damage of the porous structure caused by excessive KOH treatment.

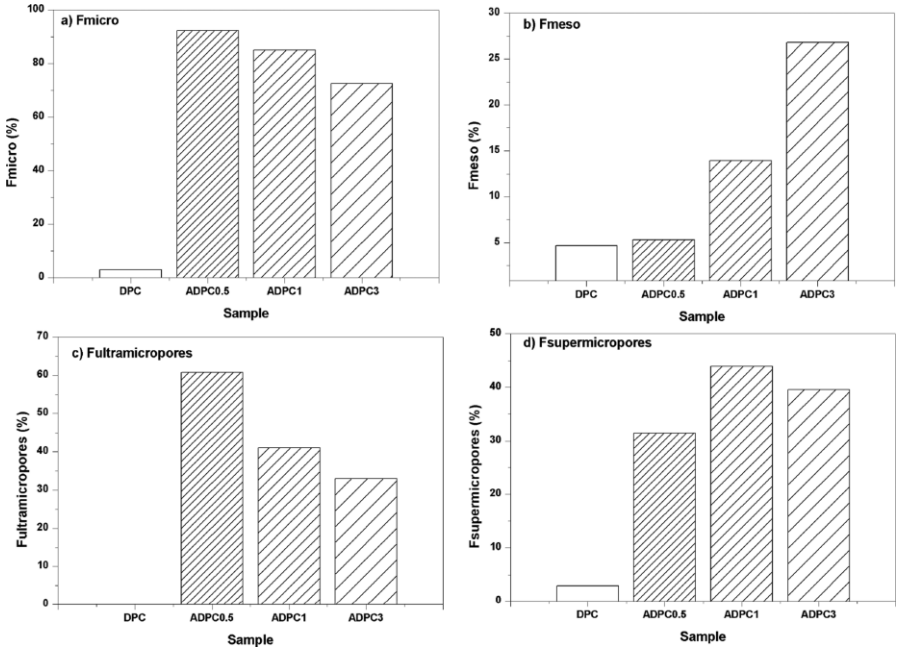

Figure 1. Fraction of pore volume.

The ADPC1 one has the highest supermicropore fraction which decreases in favor of the mesopore one when the KOH/DPC ratio increases above 1. Comparing the obtained results with literature [2,23,34,10,34,8], despite a similar PSD and lower values for both V_T and SSA, the ADPCs have a higher supermicroporous fraction which makes the pinecones an excellent precursor for the synthesis of high microporous carbons for CH_4 storage. Furthermore, a first sight to structural results seems to indicate that the optimization of synthesis parameters could further improve the samples features.

3.2.3.3 Methane adsorption

To check the CH_4 adsorption capabilities, each sample was subjected to adsorption tests up to 35 bar at RT conditions, and representative CH_4 storage data are given below in Table 2.

Table 2. Toth Equation Fitting Parameters and Methane Activity for the ADPC Samples.

Sample	CH_4 activity (wt %)	$wt\%_{max} \pm \Delta wt\%_{max}$	$t \pm \Delta t$	$K \pm \Delta K$
ADPC0.5	10.3	11.91 ± 0.39	0.89 ± 0.09	0.29 ± 0.04
ADPC1	15.0	21.95 ± 1.10	0.74 ± 0.06	0.13 ± 0.01
ADPC3	9.0	10.73 ± 0.34	1.00 ± 0.01	0.14 ± 0.02

The reliability of the ADPCs performance in term of cyclic life was tested by submitting all samples to multiple CH_4 adsorption/desorption cycles with and without any thermal treatment in between while the CH_4 activity is a calculated parameter that represents the fraction of the CH_4 adsorbed into the carbon's micropores (represented as a percentage of the carbon's mass). All ADPCs show a reversible behavior up to many cycles, within the experimental error, as reported in the Figures 2-4 (see also Figure S5).

Even if the reversibility of the process is almost the same for all of them, a different grade of interaction and storage capacity is observed as demonstrated by isotherms comparison and Töth analysis (see below).

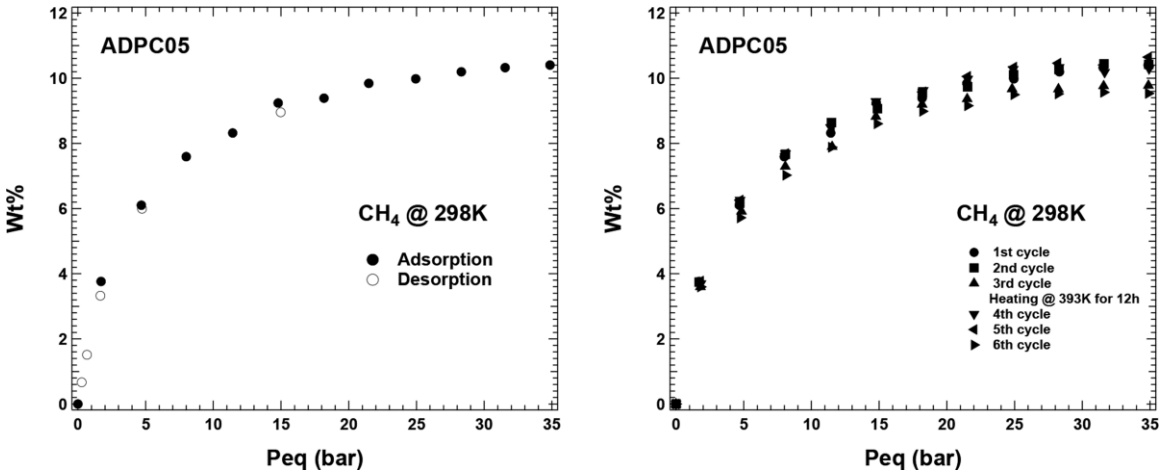

Figure 2. (a) Methane adsorption/desorption isotherms and (b) methane adsorption isotherm cycles on ADPC05 samples up to 35 bar at T ≅ 298 K.

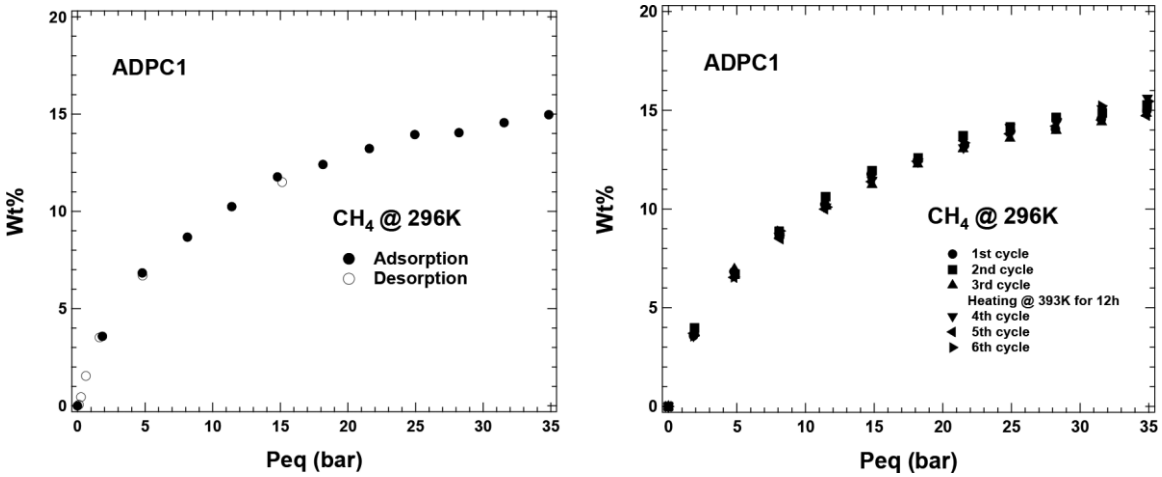

Figure 3. (a) Methane adsorption/desorption isotherms and (b) methane adsorption isotherm cycles on ADPC1 sample up to 35 bar at T ≅ 296 K.

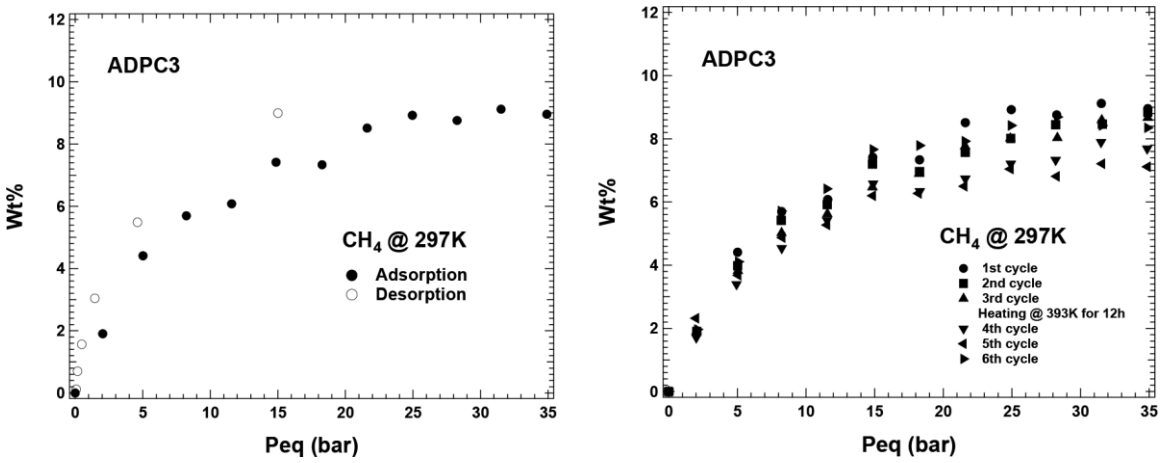

Figure 4. (a) Methane adsorption/desorption isotherms and (b) methane adsorption isotherm cycles on ADPC3 sample up to 35 bar at T ≅ 297 K.

Comparing the adsorption isotherms (see Figure 5), it is evident that the best performance is obtained by the ADPC1 who reaches an uptake value, at the maximum analyzed pressure, close to 15 wt%. It is immediately followed by the ADPC05 sample with a storage capacity of ≅ 10 wt%. The lowest value is obtained testing the ADPC3 sample that moves down to a minimum value around 9 wt%. The observed behavior gives an indication that the best synthesis parameters are the ones used to obtain the ADPC1 sample. All adsorption isotherms usually show (see Figure 5) a CH_4 uptake that rapidly increases at low pressure while moving to higher pressures approach a linear rate of increase.

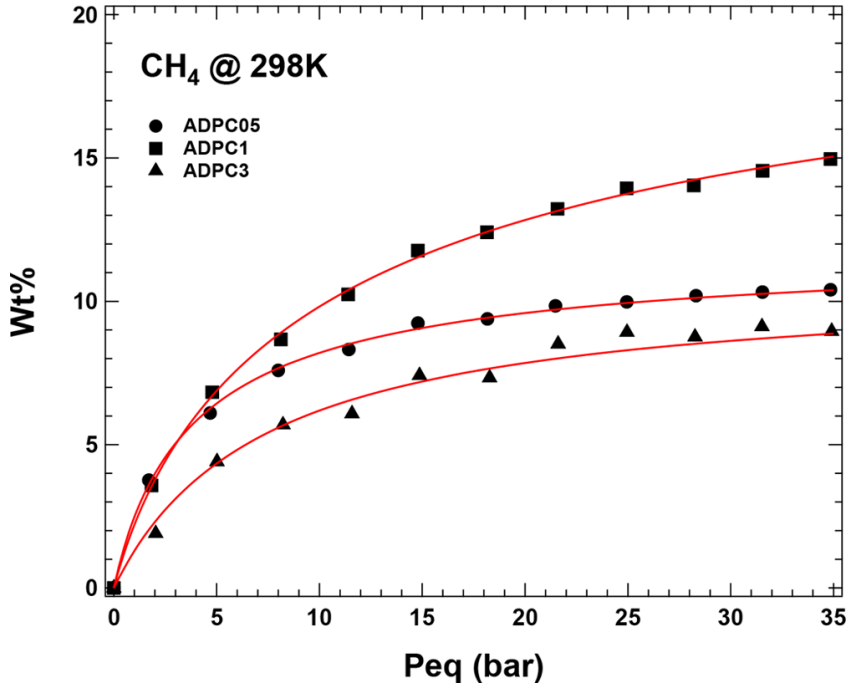

Figure 5. Comparison of CH_4 PcT isotherm obtained for ADPC samples at room temperature (T ≅ 298 K) up to 35 bar. The magnitude of the error is the symbol itself. Line between points is a Toth/Langmuir fitting equation.

According to literature [35], the adsorption occurs preferentially within supermicropores (< 2 nm) and mesopores (2-50 nm) like in the activated carbon materials [35-37], and that is the reason why the supermicroporosity is supposed to be important for CH_4 storage. The narrow width of the pores leads, in fact, to overlapping forces from opposing pore walls and therefore to increased gas density [9]. Therefore, the adsorption performances depend on both the CH_4/surface bond strength and the SSA value and, while a certain proportionality is expected with the latter parameter, an increase of the former one causes a rapid increase of the adsorbed molecules with the increase of the gas pressure. Looking at Table 1 and Figure 5, according to what has just been emphasized in fact, it is evident how the better textural parameters of the ADPC1 sample lead to its higher adsorption capacity compared with the other samples.

Therefore, as previously shown (see Figures 2-4) it appears the more stable is subjected to cycling in fact, while for the ADPC05 and ADPC3, a variation in the maximum adsorption capacity could be observed, its subsequent adsorption isotherms perfectly overlap.

To evaluate the sample's adsorption properties and their trend and to determinate the theoretical maximum storage capacity, the equilibrium constant, and homogeneity grade of the pore surfaces, the experimental adsorption-desorption isotherms were fitted by the Töth equation [38]:

$$wt\% = \frac{wt\%_{max}\,(K \cdot P_{eq})}{(1 + (K \cdot P_{eq})^{t})^{1/t}}$$

where *K* is the equilibrium constant, t, is a parameter introduced by Töth, connected to the homogeneity grade of the sample surface, and $wt\%_{max}$ is the asymptotic maximum storage capacity. The *K* constant, related to the energetic interaction between the adsorbent and the adsorbate, is indicative of the affinity of the samples toward CH_4 retention on the surface and the rate of the occupation of the adsorption sites. The Töth parameters are shown in Table 2.

The grade of homogeneity is lower for the ADPC1 sample (*t* close to 0.8) while a very homogeneous surface is found (*t* close to 1) for the remaining samples (see Table 2). It is also notable that the *K* values of all analyzed ADPC samples are almost close within the experimental error. A slight difference is observed on the ADCP05 sample which shows a larger value (higher interaction between incoming molecules and surface adsorption sites). The latter is in agreement with the observed isotherms curvature of Figure 5 where a higher *K* value corresponds to a quicker saturation of the adsorption sites directly linked to the largest supermicropore fraction shown by this sample. Our results, as already outlined, confirm the relationship between absorption and textural properties. However, in all cases we could assert that the interaction between sorbent and adsorbate is due to a weak physisorption process that results almost completely reversible.

In view of mobile and/or static applications, evaluation of the improvement of the ANG technology (based on our materials) compared to the classical CNG has been evaluated up to the maximum analyzed pressure of 35 bar. Below in Figure 6 a comparison of both technologies is shown.

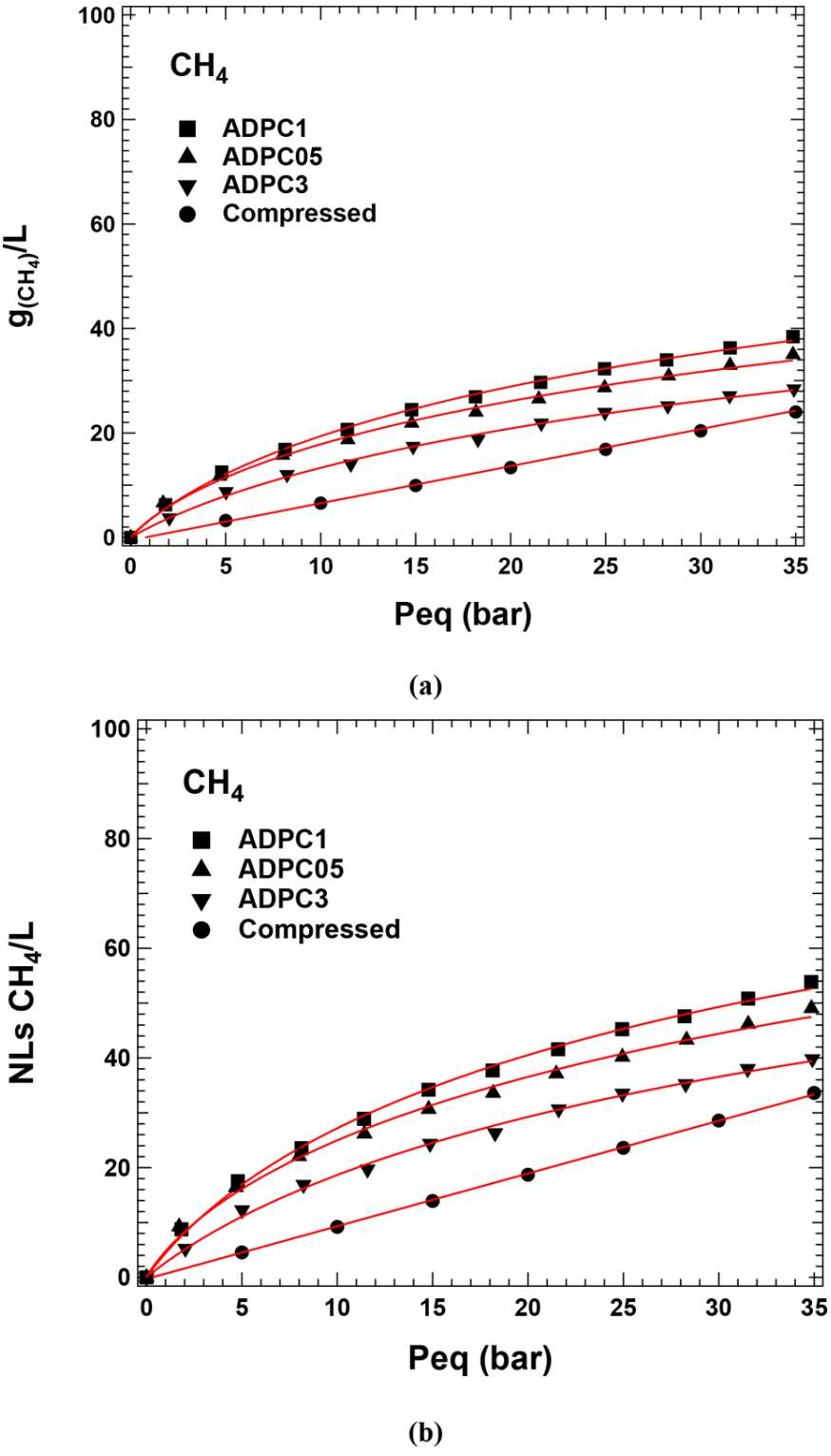

Figure 6. Methane storage capacity comparison in terms of (a) $g_{(CH4)}$/liter and (b) $NL_{(CH4)}$/L at room temperature conditions.

Figure 6a shows the storage capacity in terms of $g_{(CH4)}$/L (mass of gas per liter of tank) while in Figure 6b the same picture is reported in terms of $NL_{(CH4)}$/L (STP liters of gas per liter of tank). Looking at both, it is clear how the use of nanostructured materials, in particular ADPCx samples, helps to improve the storage capacity. In particular, the ADPC1 allows increasing at 35 bar almost 60% the quantity in grams or liters respectively of CH_4 per liter of tank. It is

also interesting to note that it is possible to maintain an improvement with respect to the compressed methane also moving to a lower operative pressure. Figure 6 shows that all ADPC samples, even if in different percentages, succeed in achieving better values than CNG.

3.2.4 Conclusion

This work presented a method to prepare activated carbons starting from biomass residues, in particular pinecones, by a KOH activation process, and how synthesis parameters influence the samples textural properties.

In particular we observed that changing of the KOH/DPC ratio leads to specific surface area, and total pore volume of the ADPC samples varied from 440 to 1150 m^2/g and from 0.16 to 0.45 cm^3/g, respectively. Therefore, those features were investigated to check the effect on the physical CH_4 adsorption/desorption properties. Volumetric measurement through Sievert-type apparatus allowed an estimation of the total CH_4 storage capacity at 298 K, reaching values up to 15 wt% at relatively low pressure (35 bar).

In terms of practical applications, the latter means an increase compared to the CNG technology of almost 60% of the quantity in terms of grams or liters, respectively, of CH_4 per liter of tank.

The composite structure offers distinct advantages over conventional materials as we demonstrate with this experimental work that it is possible to synthesize activated carbons with high microporosity from waste biomass using a small KOH amount in a simple process, and all of them own a completely reversible CH_4 adsorption/desorption process.

In conclusion, this simple production process allows tuning the porosity of materials through a single process parameter opening the possibility of development of adsorbed natural gas technology and allowing easy use of CH_4 as fuel. In particular, for example, because the process works at so low pressure, people would be able to recharge their own vehicles directly at home where the pressure is no more than a few bars.

3.2.5 Supporting Information

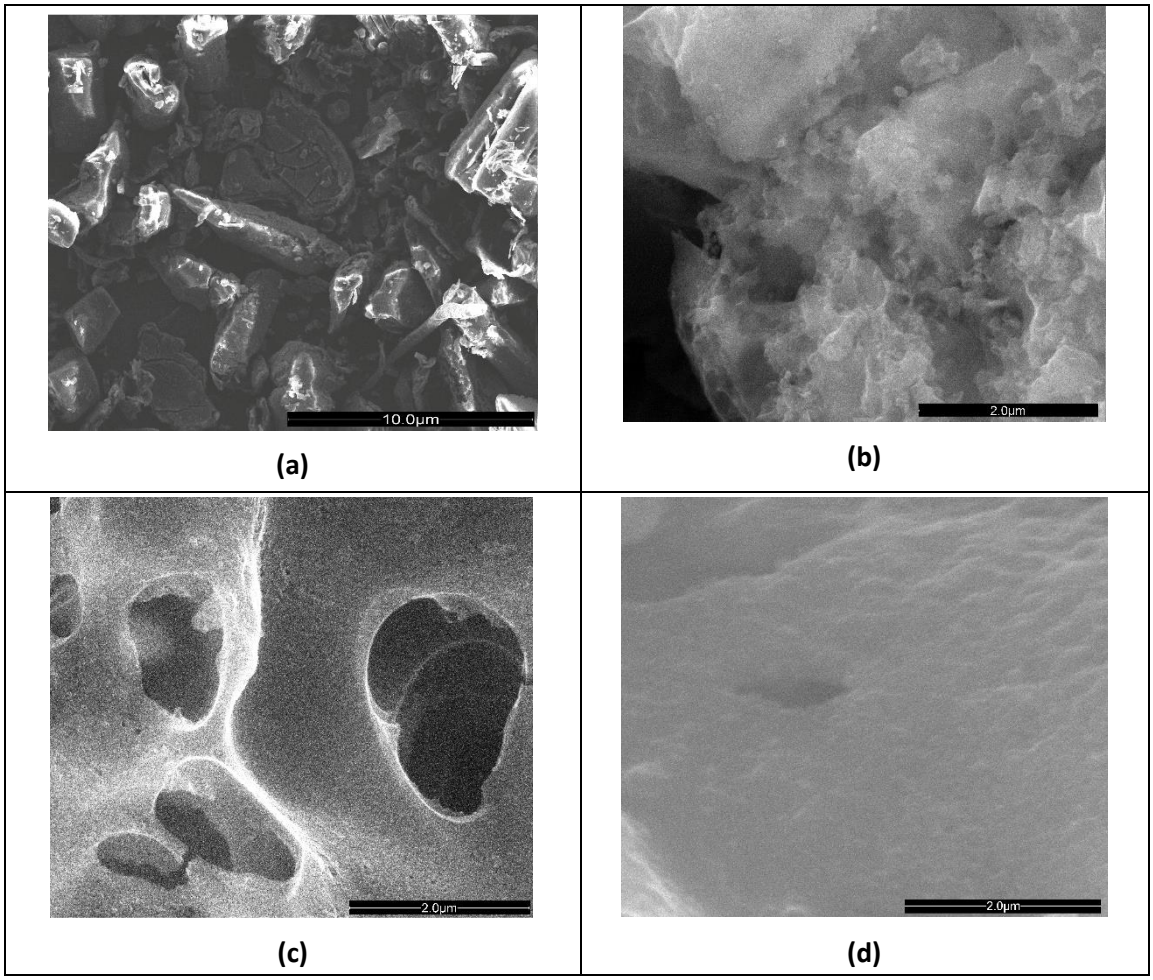

Figure S1: SEM Image of a) DPC, b) ADPC0.5, c) ADPC1, d) ADPC3.

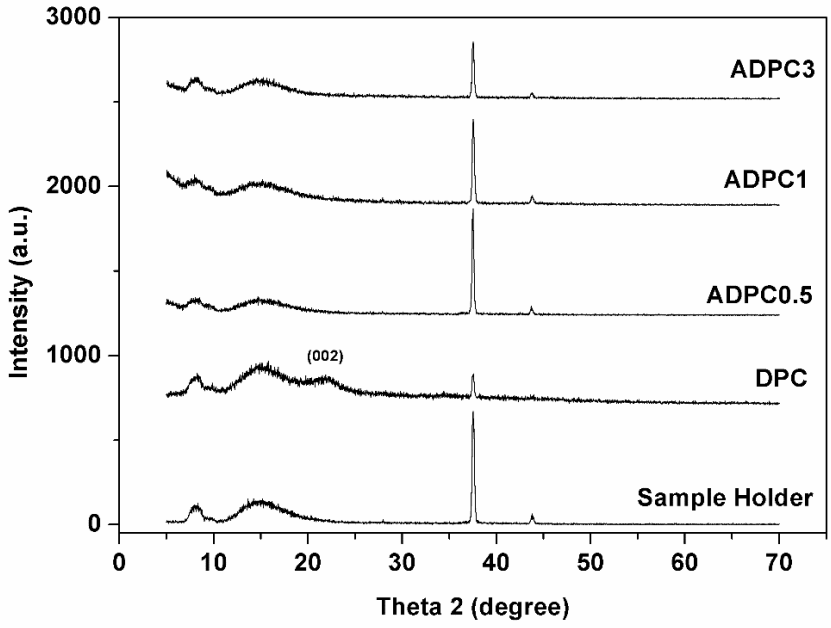

Figure S2: XRD pattern of ADPC samples between 5 and 70 degrees.

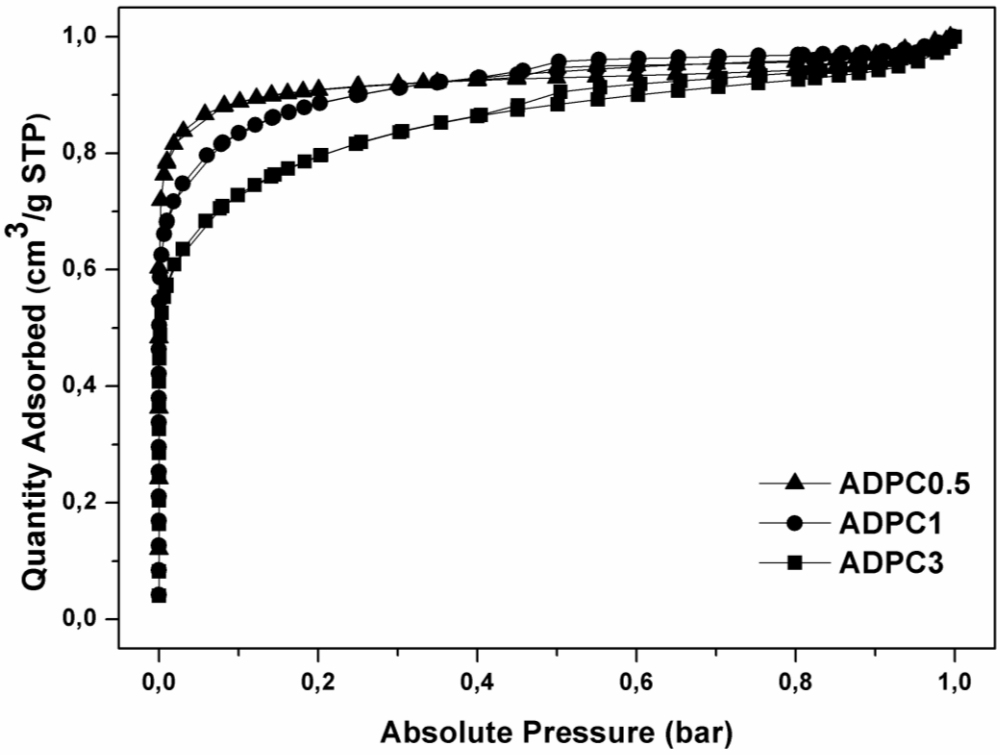

Figure S3: Normalized N_2 adsorption–desorption isotherms at 77 K.

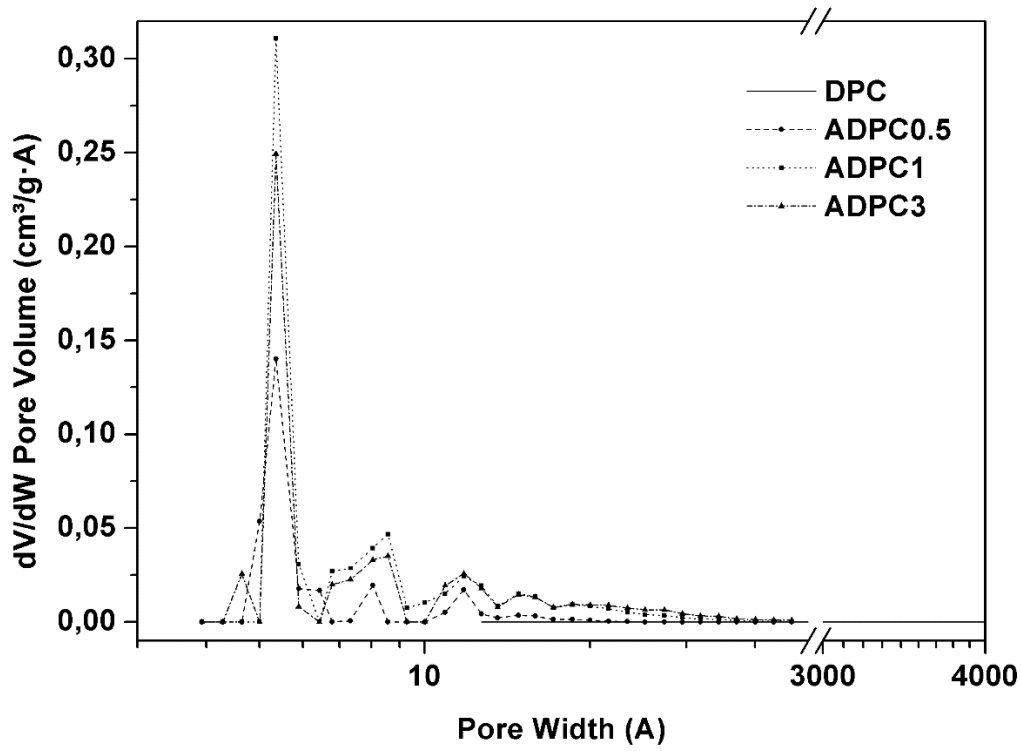

Figure S4: PSD of the analyzed samples.

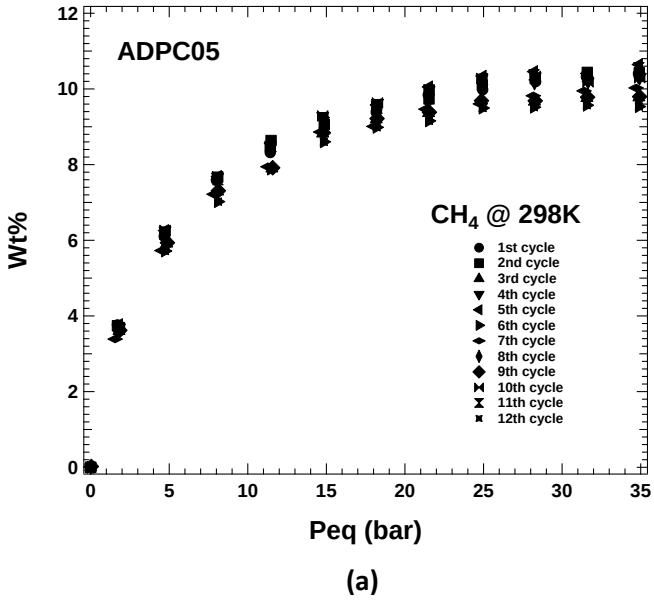

(a)

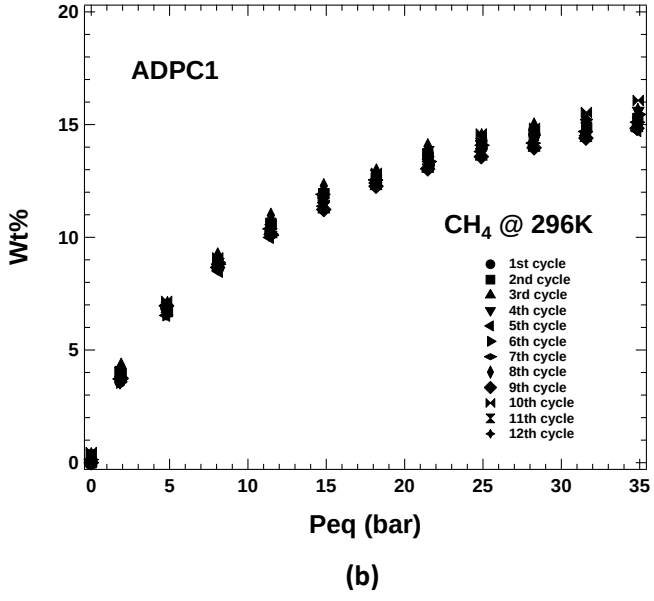

(b)

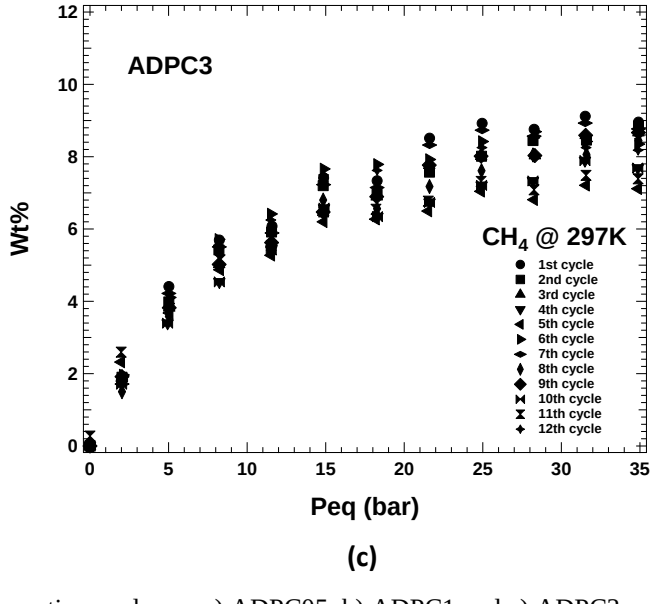

(c)

Figure S5: Multiple adsorption cycles on a) ADPC05, b) ADPC1 and c) ADPC3 samples up to 35 bar at room temperature.

References

(1) Ogden, J.; Jaffe, A. M.; Scheitrum, D.; McDonald, Z.; Miller, M. Natural gas as a bridge to hydrogen transportation fuel: Insights from the. Energy Policy 2018, 115, 317−329.

(2) Casco,M. E.; Escandell,M.M.; Ramos, E. G.; Kaneko, K.; Albero, J. S.; Reinoso, F. R. High-Pressure Methane Storage in Porous Materials: Are Carbon Materials in the Pole Position? Chem. Mater.2015, 27, 959−964.

(3) Nie, Z.; Lin, Y.; Jin, X. Research on the theory and application of adsorbed natural gas used in new energy vehicles: A review. Front.Mech. Eng. 2016, 11, 258.

(4) Alhasan, S.; Carriveau, R.; Ting, D. S.-K. A review of adsorbed natural gas storage technologies. Int. J. Environ. Stud. 2016, 73, 343−356.

(5) Romanos, J.; Rash, T.; Abou Dargham, S.; Prosniewski, M.; Barakat, F.; Pfeifer, P. Cycling and Regeneration of Adsorbed Natural Gas in Microporous. Energy Fuels 2017, 31, 14332−14337.

(6) Choi, P. S.; Jeong, J. M.; Choi, Y. K.; Kim, M. S.; Shin, G. J.; Park, S. J. A review: methane capture by nanoporous carbon materials for automobiles. Carbon Letters 2016, 17, 18−28.

(7) Beckner, M.; Dailly, A. Hydrogen and methane storage in adsorbentmaterials for automotive applications. Int. J. Energy Res. 2016, 40, 91−99.

(8) Garcia Blanco, A. A.; Vallone, A. F.; Korili, S. A.; Gil, A.; Sapag, K. A comparative study of several microporous materials to store methane by adsorption. Microporous Mesoporous Mater. 2016, 224, 323−331.

(9) Antoniou, M. K.; Diamanti, E. K.; Enotiadis, A.; Policicchio, A.; Dimos, K.; Ciuchi, F.; Maccallini, E.; Gournis, D.; Agostino, R. G. Methane storage in zeolite-like carbon materials. Microporous Mesoporous Mater. 2014, 188, 16−22.

(10) Policicchio, A.;Maccallini, E.; Agostino, R. G.; Ciuchi, F.; Aloise, A.; Giordano, G. Higher methane storage at low pressure and room temperature in new easily scalable large-scale production activated carbon for static and vehicular applications. Fuel 2013, 104, 813−821.

(11) Luo, J.; Liu, Y.; Sun, W.; Jiang, C.; Xie, H.; Chu, W. Influence of structural parameters on methane adsorption over activated carbon: Evaluation by using D−A model. Fuel 2014, 123, 241−247.

(12) Burchell, Timothy D. Carbon Materials for Advanced Technologies; Elsevier Science Ltd: Oxford, 1999.

(13) Panto,` F.; Fan, Y.; Frontera, P.; Stelitano, S.; Fazio, E.; Patane,` S.; Marelli, M.; Antonucci, P.; Neri, F.; Pinna, N.; Santangelo, S. Are Electrospun Carbon/Metal Oxide Composite Fibers Relevant Electrode Materials for Li-Ion Batteries? J. Electrochem. Soc. 2016, 163, A2930−A2937.

(14) Belaustegui, Y.; Zorita, S.; Carretero, F. F.; García-Luis, A.; Panto,` F.; Stelitano, S.; Frontera, P.; Antonucci, P.; Santangelo, S. Electro-spun graphene-enriched carbon fibres with high nitrogen contents forelectrochemical water desalination. Desalination 2017, 428, 40−49.

(15) Casco, M. E.; Escandell, M. M.; Kaneko, K.; Albero, J. S.; Reinoso, F. R. Very highmethane uptake on activated carbons prepared from mesophase pitch: A compromise between microporosity and bulk density. Carbon 2015, 93, 11−21.

(16) Titirici,M.M.;White, R. J.; Brun,N.; Budarin, V. L.; Su,D. S.; del Monte, F.; Clark, J. H.;MacLachlan,M. J. Sustainable carbonmaterials. Chem. Soc. Rev. 2015, 44, 250−290.

(17) Zhang, F.; Li, G.-D.; Chen, J.-S. Effects of raw material texture and activation manner on surface area of porous carbons derived from biomass resources. J. Colloid Interface Sci. 2008, 327, 108−114.

(18) Deng, J.; Li,M.;Wang, Y. Biomass-derived carbon: synthesis and applications in energy storage and conversion. Green Chem. 2016, 18, 4824.

(19) Manocha, S.; Manocha, L. M.; Joshi, P.; et al.et al Activated carbon from biomass. AIP Conf. Proc. 2012, 1538, 120−12.

(20) Sun, Y.; Webley, P. A. Preparation of Activated Carbons with Large Specific Surface Areas Preparation of Activated Carbons with Large Specific Surface Areas Carbon Dioxide, Nitrogen, and Hydrogen. Ind. Eng. Chem. Res. 2011, 50, 9286−9294.

(21) Prauchner, M. J.; Sapag, K.; Reinoso, F. R. Tailoring biomass-based activated carbon for CH4 storage by combining chemical activation with H3PO4 or ZnCl2 and physical activation with CO2. Carbon 2016, 110, 138−147.

(22) Zhang, F.; Ma, H.; Chen, J.; Li, G. D.; Zhang, Y.; Chen, J. S. Preparation and gas storage of high surface area microporous carbon derived from biomass source cornstalks. Bioresour. Technol. 2008, 99, 4803−4808.

(23) Srenscek-Nazzal, J.; Kaminska, W.; Michalkiewicz, B.; Koren, Z. C. Production, characterization and methane storage potential of KOH-activated carbon from sugarcane molasses. Ind. Crops Prod. 2013, 47 (2013), 153−159.

(24) Sangchoom, W.; Mokaya, R. Valorization of Lignin Waste: Carbons from Hydrothermal Carbonization of Renewable Lignin as Superior Sorbents for CO2 and Hydrogen Storage. ACS Sustainable Chem. Eng. 2015, 3, 1658−1667.

(25) Duman, G.; Onal, Y.; Okutucu, C.; Onenc, S.; Yanik, J. Production of Activated Carbon from Pine Cone and Evaluation of Its Physical, Chemical, and Adsorption Properties. Energy Fuels 2009, 23, 2197−2204.

(26) Bello, A.;Manyala, N.; Barzegar, F.; Khaleed, A. A.;Momodu, D. Y.; Dangbegnon, J. K. Renewable pine cone biomass derived carbon materials for supercapacitor application. RSC Adv. 2016, 6, 1800.

(27) Li, K.; Tian, S.; Jiang, J.; Wang, J.; Chen, X.; Yan, F. Pine cone shell-based activated carbon used for CO2 adsorption. J. Mater. Chem. A 2016, 4, 5223−5234.

(28) Song,M.; Jin, B.; Xiao, R.; Yang, L.;Wu, Y.; Zhong, Z.; Huang, Y. The comparison of two activation techniques to prepare activated carbon from corn cob. Biomass Bioenergy 2013, 48, 250−256.

(29) Kaskel, St.; Wang, J. KOH activation of carbon-based materials for energy storage. J. Mater. Chem. 2012, 22, 23710.

(30) Brunauer, S.; Emmett, P. H.; Teller, E. Adsorption of gases in multimolecular. J. Am. Chem. Soc. 1938, 60, 309.

(31) Seaton, N. A.; Walton, J.; Quirke, N. A new analysis method for the determination of the pore-size distribution of porous carbons from nitrogen adsorption measurements. Carbon 1989, 27, 853−861.

(32) Policicchio, A.; Maccallini, E.; Kalantzopoulos, G. N.; Cataldi, U.; Abate, S.; Desiderio, G.; et al.et al Volumetric apparatus for hydrogen adsorption and diffusion measurements: sources of systematic error and impact of their experimental resolutions. Rev. Sci. Instrum. 2013, 84, 103907.

(33) Sing, K.S.W.; Everett, D.H.; Haul, L.; Pierotti, R.A.; Rouquerol, J.; Siemieniewska, T. Reporting Physisorption Data for Gas/Solid Systems, Handbook of Heterogeneous Catalysis; Wiley-VCH Verlag GmbH & Co., KGaA s.l.: 2008.

(34) Garcia Blanco, A. A.; Vallone, A. f.; Korili, S. A.; Gil, A.; Sapag, K. A comparative study of several microporous materials to store methane by adsorption. Microporous Mesoporous Mater. 2016, 224, 323−331.

(35) Adsorbent Carbon Fiber Composite for the Storage of Natural Gas; Burchell, T, Howe, J, Gabbard, A, Rogers, M, Eds.; Oak Ridge National Laboratory: 2003.

(36) Lozano-Castello, D.; Cazorla-Amoros, D.; Linares-Solano, A. Usefulness of CO2 adsorption at 273 K for the characterization of porous carbons. Carbon 2004, 42, 1233−1242.

(37) Mendez-Linan, L.; Lopez-Garzon, F. J.; Domingo-Garcia, M.; Perez-Mendoza, M. Carbon adsorbents from polycarbonate pyrolysis char residue: hydrogen and methane storage capacities. Energy Fuels 2010, 24, 3394−400.

(38) Toth, J.. Adsorption: Theory, Modeling, and Analysis. Marcel Dekker, New York, 2002.

3.3 Posidonia Oceanica and Wood chips activated carbon as interesting materials for hydrogen storage

3.3.1 State of the art

Increasing global energy demands, limited fossil fuel reserves and production capacities, geopolitical conflicts, and efforts to reduce gas emissions have motivated research efforts into alternative fuels. Among the many candidates, hydrogen has been the subject of intense focus for the past two decades [1] since it is described as an energy carrier with a "great potential for clean, efficient power in stationary, portable and transport applications." [2] owing to the fact that its staggering energy content of 142 MJ kg^{-1} exceeds that of petroleum by a factor of three and that the product of its combustion is water vapor [3].

While much of the hydrogen used today is generated from steam reforming of hydrocarbons and produces carbon dioxide as a byproduct, hydrogen production from novel sources such as solar, wind, or biological processes presents the opportunity of a clean, environmentally friendly energy cycle [4-7].

However, the usage of hydrogen has its own challenges. One major challenge is its storage, which is finding systems and materials for efficient hydrogen storage [8]. To date, the proposed storage methods are liquefaction and pressurization, and an interesting alternative is represented by storage into solid-material [9]. Even if all of them are potentially suitable, up to now, none of they met all the required specifications simultaneously [10]. Nevertheless, the one who has the most interesting prospects appears the adsorption into porous solid materials, because of the fast kinetic of adsorption and desorption, reversibility and non-destruction of material structure [11, 12]. On this perspective, numerous types of materials which having an affinity toward hydrogen have been explored like covalent organic frameworks, nanoporous polymers, metal-organic frameworks and zeolites [13]. Among these materials, different carbonaceous materials like activated carbon, multiwalled carbon nanotubes and graphene have shown reversible and interestingly high hydrogen storage capability [14-17] mainly determined from their porous structure and high internal surface areas [18-20]. Activated carbons have attracted the attention of many researchers due to their excellent properties, such as thermo-stability, high performance, large surface area and high adsorptive capacity [21-24]. The most common precursors used for the preparation high grade of activated carbons are organic materials that contain lignin, cellulose and lignocellulose. Accordingly, use of biomasses could represent a valid opportunity to produce porous carbons by renewable raw materials.

In this paper, the feasibility to use a local biomass (Posidonia Oceanica and Wood chips) as a raw precursor for the production of activated carbons (AC) with a high surface area was investigated. We report about the synthesis procedure, structural characterization and hydrogen adsorption properties explored experimentally using a home-made Sievert's type apparatus [25, 26]. In the last case, the experimental studies have been conducted at both room and cryogenic temperatures and pressures up to 80 bar. The overall process of hydrogen storage in AC has been studied in detail using different experimental technique and methods.

3.3.2 Experimental Section: Materials and Analytical Method

3.3.2.1 Feedstocks preparation and characterization

Different kinds of biomass were selected to activated carbons production. In particular, two lignocellulosic materials as Wood chips and Posidonia Oceanica sea-plant have been compared. Posidonia Oceanica beached leaves (Mediterranean Sea-plant) were collected from the south-western coast of Sicily (Italy). Prior to drying step different washing with rainwater and then with distilled water to remove sea salt were carried out on Posidonia Oceanica samples. The Wood chips were acquired as a byproduct by Messina forestry sector. All feedstocks were dried in an oven (at 80 °C for 24 h), shredded and sieved into a size range between 0,3-0,4 mm.

Biomasses were characterized by proximate, ultimate analyses and High Heating Values-HHV values [27]. Proximate analysis covered measurement of moisture content, volatile matter, fixed carbon and ash content. Then, the moisture measurement was performed drying Posidonia Oceanica and Wood chips samples in a convection oven at 110 °C until constant weight were recorded. The volatile matter (VM) content was determined by measuring weight loss after heating biomass samples to 950 ± 20 °C in an alumina crucible under nitrogen (N_2) atmosphere (ASTM D-2013). The ash content was measured by heating samples (Standard E-1755-01) at 575 ± 25 °C for 3 h to constant weight in a muffle furnace and the fixed carbon (FC) fraction was calculated by subtracting the percentages of volatile matter, moisture content and ash from 100%. Elemental analysis was performed using CHNS-O Elemental Analyzer (Thermo Fisher Scientific, Flash EA 1112) while High Heating Values and biomass protein fraction were calculated as in a previous work [28-31].

3.3.2.2 Thermogravimetric analysis

Thermogravimetric (TGA/DTG) analysis measurements were used to study the thermal decomposition behavior of Posidonia Oceanica and Wood chips under N_2/Air condition but also to confirm/compare the results obtained by ASTM standards methods in terms of moisture content, volatile matter and fixed carbon. The experiments were performed using a thermogravimetric analyzer Netzsch Thermische Analyse TASC 414/2. Approximately 10 mg of sample were heated from 25 up to 800 °C (10 °C/min) under 30 ml/min of N_2 and then the temperature was decreased to 600 °C under air condition (70 ml/min) in order to determine ash and fixed carbon. Ash content was calculated by the solid residue remaining at the end of the combustion stage, while the fixed carbon was determined by subtracting the ash content from the solid obtained at the end of the TGA test carried out in nitrogen condition.

3.3.2.3 X-Ray Diffraction (XRD) analysis

The crystalline phases of biomasses and activated carbons were identified by X-ray powder diffraction (XRD) using Philips X'Pert X-ray diffractometer (model PW3710), operating with Cu/Kα radiation source (wavelength = 1.5406 Å, 40 kV, 30 mA). Data were collected over the angular range 5–80 degrees in 2θ under atmospheric pressure. The peak profiles of the (2 2 0) reflection in the face-centered cubic (fcc) structure were obtained using the Marquardt algorithm. Instrumental broadening was determined using a standard platinum sample.

3.3.2.4 Textural and adsorption measurements

The surface area and average pore size of the activated carbons were analyzed by N_2 adsorption-desorption isotherm measurements at liquid nitrogen temperature (~ −196°C) using a Micromeritics ASAP 2020 instrument. The Langmuir method was exploited to calculation the surface area of microporous samples. Furthermore, the pore size distribution was estimated by using both the Barret-Joyner-Halenda (BJH) equation, during the desorption phase, and the Horvath-Kawazoe method. Hydrogen adsorption measurements were performed using an optimized Sievert-type (volumetric) apparatus f-PcT for accurate and reliable gas adsorption measurements [25]. The gas storage capacity, as weight percent of gas adsorbed per gram of adsorbent (wt%), was determined from adsorption isotherms and reported in terms of wt% vs Peq. Before starting a new set of measurements, each sample was previously annealed for 12 h at 200°C under vacuum ($P < 10^{-6}$ mbar) to eliminate the eventual fraction of water weakly bound inside the samples. Before starting each adsorption test,

Helium (He) picnometry analysis was performed in order to get the best value of the sample skeletal density. The same analysis was performed at the end of all the adsorption tests to check possible changes induced in the analyzed sample after exposure to gas specimen. The reliability of the ACs performance in term of cyclic life was tested by submitting all samples to multiple H_2 adsorption/desorption cycles with and without any temperature treatment in between.

3.3.2.5 Morphological analysis

The morphology of the activated carbon samples was observed using a Field Emission Scanning Electron Microscope (FE-SEM Philips model XL30 S FEG) at different magnifications operating at an accelerating voltage of 20 kV. Furthermore, the equipped EDX probe has been used to determine the chemical composition of the samples.

3.3.2.6 Pyrolysis experimental plant

The experimental plant used for the biochar and activated carbons production is shown in Figure 1a. The schematic diagram shows the main configuration of the plant which consists of a gas transport system, an analysis reactor, a furnace and cold traps for the liquid fraction collection (bio-oil). Regulation and measurement of gas flow are performed by Mass Flow Controllers (model ASM-AFC 25.50).

The fixed bed reactor (see Fig. 1b) consists of a stainless-steel tube (length: 400 mm, internal diameter: 20 mm, external diameter: 26 mm) resistant to high temperature with a narrowing point at the lower end to facilitate channeling to the exit of both gaseous and liquid fraction.

Both for the biomass thermal decomposition and for the carbon activation, the reactor is placed in an electric furnace of 1.0 kW, whose temperature is led by a controller driven by a K-type thermocouple located on the oven wall. An additional thermocouple (K-type) is placed at the center of the bed to measure the temperature inside the reactor instantly. The gaseous part consists of two components, condensable (bio-oil) and incondensable (syngas) fraction. Both these products are led outwards by a carrier gas (argon) while the solid fraction (biochar), that remains inside the reactor, is discharged and recovered at the end of each test. The condensable part is collected through the use of three cold traps placed at the exit of the reactor and kept at a temperature of -78 °C by a mixture of liquid nitrogen and ethyl acetate.

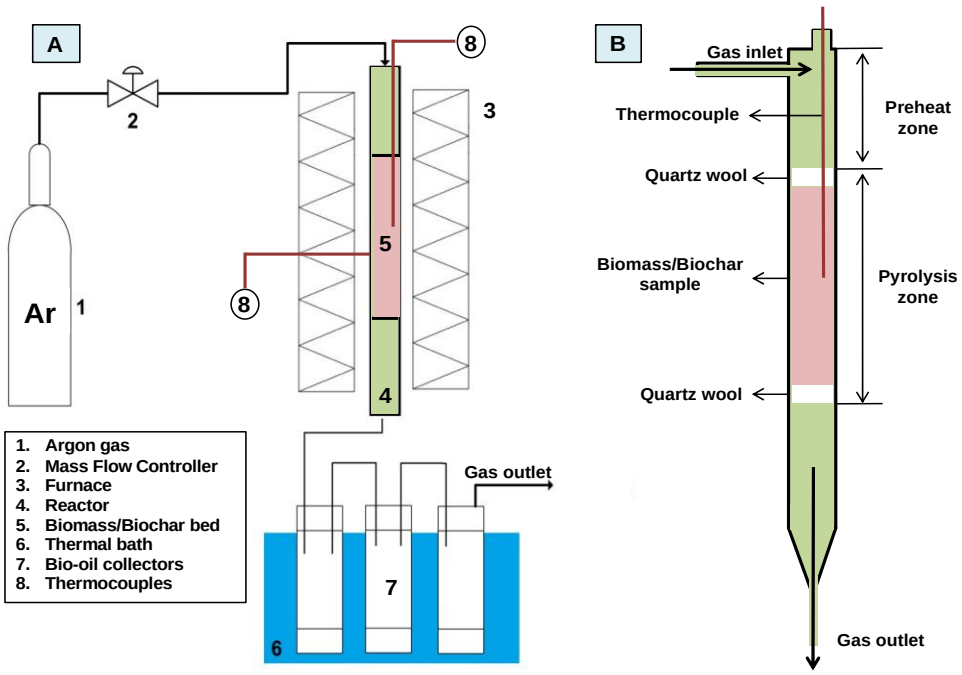

Figure 1. a) Scheme of lab-scale pyrolysis plant; b) details of the fixed-bed reactor.

3.3.2.7 Biochar fabrication and activation methodology

Biochar was prepared by the pyrolysis process of Posidonia Oceanica and Wood chips having a particle size between 0.3-0.4 mm. In particular,10 g of biomass contained in a vertical stainless-steel reactor were slowly heated (5 °C/min), under argon atmosphere (100 ml/min), until reaching 600 °C, then maintained at this temperature for 1 h. Finally, the reactor was allowed to cool down to room temperature under a nitrogen flow. All tests were repeated three times to evaluate the standard deviations (STD).

The prepared biochars, labelled “P Biochar” and “W Biochar” following the Posidonia Oceanica and Wood chips precursors, respectively, were chemically activated by impregnation with potassium hydroxide (KOH). The activation step was carried out as follows: the biochar was impregnated with 6M KOH in a mass ratio equal to 1:4 (Biochar: KOH); distilled water was used as a solvent to form a saturated solution [32-34] (see S1). This solution was evaporated at 80°C and the biochar/KOH mixture was again heated at 800°C for 1 h under argon atmosphere. After cooling down to room temperature, the activated carbon was washed with HCl solution (1M) until reaching pH = 7 then dried in an oven at 60°C. The activated carbon materials were labelled “P AC-KOH” and “W AC-KOH” following the Posidonia Oceanica and Wood chips precursors, respectively.

3.3.3 Results and discussion

3.3.3.1 Biomass characterization

Ultimate and proximate analysis of Posidonia Oceanica and Wood chips were performed to determinate the composition and evaluate the potential of materials. The analysis results were reported in Table 1. All feedstocks show similar molar H/C ratios. However, differences between the analyzed samples were recorded in terms carbon (C), nitrogen (N) and sulfur (S) fractions. In particular, the highest C fraction was detected for Wood chips (47.1 wt%) while greater concentration of nitrogen and sulfur were recorded for the Posidonia Oceanica samples, respectively 1.1 wt% and 0.3 wt%.

These results were probably due to proteins contents (see Table 1). Furthermore, the ash content of the Posidonia Oceanica sea-plant resulted higher than that Wood chips (14.0 wt% and 2.0 wt% respectively). However, the high ash rate detected (14.0 wt%) may promote char formation since inorganic elements in the ash are known to catalyze the formation of char during pyrolysis [27, 35-37]. Another interesting factor to be monitored during the carbonization process is the O/C ratio. This value for raw biomasses was 0.6 and 0.8 for Posidonia Oceanica and Wood chips respectively [21].

Whereby, the relatively high carbon content (40.3-47.1 wt%) along with the hydrogen one (6.0-6.3 wt%) make these biomasses suitable for the porous carbon productions. Thermogravimetric analysis (TG/DTG) has used to estimate the thermal behavior of Posidonia Oceanica and Wood chips. The thermal curves showed three main degradation steps for all biomasses that can be attributed to: 1) moisture and carbohydrates release T<120°C, 2) devolatilization of volatile matter (hemicellulose, cellulose and lignin) between 200-600 °C as found by Ncibi et al [21, 38], that correspond at main mass loss of the biomasses, 3) stabilization and decomposition of the carbonaceous matter formed during the previous step (600-800°C).

Fixed carbon and ash content in the starting biomass were calculated from the stage conducted in an air atmosphere by oxidation of the solid residue that remained at 800°C. However, DTG analysis showed a peak of greater intensity for Wood chips than Posidonia Oceanica related to the higher hemicellulose, cellulose and lignin content in the wood chips than other biomasses as Posidonia Oceanica [39].

Table 1. Physico-chemical properties of Posidonia Oceanica and Wood chips.

		Posidonia Oceanica	**Wood chips**
Proximate analysis (wt%)	Ash	14.0	2.0
	Moisture	12.7	4.6
	V.M. 525°C	56.9	73.5
	F.C.	16.4	20.0

Ultimate analysis (wt%) [a]	C	40.3	47.1
	H	6.0	6.3
	N	1.1	0.3
	S	0.3	0.0
	O [b]	25.7	39.8
H/C atom ratio [c]		1.4	1.7
O/C atom ratio		0.6	0.8
Protein (wt%) [d]		6.9	1.3
HHV (MJ/kg) [e]		18.2	19.7

*a. As received; b. By difference; c. Calculation H/C = 1.4125(O/C) + 0.5004 [31]; d. Wt% protein = Nwt% * NF (NF= 6.25); e. Calculation of HHV = 3.55C2−232C−2230H+51.2C×H+131N+20600 (kJ/kg) [25].*

The biomasses were also characterized by XRD analyses as depicted by Figure 2a. In particular, the XRD pattern highlights the intermediate behavior of Posidonia Oceanica sea plant between lignocellulosic and algal biomass. In particular, for both biomasses (Posidonia Oceanica and Wood chips) we observed the two major peaks at approximately 16° and 22° (corresponding to the 101 and 002 crystal plane) associated with the crystalline region of cellulose and generally attributed to carbon solids with a long-terms structural order [40]. In addition, the XRD spectrum of Posidonia Oceanica shows a peak of high intensity at 29.3° corresponding to the calcite, a typical component of marine biomasses [31, 41].

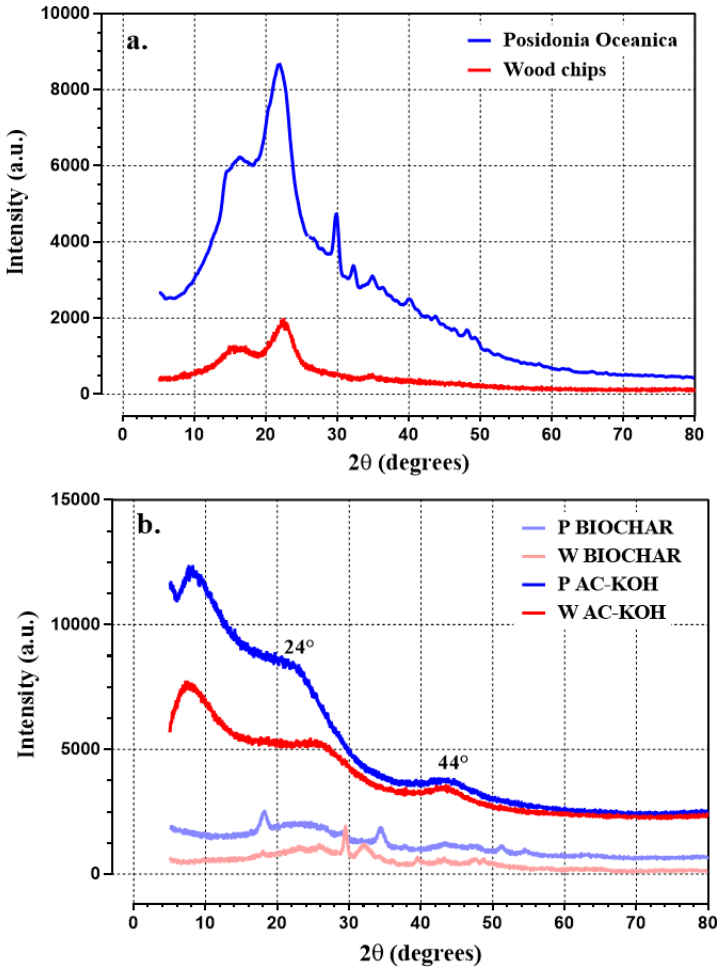

Figure 2. X-Ray diffraction patterns: a) Fresh biomasses, b) biochars and activated carbons.

3.3.3.2 Biochars and Activated Carbons: Chemical and Structural Characterization

Biochars and activated carbons characterization by XRD analysis show a broad band instead of cellulose signals due to the destruction of biomass structure in following the carbonization/pyrolysis phase (see Figure 2b). The peaks present in the biochar samples are due to the presence of impurities in the structure; now visible due to the decomposition of the main peaks (cellulose) and to the decrease in the intensity of the signals. Furthermore, the high intensity in the low angle region (5-15°) may be ascribed to the development of an abundant microporous structure in the samples [32]. However, in the activated carbons two broad humps are noticeably present, one at $2\theta = 24°$ and the other at approximately $2\theta = 44°$, that can be assigned to graphitic planes (002) and (100) with very low long-range order degree, respectively [32]. The bio-chars and activated carbons prepared by chemically activation with KOH were characterized in terms of elemental analysis and textural properties. Principal data were reported in Table 2 and 3. The results clearly show that the activation step affects considerably the porous carbons properties both in terms of carbon content and surface area. Thus, the carbon content following the activation phase increased from 58 wt% to 95.6 wt%, while the specific surface area from 41 m^2/g to 2835 m^2/g. The minor value of O/C factor found for porous carbons P AC-KOH and W AC-KOH (0.05 and 0.03, respectively) compared to the non-activated samples PBIOCHAR and W BIOCHAR (0.65 and 0.42, respectively) indicate an aromaticity development in the bio-char structure due to removing of H and O from inside the material [23, 27, 42].

Table 2. Biochar and activated carbons elemental analysis wt%.

	C	**H**	**N**	**O**	**O/C**
P BIOCHAR	58	2.8	1.8	37.5	0.65
W BIOCHAR	69.2	1.8	0.2	28.8	0.42
P AC-KOH	92.7	2.1	0.6	4.6	0.05
W AC-KOH	95.6	1.2	0.0	3.2	0.03

Table 3. Adsorption-desorption measurements.

	[1]Specific surface Area (m^2/g)	**Micropore Area (m^2/g)**	**[2]Median pore width (nm)**	**Pore volume (cm^3/g)**
P BIOCHAR	41	17.7	24.46	0.10
W BIOCHAR	425	234	13.68	0.11
P AC-KOH	2810	743	1.16	0.48
W AC-KOH	2835	1300	1.15	0.73

1 = Langmuir method; **2** = Horvath Kawazoe method.

Finally, as clearly visible in Table 3 and through the SEM analysis, the activation methodology also affects the average pore size. In fact, the activation has led to a shift in the size of the pores from larger (mesopores) present in the biochar samples (13.68-24.46 nm) to smaller ones (micropores) of the activated samples (1.15-1.16 nm).

A confirmation of the microporous structures of both activated carbons samples is obtained by SEM analyses. Figure 3 (Wood chips) and figure 4 (Posidonia Oceanica) were compared considering the same unit scale (20 µm and 2 µm).

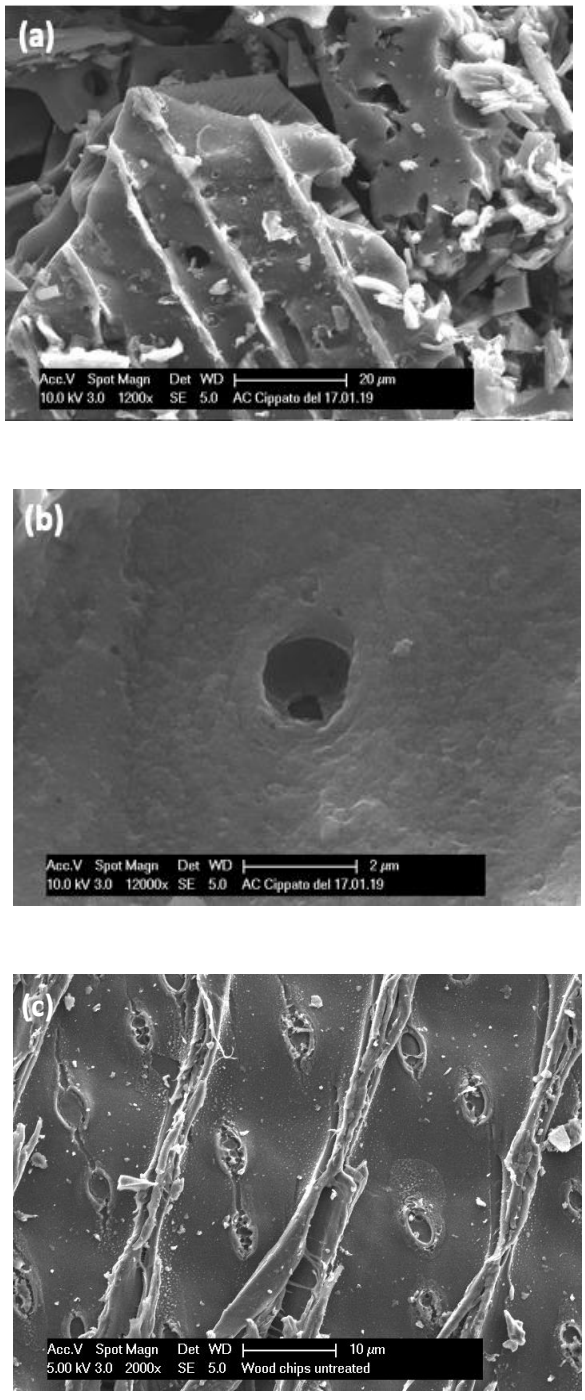

Figure 3. SEM analyses of Activated Wood chips at 1200X (a) and 12000X (b) of magnitude and (c) untreated Wood chips.

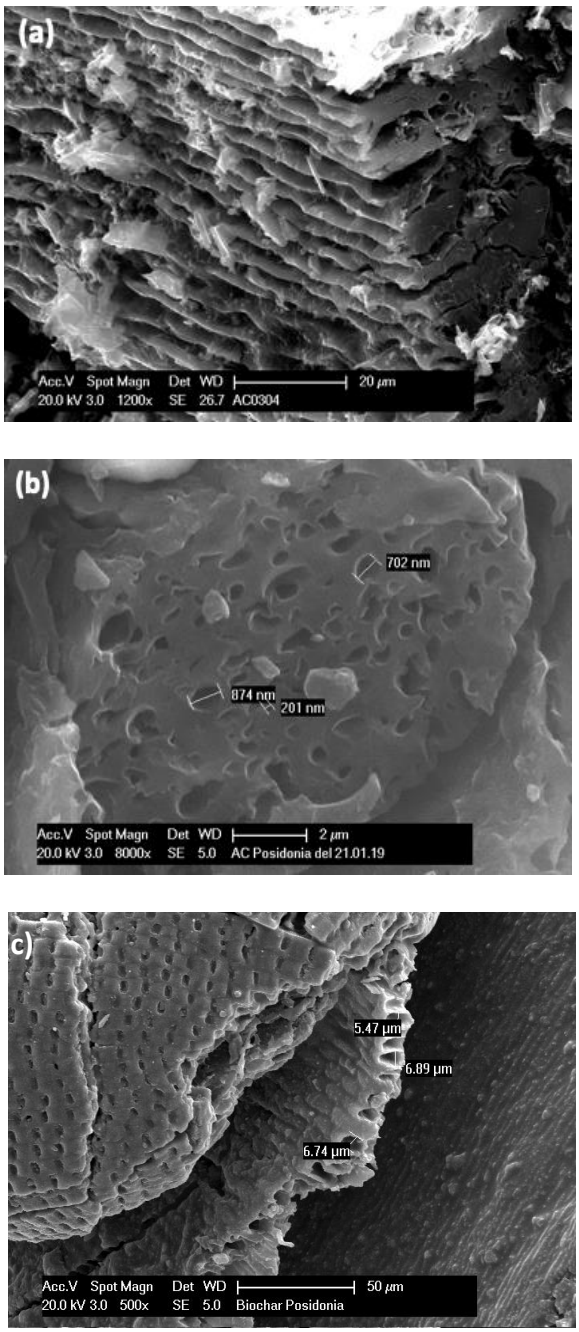

Figure 4. SEM analyses of Activated Posidonia Oceanica at 1200X (a) and 12000X (b) of magnitude and (c) untreated Posidonia Oceanica.

The chemical and thermal treatment on both Wood chips and Posidonia Oceanica samples gives a change of morphology, in fact, the pores formation (fig. 3c) and their reduction in size (fig. 4c) after these treatments are evident.

The activated carbon by Wood chips show an inhomogeneous pores size distribution starting from 80nm to 2mm, moreover, it can be deduced from figure 3a, the micropores structure is not stable and finally collapsed leaving the channel structure cracked [43]. In figure 4a a flat sheet like-structure is observed. Each layer contains micropores, having size dimension in a range of 200-900 nm, as clearly reported in figure 4b [21, 44]. To verify the possible presence

of other elements besides carbon and oxygen, a qualitative analysis by EDX technique was performed on both activated carbons samples. This analysis confirmed that, for both Posidonia and Wood chips samples, the total percentage is given only by Carbon (W AC-KOH 98% and P AC-KOH 97%) and Oxygen (W AC-KOH 2% and P AC-KOH 3%) (see S2).

3.3.3.3 Hydrogen adsorption isotherms

In order to evaluate the hydrogen adsorption capacity of the synthetized samples, high-pressure hydrogen adsorption and desorption tests were performed. In particular, having in mind different possible applications, both room and liquid nitrogen temperature conditions (25°C and -196°C respectively) were analyzed. The sample labeled as W AC-KOH shows a skeletal density of 1.95 ± 0.16 g/cc, obtained from helium pycnometry measurements. Sample aging and reversibility of the adsorption process were tested submitting them to multiple adsorption/desorption cycles. Figure 5 below shows the hydrogen adsorption behavior at room temperature up to 80 bars where an average maximum storage capacity of 0.5 wt% is reached. Here, the totally reversibility of the adsorption process is clearly visible by looking at the different subsequent cycles with and without thermal treatment in between (the slightly changes are connected to slight variations of the laboratory temperature). In particular, the first three isotherms have been acquired subsequently while the next three have been preceded by heating at 200°C for 12 h. The last test is important to check the aging of the material.

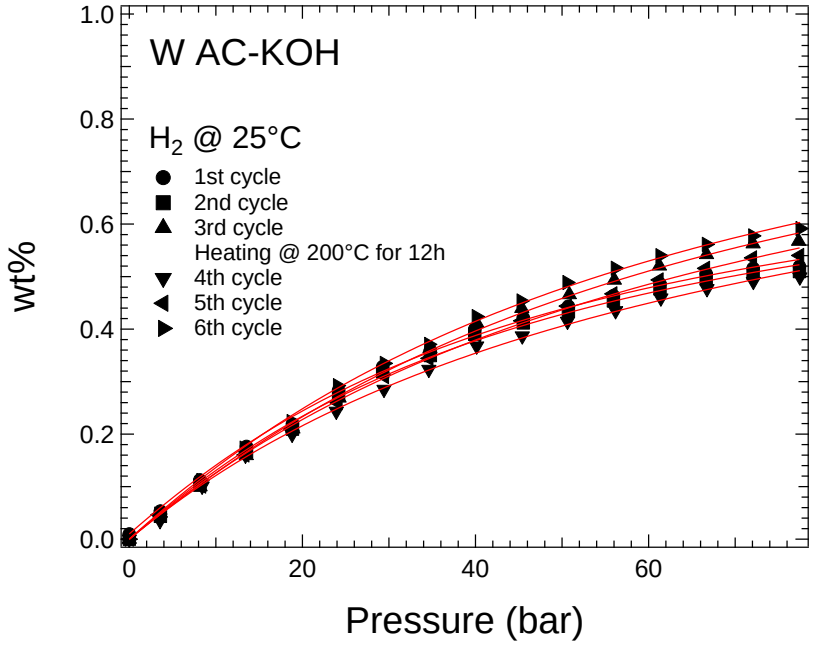

Figure 5. Hydrogen adsorption isotherms obtained at 25°C up to 80 bars. Line between points is a Toth/Langmuir fitting equation. The magnitude of the error is the symbol itself.

The same conclusion is obtained by looking at the adsorption/desorption test (not shown) where the adsorption and desorption curves overlap. This corroborates the previous observations, i.e. the H_2 molecule adsorption capacity of the sample is fully reversible. To get a further insight on the adsorption properties, liquid nitrogen temperature up to 80 bar tests were performed on the same sample (Figs. 6 and 7). The adsorption/desorption tests were performed with and without thermal treatment in between them. The maximum storage capacity increases up to almost 6.3 wt% related to the formation of a condensed layer of H_2 molecules on the surface. After the first adsorption cycle, the storage capacity slightly decreases (less than 0.5 wt%) down to 6 wt% but the maximum uptake is easily recovered through a thermal treatment to high temperature. The adsorption process if fully reversible as depicted in Fig. 7.

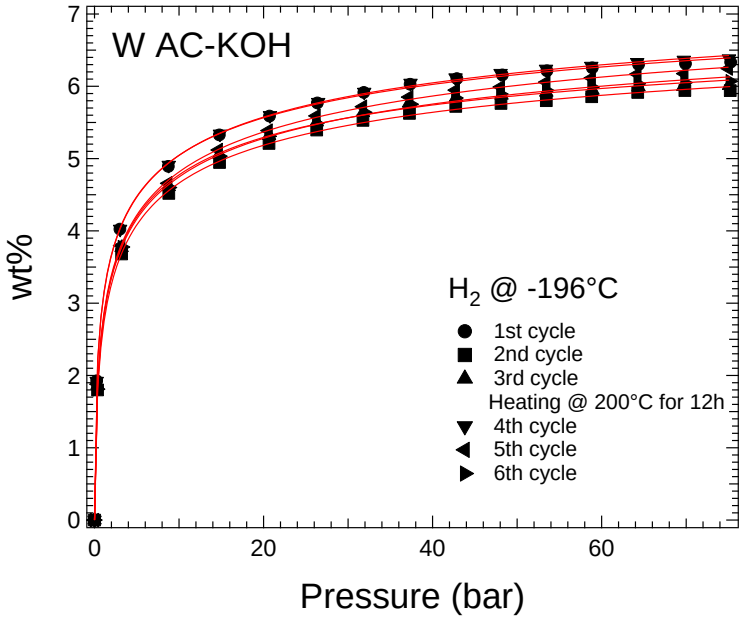

Figure 6.
Hydrogen adsorption/desorption cycle obtained at -196°C up to 80 bars. Line between points is a Toth/Langmuir fitting equation. The magnitude of the error is the symbol itself.

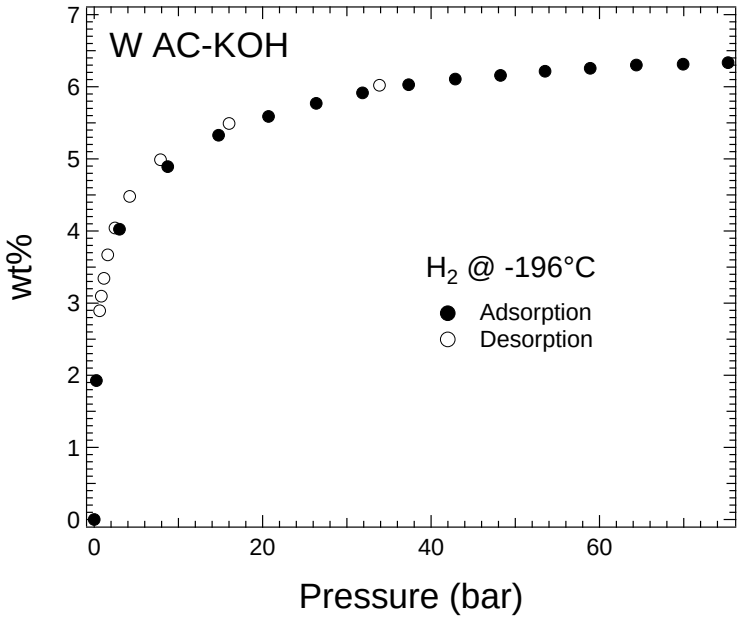

Figure 7.
Hydrogen adsorption/desorption isotherm obtained at -196°C up to 80 bars. The magnitude of the error is the symbol itself.

The skeletal density of the P AC-KOH sample, measured before performing hydrogen storage tests, is 1.62 ± 0.20 g/cc. This sample was tested at both room and liquid nitrogen temperatures conditions to evaluate the different behavior, too.

Figure 8 shows the hydrogen adsorption isotherms acquired at 26 °C at maximum pressure of 80 bar. Even if the adsorption process appears reversible as in the W AC-KOH, the P AC-KOH sample does not appear as stable as expected.

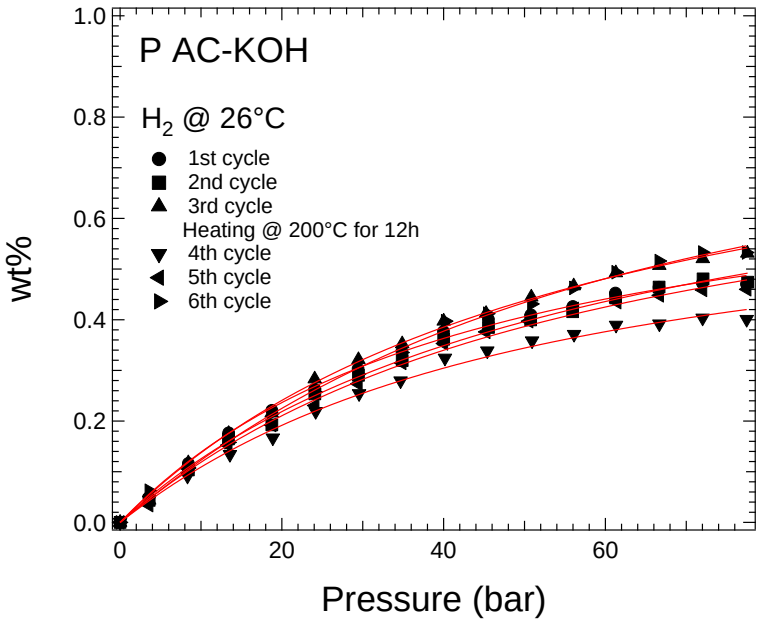

Figure 8. Hydrogen adsorption/desorption cycle obtained at 26°C up to 80 bars. Line between points is a Toth/Langmuir fitting equation. The magnitude of the error is the symbol itself.

Looking deeper in details to the isotherms of Fig. 8, in fact, it is easily to note different trends/slopes of the isotherm. This could be related to a lower stability at room temperature or, alternatively, to slight changes in the analysis room temperature. In any case, we could assert that the average storage capacity, around 0.5 wt%, is similar to that of the W AC-KOH sample.

A more stable behavior is observed cooling down the sample to liquid nitrogen temperature (Figs 9 and 10). Here, in fact, the adsorption isotherm curves perfectly overlap reaching a maximum storage capacity of 6.3-6.4 wt% as for the P AC-KOH sample, but with higher stability since we do not observe any decrease in the storage capacity after the first cycles.

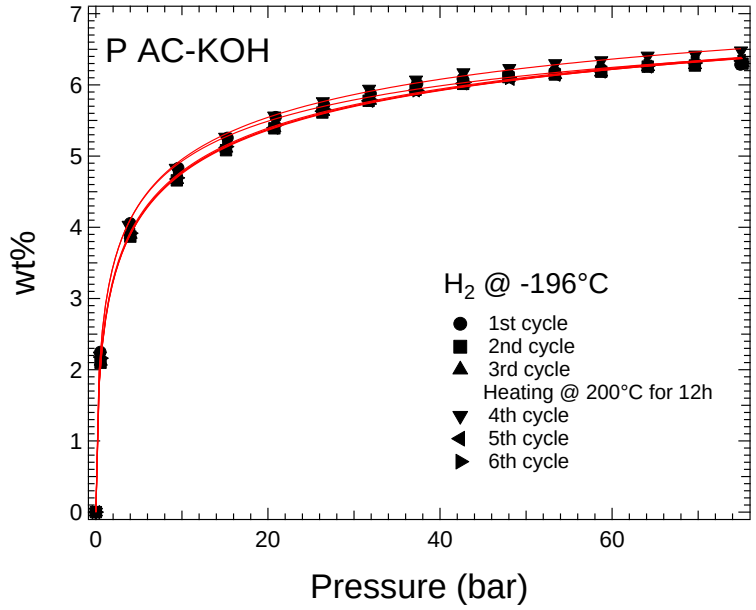

Figure 9. Hydrogen adsorption/desorption cycle obtained at -196°C up to 80 bars. Line between points is a Toth/Langmuir fitting equation. The magnitude of the error is the symbol itself.

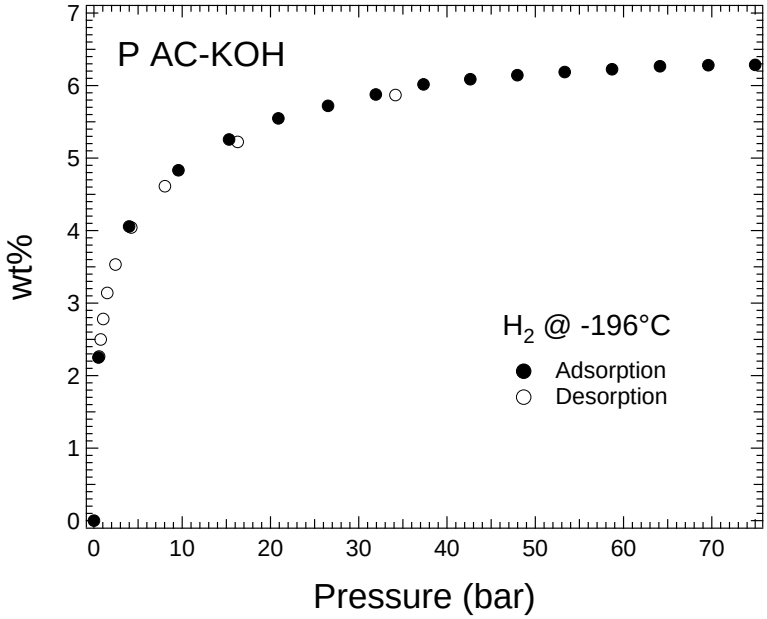

Figure 10. Hydrogen adsorption/desorption isotherm obtained at -196°C up to 80 bars. The magnitude of the error is the symbol itself.

Figure 11 shows a comparison between the results for the W AC-KOH and P AC-KOH samples. Both samples reach the same hydrogen uptake (~ 6.3 wt%) at the maximum analyzed pressure. This result is greater of the value expected according to the Chahine rule, i.e. 5.6 wt% [45-48] showing the effects of the microporous structure of the sample [49]. They show a totally reversible hydrogen adsorption process with a rapid increase in the low-pressure range reaching at 10 bars almost the 80% of the total amount stored at 80 bars.

This is further evidence of an interesting microporosity that could allow those materials to be used for low-pressure applications. Looking at the room temperature analysis it clearly visible the low storage capacity of both samples that, even if not negligible, could not find, to know, any immediate application.

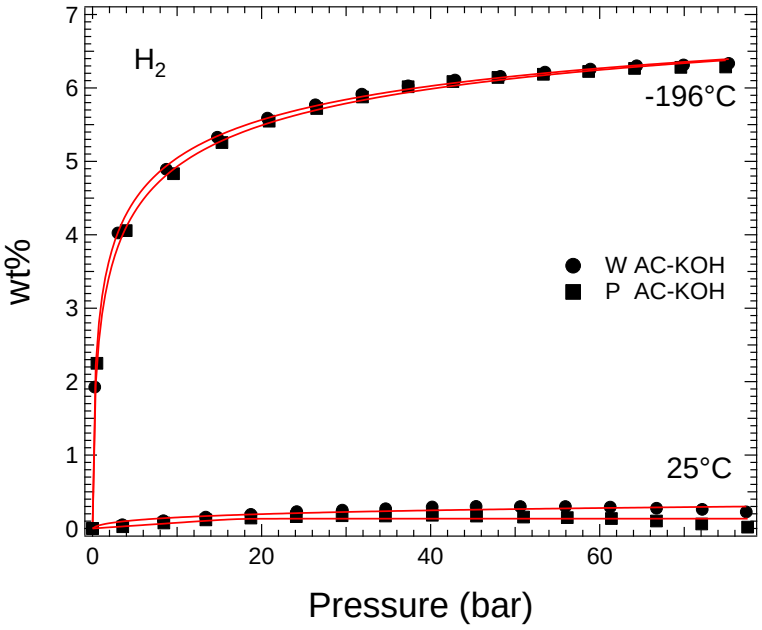

Figure 11. Hydrogen adsorption isotherms at 25°C and -196°C up to 80 bars on (circle) W AC-KOH and (square) P AC-KOH. Line between points is a Toth/Langmuir fitting equation used as guide for the eyes. The magnitude of the error is the symbol itself.

3.3.4 Conclusions

The use of biochar as precursor of activated carbon for H_2 adsorption was highlighted. Porous carbons with the high surface area, large pore volume and notable capacity of H_2 adsorption have been successfully produced from beached Posidonia Oceanica leaves and Wood chips. The activation methodology with KOH brought a considerable improvement of the activated carbon properties in terms of carbon content (58-95.6 wt%), superficial area (41-2835 m^2/g) and H_2 adsorption properties (32 mmol/g). Porous carbon with high microporosity structure, surface area and notable capacity of H_2 capture have been successfully produced from Posidonia Oceanica and Wood chips that are a cheap, sustainable and renewable start materials.

3.3.5 Supporting Information

S1. Activation of biochars using KOH - physical and chemical changes in biochars during activation process.

It is widely reported in literature [32, 33] by many authors that the use of a chemical agent combined with the inert agent as nitrogen or argon is a common practice that generates an increase of carbon content and better development of the internal porosity in the material. The chemical agents help to develop the porosity, by means of dehydration and degradation of biomass structure, especially when the activation agent is highly alkaline (e.g. KOH, NaOH). Further, differently from physical or acid the alkali agents produce narrow and wide microporosity. It has been observed that the ratio alkali/precursor is a significant factor for the disintegration of the raw material whereby a low alkali ratio leads to a low disintegration; whereas, high ratios of KOH to carbon result in the disintegration of the material. Hence, the amount of KOH plays a decisive role in the formation of pores. Essentially the porosity is generated from hydroxide reduction and carbon oxidation that generates gaseous molecules (CO_2 and H_2) whose escape of the structure induces the development of the microporosity. The reactions are listed below.

$2\ KOH \rightarrow K_2O + H_2O$

$C + H_2O \rightarrow H_2 + CO$

$CO + H_2O \rightarrow H_2 + CO_2$

$K_2O + CO_2 \rightarrow K_2CO_3$

$K_2O + H_2 \rightarrow 2K + H_2O$

$K_2O + C \rightarrow 2K + CO$

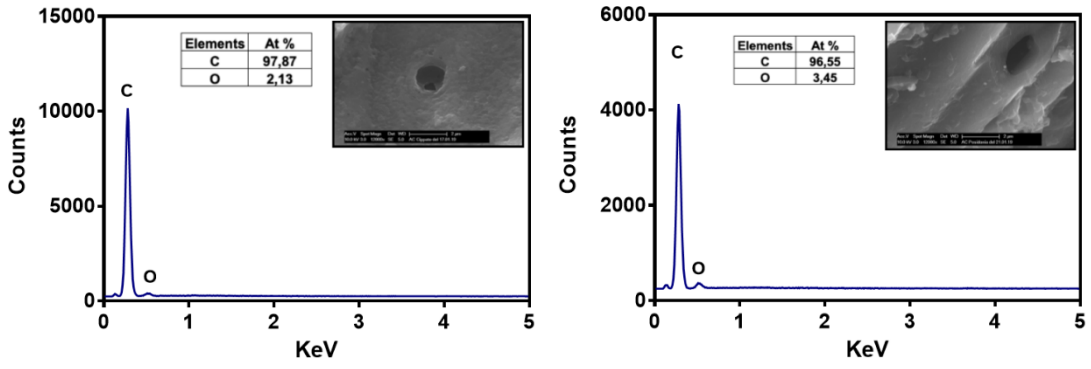

(a) (b)

Figure S2. EDX analysis acquired on a) W AC-KOH and b) P AC-KOH samples.

References

1. Demirdöven, N. and J. Deutch, *Hybrid Cars Now, Fuel Cell Cars Later.* Science, 2004. **305**(5686): p. 974-976.

2. Hirscher, M., et al., *Materials for hydrogen-based energy storage – past, recent progress and future outlook.* Journal of Alloys and Compounds, 2020. **827**: p. 153548.

3. Tozzini, V. and V. Pellegrini, *Prospects for hydrogen storage in graphene.* Physical Chemistry Chemical Physics, 2013. **15**(1): p. 80-89.

4. Ryan, O.H.S.-W., Cha; Whitney, Colella; Fritz, B. Prinz;, *Fuel Cell Fundamentals*. 1st Ed. ed. 2005, New York: Wiley.

5. James, L.A., Dicks;, *Fuel Cell Systems Explained, Second Edition*. 2nd ed. May 1, 2003, New York: SAE International.

6. Appleby, A.J., *Fuel cell handbook / A.J. Appleby, F.R. Foulkes*, ed. F.R. Foulkes. 1989, New York: Van Nostrand Reinhold.

7. Eg and G. Services, *Fuel cell handbook [electronic resource] / EG&G Technical Services, Inc*, ed. L. National Energy Technology. 2004, Morgantown, WV: U.S. Dept. of Energy, Office of Fossil Energy, National Energy Technology Laboratory.

8. Chauhan, P.K., et al., *Experimental investigation of multilayered graphene systems for hydrogen storage.* Materials Research Express, 2019. **6**(10): p. 105617.

9. Minuto, F.D., et al., *Liquid-like hydrogen in the micropores of commercial activated carbons.* International Journal of Hydrogen Energy, 2015. **40**(42): p. 14562-14572.

10. Van den Berg, A.W.C. and C.O. Areán, *Materials for hydrogen storage: current research trends and perspectives.* Chemical Communications, 2008(6): p. 668-681.

11. Oh, H., et al., *Experimental assessment of physical upper limit for hydrogen storage capacity at 20 K in densified MIL-101 monoliths.* RSC Advances, 2014. **4**(6): p. 2648-2651.

12. Schlichtenmayer, M. and M. Hirscher, *Nanosponges for hydrogen storage.* Journal of Materials Chemistry, 2012. **22**(20): p. 10134-10143.

13. Kalantzopoulos, G.N., et al., *Hydrogen storage in ordered and disordered phenylene-bridged mesoporous organosilicas.* International Journal of Hydrogen Energy, 2014. **39**(5): p. 2104-2114.

14. Sethia, G. and A. Sayari, *Activated carbon with optimum pore size distribution for hydrogen storage.* Carbon, 2016. **99**: p. 289-294.

15. Zheng, Q., et al., *Analysis of adsorption equilibrium of hydrogen on graphene sheets.* International Journal of Hydrogen Energy, 2013. **38**(25): p. 10896-10902.

16. Ma, L.-P., et al., *Hydrogen adsorption behavior of graphene above critical temperature.* International Journal of Hydrogen Energy, 2009. **34**(5): p. 2329-2332.

17. Srinivas, G., et al., *Synthesis of graphene-like nanosheets and their hydrogen adsorption capacity.* Carbon, 2010. **48**(3): p. 630-635.

18. Gatto;, R.P.M.F.G.I., *Waste and Natural Materials for Hydrogen Storage Application.* International Journal of Green Technology, 2019. **5**: p. 23-30.

19. Pedicini, R.P., R.; Gatto, I.; Gatto, M.F.; Gatto, M.F; Passalacqua, E.;, *Carbonaceous Materials in Hydrogen Storage*, in *Hydrogen Storage Technologies*. 2018. p. 260-298.

20. Bader, N., et al., *How the activation process modifies the hydrogen storage behavior of biomass-derived activated carbons.* Journal of Porous Materials, 2018. **25**(1): p. 221-234.

21. Ncibi, M.C., et al., *Preparation and characterisation of raw chars and physically activated carbons derived from marine Posidonia oceanica (L.) fibres.* Journal of Hazardous Materials, 2009. **165**(1): p. 240-249.

22. Zhang, X.-q., W.-c. Li, and A.-h. Lu, *Designed porous carbon materials for efficient CO2 adsorption and separation.* New Carbon Materials, 2015. **30**(6): p. 481-501.

23. Cataldo, S., et al., *Biochar from byproduct to high value added material – A new adsorbent for toxic metal ions removal from aqueous solutions.* Journal of Molecular Liquids, 2018. **271**: p. 481-489.

24. Mohan, M., et al., *Hydrogen storage in carbon materials—A review.* Energy Storage, 2019. **1**(2): p. e35.

25. Policicchio, A., et al., *Volumetric apparatus for hydrogen adsorption and diffusion measurements: Sources of systematic error and impact of their experimental resolutions.* Review of Scientific Instruments, 2013. **84**(10): p. 103907.

26. Pedicini, R., et al., *Progress in polymeric material for hydrogen storage application in middle conditions.* Energy, 2014. **64**: p. 607-614.

27. Maisano, S., et al., *Catalytic pyrolysis of Mediterranean sea plant for bio-oil production.* International Journal of Hydrogen Energy, 2017. **42**(46): p. 28082-28092.

28. Friedl, A., et al., *Prediction of heating values of biomass fuel from elemental composition.* Analytica Chimica Acta, 2005. **544**(1): p. 191-198.

29. Maddi, B., S. Viamajala, and S. Varanasi, *Comparative study of pyrolysis of algal biomass from natural lake blooms with lignocellulosic biomass.* Bioresource Technology, 2011. **102**(23): p. 11018-11026.

30. Maisano, S., et al., *Syngas production by BFB gasification: Experimental comparison of different biomasses.* International Journal of Hydrogen Energy, 2019. **44**(9): p. 4414-4422.

31. Chiodo, V., et al., *Pyrolysis of different biomass: Direct comparison among Posidonia Oceanica, Lacustrine Alga and White-Pine.* Fuel, 2016. **164**: p. 220-227.

32. Sun, F., et al., *Converting biomass waste into microporous carbon with simultaneously high surface area and carbon purity as advanced electrochemical energy storage materials.* Applied Surface Science, 2018. **436**: p. 486-494.

33. González-García, P., *Activated carbon from lignocellulosics precursors: A review of the synthesis methods, characterization techniques and applications.* Renewable and Sustainable Energy Reviews, 2018. **82**: p. 1393-1414.

34. Akasaka, H., et al., *Hydrogen storage ability of porous carbon material fabricated from coffee bean wastes.* International Journal of Hydrogen Energy, 2011. **36**(1): p. 580-585.

35. Grierson, S., V. Strezov, and P. Shah, *Properties of oil and char derived from slow pyrolysis of Tetraselmis chui.* Bioresource Technology, 2011. **102**(17): p. 8232-8240.

36. Fernando;, D.A.G.T.J.F.S.D., *Exploiting Algae As a Biomass Source to Produce Gasoline Grade Hydrocarbons by High Pressure Pyrolysis.* International Journal of Sustainable and Green Energy, 2013. **2**(2): p. 41-45.

37. Jones, J.M.N., M.; Darvell, L.I.; Ross, A.B.; Pourkashanian, M.; Williams, A.;, *Towards biomass classification for energy applications,* in *Science in Thermal and Chemical Biomass Conversion,* A.V. In: Bridgwater, Boocock, D.G.B. (Eds.), Editor. 2006, CPL Press. p. 331339.

38. Ncibi, M.C., B. Mahjoub, and M. Seffen, *Adsorptive removal of textile reactive dye using Posidonia oceanica (L.) fibrous biomass.* International Journal of Environmental Science & Technology, 2007. **4**(4): p. 433-440.

39. Plis, A., et al., *Combustion performance evaluation of Posidonia oceanica using TGA and bubbling fluidized-bed combustor (batch reactor).* Journal of Sustainable Mining, 2016. **15**(4): p. 181-190.

40. Mimmo, T., et al., *Effect of pyrolysis temperature on miscanthus (Miscanthus × giganteus) biochar physical, chemical and functional properties.* Biomass and bioenergy, 2014. **2014 v.62**: p. pp. 149-157.

41. Borysiak, S. and B. Doczekalska, *X-ray Diffraction Study of Pine Wood Treated with NaOH.* Fibers Text. East Eur., 2005. **13**.

42. Spokas, K.A., *Review of the stability of biochar in soils: predictability of O:C molar ratios.* Carbon Management, 2010. **1**(2): p. 289-303.

43. Zhou, J., A. Luo, and Y. Zhao, *Preparation and characterisation of activated carbon from waste tea by physical activation using steam.* Journal of the Air & Waste Management Association, 2018. **68**(12): p. 1269-1277.

44. Boukmouche, N., et al., *Activated carbon derived from marine Posidonia Oceanica for electric energy storage.* Arabian Journal of Chemistry, 2014. **7**(3): p. 347-354.

45. Chahine, R. and T.K. Bose, *Characterization and optimization of adsorbents for hydrogen storage.* Hydrogen Energy Progress XI, 1996: p. 1259-1263.

46. Masika, E. and R. Mokaya, *Hydrogen Storage in High Surface Area Carbons with Identical Surface Areas but Different Pore Sizes: Direct Demonstration of the Effects of Pore Size.* The Journal of Physical Chemistry C, 2012. **116**(49): p. 25734-25740.

47. Gogotsi, Y., et al., *Importance of pore size in high-pressure hydrogen storage by porous carbons.* International Journal of Hydrogen Energy, 2009. **34**(15): p. 6314-6319.
48. Cabria, I., M.J. López, and J.A. Alonso, *The optimum average nanopore size for hydrogen storage in carbon nanoporous materials.* Carbon, 2007. **45**(13): p. 2649-2658.

49. Minuto, F.D., et al., *Assessment methodology of promising porous materials for near ambient temperature hydrogen storage applications.* International Journal of Hydrogen Energy, 2018. **43**(31): p. 14550-14556.

3.4 Assessment of activated carbon fibers from commercial Kevlar® as nanostructured material for gas storage: effect of activation procedure and adsorption of CO_2 and CH_4

3.4.1 State of the art

In strategic sectors such as energy and green transport, store and distribute some types of gas in an innovative manner, minimizing energy expenditure and costs compared to current methods, has become a significant technological challenge [1-3]. For example, the increase in the use of cleaner and alternative fuels (e.g. natural gas, methane, hydrogen) in the automotive industry depends a lot on the development of advanced storage solutions [4-7]. Furthermore, the continued increase of greenhouse gases in the atmosphere has led to putting the need to implement solutions aimed at Carbon Capture and Storage/Utilization (CCS/U) [8, 9] for the mitigation of the climate changes. Even if there are already CO_2 storage methods (solvent absorption, chemical absorption, etc.), some problems such as high volatility or degradability have made it necessary to find more effective alternative methods.

Therefore, the increasing need to store gases with greater efficiency and safety has prompted scientific research towards the development of effective absorbent materials capable of improving these requirements, together with low-cost manufacture and the ability to release the sorbed species without wasting energy [6, 10].

Over the past few decades, a number of novel-structured porous solid physical adsorbents (e.g. zeolites, metal organic frameworks, covalent organic frameworks etc.) have been investigated as active materials for energy related applications [11, 12]. Among the investigated adsorbents, carbon-based materials appear to be the most effective in separation and storage [4, 13-15]. Through their use, in fact, it is possible to develop reversible and sustainable gas storage technology based on the physisorption method [16] since the weak interaction forces through adsorbate and adsorbant allow to produce a dense molecules film at the gas-solid interface and to release gas changing thermodynamic conditions. The mentioned reasons, make the gas storage into porous materials by physisorption process one of the most promising and sustainable methods thanks to reversible process [17, 18] and fast kinetics of adsorption/desorption without damage the absorbent material [19, 20].

In particular, the activated carbons (ACs) with nanoporous structure are considered a very interesting material for CO_2 storage through physisorption, thanks to characteristics such as good structural stability, high cyclability and regeneration of the material [21-23]. Moreover,

the higher adsorption potential in the nanopores allows condensing the same quantities of CH_4 at reduced pressures (30-40 bar) compared to those of the compressed gas in the cylinder (250 bar) [7, 23-25]. At the same time, it should be remembered that the preparation processes of porous carbons require heat treatments at high temperatures or chemical agents of activation, whose residues must be eliminated with a washing phase.

Accordingly, develop and provide functional materials with the above-mentioned adsorption features using a more sustainable process, is among the purposes of the following research work.

Among these, activated carbon fibers (ACFs) is one of the most important carbon nanoporous materials to consider. They have several advantages over other ACs, such as the shape, the well-defined porous structure and higher adsorption rates, but costs and extra processing step of converting the initial material into fibrous form is a disadvantage of ACFs [26]. They can be produced from fibers of natural origin or from synthetic carbon fibers subjected to the activation process, obtaining materials with different characteristics and production costs [27, 28].

ACFs manufactured from poly p-phenylene terephthalamide (PPTA), organic polyaramid fiber known a commercial name Kevlar®, through physical activation gets the typical characteristics of a microporous material based on carbon [29-34]. The ideal goal is to obtain homogeneous porous structures with the most uniform pore sizes possible, in order to correlate these characteristics with the adsorption properties. In fact, the structural features, in terms of specific surface area (SSA), pore volume (PV) and pore size distribution (PSD), may vary according to the application of the different procedure phases. The choice of inert atmosphere in the pyrolysis (N_2, Ar, He) [31, 34], but most of all activation temperature and gas (O_2, water steam, or CO_2) [28, 30, 32-34] can be varied. Other methods of preparing ACFs from Kevlar® employ chemical activation techniques with the use of agents such as phosphoric acid [33, 35] or potassium hydroxide [34].

In general, the preparation method consists of two principal steps: carbonization, and activation [23, 26-28, 33]. After a dehydration phase of the fibers, that eliminates moisture and volatile components present in the raw material, carbonization provides heat in an inert atmosphere to break molecular bonds and create carbon structures. Subsequently, the activation allows to have the feature of high porosity in the materials but requires exposure to additional chemicals or oxidizing agents in gas flow (chemical or physical activation). Usually, raw materials are carbonized at temperatures up to about 1003 K while the activation step occurs up to 1173 K [23, 26-28, 33]. During physical activation, gas flow, temperature and time are the parameters that influence material pore structure. The activation with O_2 is a

very aggressive type compared to those with CO_2 or steam; therefore, the latter molecules are used most frequently to get mild activation and the development of a uniform porous structure. While chemical methods require the addition of inorganic species in solution, that act before or during the carbonization on precursor materials. In fact, a commonly employed activation technique is the use of an alkaline hydroxide (KOH, NaOH) in a solid form [34] or phosphoric acid (H_3PO_4) [35].

The use of chemicals is balanced by the good performance of the process in developing a wide microporous structure with high SSA, instead the following research work has sought to maximize the adsorbents properties of ACFs from Kevlar® (porosity, SSA, skeletal density) through a more environmentally friendly conversion process (physical activation). The aim is to determine thermodynamic conditions and key activation parameters (gas flow, temperature and time) that control material porosity and to demonstrate that production of carbon-based materials by low energy consumption and the greener process can be obtained.

The studies present in literature show that is difficult to customize the porosity and to form a high microporosity with interesting adsorbing properties. ACFs from Kevlar have highlighted lower SSA and PV development and wider PSD than ACFs prepared from other precursors. Therefore, the following research work aims to explore the possibility of achieving some control in the activation process and of obtaining a homogeneous PSD with a pore size width in the order of a few nanometers, that could allow higher adsorption/desorption rates. In fact, a predominantly microporous homogeneous structure makes it more effective to retain gases at room temperature (RT) and can be an important alternative to various carbon-based materials [22]. Physical adsorption of gas requires a strong potential for interaction with the adsorption sites of the solid, therefore materials with optimal nanoporous structures must be produced.

Hence, considering the previous studies, a series of ACFs samples from commercial Kevlar® [30, 34] (hereafter called AKFs) were prepared. By regulating the physical activation process in its key parameters (time, temperature, and gas flow) and by using a crystalline organic precursor such as PPTA, we want to facilitate the creation of homogeneous structures with high microporosity with good gas adsorption performance.

3.4.2 Experimental section

3.4.2.1 Materials

Poly p-phenylene terephthalamide (PPTA) namely Kevlar® is an aramidic synthetic fiber with a high content of carbon and, typically, high mechanical properties as resistance to traction, cut, heat and flames. The chemical formula of Kevlar® monomer is [-CO-C_6H_4-CO-NH-C_6H_4-NH-]$_n$ while its molecular structure is depicted below in figure 1. The fibers are fully crystalline with a small fraction of randomly oriented material [36, 37].

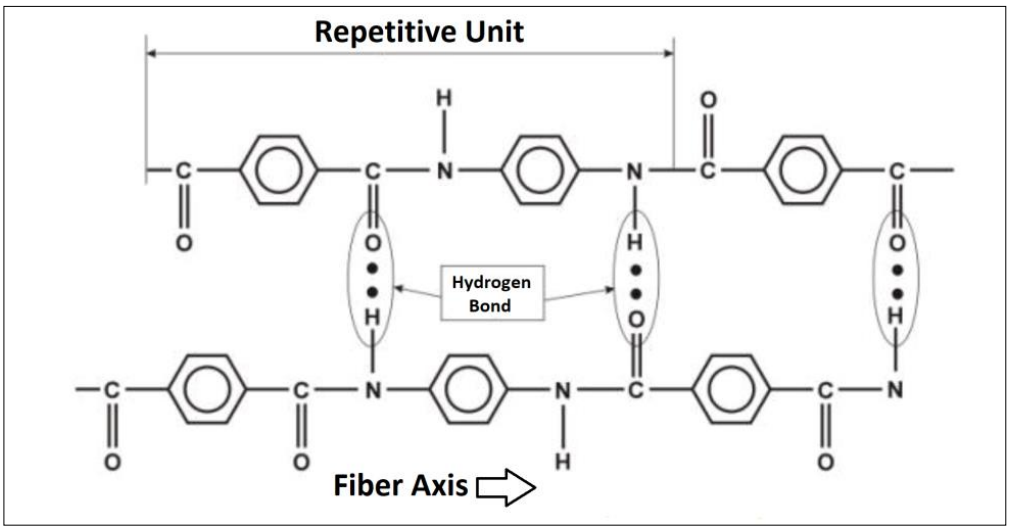

Figure 1. Typical Kevlar® molecular structure.

3.4.2.2 Synthesis of ACFs from commercial Kevlar® (AKFs)

The AKFs synthesis and preparation process involves two main steps: I) pyrolysis of the raw material; II) activation of the carbonized material. For the material production it was used an experimental apparatus consisting of an electric furnace equipped with a cylindrical stainless steel reactor which acts as sample holder. The reactor (dimensions: length 15 cm and 5 cm of internal diameter) is linked to a pipeline (1/4 inch) for the inlet/outlet gas regulated by a Mass Flow Controller. Process parameters (temperature, heating rates, gas flow) setting and monitoring were performed in real-time on computers through a home-made software developed in the LabView environment (National Instrument).

The AKFs samples were obtained starting from commercial Kevlar® fibers, dehydrated at 393 K for 180 min and then charred at 833 K for 30 min (heating rate 10 K/min) in a nitrogen flow of 0.9 Nl/min. Keeping the same flow with a heating rate of 4 K/min the activation step is reached. At this point, to have an oxidant atmosphere N_2 is replaced by CO_2. Changing gas

flow, temperature or time (see Table 1) various samples were produced with the aim to obtain the formation of different microporous structures.

The starting sample (AKFs1) was obtained using a temperature of 1023 K, a gas flow of 0.3 Nl/min and time of 180 minutes as activation parameters, according to the procedure reported by Choma et al. [34]. During the first step, all the samples are dehydrated and carbonized using the same process parameters; while in the activation step it is investigated the effect of process parameters modification on the AKFs structure. Changing synthesis parameters allows obtaining AKFs with different porous structures and adsorption capacity. The synthesis apparatus allows to control simultaneously the three activation parameters: temperature, inlet gas flow and exposition time.

The aim is to verify the trend (improvement or deterioration) of the porosity and SSA of the samples by changing key activation parameters of the material (see section 3) trying to improve adsorption properties.

3.4.2.3 Characterization techniques and analysis

The commercial Kevlar® sample was subjected to thermogravimetric analysis (TGA) using a DTG-60 simultaneous thermogravimetric and differential thermal analyzer from Shimadzu to measure the change in weight of the material, as a consequence of any decompositions that it undergoes following the development of gaseous products.

In order to observe morphology changes in the samples subjected to different activation processes, Scanning Electron Microscope (SEM) measurements were carried out using an EVOMA 10 (Zeiss, Milan, Italy). Prior to each analysis, all samples were sputter coated with a thin layer of gold in order to make them conductive, using a Quorum Q150 RS (Quorum Technologies, Lewes, UK). To evaluate fibers' diameters, SEM pictures were elaborated with the image processing program "ImageJ". More than twenty measurements for each sample were taken and the standard deviation was then calculated. Furthermore, Energy Dispersive X-ray Spectrometry (EDS) technique (EP=15 keV) was used for elemental analysis characterization with particular attention to carbon/oxygen ratio.

Analysis of the sample's textural properties were carried out by physical adsorption of N_2 at 77 K [38, 39] using a Micromeritics ASAP 2460 porosimeter and, before each test, all samples were outgassed at 473 K for 12 h under high vacuum (10^{-5} mbar). Brunauer-Emmette-Teller (BET) model [40] applied on adsorption data points in the relative pressure p/p_0 range 0.01-0.30 was used to determine SSA information.

The Total Pore Volume (TPV) was calculated from the N_2 uptake at relative pressure p/p_0 of 0.998, while the micropores volume (V_{mic}) and the Pore Size Distribution (PSD) were

calculated by using the Non Local Density Functional Theory (NLDFT) considering slit-shaped pores with energetically heterogeneous and rough walls [41].

The gas adsorption measurements were carried out with a home-made volumetric Sieverts' apparatus (fPcT) built by DeltaE S.r.l [42]. CO_2 and CH_4 adsorption/desorption measurements were carried out at three different temperatures: room temperature (RT = ~ 298 K), low temperature (LT = ~ 280 K) and high temperature (HT = ~ 314 K), and in a pressure range (0-15) bar and (0-40) bar respectively. Before starting gas storage measurements, Helium (He) picnometry analysis was performed in order to get the sample skeletal density value. He pycnometry measurements took place on a Sieverts' apparatus by making use of He as the probe gas in RT and in the pressure range of 0-900 mbar. All measurements were repeated several times (>35) to minimize the experimental error. Prior to each adsorption/desorption measurement, all samples were outgassed at 473 K overnight under vacuum ($P<10^{-6}$ mbar) to eliminate the eventual fraction of water weakly bound inside the samples.

3.4.3 Results and discussion

3.4.3.1 Bulk and Surface characterization

Based on the thermal degradation behaviour of Kevlar® observed through TGA (see figure S1-Supporting Information), according to the literature [33], different samples were synthesized by tuning process parameters. Figure 2-a shows temperature, CO_2 flux and exposition time values for each sample; the change of a single parameter is indicated in the figure by a black arrow, while a turquoise arrow indicates the change of two parameters simultaneously.

Changing of activation parameters leads to a proportional burn-off as clearly visible in figure 2-b, in particular increasing temperature leads to an increase in the burn-off ranging from 70% up to 85%. It is also noteworthy that the increase of the burn-off is directly connected to an increase in the skeletal density of all synthesized samples (see figure 2-c).

Knowing from TGA measurements (see figure S1) that the Kevlar® fiber loses 67% of its mass during carbonization process up to 833 K, we can infer that the exceeding weight loss of all the sample is due to the activation step and the extent of it depends on the specific activation parameters.

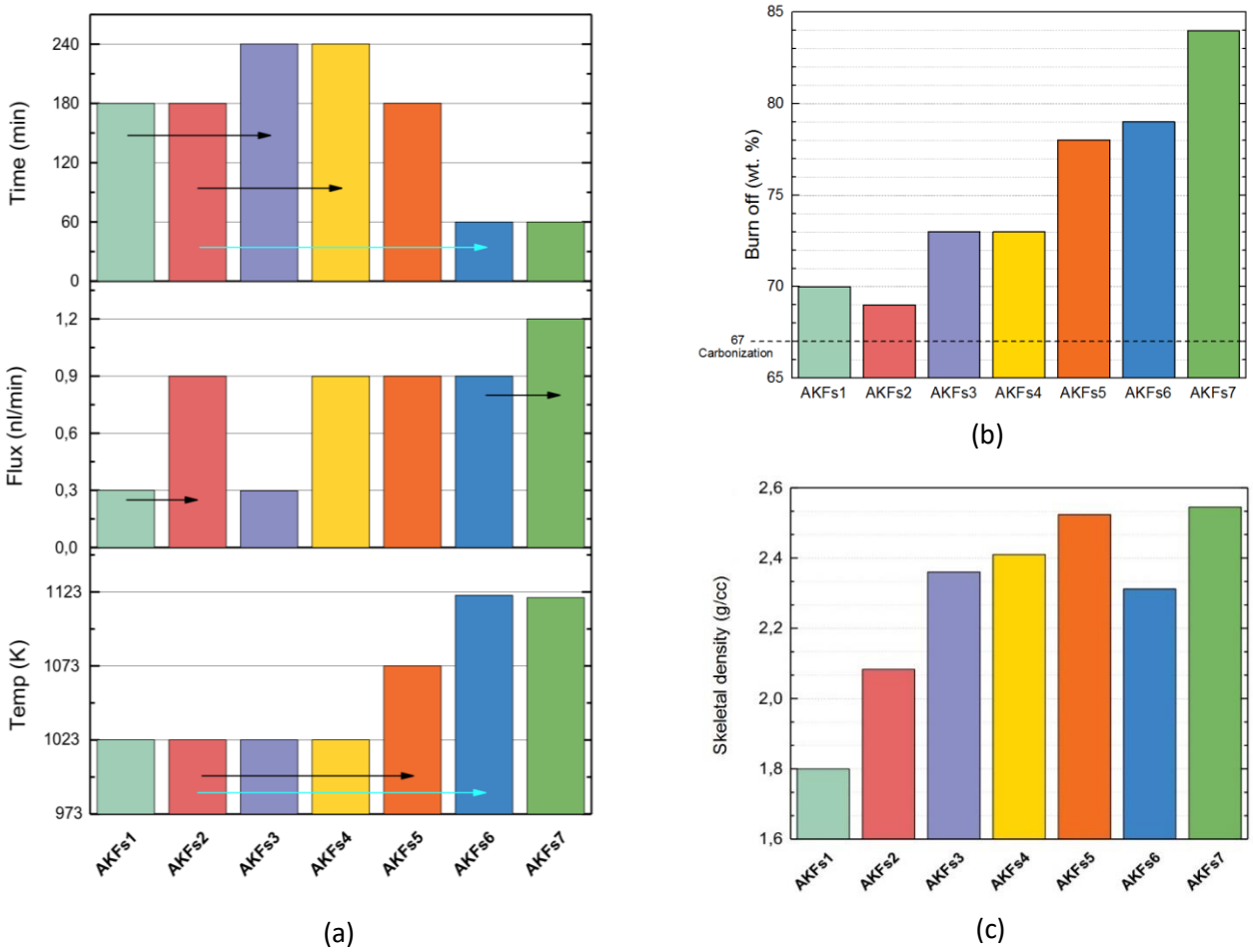

Figure 2. (a) Comparison of the sample's activation parameter used in the process; (b) Kevlar® burn-off (wt. %) after the synthesis process; (c) sample's skeletal density (g/cc) measured by He pycnometry.

The relation between the burn-off and the activation parameter is not always straightforward: comparing the couple AKFs1-AKFs2 and AKFs6-AKFs7 we can see that changing the flux parameter the burn-off remains the same in the first case whereas it increases from 79.6% up to 85% in the second one; comparing AKFs1-AKFs3 and AKFs2-AKFs4 on the exposure time we can say that it increases the burn-off percent of about the same amount for both samples (AKFs3 and AKFs4); as last, the temperature parameter is, among the other, the one that substantially drives the burn-off as visible comparing the sample AKFs2-AKFs5 where mass loss increases by +8.5%.

The latter is also confirmed by observing that changing both temperature and exposition time (AKFs2-AKFs6), i.e. increasing the activation temperature from 1023 K up to 1123 K and decreasing the exposition time from 180 min up to 60 min, the burn-off increases by almost +10%.

Table 1. Sample's activation parameters and textural properties.

	Activation parameters			Textural properties						
Sample	**Temp (K)**	**CO_2 Flow (Nl/min)**	**Time (min)**	**Skeletal density (g/cc)**	**Burn off (wt.%)**	**SSA (m^2/g)**	**TPV (cc/g)**	**V_{Ultra-} (cc/g)**	**V_{Super-} (cc/g)**	**V_{Meso-} (cc/g)**
AKFs1	1023	0.3	180	1.79	70	469	0.265	0.195	0.034	0.036
AKFs2	1023	0.9	180	2.08	69	538	0.249	0.175	0.034	0.040
AKFs3	1023	0.3	240	2.36	73	630	0.280	0.195	0.052	0.033
AKFs4	1023	0.9	240	1.85	73	752	0.335	0.241	0.058	0.036
AKFs5	1073	0.9	180	2.52	78	997	0.436	0.248	0.135	0.053
AKFs6	1123	0.9	60	2.31	79	935	0.389	0.194	0.173	0.022
AKFs7	1123	1.2	60	2.55	84	1109	0.491	0.220	0.208	0.063

ACs in general exhibit a skeletal density in the order of 1.8÷2.0 g/cc; looking at figure 2-c we can see that all the samples exceeded this value, except the sample AKFs1 (the sample with the starting parameters of the experiment) whose density lie in the expected range. This density 30% higher than the expected could be due to high heat resistance of the material. Moreover, we can observe that at the increasing of the mass loss an increase of the skeletal density occurs. Apparently, slightly different behavior is observed for the AKFs6 sample that shows a skeletal density value lower compared to the one expected; however, within the experimental error (± 0.10÷0.15 g/cc), it could be considered perfectly part of the highlighted linear trend. The burn-off of the fibers and the morphology of the samples were highlighted by SEM images shown below in figure 3. The reduction of the material bulk is clearly evident from the thinning of the fibers compared to the raw material, with values similar to all the synthesized samples. At the same time, it is noteworthy to note that the morphology of the fibers was preserved after the carbonization process. The fibers diameter of Raw Kevlar® sample was about 12 μm, while the carbonized fibers own a diameter ranging from about 7.2 to 7.6 μm (see figure 3-right and table S-T1). As expected the carbonized fibers, compared to the untreated raw Kevlar® sample, exhibited a smaller diameter as a consequence of a shrinking effect induced by the carbonization process, as already observed and reported in the literature [34, 43, 44]. Besides, the activation process determines the porous structure, highlighted in the various images by an increase in roughness on the surface of the fibers compared to the starting material. The activation parameters influenced also the carbon, oxygen and nitrogen contents in the final material (see S7 and S-T2).

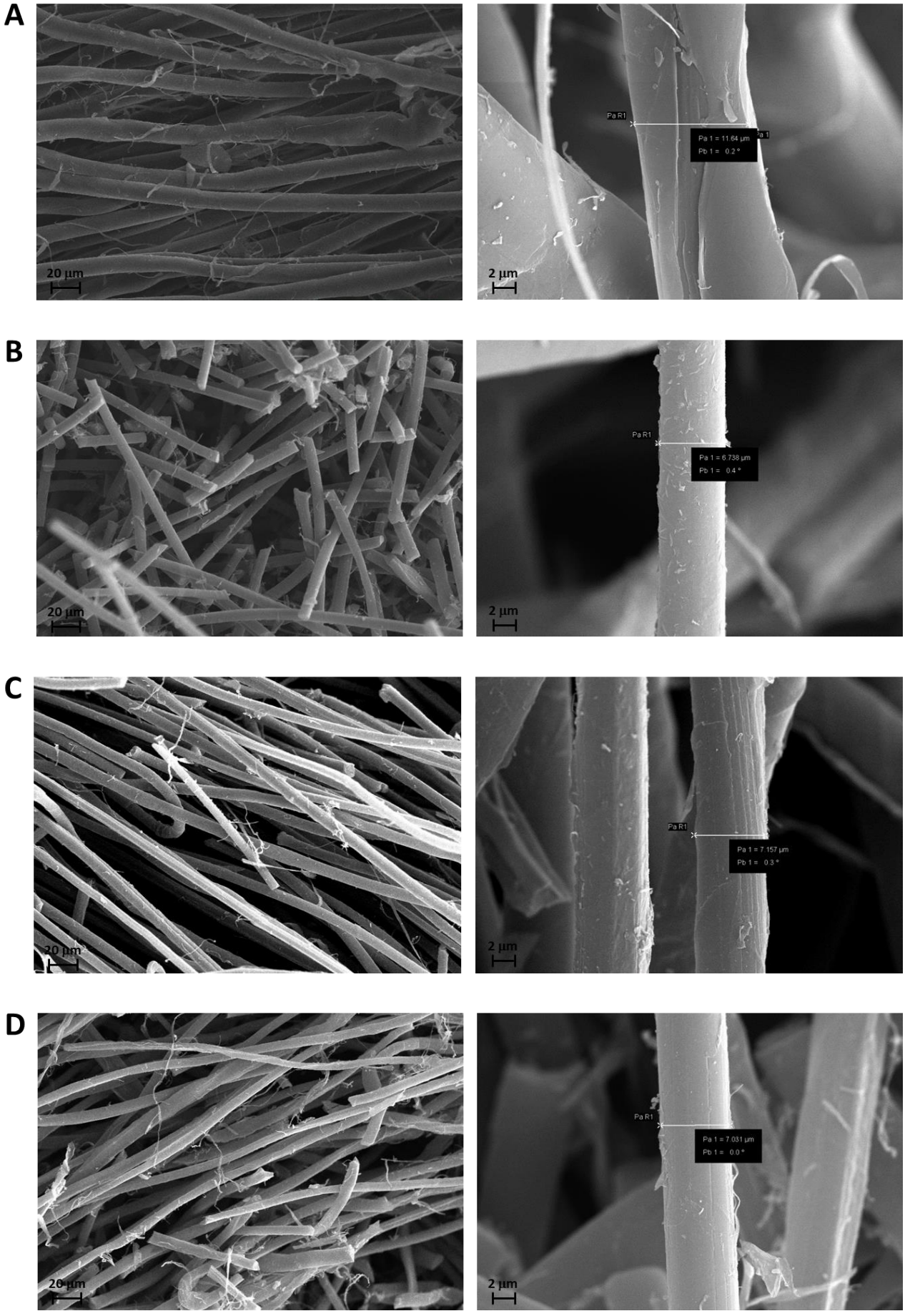
A
20 µm
Pa R1
Pa 1 = 11.64 µm
Pb 1 = 0.2 °
2 µm
B
20 µm
Pa R1
Pa 1 = 6.738 µm
Pb 1 = 0.4 °
2 µm
C
20 µm
Pa R1
Pa 1 = 7.157 µm
Pb 1 = 0.3 °
2 µm
D
20 µm
Pa R1
Pa 1 = 7.031 µm
Pb 1 = 0.0 °
2 µm

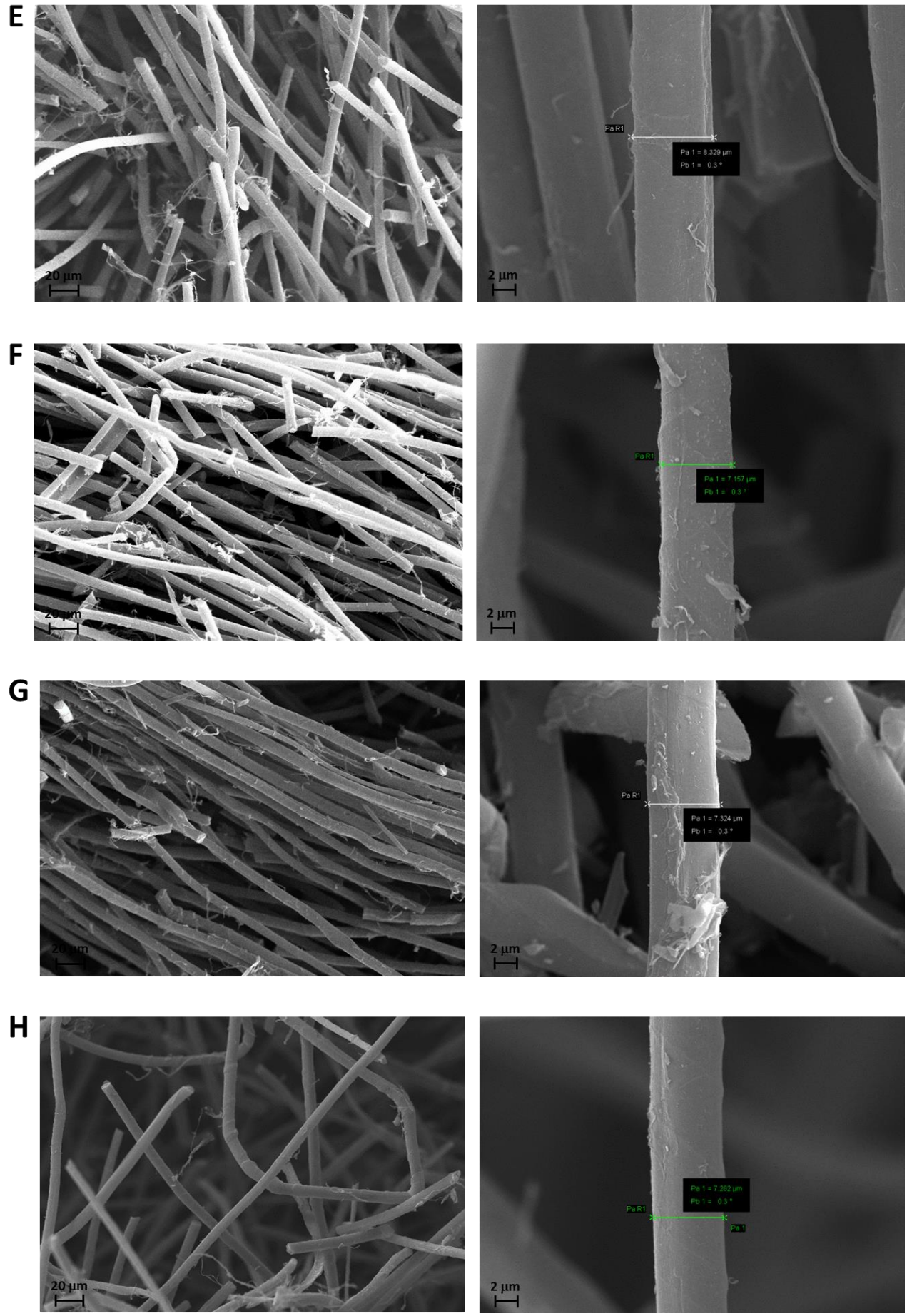

Figure 3. SEM pictures of the evaluated samples, overview (left) and fiber magnification (right). A) Raw Kevlar, B) AKFs1, C) AKFs2, D) AKFs3, E) AKFs4, F) AKFs5, G) AKFs6 and H) AKFs7.

Figure 4 shows the N_2 adsorption/desorption isotherms performed at 77 K for all the investigated samples. All the isotherms belong to the type I with some contribution of type IV at medium and high relative pressures according to IUPAC classification [45] and similar to other ACFs [34, 46, 47], in fact, none of them show a phase change transition at $p/p_0=1$. Thus, we can infer that all AKFs samples have a high porous structure with no macropores and mainly constituted by micropores. Moreover, a deeper look at the shape of the isotherms suggests that the N_2 adsorption mechanism is the micropore filling because of the absence of desorption hysteresis below 0.42 p/p_0 [38]. For this reason, it is expected that samples with a higher amount of N_2 uptake have a higher extent of the available surface area. Besides, the presence of H4 type hysteresis above 0.42 p/p_0 indicates residual presence of mesopores [45].

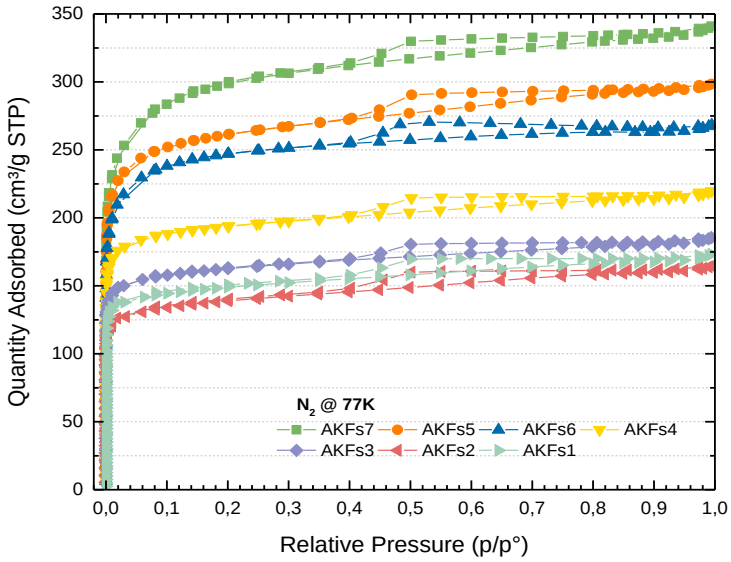

Figure 4. N_2 adsorption isotherms at 77 K.

A more detailed description of the sample's pore structure is achieved by calculating the PSD from the nitrogen adsorption isotherms by mean of the NLDFT analysis [48].

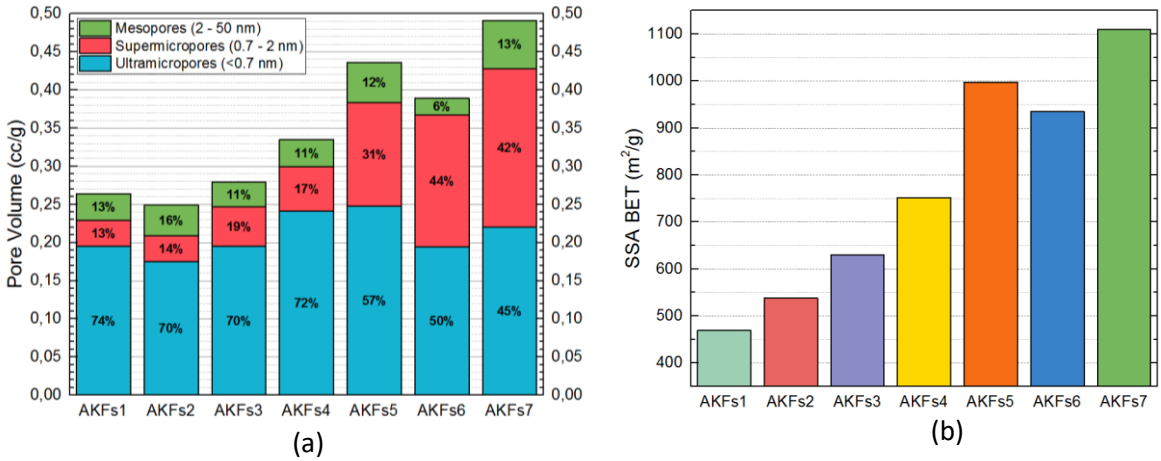

Figure 5. Comparison of the sample's PV (a) and SSA (b); the sample's PV is decomposed by the IUPAC pore classification (mesopores, supermicropores, ultramicropores) for each interval is reported the value percent respect to the TPV.

Figure 5-a shows the sample's PV divided accordingly to the IUPAC pore classification in mesopores (2-50 nm), supermicropores (0.7-2 nm) and ultramicropores (<0.7 nm) [39, 49] and the value percent of the interval PV over the total. The macropore interval is not considered since NLDFT range limit is 30 nm [48]. Accordingly with what previously stated, looking at figure 5-a it is clear that all the samples are mainly microporous with a very small fraction of mesoporosity, lying between 5%-16% of the TPV, comparable to that reported in other works [34, 46]. A comparison of the sample's SSA calculated by the BET method is reported in figure 5-b, also in this case the range of values is similar to literature [34, 46]. The highest value of SSA is exhibited by the AKFs7 sample with 1108±4 m^2/g.

By looking at both figure 5 histograms, it might notice a quite correlation between PV and SSA; in particular, a quite linear relation between the TPV and the SSA is showed in figure 6-a. Moreover, by looking at the different pore ranges, it is evident that the increase of the sample's SSA is mainly originated by an increase of the supermicropores, while the content of ultramicro and mesopores remain almost constant.

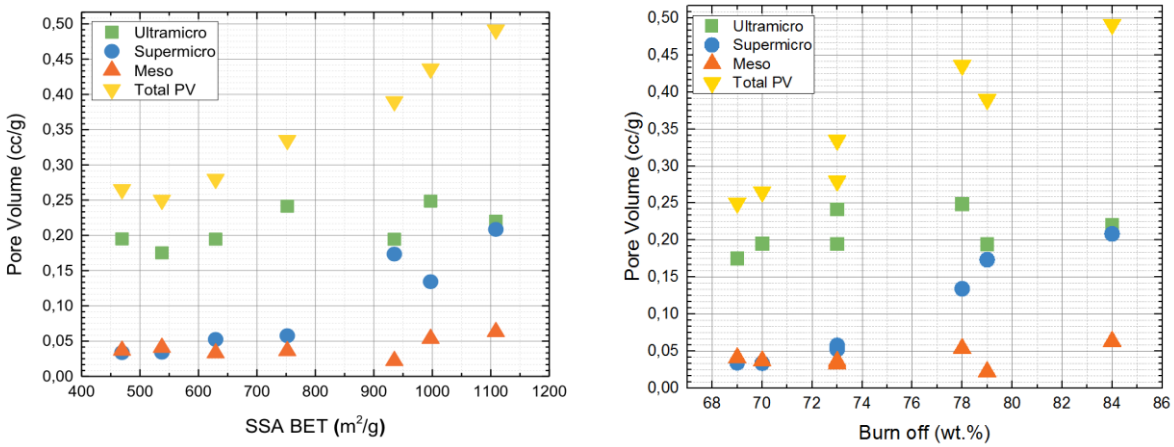

Figure 6. Correlation between the sample PV and the SSA (a); correlation between the sample PV and the activation burn off (wt. %) during the synthesis process (b).

Another important linear relation between the TPV and the activation burn off (wt.%) can be observed in figure 6-b, which gives an indication that the porous structure, in particular the supermicropores fraction, is created by eroding the sample skeleton during the activation process. Evidence of that is given by the PSD considering a sample subjected only to the carbonization phase (see figure S2). Here can be observed how the mesopores and supermicropores fraction are created in the carbonization phase while the ultramicroporosity during the activation process. Moreover, by looking at the pore composition of each sample, the pore ratios are rather constant up to a 74% burn-off, after which the amount of very small pores (ultramicropores) decreases in favor of the larger ones (supermicropores), while the

percentage of mesopores remains similar. The PSD analysis shows that the AKFs1, AKFs2, AKFs3 and AKFs4 samples have a quite similar pore composition. One hypothesis to explain their difference in PV, i.e. the ratio between the accessible pore volumes and the sample mass, is that the gasification reaction produce bulk erosion without affecting the pore structure and volumes already formed during the carbonization process. On the contrary, the AKFs5, AKFs6, and AKFs7 samples that have quite similar content of useful pores show a different pore composition due to the increase of the supermicropores and mesopores content. This can be due to the less selective gasification reaction, occurring for activation at higher temperatures, which might lead the widening of ultramicropores into supermicropores.

3.4.3.2 Gas adsorption analysis

CO_2 and CH_4 adsorption isotherms comparison of the AKFs samples with different compositions are showed in figures 7 and 8 below. Different pressure range and temperature conditions were investigated; in particular, 0-15 bar for CO_2 and 0-40 bar for CH_4 at 280 K (Low), 298 K (RT) and 314 K (High) for both gases.

Comparing the sample performance toward the two adsorbates, it is possible to unveil peculiar adsorption properties abducted to the different interactions between sorbent and adsorbant species, that can be usually related to the structural, morphological and chemical properties of the samples and/or to analysis conditions (i.e. pressure, temperature).

Looking deeper at the adsorption isotherms, two different blocks can be clearly distinguished. In detail, a first block including from AKFs1 to AKFs4 sample shows medium-low and similar adsorption values for all of them, while a second block (including AKFs5-AKFs7 samples) shows significantly higher values than the previous one. The observed behavior highlights, in agreement with the porosity results showed above, the marked improvement in the production process of the samples between those initially synthesized (AKFs1-AKFs4) and the last three (AKFs5-AKFs7).

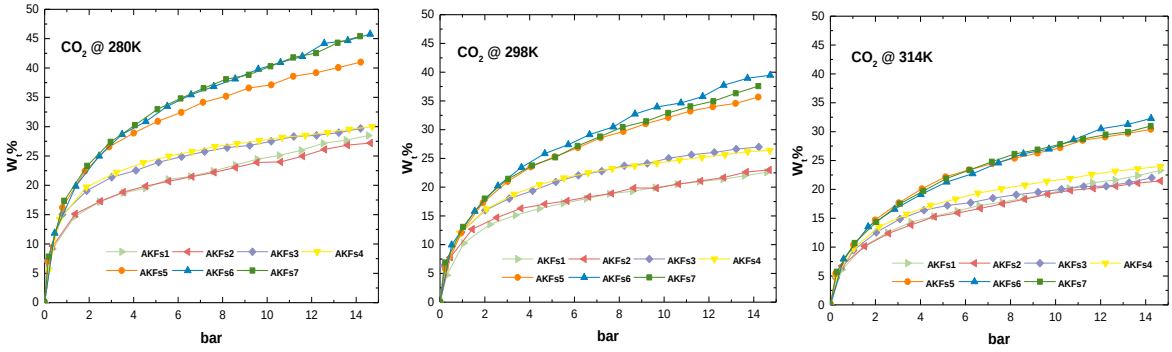

Figure 7. CO_2 adsorption isotherms comparison at three different temperatures and pressure up to 15 bar, for all analyzed AKFs samples.

Figure 7 highlights that the CO_2 adsorption capacity reaches interesting uptake for AKFs5, AKFs6 and AKFs7 at temperature of 280 K, with a slightly better behaviour for the last two samples able to reach a maximum storage capacity around 46 wt%. As expected, the differences in the CO_2 absorbed for those samples decreases by increasing temperature (298 K and 314 K). For all the investigated temperatures, the CO_2 adsorption isotherms do not reach saturation and show hysteresis phenomena during the desorption phase (see figure S3). Nevertheless, all samples show good cyclability after multiple adsorption/desorption steps (see figure S4). Besides, respect to the literature data, it is possible to note as the values for AKFs5, AKFs6 and AKFs7 samples are comparable with storage capacity of other physical activated carbons or materials [44, 50, 51] and in some case, at 280 K, they are similar to adsorption values of chemical activated carbons [50, 52] (see Table 3). This confirms the fundamental influence of the process parameters and the porosity of the materials on the adsorption capacity.

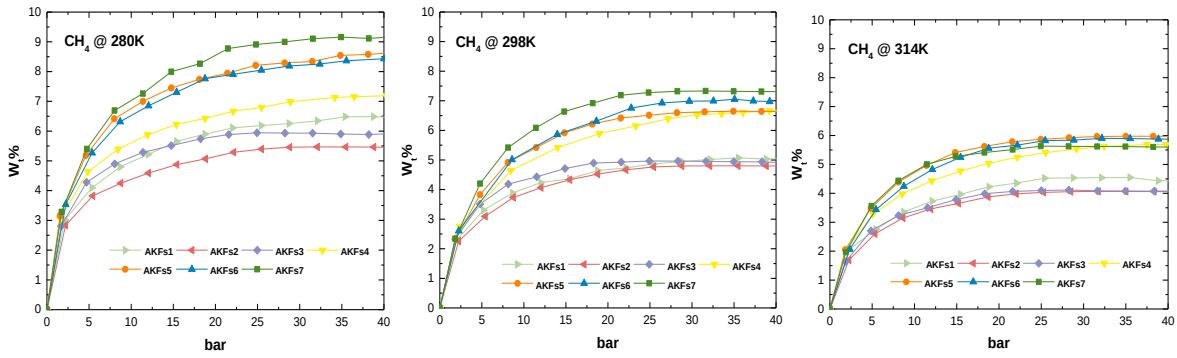

Figure 8. CH_4 adsorption isotherms comparison at three different temperatures and pressure up to 40 bar, for all analyzed AKFs samples.

Looking figure 8, the trend is quite similar for CH_4 adsorption where the AKFs7 shows higher adsorption values than the other samples, particularly at 280 K and 298 K reaching uptake values respectively of 9.6 wt% and 7.3 wt%. While the maximum uptake at higher temperature (314 K) is similar for all the three samples. The isotherms reach an adsorption saturation value at about 20 bar with a plateau up to the maximum investigated pressure (40 bar). Therefore, almost all methane is stored at low pressure in a range of 0-20 bar.

The CH_4 adsorption process appears completely reversible without any hysteresis and a high cyclability on multiple adsorption/desorption steps is observed (see figure S5). Also in this case, it is possible to note as the AKFs5, AKFs6 and AKFs7 show an adsorption capacity similar to other activated carbons [24, 25, 44] and, at 280 K, these values are quite similar to chemical activated carbons [7, 44] (see Table 4).

The adsorption results for both CO_2 and CH_4 are summarized in Table 2 below, where the amounts of gas by the samples at maximum measurement pressure are reported. In both cases,

based on EDS results (see S7 and S-T2), we can assert that a higher storage capacity should be mainly related to sample textural properties, in particular slightly higher content of carbon suggests a different and/or more performing structure, excluding improvement effects related to possible functionalization.

Table 2. CO_2 (at 15 bar) and CH_4 (at 40 bar) uptake reported as wt% and mmol/g for the different investigated temperatures.

SAMPLE	CARBON DIOXIDE (CO_2)						
	280 K wt% $_{15}$	298 K wt% $_{15}$	314 K wt% $_{15}$	280 K (mmol/g)	298 K (mmol/g)	314 K (mmol/g)	ΔH_{mean} (kJ/mol)
AKFs1	28.5	22.6	23.3	6.5	5.1	5.3	29 ± 4
AKFs2	27.2	24.5	23.3	6.2	5.6	5.3	37 ± 5
AKFs3	29.7	27.0	22.9	6.8	6.1	5.2	48 ± 7
AKFs4	30.3	27.2	24.0	6.9	6.2	5.5	18 ± 2
AKFs5	41.7	35.7	30.4	9.5	8.1	6.9	25 ± 1
AKFs6	45.9	39.5	32.3	10.4	9.0	7.7	21 ± 1
AKFs7	45.4	37.5	31.4	10.3	8.5	7.1	27 ± 1
SAMPLE	**METHANE (CH_4)**						
	280 K wt% $_{40}$	298 K wt% $_{40}$	314 K wt% $_{40}$	280 K (mmol/g)	298 K (mmol/g)	314 K (mmol/g)	ΔH_{mean} (kJ/mol)
AKFs1	6.8	5.1	4.6	4.2	3.2	2.9	20 ± 2
AKFs2	5.7	4.8	4.1	3.6	3.0	2.6	16 ± 1
AKFs3	6.4	5.7	4.4	4.0	3.6	2.7	17 ± 1
AKFs4	7.4	6.7	5.7	4.9	4.4	3.6	25 ± 4
AKFs5	9.4	6.8	6.2	5.9	4.6	4.0	22 ± 1
AKFs6	9.0	7.1	6.2	5.6	4.8	4.1	21 ± 4
AKFs7	9.6	7.3	5.9	6.0	4.9	3.7	12 ± 1

As expected, it is easy to verify that for both gases the absolute adsorption values decrease by increasing the measurement temperature. In both CO_2 and CH_4 cases, the slight differences in the wt% at the maximum analyzed pressure could be considered within the experimental error. However, both CO_2 and CH_4 show good uptake values at RT, always important in view of practical applications. In this regard, it is interesting to note that already at low pressure, in

particular 10 bar for CH_4 and 6 bar for CO_2, the synthesized materials are able to store almost the 80% of the total amount stored at the maximum analyzed pressure.

Table 3. Comparison of CO_2 uptake among AKFs samples and similar materials available in literatures.

SAMPLE		**CO_2 storage (mmol/g) at 298 K @ Pressure (bar)**
Name	**Activation**	
AKFs5	Physical	8.1@15
AKFs6		9.0@15
AKFs7		8.5@15
P-CC-PNP [44]	Physical	7.5@20
Amorphous Carbon [50]	Physical	10.63@8
Ribbon CNFs [50]	Physical	0.46@8
C85-CC-PNP [44]	Chemical	8.9@20
Activated Amorphous Carbon [50]	Chemical	16.53@8
AC- Ribbon CNFs [50]	Chemical	3.77@8
PAC-500 [52]	Chemical	2.79@1
fPLA [51]	No-treatment	3.64@15

Table 4. Comparison of CH_4 uptake among AKFs samples and similar materials available in literatures.

SAMPLE		**CH_4 storage (mmol/g) at 298 K @ Pressure (bar)**
Name	**Activation**	
AKFs5	Physical	4.6@40
AKFs6		4.8@40
AKFs7		4.9@40
P-CC-PNP [44]	Physical	4.26@20
C85-CC-PNP [44]	Chemical	5.35@20
ADPC3 [7]	Chemical	5@35
Filtercarb PHA [24]	Physical	5.65@35
Filtercarb GCC8X30 [24]	Physical	5@35

Figure 9 shows the correlation of the sample's maximum uptake capacity, at different temperature, with the TPV for both gases (CO_2 and CH_4). Analyzing first the CO_2 graphs (figure 9-a) we can notice that up to AKFs4 sample the adsorption uptake slightly increases

with the increase of the TPV. On the other side, a net increase in uptake is observed in the AKFs5, AKFs6 and AKFs7 samples even though it remains constant at the increasing of the TPV.

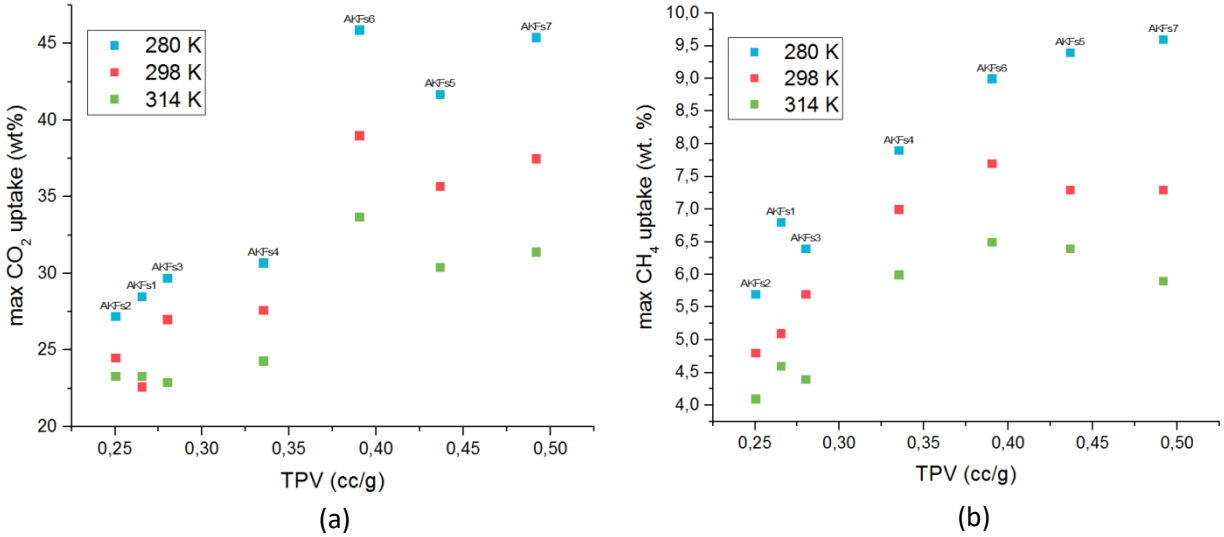

Figure 9. Comparison between sample's maximum measured gas uptake (wt.%), CO_2 (a) and CH_4 (b), their total pore volume (cc/g).

Another aspect to observe in the AKFs5, AKFs6 and AKFs7 samples is the similarity in the reduction of maximum uptake at the increasing of the temperature, indicating that the pores involved in the interaction with the adsorbent have a similar enthalpy of adsorption (ΔH_{ads}). This hypothesis is confirmed by looking at figure 10-a where the boxplot represents, for each sample, the CO_2 enthalpy of adsorption distribution up to 5 wt% (see figure S6).

The AKFs5, AKFs6 and AKFs7 samples show a very close mean ΔH_{ads} despite the difference in pore composition; in fact, the samples AKFs5, AKFs7 have a higher content of mesopores compared to the AKFs6 (figure 5-a). This implies that, in the investigated pressure range, the mesopores are not primarily involved in the adsorption of the CO_2, explaining why, in the case of the AKFs5, AKFs6 and AKFs7 samples, the CO_2 uptake does not depend linearly on the TPV.

Moreover, figure 10-a shows that the samples AKFs1, AKFs2 and AKFs3 have a progressive increase in the enthalpy of adsorption, which is more related to the increase in SSA (figure 6-a) rather than to the pore volume composition (figure 5-a). On this basis, we can infer that the increase in ΔH_{ads} is due to the development of ultramicro and supermicropore channel networks that exhibit higher SSA at parity of pore volume. The sample AKFs4 is very interesting because it has an enthalpy of adsorption similar to the AKFs5, but its CO_2 isotherm adsorption is very close to the AKFs3, even though it has a 25% higher TPV. Based on our

findings, we cannot fully interpret the AKFs4 CO_2 adsorption mechanism because of its controversial behavior, which requires a more in-depth investigation.

On the other side, the CH_4 maximum uptake at 280 K (figure 9-b) shows an uptake proportional to the TPV indicating the contribution of all pores to the total adsorption. Moreover, it is noticeable that the sample's maximum uptake at the increasing of the temperature does not decrease uniformly for all the samples as the drop in uptake is more pronounced for the AKFs5, AKFs6 and AKFs7 rather than the AKFs4. This behaviour might be linked primarily to their lower enthalpy of adsorption, as it showed in figure 10-b. Nevertheless, even though the AKFs4 sample has the highest ΔH_{ads}, it achieves a lower value of maximum uptake respect to the other samples because of its lower total pore volume (TPV).

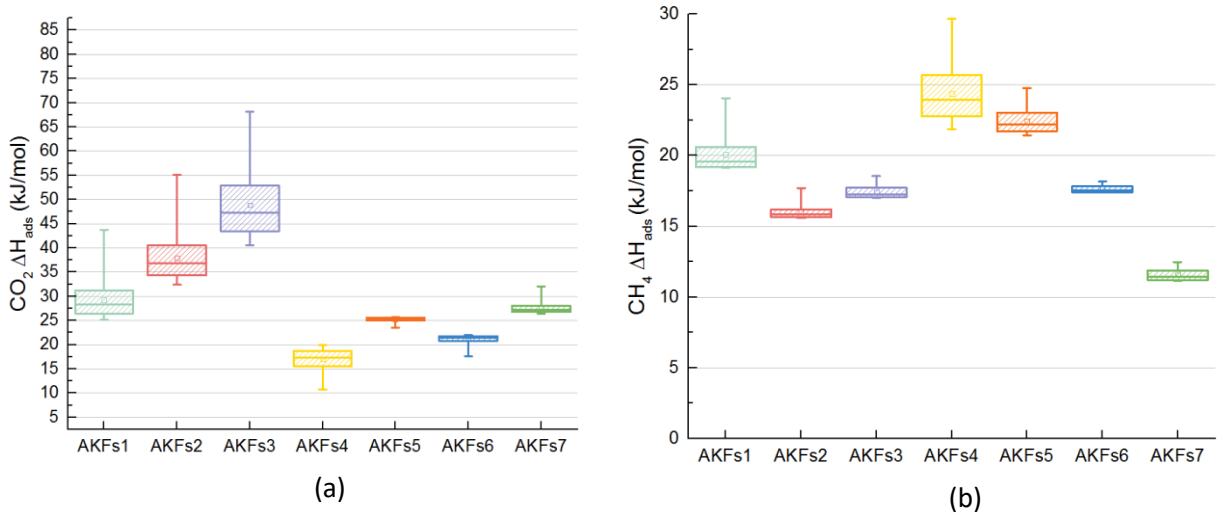

Figure 10. The boxplot represents for each sample the distribution of enthalpy of adsorption (ΔH_{ads}) up to 5 wt% for the CO_2 (a) and up to 2 wt% for the CH_4 (b).

3.4.4 Conclusions

A series of activated carbon fiber samples were prepared from Kevlar® (AKFs) through a synthesis process consisting of carbonization and subsequent physical activation in a CO_2 atmosphere within the same apparatus. The innovative pyrolysis system developed made it possible to modify and manage the key activation parameters (time, temperature and gas flow) throughout the process and, therefore, to study and analyse the formation of the porous structure under varying conditions. In this way, a series of AKFs samples with increasingly better structural properties aimed to gas adsorption were produced.

Average SSA around 1000 m^2/g together with high ultra/super microporosity characteristics (over 85% of the pores) allowed to obtain interesting adsorption properties toward CO_2 and CH_4 gases. In both cases, the best results were obtained on the AKFs5, AKFs6 and AKFs7

samples through a slight increase in the activation temperature (up to 1123 K), with a marked improvement in the values of the TPV linked to the microporosity. The procedure used for sample preparation, even if leads to porous structures comparable to those already developed and reported in the literature [34], allowed to simplify the overall process (dehydration, carbonization and activation within the same apparatus) and shortening the duration (activation time reduced to 1 hour) therefore in favour of significant energy savings.

From the obtained results we conclude that excessive increase in time and gas flow during the activation phase leads to an erosion of the bulk structure with consequent loss of microporosity and increase in mesoporosity; therefore, a decrease in efficiency in gas storage. On the contrary, by keeping these two parameters low, a key role in the formation of a microporous structure is played by temperature which also contributes to the increase of the carbon content in the material.

The above can be easily observed in the three best-obtained samples. The AKFs6 even if owns a lower SSA compared to AKFs5 and AKFs7 samples, shows higher values of CO2 uptake in all the analyzed temperature conditions (≈ 46 wt% at 280 K, ≈ 39.5 wt% at 298 K and ≈ 32 wt% at 314 K) thanks to a greater microporosity (94% of TPV) compared to the other two samples (88% and 87%).

Furthermore, it is important to underline that, the quantity of CO_2 stored at a temperature of 298 K and a pressure of about 1 bar gives a slightly higher value (3.0 mmol/g) than reported data in the literature [34]. The quantities of gas measured at 280 K (4.2 mmol/g) and 314 K (2.4 mmol/g) also show effective adsorption at temperatures of operational interest. In summary, the CO_2 uptake achieved is comparable with the values of other physically and chemically activated carbons (see tables 3 and 4).

The CH_4 adsorption recorded up to 40 bar for all the best samples is quite similar. In particular the maximum adsorption values obtained at 298 K (around 7.5 wt%) are part of the expected trend for porous materials with the similar textural properties (i.e. SSA and PSD) [7]. On the contrary, a clear improvement in the performances is obtained at a temperature of 280 K reaching average values around 9.5 wt%, similar to chemically activated carbons [7, 44]. We can also conclude that an increase in the ΔH_{ads} is directly connected to the development of ultramicro and supermicropore channel networks that exhibit higher SSA at parity of pore volume.

In addition to the reported results, it is noteworthy that all the synthetized samples show higher skeleton density (>> 2.0 g/cc) beyond the average expected value typical of activated carbon (1.8÷2.0 g/cc) which brings a greater volume of the voids made available to the gases.

3.4.5 Supporting Information

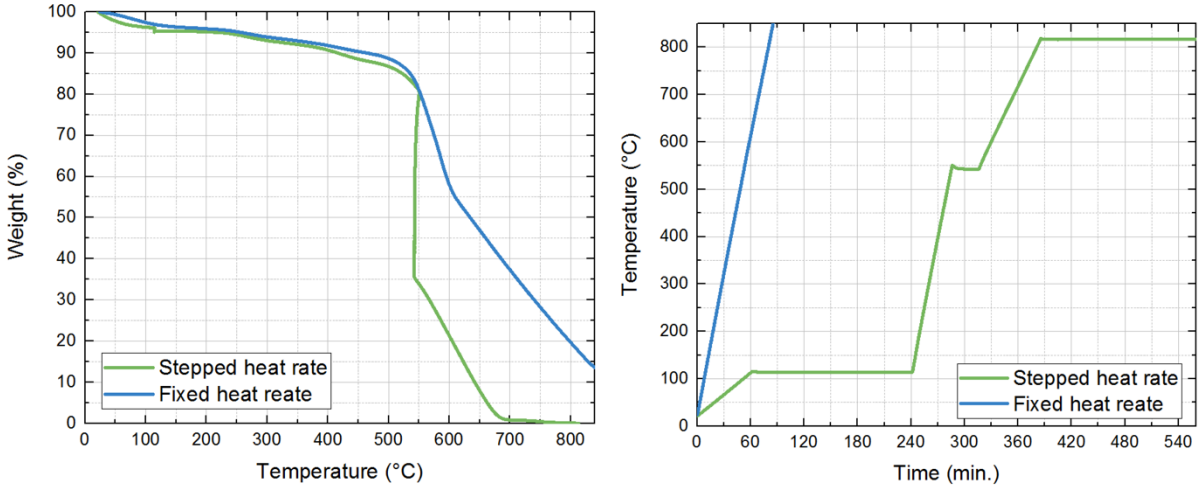

Figure S1. (left) TGA measurement measured at "fixed heat rate" and "stepped heat rate". The "stepped heat rate" program follows the heating steps used during the samples preparation (carbonization process); (right) heat rate used in the "fixed heat rate" and "stepped heat rate" TGA measurements.

Sample Name	Fiber Diameter (μm)	Error (μm)
Raw Kevlar®	12.20	± 0.68
AKFs1	7.20	± 0.50
AKFs2	7.50	± 0.50
AKFs3	7.45	± 0.57
AKFs4	7.60	± 0.70
AKFs5	7.50	± 0.40
AKFs6	7.20	± 0.63
AKFs7	7.60	± 0.60

Table S-T1. Fiber diameters measured for all the evaluated samples.

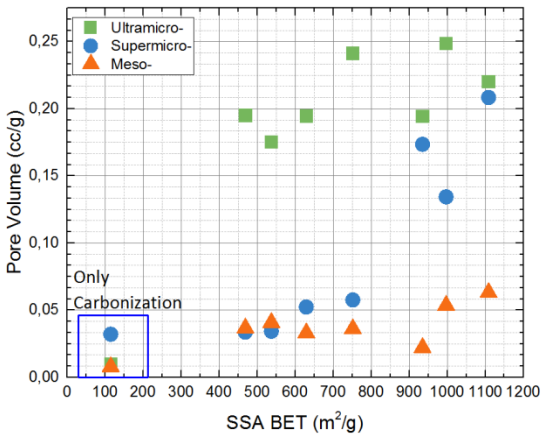

Figure S2. Correlation between the sample PV and SSA considering sample's carbonization.

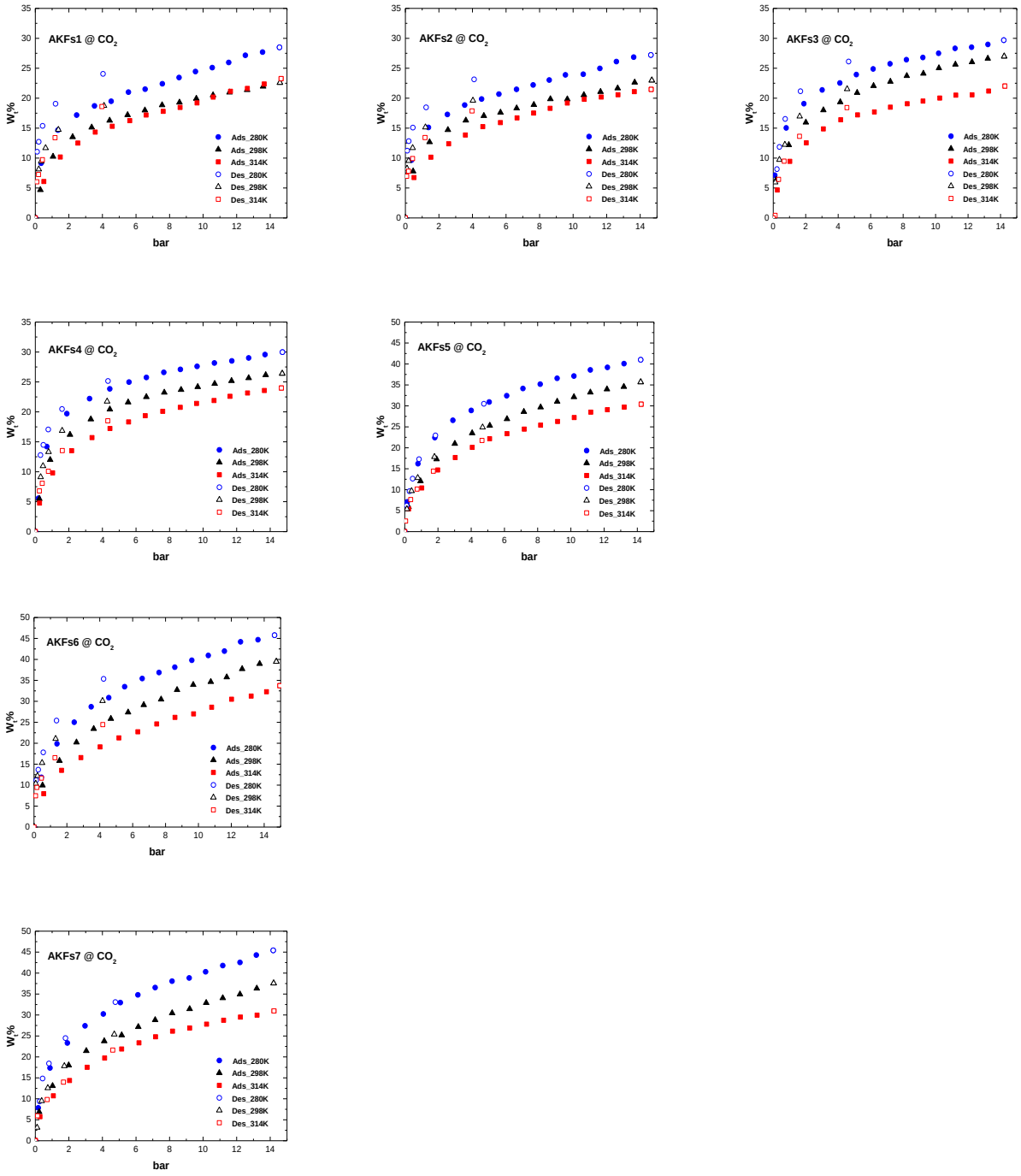

Figure S3. CO_2 adsorption/desorption isotherms at 280 K, 298 K and 314 K measured up to 15 bar for all the analyzed Kevlar sample.

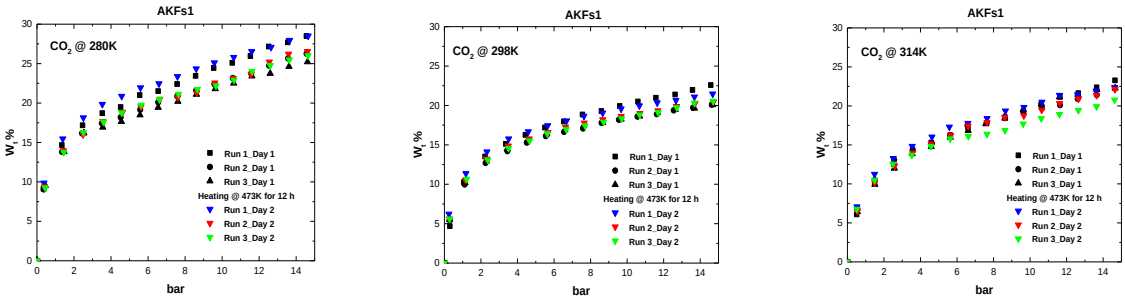

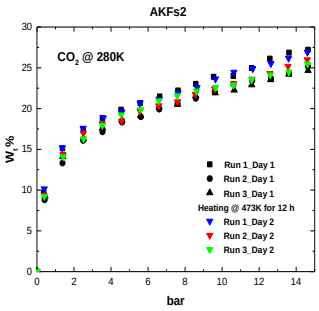
AKFs2
CO2 @ 280K
Wt %
bar
Run 1_Day 1
Run 2_Day 1
Run 3_Day 1
Heating @ 473K for 12 h
Run 1_Day 2
Run 2_Day 2
Run 3_Day 2

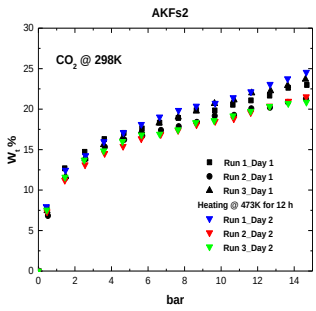
AKFs2
CO2 @ 298K
Wt %
bar
Run 1_Day 1
Run 2_Day 1
Run 3_Day 1
Heating @ 473K for 12 h
Run 1_Day 2
Run 2_Day 2
Run 3_Day 2

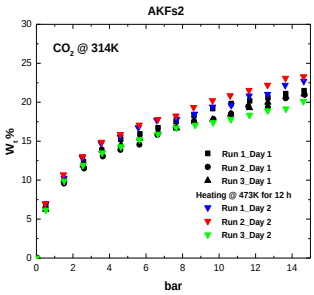
AKFs2
CO2 @ 314K
Wt %
bar
Run 1_Day 1
Run 2_Day 1
Run 3_Day 1
Heating @ 473K for 12 h
Run 1_Day 2
Run 2_Day 2
Run 3_Day 2

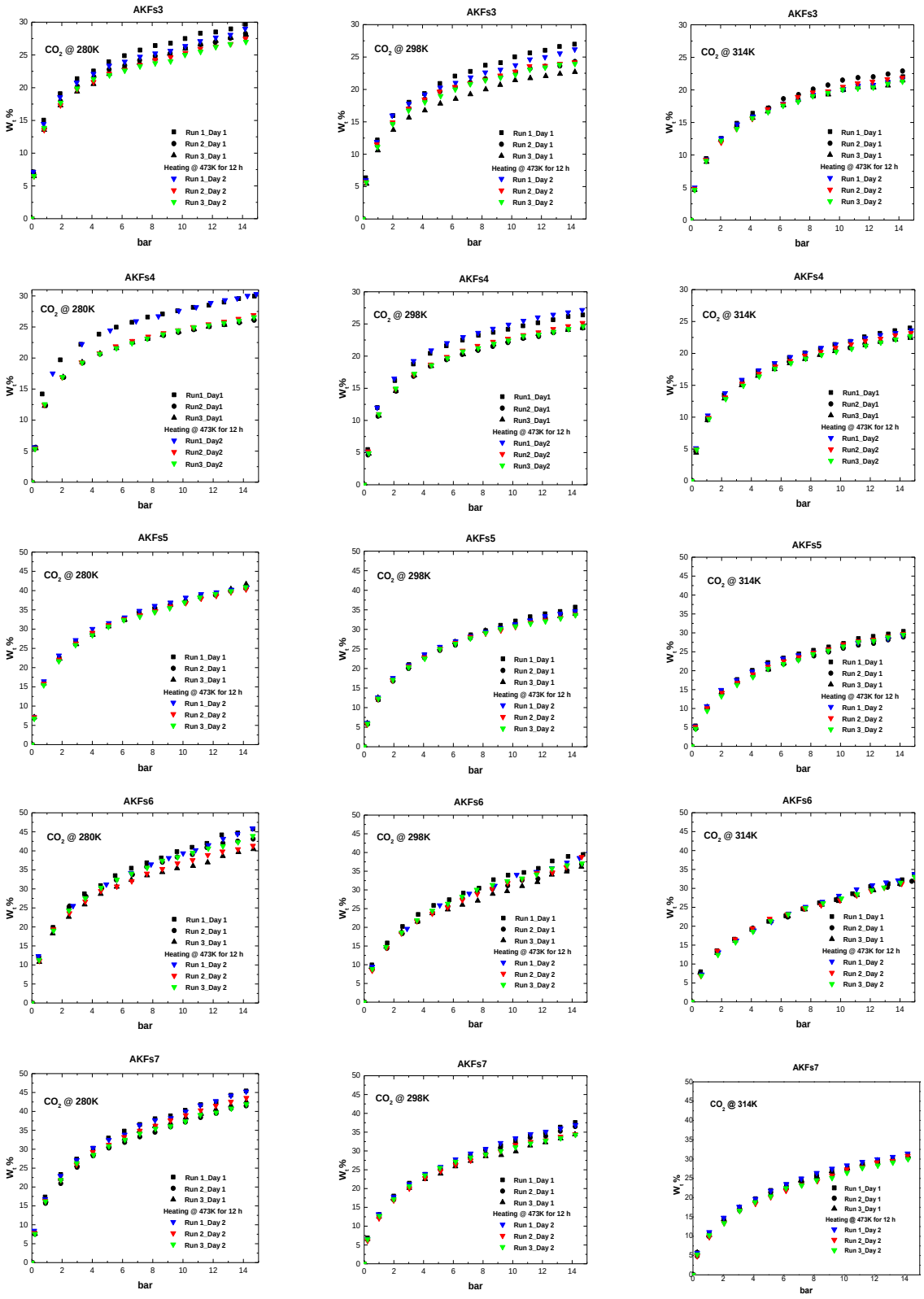

Figure S4. CO_2 adsorption/desorption cycles at 280K, 298K and 314K measured up to 15 bar for all the analyzed Kevlar samples.

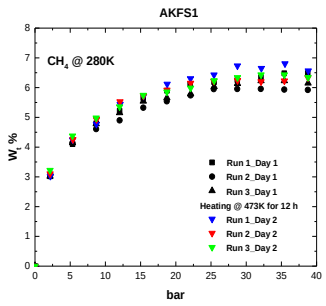
AKFS1
CH4 @ 280K
Wt %
bar
Run 1_Day 1
Run 2_Day 1
Run 3_Day 1
Heating @ 473K for 12 h
Run 1_Day 2
Run 2_Day 2
Run 3_Day 2

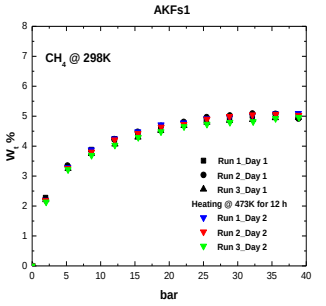
AKFs1
CH4 @ 298K
Wt %
bar
Run 1_Day 1
Run 2_Day 1
Run 3_Day 1
Heating @ 473K for 12 h
Run 1_Day 2
Run 2_Day 2
Run 3_Day 2

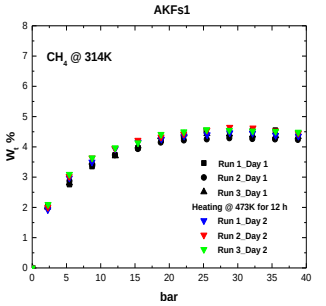
AKFs1
CH4 @ 314K
Wt %
bar
Run 1_Day 1
Run 2_Day 1
Run 3_Day 1
Heating @ 473K for 12 h
Run 1_Day 2
Run 2_Day 2
Run 3_Day 2

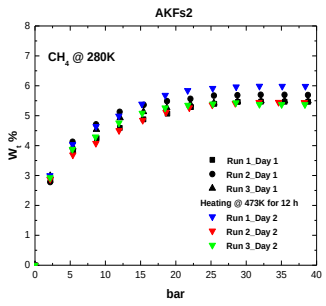
AKFs2
CH4 @ 280K
Wt %
bar
Run 1_Day 1
Run 2_Day 1
Run 3_Day 1
Heating @ 473K for 12 h
Run 1_Day 2
Run 2_Day 2
Run 3_Day 2

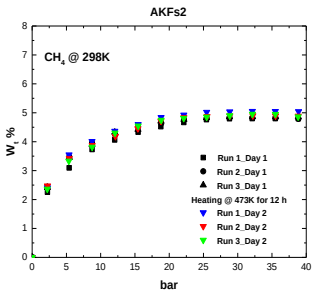
AKFs2
CH4 @ 298K
Wt %
bar
Run 1_Day 1
Run 2_Day 1
Run 3_Day 1
Heating @ 473K for 12 h
Run 1_Day 2
Run 2_Day 2
Run 3_Day 2

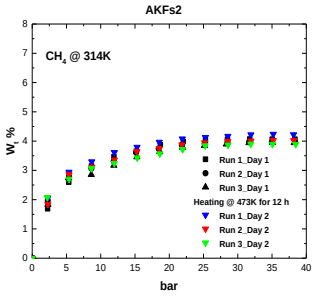
AKFs2
CH4 @ 314K
Wt %
bar
Run 1_Day 1
Run 2_Day 1
Run 3_Day 1
Heating @ 473K for 12 h
Run 1_Day 2
Run 2_Day 2
Run 3_Day 2

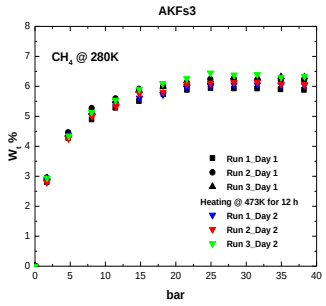
AKFs3
CH4 @ 280K
Wt %
bar
Run 1_Day 1
Run 2_Day 1
Run 3_Day 1
Heating @ 473K for 12 h
Run 1_Day 2
Run 2_Day 2
Run 3_Day 2

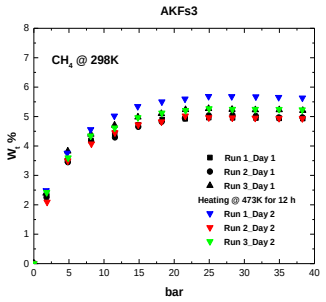
AKFs3
CH4 @ 298K
Wt %
bar
Run 1_Day 1
Run 2_Day 1
Run 3_Day 1
Heating @ 473K for 12 h
Run 1_Day 2
Run 2_Day 2
Run 3_Day 2

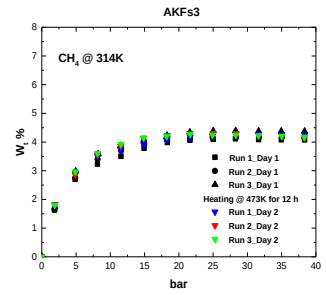
AKFs3
CH4 @ 314K
Wt %
bar
Run 1_Day 1
Run 2_Day 1
Run 3_Day 1
Heating @ 473K for 12 h
Run 1_Day 2
Run 2_Day 2
Run 3_Day 2

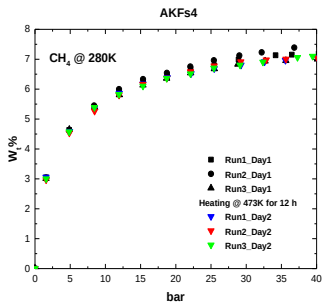
AKFs4
CH4 @ 280K
Wt %
bar
Run1_Day1
Run2_Day1
Run3_Day1
Heating @ 473K for 12 h
Run1_Day2
Run2_Day2
Run3_Day2

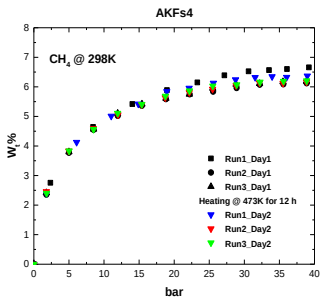
AKFs4
CH4 @ 298K
Wt %
bar
Run1_Day1
Run2_Day1
Run3_Day1
Heating @ 473K for 12 h
Run1_Day2
Run2_Day2
Run3_Day2

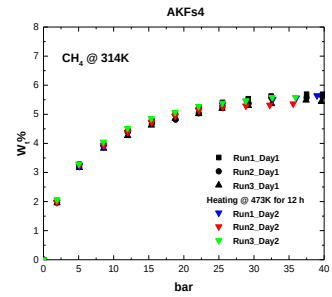
AKFs4
CH4 @ 314K
Wt %
bar
Run1_Day1
Run2_Day1
Run3_Day1
Heating @ 473K for 12 h
Run1_Day2
Run2_Day2
Run3_Day2

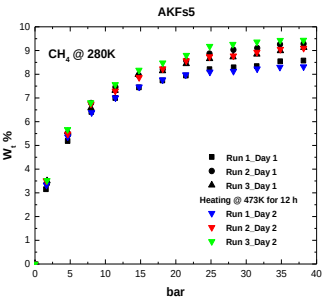
AKFs5
CH4 @ 280K
Wt %
bar
Run 1_Day 1
Run 2_Day 1
Run 3_Day 1
Heating @ 473K for 12 h
Run 1_Day 2
Run 2_Day 2
Run 3_Day 2

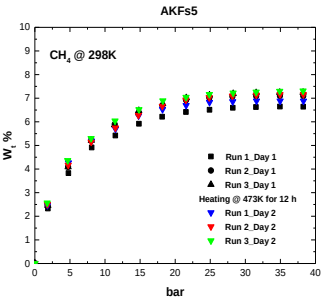
AKFs5
CH4 @ 298K
Wt %
bar
Run 1_Day 1
Run 2_Day 1
Run 3_Day 1
Heating @ 473K for 12 h
Run 1_Day 2
Run 2_Day 2
Run 3_Day 2

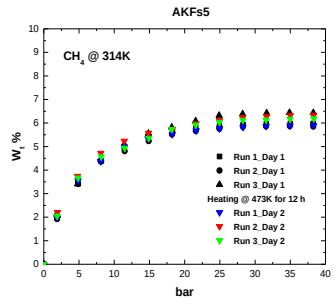
AKFs5
CH4 @ 314K
Wt %
bar
Run 1_Day 1
Run 2_Day 1
Run 3_Day 1
Heating @ 473K for 12 h
Run 1_Day 2
Run 2_Day 2
Run 3_Day 2

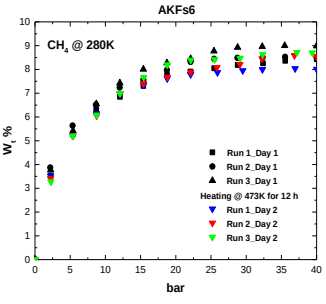
AKFs6
CH4 @ 280K
Wt %
bar
Run 1_Day 1
Run 2_Day 1
Run 3_Day 1
Heating @ 473K for 12 h
Run 1_Day 2
Run 2_Day 2
Run 3_Day 2

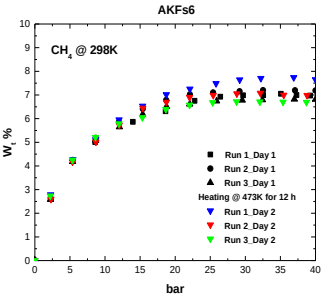
AKFs6
CH4 @ 298K
Wt %
bar
Run 1_Day 1
Run 2_Day 1
Run 3_Day 1
Heating @ 473K for 12 h
Run 1_Day 2
Run 2_Day 2
Run 3_Day 2

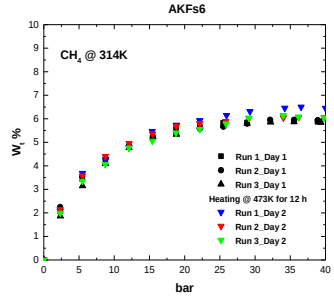
AKFs6
CH4 @ 314K
Wt %
bar
Run 1_Day 1
Run 2_Day 1
Run 3_Day 1
Heating @ 473K for 12 h
Run 1_Day 2
Run 2_Day 2
Run 3_Day 2

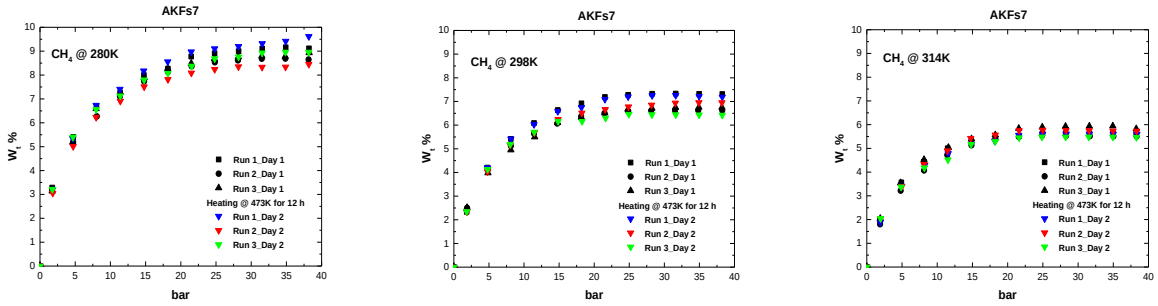

Figure S5. CH_4 adsorption/desorption cycles at 280K, 298K and 314K measured up to 40 bar for all the analyzed Kevlar samples.

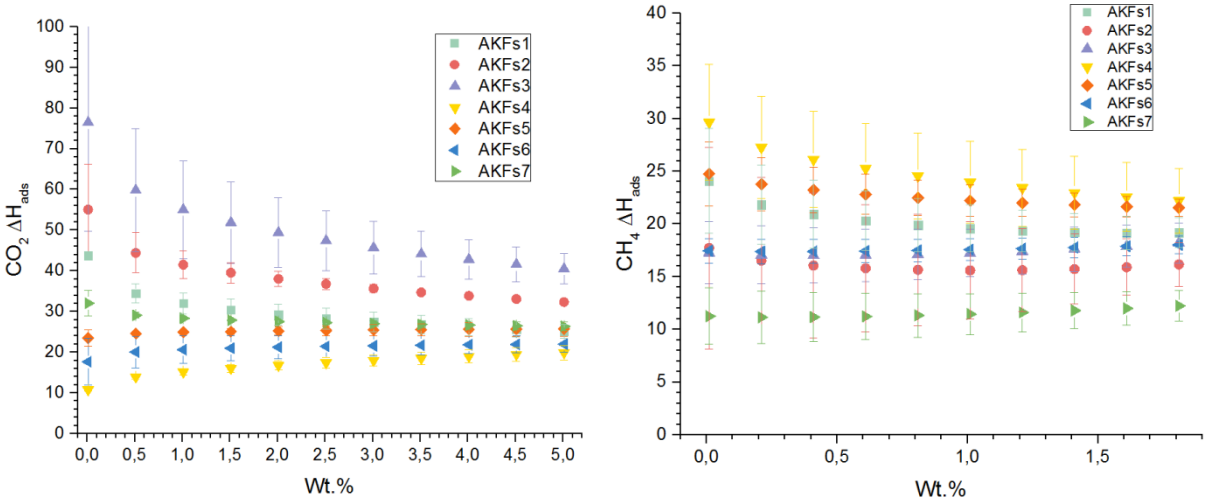

Figure S6. Sample's distribution of enthalpy of adsorption (ΔH_{ads}) up to 5 wt% for the CO_2 (left) and up to 2 wt% for the CH_4 (right).

SAMPLE	C (%)	N (%)	O (%)	Na (%)	S (%)	O/C	N/C	(O+N)/C
AKFs1	73,11	15,03	10,82	0,89	0,16	0,15	0,21	0,35
AKFs2	60,61	19,68	17,57	1,99	0,16	0,29	0,32	0,61
AKFs3	72,74	15,91	10,29	0,9	0,17	0,14	0,22	0,36
AKFs4	74,80	13,65	10,14	1,28	0,16	0,14	0,18	0,32
AKFs5	75,76	13,44	8,96	1,56	0,29	0,12	0,18	0,30
AKFs6	77,35	11,79	9,37	1,38	0,12	0,12	0,15	0,27
AKFs7	76,73	11,37	10,49	1,28	0,15	0,14	0,15	0,28

Table S-T2. Elemental analysis in atomic concentration (%) for AKFs samples.

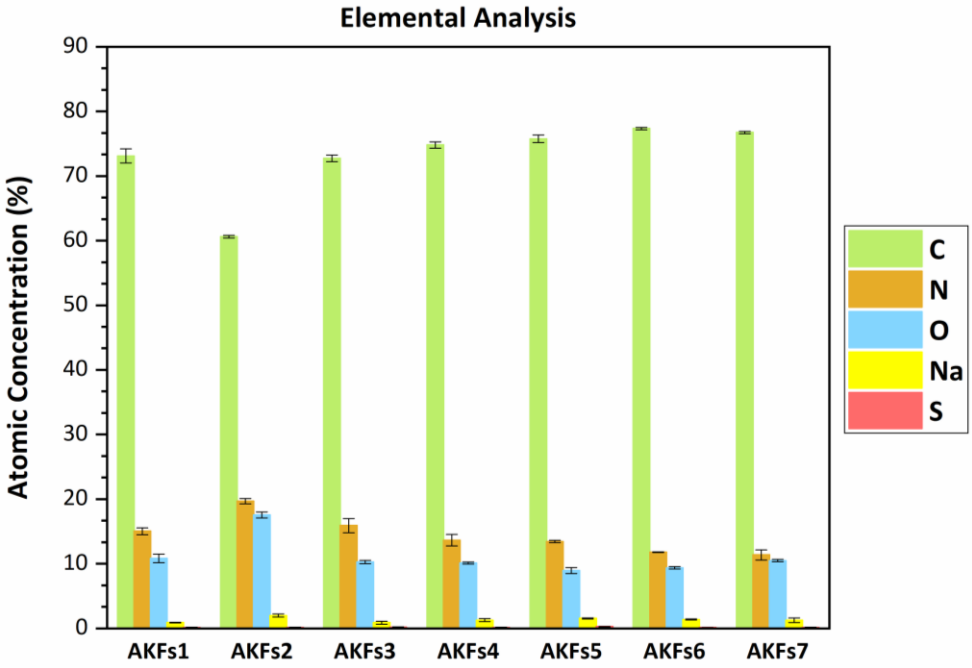

Figure S7. Histograms of atomic concentration (%) for AKFs samples.

References

1. Blanco, H. and A. Faaij, *A review at the role of storage in energy systems with a focus on Power to Gas and long-term storage.* Renewable and Sustainable Energy Reviews, 2018. **81**: p. 1049-1086.
2. Speirs, J., et al., *A greener gas grid: What are the options.* Energy Policy, 2018. **118**: p. 291-297.
3. Meysam Qadrdan, M.A., Jianzhong Wu , Nick Jenkins , Bethan Winter., *The Future of Gas Networks.* Springer International Publishing, 2020. **1**: p. VIII, 69.
4. Choi, P.-S., et al., *A review: methane capture by nanoporous carbon materials for automobiles.* 2016. **17**.
5. Hirscher, M., et al., *Materials for hydrogen-based energy storage – past, recent progress and future outlook.* Journal of Alloys and Compounds, 2020. **827**: p. 153548.
6. Alhasan, S., R. Carriveau, and D.S.K. Ting, *A review of adsorbed natural gas storage technologies.* International Journal of Environmental Studies, 2016. **73**(3): p. 343-356.
7. Stelitano, S., et al., *Low Pressure Methane Storage in Pinecone-Derived Activated Carbons.* Energy & Fuels, 2018. **32**(10): p. 10891-10897.
8. Boot-Handford, M.E., et al., *Carbon capture and storage update.* Energy & Environmental Science, 2014. **7**(1): p. 130-189.
9. Policicchio, A., et al., *Assessment of commercial poly(ε-caprolactone) as a renewable candidate for carbon capture and utilization.* Journal of CO2 Utilization, 2017. **19**: p. 185-193.
10. Nie, Z., Y. Lin, and X. Jin, *Research on the theory and application of adsorbed natural gas used in new energy vehicles: A review.* Frontiers of Mechanical Engineering, 2016. **11**(3): p. 258-274.
11. Zhang, Q., et al., *Nanomaterials for energy conversion and storage.* Chemical Society Reviews, 2013. **42**(7): p. 3127-3171.

12. Christensen, K.E.H.J.M.L.C.B.S.T., *Nanomaterials for Energy Applications*, in *Metrology and Standardization of Nanotechnology*. 2017. p. 505-518.

13. Burchell, T.D., *Carbon Materials for Advanced Technologies*, T.D. Burchell, Editor. 1999, Elsevier Science Ltd: Oxford. p. xv-xviii.

14. Ma, Q., et al., *Carbon-Based Functional Materials Derived from Waste for Water Remediation and Energy Storage.* Advanced Materials, 2017. **29**(13): p. 1605361.

15. Zhao, H., et al., *Carbon-based adsorbents for post-combustion capture: a review.* Greenhouse Gases: Science and Technology, 2018. **8**(1): p. 11-36.

16. Cychosz, K.A. and M. Thommes, *Progress in the Physisorption Characterization of Nanoporous Gas Storage Materials.* Engineering, 2018. **4**(4): p. 559-566.

17. Zhou, L., *Progress and problems in hydrogen storage methods.* Renewable and Sustainable Energy Reviews, 2005. **9**(4): p. 395-408.

18. Fichtner, M., *Nanotechnological Aspects in Materials for Hydrogen Storage.* Advanced Engineering Materials, 2005. **7**(6): p. 443-455.

19. Schlichtenmayer, M. and M. Hirscher, *Nanosponges for hydrogen storage.* Journal of Materials Chemistry, 2012. **22**(20): p. 10134-10143.

20. Oh, H., et al., *Experimental assessment of physical upper limit for hydrogen storage capacity at 20 K in densified MIL-101 monoliths.* RSC Advances, 2014. **4**(6): p. 2648-2651.

21. Lu, A.-H., G.-P. Hao, and X.-Q. Zhang, *Porous Carbons for Carbon Dioxide Capture*, in *Porous Materials for Carbon Dioxide Capture*, A.-H. Lu and S. Dai, Editors. 2014, Springer Berlin Heidelberg: Berlin, Heidelberg. p. 15-77.

22. Zhao, Y., X. Liu, and Y. Han, *Microporous carbonaceous adsorbents for CO2 separation via selective adsorption.* RSC Advances, 2015. **5**(38): p. 30310-30330.

23. Rodríguez-Reinoso, K.K.F., *Nanoporous materials for gas storage.* 1st ed. 2019 ed. Green Energy and Technology. 2019, Singapore Springer, 2019.

24. Policicchio, A., et al., *Activated carbon and metal organic framework as adsorbent for low-pressure methane storage applications: an overview.* Journal of Porous Materials, 2017. **24**(4): p. 905-922.

25. Casco, M.E., et al., *High-Pressure Methane Storage in Porous Materials: Are Carbon Materials in the Pole Position?* Chemistry of Materials, 2015. **27**(3): p. 959-964.

26. Hassan, M.F., et al., *Recent trends in activated carbon fibers production from various precursors and applications—A comparative review.* Journal of Analytical and Applied Pyrolysis, 2020. **145**: p. 104715.

27. Lee, T.H., et al. *ACTIVATED CARBON FIBER - THE HYBRID OF CARBON FIBER AND ACTIVATED CARBON*. 2014.

28. Chen, J.Y., *Preface*, in *Activated Carbon Fiber and Textiles*, J.Y. Chen, Editor. 2017, Woodhead Publishing: Oxford. p. xi-xii.

29. Freeman, J.J., et al., *Adsorptive Properties of Activated Carbons Prepared from Kevlar**Kevlaris the registered trade mark of E. I. Du Pont De Nemours & Co. Inc*, in *Studies in Surface Science and Catalysis*, F. Rodriguez-Reinoso,et al., Editors. 1991, Elsevier. p.319-328.

30. Freeman, J.J., et al., *Adsorption of nitrogen and water vapour by activated Kevlar® chars.* Carbon, 1993. **31**(6): p. 865-869.

31. Martínez-Alonso, A., et al., *Microporous texture of activated carbon fibers prepared from aramid fiber pulp.* Microporous Materials, 1997. **11**(5): p. 303-311.

32. Villar-Rodil, S., et al., *Activated Carbon Materials of Uniform Porosity from Polyaramid Fibers.* Chemistry of Materials, 2005. **17**(24): p. 5893-5908.

33. Giraldo, L., et al., *Synthesis and characterization of activated carbon fibers from Kevlar*. Eclética Química, 2007. **32**: p. 55-62.

34. Choma, J., et al., *Developing microporosity in Kevlar®-derived carbon fibers by CO2 activation for CO2 adsorption.* Journal of CO2 Utilization, 2016. **16**: p. 17-22.

35. Castro-Muñiz, A., et al., *Activated carbon fibers with a high content of surface functional groups by phosphoric acid activation of PPTA.* Journal of Colloid and Interface Science, 2011. **361**(1): p. 307-315.

36. Panar, M., et al., *Morphology of poly(p-phenylene terephthalamide) fibers.* Journal of Polymer Science: Polymer Physics Edition, 1983. **21**(10): p. 1955-1969.

37. Ahmed, D., et al., *Microstructural developments of poly (p-phenylene terephthalamide) fibers during heat treatment process: a review*. Materials Research, 2014. **17**: p. 1180-1200.

38. Rouquerol, F., et al., *1 - Introduction*, in *Adsorption by Powders and Porous Solids (Second Edition)*, F. Rouquerol, et al., Editors. 2014, Academic Press: Oxford. p. 1-24.

39. Thommes, M., et al., *Physisorption of gases, with special reference to the evaluation of surface area and pore size distribution (IUPAC Technical Report).* Pure and Applied Chemistry, 2015. **87**(9-10): p. 1051.

40. Brunauer, S., P.H. Emmett, and E. Teller, *Adsorption of Gases in Multimolecular Layers.* Journal of the American Chemical Society, 1938. **60**(2): p. 309-319.

41. Jagiello, J. and J.P. Olivier, *Carbon slit pore model incorporating surface energetical heterogeneity and geometrical corrugation.* Adsorption, 2013. **19**(2): p. 777-783.

42. Policicchio, A., et al., *Volumetric apparatus for hydrogen adsorption and diffusion measurements: Sources of systematic error and impact of their experimental resolutions.* Review of Scientific Instruments, 2013. **84**(10): p. 103907.

43. Kretzschmar, A., et al., *Tailored Gas Adsorption Properties of Electrospun Carbon Nanofibers for Gas Separation and Storage.* ChemSusChem, 2020. **13**(12): p. 3180-3191.

44. Attia, N.F., et al., *Flexible nanoporous activated carbon cloth for achieving high H2, CH4, and CO2 storage capacities and selective CO2/CH4 separation.* Chemical Engineering Journal, 2020. **379**: p. 122367.

45. Sing, K.S.W., et al., *Reporting Physisorption Data for Gas/Solid Systems, Handbook of Heterogeneous Catalysis*. 2008.

46. Tavanai, H., R. Jalili, and M. Morshed, *Effects of fiber diameter and CO2 activation temperature on the pore characteristics of polyacrylonitrile based activated carbon nanofibers.* Surface and Interface Analysis, 2009. **41**(10): p. 814-819.

47. Iqbal, N., et al., *Chapter 20 - Electrospun Nanofibers for Carbon Dioxide Capture*, in *Electrospinning: Nanofabrication and Applications*, B. Ding, X. Wang, and J. Yu, Editors. 2019, William Andrew Publishing. p. 619-640.

48. Kupgan, G., T.P. Liyana-Arachchi, and C.M. Colina, *NLDFT Pore Size Distribution in Amorphous Microporous Materials.* Langmuir, 2017. **33**(42): p. 11138-11145.

49. Rouquerol, J., et al., *Recommendations for the characterization of porous solids (Technical Report)*, in *Pure and Applied Chemistry*. 1994. p. 1739.

50. Jiménez, V., et al., *CO2 Capture in Different Carbon Materials.* Environmental Science & Technology, 2012. **46**(13): p. 7407-7414.

51. Stelitano, S., et al., *Assessment of poly(L-lactide) as an environmentally benign CO2 capture and storage adsorbent.* Journal of Applied Polymer Science, 2020. **137**(48): p. 49587.

52. Li, K., et al., *Pine cone shell-based activated carbon used for CO2 adsorption.* Journal of Materials Chemistry A, 2016. **4**(14): p. 5223-5234.

3.5 Hydrogen storage performances for mesoporous silica synthesized with mixed tetraethoxysilane and methyltriethoxysilane precursors in acidic condition

3.5.1 State of the art

There has been a big interest in the storage of gases, in materials of different types like: template-synthesized carbon [1] or activated carbon [2, 3], graphite nanofibers [4], graphene [5] or metal organic frameworks [6]. In addition, the functionalized mesoporous silica with different organic groups have been widely used in carbon dioxide (CO_2), methane (CH_4) and hydrogen (H_2) adsorption [7, 8]. Considering hydrogen adsorption, the appropriate selection and the enrichment of the surface of the adsorbent with atoms that attract hydrogen molecules can strongly enhance the hydrogen molecule-surface interaction [9, 10]. Hydrogen is stored within a porous material as an effect of the intermolecular forces between the solid (adsorbent) and the bulk gas (adsorptive), leading to an increase in the density of H_2 at the surface of the solid (adsorbate) [11]. Physisorption describes the adsorption of a molecule to a surface by van der Waals and electrostatic interactions alone, as opposed to chemisorption, in which intramolecular bonds in the adsorptive break and then individual atoms bond covalently to the adsorbate [12, 13]. An important key parameter to increase the storage capacity by physisorption is the surface area [14]. Porous materials have been found to optimally increase surface area while discouraging particle aggregation. A reduction in pore size results in increased adsorption, once a firm diameter is reached [15]. These strategies in varying the sizes of pores and of the specific surface area have been successfully used in tailoring silica nanotubes as membrane filters [16], for aluminosilica size-selective macromolecule cargos [17], as well for the adsorption of heavy metals [18] and organic dyes [14] from environmental and waste disposal samples.

In micropores, with diameters less than two nanometers, van der Waals potentials of atoms on the pore wall surface begin to overlap, causing an increase in hydrogen adsorption affinity [15, 19]. In case of ultra microporosity (pore diameter < 0.7 nm) the storage capacity could increase even more than what expected by the Chahine rule [20]. Thus, the general rule is to increase surface area, while simultaneously decreasing pore diameter [21], in addition to introducing specific atoms or molecular groups on the surface that may increase the affinity for hydrogen adsorption [7]. The mechanism of hydrogen adsorption has been linked to electrostatic interactions with cations and metals [22, 23]. Different

organic groups have been used such as methyl and vinyl [8]. It was demonstrated that with the increase of the amount of vinyl functionalized precursor, a greater hydrogen storage capacity [7] can be achieved. Kubo et al. found that the functionalized silica with π-electron bearing groups exhibited higher heats of adsorption, and thus, greater hydrogen adsorption capacity, than the unmodified or the functionalized ones with non- π-electron bearing groups [24]. The synthesis of these functionalized materials took advantage of the different hydrophilic/hydrophobic character of the different organic groups of the used silanes [25, 26] as silica precursors. The use of templating molecules with shorter chain lengths provides the development of materials with increasing storage capacity and strength of the interaction between the surface and the adsorbate [27]. In the present study, we synthesized two series of samples by using cationic surfactants templates with 12 carbon atoms (DTAB) and 14 carbon atoms (TTAB). In each of these two series, the molar ratio of the functionalized precursor to TEOS has been varied, in order to adjust the pore diameter and the specific surface area. The expected result is to improve their performances as gas storage materials. The effect of adding methyltriethoxysilane (MTES) precursor in different concentrations and the effect of directing agent chain length upon: the ordering degree and upon the structure of the mesoporous materials was related to the hydrogen storage capacity.

3.5.2 Experimental

3.5.2.1 Sample synthesis

Chemicals: tetraethoxysilane (TEOS), (99%, for analysis, Fluka); methyltriethoxysilane (MTES 97%, Merck); n-dodecyl-trimethylammonium bromide (DTAB, Merck); tetradecyltrimethyl ammonium bromide (TTAB, Merck); nitric acid (Merck, 65% HNO3). Porous silica materials were synthesized at room temperature under acidic conditions. In the present study, the TEOS precursor was partially substituted by MTES, in different mole ratios, such as, MTES:TEOS=0:10; 1:9; 2:8; 3:7; 4:6 and 5:5. Keeping the same synthesis parameters, two series of samples were prepared by using DTAB for the first series of samples, and TTAB for the second series. The DTAB series was labelled with D and the TTAB series with T. The molar ratio of the reactants was: (TEOS+MTES): C_nTAB: H_2O: HNO_3= 3: 1: 18.7: 741. The directing agent (4.63 g DTAB or 5.04 g TTAB) was dissolved in a nitric acid solution in water (19.42 mL HNO_3 65% was dissolved in 195.66 mL H_2O). The mixtures were vigorously magnetic stirred at room temperature, for at least 30 min. Then, the silica precursors (10 mL TEOS or TEOS+MTES mixed in advance) were slowly

dripped (within 10 minutes) into the reaction mixture and the stirring was continued for 3 hours (rotation speed 300 rpm) at room temperature. Next, the formed gel was aged for one day, in static condition. On the next day, the resulted white precipitate was washed several times with distilled water until the pH of the supernatant approached the pH value of the distilled water. Subsequently, the samples were filtered and dried at 373K. Afterwards, the directing agent was removed by extraction with acidified ethanol. The dry xerogel was mixed with 50.5 mL of acidified ethanol (ethanol with 0.5 mL of concentrated HCl) under magnetic stirring (250 rot/min), at room temperature. The stirring time was 3 hours. The procedure was repeated twice and in between; the samples were washed with ethanol. Subsequently, the samples were dried at 373K. The samples were labelled as: Tx-EtOH or Dx-EtOH, where "x" is a number from 0 (no MTES content) to 5 (the highest MTES content), with the increase of the MTES concentration. The precursor compositions are listed in Table 1.

Table 1. Synopsis of the synthesized samples.

TTAB synthesised samples	**DTAB synthesised samples**	**MTES: TEOS (molar ratio)**
T0	**D0**	**0:10**
T1	**D1**	**1:9**
T2	**D2**	**2:8**
T3	**D3**	**3:7**
T4	**D4**	**4:6**
T5	**D5**	**5:5**

3.5.2.2 Sample characterization

Fourier Transform Infrared Spectroscopy (FTIR) spectra were acquired on KBr pellets by using a JASCO –FT/IR-4200 apparatus.

Low-temperature (at 77K) nitrogen adsorption-desorption on the mesoporous silica samples were performed by using a QuantaChrome Nova 1200e analyzer. Before measurements, each sample was outgassed at 373K for 4 hours in vacuum. Evaluation of the specific surface area S_{BET} (m^2/g) was carried out by Brunauer–Emmett–Teller (BET) method in the relative pressure range P/P_0 from 0.01–0.25. The analysis of pore size distribution was obtained using the density functional theory (DFT) method (cylindrical pore, NLDFT adsorption branch model). The pore sizes were determined by both the BJH

(Barrett-Joyner-Halenda) and the DFT methods. The total pore volumes were determined using the point closest to 1 value for the relative pressure P/P_0.

X-ray diffraction has been performed on a Bruker AXS D8 Discover diffractometer, equipped with a Göbel mirror and a scintillation detector using Cu Kα radiation. Measurements were performed over the interval 2-7° with a step size of 0.04° and scan speed of 0.10°/min. The materials were placed on a double-sided adhesive tape glued to the instrument sample table. Transmission electron microscopy (TEM) investigation was carried out on a Philips CM20 transmission electron microscope equipped with a LaB6 electron gun, operating at 200 kV. The samples for TEM were prepared by drop-drying suspensions on holey carbon foil coated copper grids.

3.5.2.3 Hydrogen storage capacity

The H_2 adsorption/desorption measurements, at liquid nitrogen (LN_2 = 77 K) and room (RT = ~ 298 K) temperatures, were carried out in the pressure range 0÷80 bar by using a Sievert-type volumetric apparatus (f-PcT) for accurate and reliable gas adsorption characterization. The gas storage capacity, as weight percent of gas adsorbed per gram of adsorbent (*wt%*), was determined from adsorption isotherms. All the adsorption data were evaluated by Toth/Langmuir isotherm model with a very high accuracy. Before each gas storage test, each sample was previously annealed for 10÷12 hours at 393 K under vacuum ($P < 10^{-6}$ mbar) to eliminate the eventual fraction of water weakly bound inside the samples. Before starting gas adsorption tests, Helium (He) pycnometry analysis was performed to get the best value of the sample skeletal density, a fundamental parameter for the storage capacity evaluation. The Toth/Langmuir isotherm model allows obtaining information about the strength of interaction that occurs between the surface of the adsorbent and the adsorbed gas. The theoretical maximum storage capacity, the equilibrium constant and homogeneity grade of the pore surfaces have been evaluated analyzing the adsorption isotherms according to the Toth equation: $wt\% = (wt\%_{max} \cdot K \cdot P) / (1 + (K \cdot P)^t)^{1/t}$ where $wt\%_{max}$ is the asymptotic maximum storage capacity, K is the equilibrium constant and t is a parameter introduced by Toth in order to consider the homogeneity grade of the sample surface (t = 1 totally homogeneous surface). The K constant is determined by the energetic interaction between the adsorbent and the adsorbate. The reliability of the silica materials performance in term of cyclic life was tested by submitting all samples to multiple H_2 adsorption/desorption cycles with and without any temperature treatment in between.

3.5.3 Results and discussion

3.5.3.1 FT-IR measurements

The FT-IR spectra reveal the characteristic bands for the methylated mesoporous silica materials. All samples show the specific vibration bands assigned to the silica skeleton at 1050, 800 and 450 cm^{-1}, corresponding to the asymmetric stretching, symmetric stretching and bending vibration of the Si-O-Si network, respectively [28]. The presence of the silanol groups were confirmed by the existence of the band centered about 960 cm^{-1}, which is associated with the stretching mode of the Si−OH groups [29]. The characteristic vibration bands of the surfactant molecules at 2920 cm^{-1} and 2850 cm^{-1} were observed in the xerogel samples (data not shown), while in the extracted series (Fig. 1) these bands are not present, demonstrating their removal via the extraction treatment with the acidified ethanol solution.

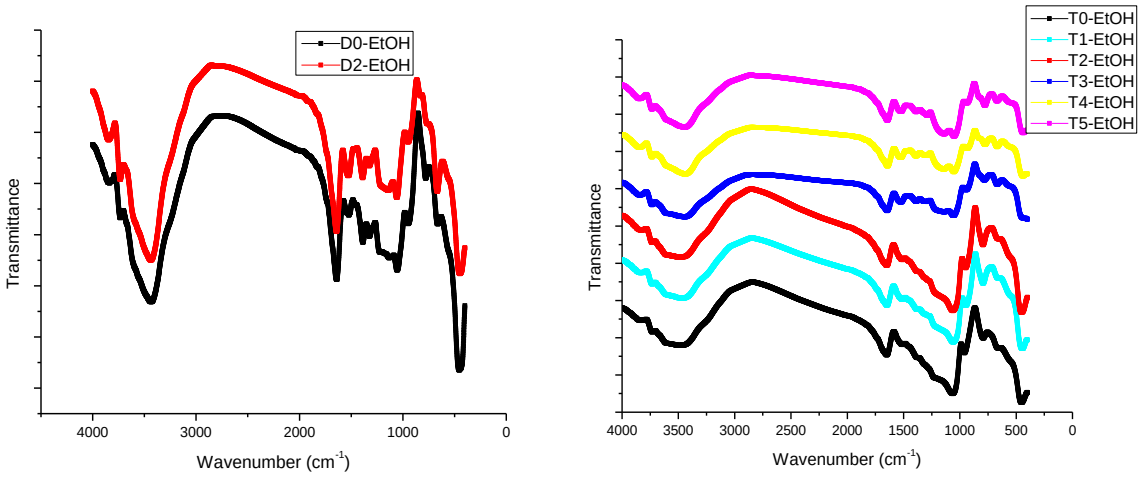

(a) (b)

Fig. 1. FT-IR spectra of the EtOH extracted samples from the a) C12 series and b) C14 series.

3.5.3.2 Nitrogen adsorption measurements

All the mesoporous silica samples, obtained after the directing agent removal via the extraction with the acidified ethanol, were subjected to nitrogen adsorption analysis, in order to extract quantitative information regarding porosity and specific surface areas. The nitrogen adsorption isotherms for both series of samples are presented in Fig. 2a for Dx-EtOH series and in Fig. 3a, for Tx-EtOH series of samples. The isotherms for the first two samples, from each series (D0-EtOH, D1-EtOH, and T0-EtOH, T1-EtOH samples) are of IVb Type, with no hysteresis (or with very small hysteresis) according to IUPAC (International Union of Pure and Applied Chemistry) classification. Type IV b is specific for mesoporous materials with smaller pores of conical or cylindrical shape, closed at the

tapered end [30]. The sharp capillary condensation steps around P/P_0=0.35 are observed for the samples with zero or the smallest MTES content and around P/P_0=0.2, with higher MTES content. The isotherms from the samples T2-EtOH, T3-EtOH, T4-EtOH and T5-EtOH are of Type Ib which are characteristic for the physisorption on materials having pore size distributions over a broad range including wider micropores and narrow mesopores (smaller than 2.5 nm) [30,31]. This shape for Type I isotherm is a result of unrestricted monolayer-multilayer adsorption up to high P/P_0 [30]. A sharp knee usually corresponds to the completion of monolayer coverage and this is the case of samples T2-EtOH and T3-EtOH. A less distinctive knee like for the T4-EtOH and T5-EtOH samples, is an indication of significant amount of overlap of monolayer coverage and the onset of multilayer adsorption [30]. In the case of T5-EtOH sample, also a slight hysteresis is visible.

In Fig. 2b and Fig. 3b the pore size distributions calculated from DFT method are presented. The results indicate a narrow distribution with a mean value of 2 nm for the two Dx- EtOH samples and for the Tx- EtOH series of samples, as well; except for, the T0-EtOH s and T1-EtOH samples, where additionally a narrow distribution with a mean value of 3.5 nm was observed. The textural parameters, specific surface area (S_{BET}), total pore volume and mean pore diameters are reported below in Table 2. With the variation of MTES content, the S_{BET} value is varying too and in particular, the maximum values of 955.87 m^2/g is obtained for the sample with no MTES and 856.64 m^2/g for the sample with the lowest MTES content (T1-EtOH). The total pore volume and the pore size present a maximum value for the samples with no MTES (total pore volume=0.51 cm^3/g and pore size=3.29 nm) and with the lowest MTES content, T1-EtOH (total pore volume=0.47 cm^3/g and pore size=3.29 nm). We do not have any nitrogen porosimetry measurements for D1-EtOH, D3-EtOH, D4-EtOH and D5-EtOH samples. The materials obtained present different textures as observed also in their surface fractal dimensions evaluated by the Frenkel-Halsey-Hill (FHH) method [32]. The FHH method is used to determine the fractal geometry and calculate their surface irregularities and porous structure. When the value of Df is 2 the material presents a surface fractal and if the value of Df is 3 the material presents a mass fractal. For our samples we may observe mass fractal behavior, since our fractal dimension value is closer to 3.

In Fig. 4 the specific surface area and the cumulative pore volume for all the analyzed samples from Tx series is presented.

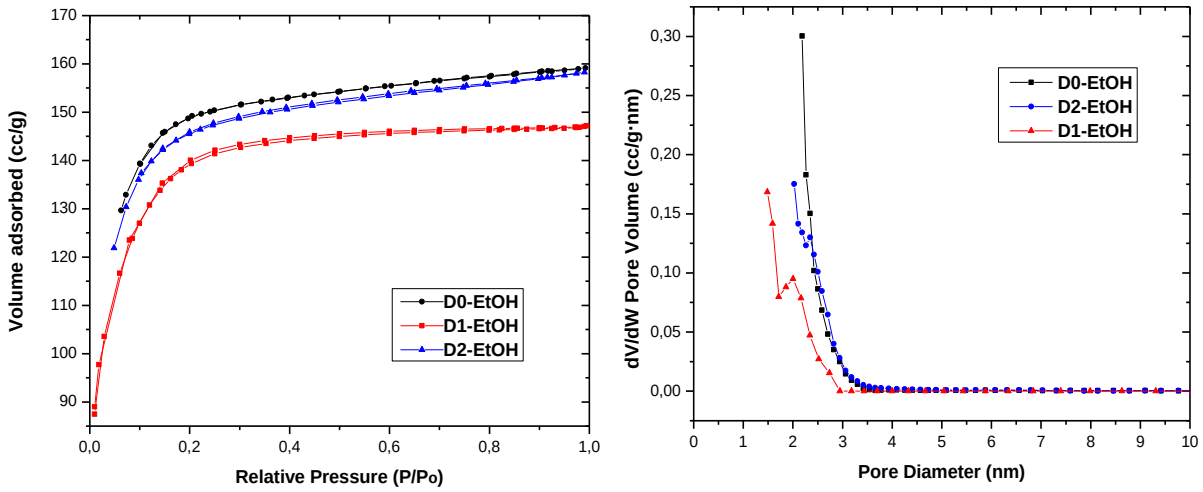

Figure 2. Nitrogen adsorption/desorption isotherms (a) and the pore size distributions (b) revealed by the DFT method of the samples of series Dx-EtOH.

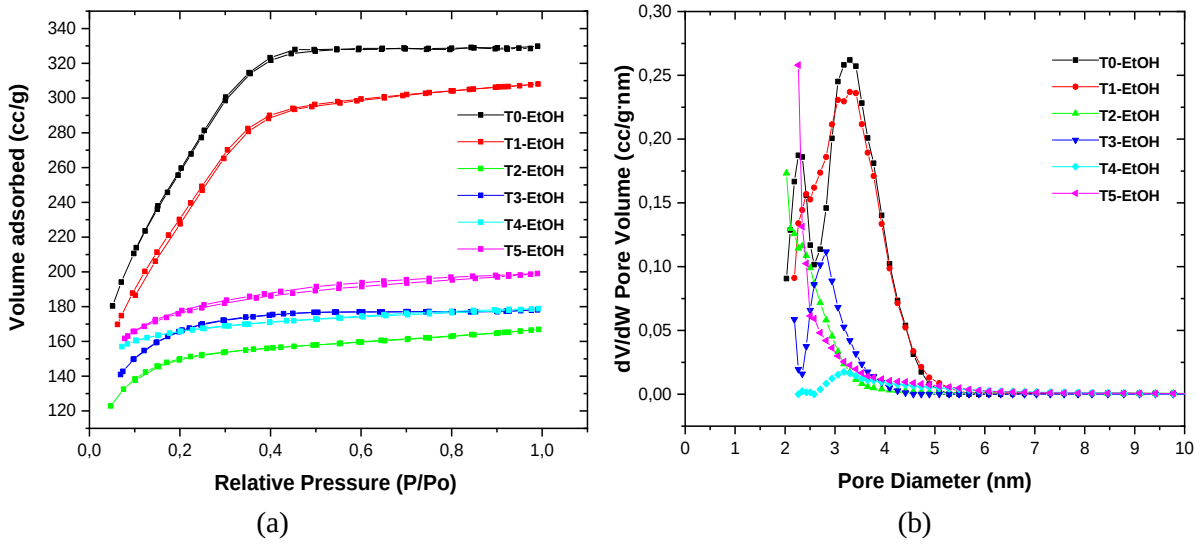

Figure 3. Nitrogen adsorption/desorption isotherms (a) and the pore size distributions (b) revealed by the DFT method of the samples of series Tx-EtOH.

Table 2. The textural properties of all series of samples.

Sample	Surface area (**BET**) [m^2/g]	Micropore area **(V-t method)** [m^2/g]	Pore width (**DFT**) [nm]	Pore width Ads (**BJH**) [nm]	Pore width Des (**BJH**) [nm]	Total pore volume (**TPV**) [cm^3/g]	FHH adsorption
D0-EtOH	562.8	537.7	2.19	3.08	3.32	0.25	^2.92
							*2.98
D2-EtOH	563.8	533.5	2.03	3.08	3.37	0.25	^2.91
							*2.97

T0-EtOH	955.9	252.7	3.3	3.08	3.06	0.51	^2.75
							*2.92
T1-EtOH	856.6	211.1	3.3	3.05	3.05	0.48	^2.72
							*2.91
T2-EtOH	563.9	493	2.03	3.12	3.28	0.26	^2.89
							*2.96
T3-EtOH	619	499	2.82	3.09	3.35	0.27	^2.93
							*2.98
T4-ETOH	609	543.1	3.18	3.06	3.35	0.28	^2.93
							*2.98
T5-ETOH	650.1	528.4	2.27	3.12	3.02	0.31	^2.89
							*2.96

(^) Neglecting or (*) Accounting, for Adsorbate Surface Tension Effects.

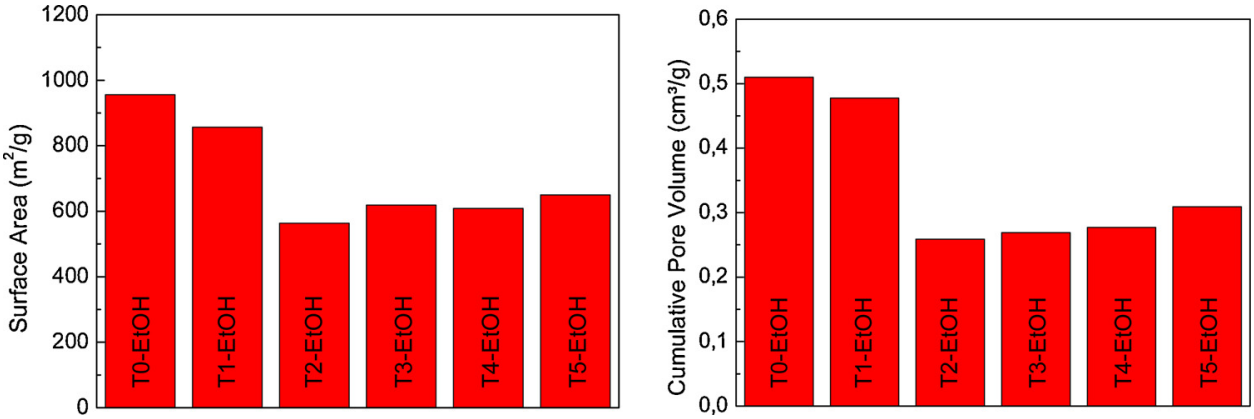

Figure 4. Specific surface area (left) and cumulative pore volume (right) for the Tx-EtOH series of samples.

3.5.3.3 X-ray diffraction

X-ray patterns for the two series of mesoporous silica, prepared with DTAB and TTAB surfactants, are shown in Fig. 5. The characteristic diffraction peaks observed around 2Θ = 3.8 - 4.0° for the Dx-EtOH series and 2Θ = 3.6 - 3.8° for first four samples of the Tx-EtOH series, indicate the development of a weakly ordered structure. Compared with the best-structured MCM-41 type materials [28,33–35] only the first diffraction peak can be discerned in most of the samples, and its position can be related to the pore spacing. The high background under the peaks is due to the amorphous non-ordered domains in the

materials. In the T4-EtOH and T5-EtOH samples the diffraction peak disappears, indicating that in these samples the porosity is less ordered. Similar trend of decreasing the long-range order of the hexagonal porosity was observed in series of TEOS-MTES silica prepared with CTAB surfactants in acidic and basic conditions [28,35–37]. The XRD results are showing that the samples contain partial amorphous domains and domains of ordered porosity.

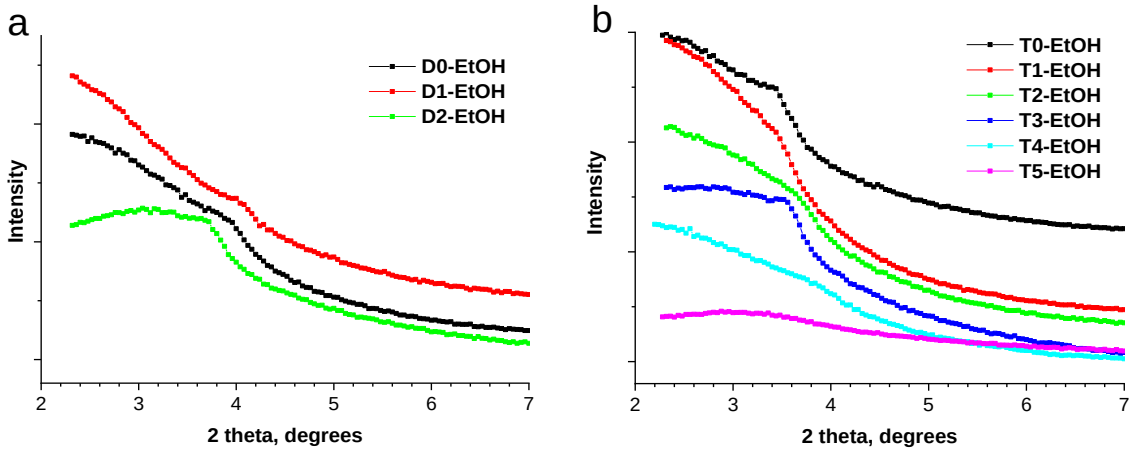

(a) (b)

Figure 5. X-ray patterns of mesoporous silica samples prepared with (a) DTAB and (b) TTAB pore forming agents.

3.5.3.4 Electron microscopy investigation

TEM investigations have been carried out on several samples, and all they showed nearly similar inner structures, shown in Fig. 6 for the D0-EtOH sample. An irregular porous network can be discerned in some parts of the materials, with wormlike pore channels of about 3 nm width, which is in agreement with the periodicity observed in the XRD data, and with typical micelle size formed by the short alkyl chain length surfactants.

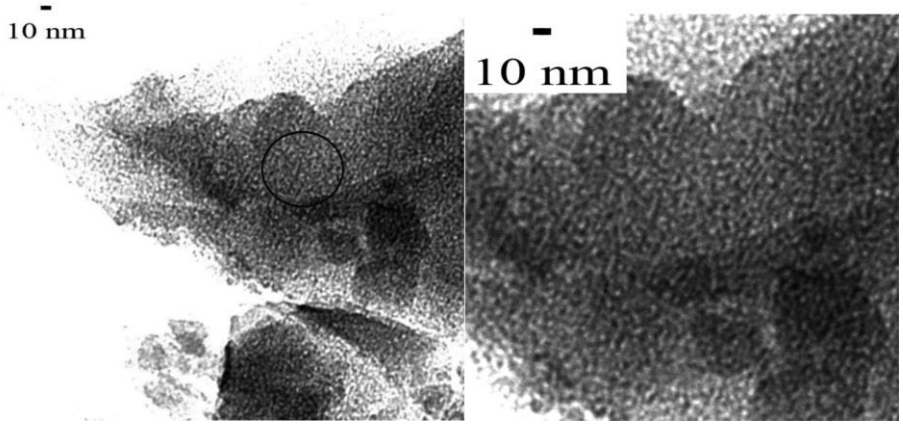

Figure 6. TEM images of silica particles for sample D0-EtOH.

3.5.3.5 Hydrogen adsorption capacity

- Dx-EtOH series of samples.

- D0-EtOH

The D0-EtOH sample, the first one from the series with MTES, shows a skeletal density of 2.01 g/cm^3. The H_2 adsorption capabilities was initially tested at room temperature (RT≅ 298 K) up to 80 bar, as reported in Fig. 7a. The maximum adsorption value reaches a very low saturation value close to 0.05 wt%. The storage capacity does not increase significantly, increasing pressure indicating a very weak interaction of the adsorbent molecules toward samples surface and thus, the non-relevant capability of the sample to hold gas molecules in these operative conditions. Even if the maximum uptake value is not relevant at RT, reversibility and aging tests were performed multiple times. The H_2 adsorption capacity of the D0-EtOH sample is completely reversible up to different cycles, Fig. 7b and c. Both the adsorption (full circle) and desorption (empty circle) perfect overlap as multiple adsorption isotherms. As expected, a different behaviour due to the lower thermal energy is observed moving down to 77 K. In these conditions, as shown below in Fig. 8a, an increase in the maximum storage capacity is clearly visible, with a steep growth already below 10 bar. Increasing pressure, a slope change is observed with a consequently slower increase that leads to a maximum H_2 uptake at 80 bar of 1.8 wt%. To compare the sample's behaviour at low temperature, aging and reversibility tests were performed submitting the D0-EtOH to multiple adsorption/desorption cycles. Fig. 8b below shows a typical adsorption/desorption cycle where the two isotherms perfectly overlap indicating a perfect reversibility of the adsorption process, i.e. the ability of the sample to adsorb and desorb H_2 molecules without modifying its own adsorption properties and/or maximum storage capacity. Further confirmation of that is given by the results reported in Fig. 8c where, like for the RT condition, multiple cycles are shown. Within the experimental error (related to slight temperature changes), the different isotherms are equivalent. Toth analysis on adsorption isotherms up to 80 bar allows to extrapolate information about molecules-surface interaction moving to higher pressure. We found that the sample shows a homogeneity grade of the surface equal to t=0.53, with a maximum asymptotic uptake wt%max ≅ 2.23. The K value, related to the energetic interaction between the adsorbent and the adsorbate, as expected increase toward lower temperature (it was not appreciable at RT), reaching a value of K=0.74 and this confirms the ability to attract more efficiently the H_2 molecules compared to higher temperature condition. Usually, moving to higher pressure, the adsorption sites participating in the process are more compared with the one identified as high-energy adsorption sites usually considered in the low-pressure analysis.

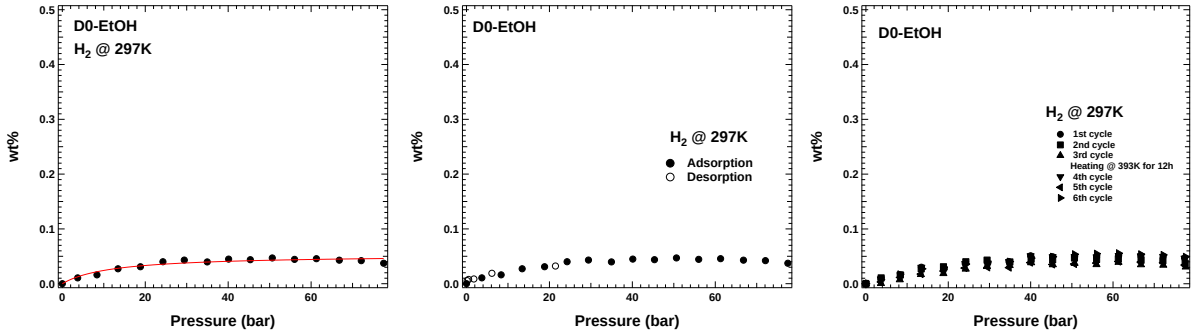

(a) (b) (c)

Figure 7. a) PcT adsorption isotherm obtained with H_2 at RT up to 80 bar. b) H_2 PcT adsorption-desorption isotherm obtained on D0-EtOH sample at T=297 K up to 80 bar. c) H_2 adsorption isotherm cycles.

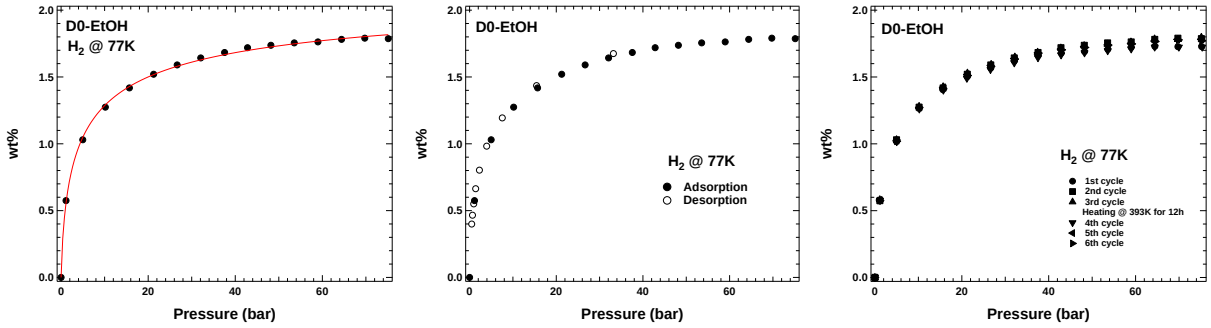

(a) (b) (c)

Figure 8. a) H_2 PcT adsorption isotherm at liquid N_2 temperature (77 K) up to 80 bar. b) H_2 adsorption-desorption isotherm obtained on D0-EtOH sample. c) H_2 adsorption isotherm cycles.

- *D1-EtOH*

The sample labeled as D1-EtOH shows a skeletal density of 1.63 g/cc. Both conditions, room and liquid nitrogen temperature, were analyzed to check the H_2 adsorption capacity and compared to both the other sample the D1-EtOH is the one who shows the better behavior at RT (≅ 295 K). As reported in Fig. 9a below, the maximum uptake value reaches almost 0.2 wt%. Even if it does not look very stable, looking at Fig. 9a and b it is revealed the almost reversible behavior of the sample toward H_2 adsorption. In Fig. 9c, even if only few points are available on the desorption curve, they (open circle) overlap the adsorption ones (close circle). At the same time, multiple adsorption cycles with and without thermal treatment in between show an arguable reversibility of the adsorption process; being the adsorption not very high, slightly changes in the RT can affect the measurement, leading to these changes in the maximum uptake value. However, like the other two samples, also the D1-EtOH seems to be able to adsorb and desorb H_2 molecule reversibly without modifying its adsorption properties.

The Figures 10a–c show high-pressure tests at LN_2 temperature. It is notable a sudden increase in the storage capacity already between 10−20 bar, followed by a slower trend approaching the plateau with a 1.7 wt% at the maximum analyzed pressure.

Toth analysis performed on the adsorption isotherm (see Fig. 10a), shows a homogeneity grade of the surface equal to t=0.80, with a maximum asymptotic uptake $wt\%_{max} \cong 1.93$ and K=0.21. This K value, lower compared with the previous one, indicates a lower interaction and could be responsible of the lower ability to attract and hold H_2 molecules. The reversibility of the adsorption process was tested up to different cycles. The adsorption of H_2 molecules inside the D1-EtOH sample appears completely reversible, the adsorption (full circle) and desorption (empty circle) isotherms clearly overlap as well as the multiple adsorption cycles (Fig. 10b and c).

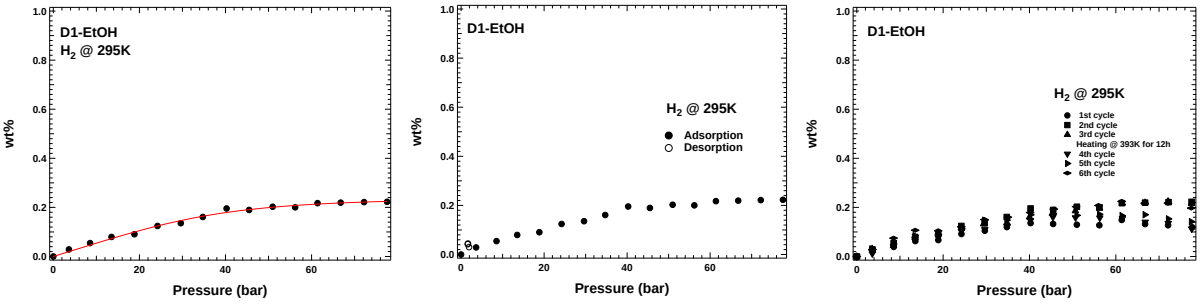

(a) (b) (c)

Figure 9. a) PcT adsorption isotherm obtained with H2 at RT up to 80 bar. b) H2 adsorption-desorption isotherm obtained on D1-EtOH sample. c) H2 adsorption isotherm cycles.

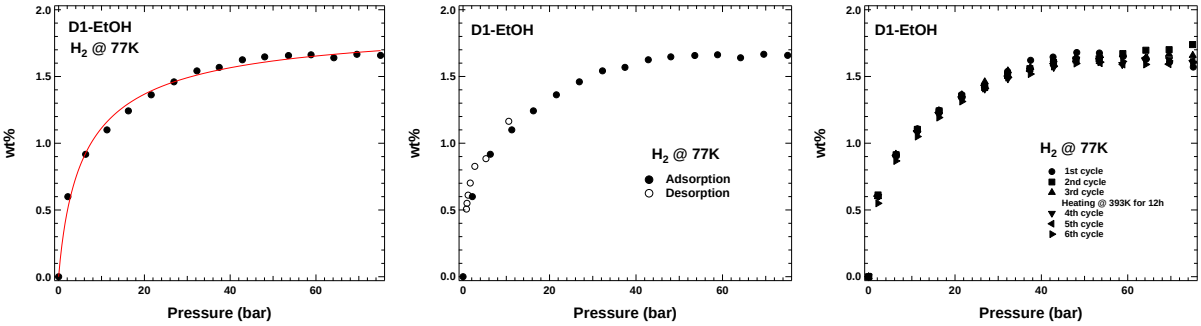

(a) (b) (c)

Figure 10. a) H_2 PcT adsorption isotherm at LN_2 temperatures up to 80 bar. b) H_2 adsorption-desorption isotherm obtained on D1-EtOH sample. c) H_2 adsorption isotherm cycles.

- *D2-EtOH*

The sample labeled as D2-EtOH shows a skeletal density of 1.91 g/cc. The adsorption behavior is close to the one already observed for the other samples, as reported below in Fig. 11a, at the maximum analyzed pressure the adsorption capacity reaches a saturation value of 0.05 wt%. The perfect overlapping of the adsorption (open circle) and desorption (close circle) isotherms and/or multiple adsorption cycles with and without thermal treatment in between, demonstrate the reversible behavior of the sample toward H_2 adsorption (Fig. 11b and c). Like the two previous samples, also the D2-EtOH one seems to be able to adsorb and desorb H_2 molecule reversibly, also if in small quantity, without modifying its adsorption properties at RT conditions.

Deeper investigations were performed submitting the D2-EtOH sample to 77 K condition where an increasing of the adsorption capacity was observed. Adsorption tests revealed a reversible H_2 uptake of 2.0 wt% at the maximum analyzed pressure as reported in Fig. 12a-c below. This means, that: no passivation of the adsorption sites and/or occlusion of accessible volumes and/or strong physical/chemical bonding are present in the sample during hydrogen adsorption/desorption processes. Consequently, the maximum adsorption capacity of H_2 by the sample can be simply restored by vacuum procedure and no thermal treatments are needed.

Toth analysis performed on hydrogen isotherms allows extrapolating a maximum uptake value wt%max around 2.54 wt%, almost 25% more than the measured value. The Toth analysis considers all the available adsorption sites (higher and lower energy of adsorption) leading to a homogeneity of the surface equal to t ≅ 0.58 and an average interaction between incoming molecules and surface resulting in a K value approximately equal to 0.5.

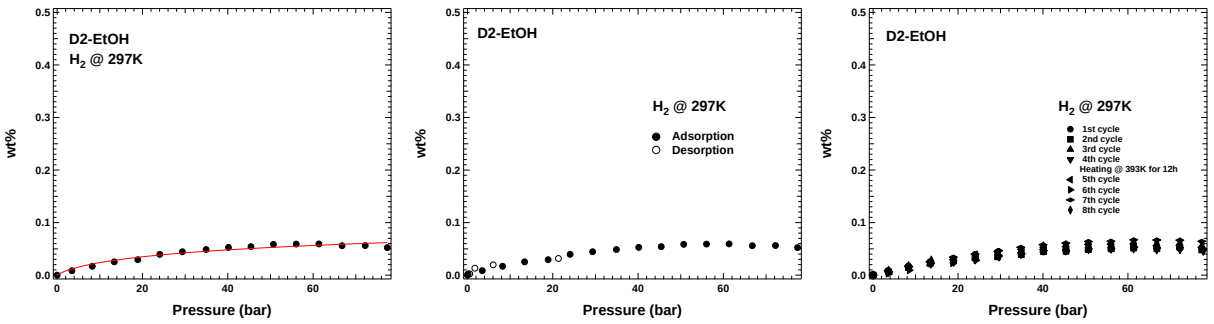

(a) (b) (c)

Figure 11. a) PcT adsorption isotherm obtained with H_2 at RT up to 80 bar. b) H_2 adsorption-desorption isotherm obtained on D2-EtOH sample. Full circle=adsorption, empty circle=desorption. c) H_2 adsorption isotherm cycles.

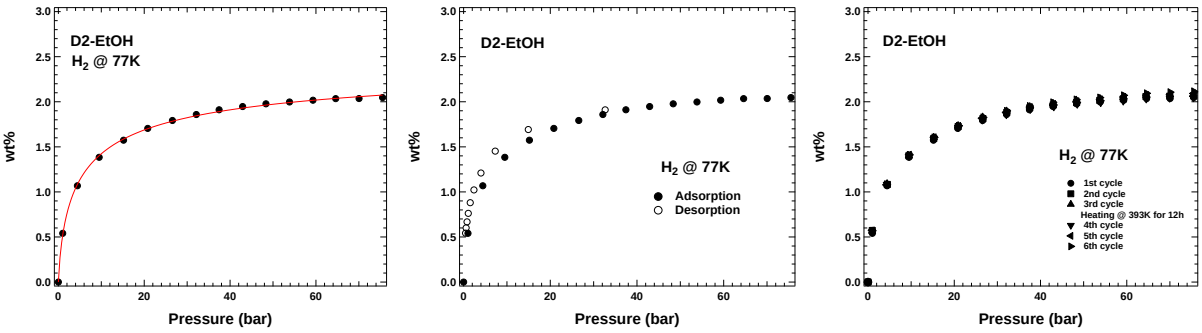

(a) (b) (c)

Figure 12. a) H_2 PcT adsorption isotherm at LN_2 temperatures up to 80 bar. b) H_2 adsorption-desorption isotherm obtained on D2-EtOH sample. Close circle=adsorption, open circle=desorption. c) H_2 adsorption isotherm cycles.

The H_2 adsorption isotherms comparison of Dx-EtOH series of samples with different compositions are reviewed in Table 3. Except for the maximum storage capacity, by analyzing both the adsorption isotherms, the trend of the all analyzed samples, as shown in Fig. 13, it is quite similar. Moving to higher-pressure the curvature of the isotherms became different indicating, together with the relative K value, the different speed of saturation of the adsorption sites. A different grade of interaction with the incoming hydrogen molecules (K) and different values of homogeneity (t) are observed for the analysed samples. Going down to lower wt%max, in sequence we found the D2-EtOH followed by the D0 and D1-EtOH samples. For the Dx-EtOH series, the hydrogen storage capacity increased with the increase of the specific surface area but with the decrease of the micropore area and the pore width.

Sample	Skeletal density (g/cc)	$wt\%_{max} \pm \Delta wt\%_{max}$	$K \pm \Delta K$	$t \pm \Delta t$
D0-EtOH	2.01 ± 0.06	2.23 ± 0.06	0.74 ± 0.11	0.53 ± 0.03
D1-EtOH	1.63 ± 0.13	1.93 ± 0.03	0.21 ± 0.02	0.80 ± 0.01
D2-EtOH	1.91 ± 0.10	2.54 ± 0.06	0.50 ± 0.05	0.58 ± 0.03

Table 3. Skeletal density, asymptotic maximum H_2 uptake value and Toth fit parameters for all analysed DX-EtOH series of samples at 77 K up to 80 bar.

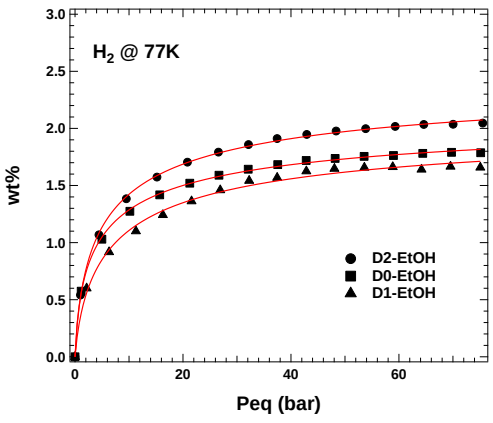

Figure 13. Comparison of H_2 PcT isotherms obtained for Dx-EtOH samples at liquid nitrogen temperature (77 K) up to 80 bar.

➢ Tx-EtOH series of samples.

- *T0-EtOH*

The sample labeled as T0-EtOH shows a skeletal density of 2.18 g/cc. Hydrogen adsorption measurements show, up to the maximum analyzed pressure, a negligible reversible adsorption capacity lower than 0.05 wt% (isotherms not shown) at RT. An interesting uptake value could be observed lowering temperature down to 77 K (see Fig. 14a) where it shows, at 80 bar, a maximum uptake value of 2.5 wt% but, almost 60 % of this value is already reached at 10 bar. This is an interesting result since it means that the sample can store a substantial amount of H_2 already at low pressure.

Toth analysis performed on the acquired isotherms leading to a maximum uptake value wt%max around 2.89 wt% is indicating the possibility for the T0-EtOH to further store up to 16 wt% more increasing pressure. We get a value for the t parameter of 0.8 indicating a homogeneous surface of the sample; at the same time, because all adsorption sites are considered, the average interaction of the molecules with the sample surface results in a K value approximately equal to 0.20.

Reversibility tests on the T0-EtOH sample result in a full capability to adsorb and desorb hydrogen molecules with and without thermal treatment. Looking at Fig. 14b, in fact, the overlapping of the adsorption and the desorption isotherms is evident for a single cycle; a further confirmation of that is obtained by the overlapping of the multiple adsorption cycles reported in Fig. 14c. The little visible variation among the isotherms is related to slight temperature changes during each test, so it could be considered negligible in terms of process reversibility.

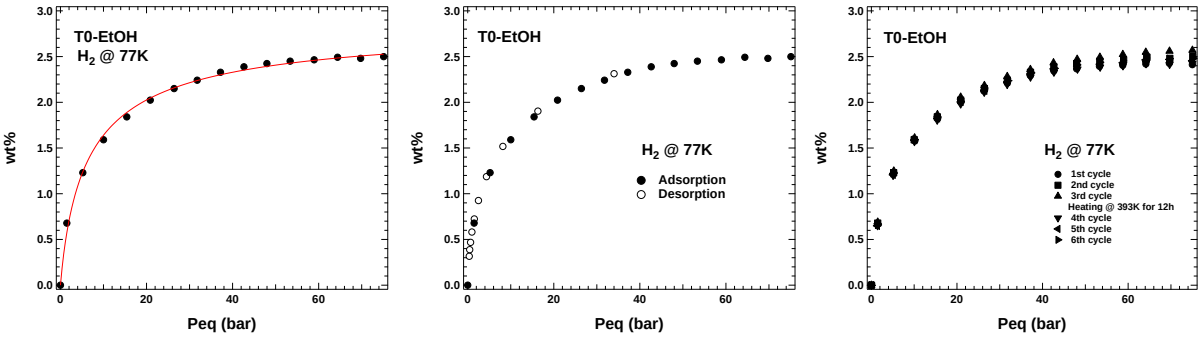

(a) (b) (c)

Figure 14. a) H_2 PcT adsorption isotherm at LN_2 temperatures up to 80 bar. b) H_2 adsorption-desorption isotherm obtained on T0-EtOH sample. c) H_2 adsorption isotherm cycles.

- *T1-EtOH*

The helium pycnometry analysis performed on the T1-EtOH result in a skeletal density value of 2.11 g/cc. It does not show appreciable hydrogen adsorption capacity (< 0.05 wt%) at RT (here not shown) but, a storage capacity of 2.4 wt% is evaluated at 77 K up to the maximum analyzed pressure. The maximum uptake value at 80 bar is 3.8 wt%, which is lower than the previous sample, while the reversibility of the adsorption process is exactly the same (see Fig. 15a and b).

Looking at Fig. 15c below where multiple adsorption cycles, with and without thermal treatment in between are reported, we can clearly note the overlapping of the subsequent adsorption isotherms. Further confirmation of that is shown in Fig. 15c with adsorption and desorption cycle. Therefore, also for this sample, the H_2 molecules adsorbed into the sample do not lead to any permanent structure modification.

The red line between points in Fig. 15a represents the Toth fit and the result of Toth analysis shows a heterogeneity of the surface comparable with that of the previous analyzed sample ($t \cong 0.85$) such as the sorbent-adsorbant interaction ($K \cong 0.18$). Nevertheless, even if the homogeneity and the strong of interaction between molecules and surface are similar in both samples, the difference in the maximum uptake value at 80 bar it is also extends to the maximum asymptotic uptake evaluated in wt%max ≅ 2.78.

The slight difference between the T0-EtOH and the T1-EtOH is related also to differences in the textural properties and/or, alternatively, to the different K values.

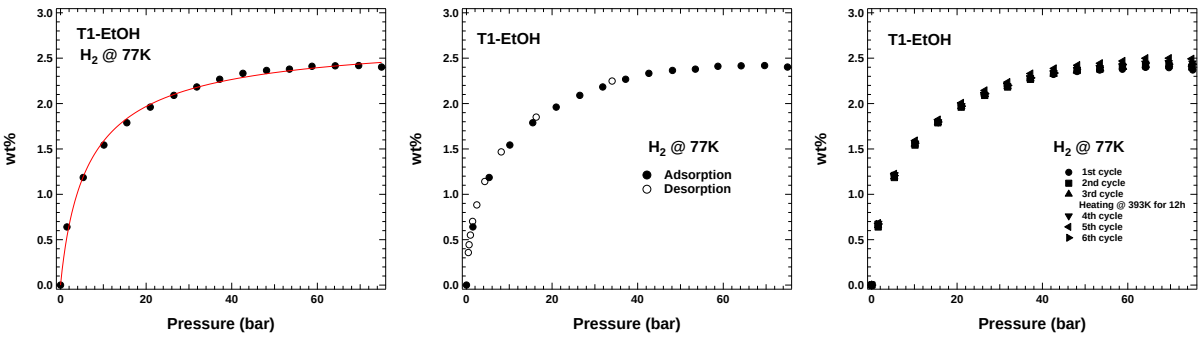

(a) (b) (c)

Figure 15. a) H_2 PcT adsorption isotherm at LN_2 temperatures up to 80 bar. b) H_2 adsorption-desorption isotherm obtained on T1-EtOH sample. Close circle=adsorption, open circle=desorption. c) H_2 adsorption isotherm cycles.

- *T2-EtOH*

The T2-EtOH sample shows a skeletal density of 1.82 g/cc, slightly lower compared to the two previous samples. Also, the T2-EtOH shows an adsorption capacity at RT lower than 0.05 wt% while moving down to LN_2 the sample increases its storage capacity, at the maximum analyzed pressure, up to 2.4 wt%. This value is close to those obtained on the two previous analyzed samples, showing a similar interaction between the hydrogen molecules and the T2-EtOH surface. Toth analysis performed on the adsorption isotherm, Fig. 16a, shows that, even if the t parameter (0.52) is lower compared to the previous samples, an increase in the interaction between the incoming molecules and the surface is evidenced by K=0.38 and consequently, a maximum asymptotic uptake wt%max ≅ 3.35 wt%. This value, higher compared with those obtained on the T0-EtOH and T1-EtOH, indicates a higher storage capacity of the T2-EtOH sample moving to higher pressure. This behavior could be related mainly to a synergic effect of chemistry and porosity as well as to a better-optimize textural properties like lower surface area of micropore and/or porosity of the sample. Even if the T2-EtOH sample shows a higher storage capacity, contrarily to the previous samples, it does not show an easy reversible H_2 adsorption process. Looking at Fig. 16b, in fact, it is clearly visible a hysteresis in the desorption curve (open circle) that does not perfectly overlap the adsorption one (close circle). Confirmation of that behavior is given by the multiple adsorption-desorption test performed on it and reported in Fig. 16c. This slight hysteresis is indicating that the gas is slightly retained as pressure decreases [7]. It is evident, that after the first cycle, the maximum adsorption uptake decreases down to 1.9 wt% losing almost 20% of the capacity at 80 bar. This is indication that not all the adsorbed H_2 is easily released by the sample (vacuum pumping in between is not enough). In order to recover the T2-EtOH and its maximum uptake capacity a thermal treatment is necessary as clearly visible in Fig. 16c.

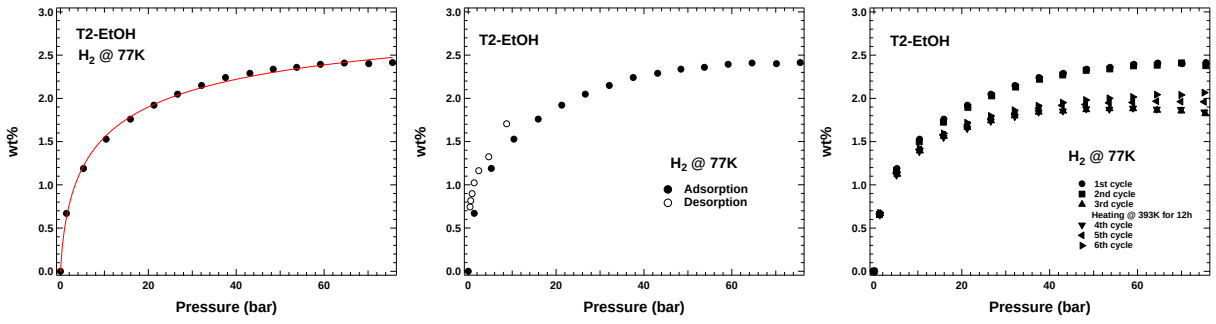

(a) (b) (c)

Figure 16. a) H_2 PcT adsorption isotherm at LN_2 temperatures up to 80 bar. b) H_2 adsorption-desorption isotherm obtained on T2-EtOH sample. Close circle=adsorption, open circle=desorption. c) H_2 adsorption isotherm cycles.

- *T3-EtOH*

Helium pycnometry measurements performed on the T3-EtOH sample gives a skeletal density of 1.57 g/cc and this value compares with those obtained on the previous samples is much lower indicating a different structure compared to the previous ones. Also, the T3-EtOH was submitted to hydrogen adsorption tests up 80 bar in both RT and liquid nitrogen conditions and the adsorption capacity at RT is negligible, reaching an adsorption capacity close to the one previously observed. Moving down to LN_2, T3-EtOH has been able to store an amount close to 2.1 wt% up to 80 bar (see Fig. 17a). The observed trend is similar to the previous samples, with a rapid increase of the adsorption capacity already below 20 bar and this could be an interesting point for practical application since lower pressure is always requested. Even if the adsorption capacity at 80 bar is lower compared to previous Tx-EtOH samples, the asymptotic extrapolated value obtained through Toth analysis shows that at 80 bar we are almost at 72% of the maximum storage capacity of the sample and the $wt\%_{max} \cong 2.9$ wt% has been obtained. This means that moving to higher pressure, the T3-EtOH sample is similar to the T0-EtOH and T1-EtOH ones. The fitting procedure performed on the adsorption isotherms (Fig. 17a), leads to an interaction between adsorbate and adsorbent $K \cong 0.68$ and a homogeneity grade of the sample $t \cong 0.47$. The desorption isotherm does not perfectly overlap the adsorption one (Fig. 17b), though the reversibility of the adsorption process is not affected. Multiple adsorption cycles performed on the sample (Fig. 17c) show that following adsorption isotherms perfectly overlap. This means that the H_2 molecules adsorbed into the T3-EtOH sample can be easily desorbed from the sample surface. Another explanation could be a slow desorption process that need more time. In both cases, the T3-EtOH sample appears like a stable porous structure able to hold H_2 molecule and give them back when required.

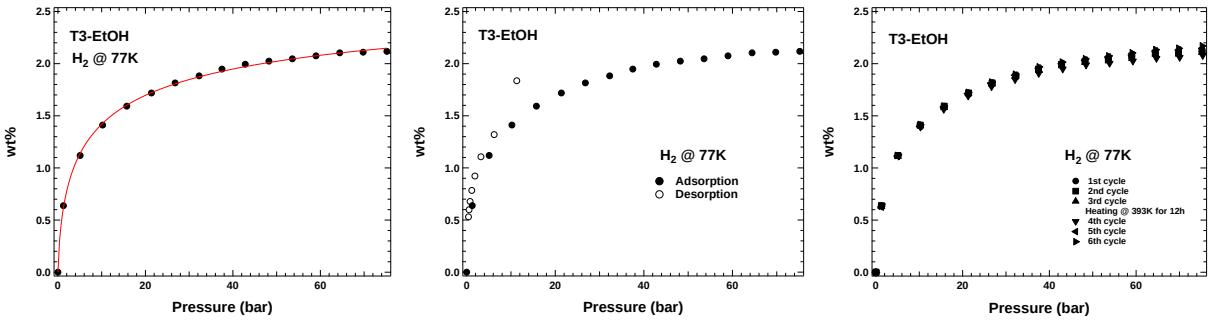

(a) (b) (c)

Figure 17. a) H_2 PcT adsorption isotherm at LN_2 temperatures up to 80 bar. b) H_2 adsorption-desorption isotherm obtained on T3-EtOH sample. Close circle=adsorption, open circle=desorption. c) H_2 adsorption isotherm cycles.

- *T4-EtOH*

The T4-EtOH owns a skeletal density of 1.38 g/cc. It shows a negligible reversible adsorption capacity lower than 0.05 wt% at RT up to 80 bar (isotherms not shown), that increase moving to 77 K. Compared to previous analyzed samples, the T4-EtOH one has, up to now, both the lower skeletal density value and maximum uptake value. At the pressure of 80 bar, it reaches only 1.7 wt% even if, compared to the previous one, at 20 bar it is already store almost 82% of the total amount.

Toth analysis performed on the acquired isotherms, Fig. 18a, leading to a maximum uptake value (wt%max) around 2.18 wt%, is indicating the possibility for the T4-EtOH to further store up to 2.8 wt% more increasing pressure. The t parameter indicates a not completely homogenous surface (t = 0.49) but at the same time a very strong interaction between the incoming hydrogen molecules and the surface, is quite strong (K=1). The strong interaction could be responsible of the hysteresis process clearly visible in Fig. 18b.

The overlapping of the adsorption and desorption curve is avoided. Even if the interaction looks strong and even if an evident hysteresis is present, multiple adsorption cycle performed on the T4-EtOH sample show a total reversible H_2 adsorption into the sample. Consequently, we can assert a total reversibility of storage capacity with and without thermal treatment, obtained by the overlapping of the multiple adsorption cycles (Fig. 18c). The strong interaction between H_2 molecules and T4-EtOH surface only affects the speed of the desorption process, but not the reversibility of the process itself or the structure of the sample.

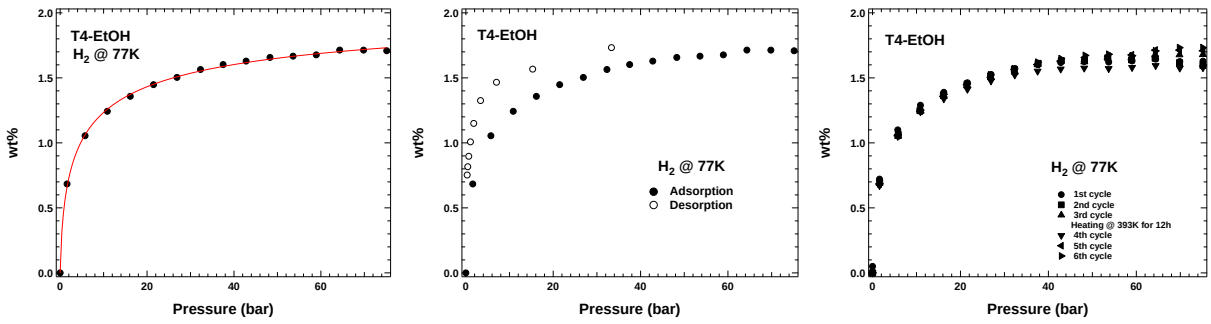

(a) (b) (c)

Figure 18. a) H_2 PcT adsorption isotherm at LN_2 temperatures up to 80 bar. b) H_2 adsorption-desorption isotherm obtained on T4-EtOH sample. Close circle=adsorption, open circle=desorption. c) H_2 adsorption isotherm cycles.

- *T5-EtOH*

For T5-EtOH, a skeletal density of 1.56 g/cc and a negligible adsorption capacity at RT has been obtained. At LN_2, reached an uptake value of 1.9 wt%, slightly higher than the T4-EtOH, and it increases up to 21% more, by increasing pressure.

Toth analysis performed on the adsorption isotherms (see Fig. 19a below), allow to extrapolate a maximum asymptotic uptake value $wt\%_{max}$=2.3 wt% together with a heterogeneity of the surface t ≅ 0.59 such as a sorbent-adsorbant interaction K ≅ 0.61. The interaction between molecules and surface could be responsible of the slightly hysteresis visible in Fig. 19b.

Even if there is a hysteresis phenomenon, multiple adsorption cycles show a totally reversible hydrogen adsorption into the sample. Thus, we can assert that the total reversibility of storage capacity with and without thermal treatment as confirmed by the overlapping of the multiple adsorption cycles reported in Fig. 19c.

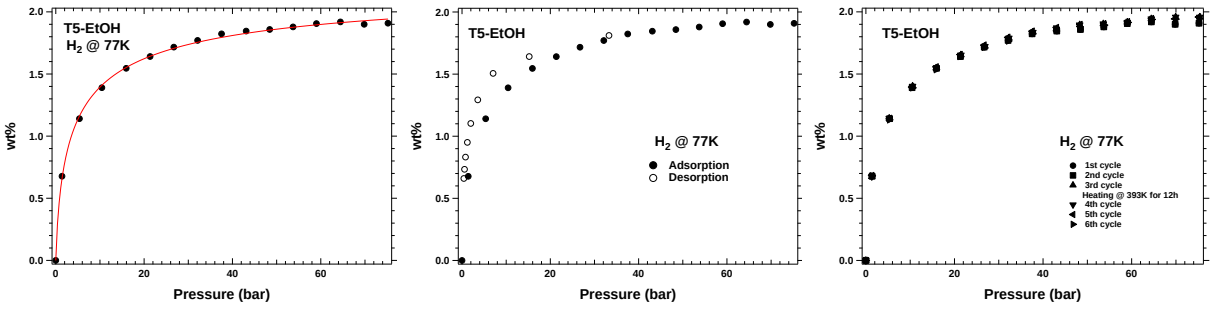

(a) (b) (c)

Figure 19. a) H_2 PcT adsorption isotherm at LN_2 temperatures up to 80 bar. b) H_2 adsorption-desorption isotherm obtained on T5-EtOH sample. Close circle=adsorption, open circle=desorption. c) H_2 adsorption isotherm cycles.

By reviewing the analysis for the Tx-EtOH series of samples (Table 4) and by analyzing the adsorption isotherms at 77 K, Fig. 20, the trend of the all analyzed samples is quite similar for the T0-EtOH/T1/T2 samples, while it is different for the rest of samples from this series, T3, T4 and T5. The first four samples appear the most performing at 77 K, immediately followed by the T5 and T4 samples. The T4-EtOH sample, according with a higher value of K compared with the other samples, exhibits a faster saturation. For the Tx-EtOH series, the hydrogen storage capacity increased with the specific surface area and with the micropore area.

Table 4. Skeletal density, asymptotic maximum H2 uptake value and Toth fit parameters for all analysed Tx-EtOH samples at 77 K up to 80 bar.

Sample	Skeletal density (g/cc)	$wt\%_{max} \pm \Delta wt\%_{max}$	$K \pm \Delta K$	$t \pm \Delta t$
T0-EtOH	2.18 ± 0.01	2.89 ± 0.03	0.20 ± 0.01	0.80 ± 0.01
T1-EtOH	2.11 ± 0.07	2.78 ± 0.03	0.18 ± 0.01	0.85 ± 0.01
T2-EtOH	1.82 ± 0.07	3.35 ± 0.22	0.38 ± 0.09	0.52 ± 0.06
T3-EtOH	1.57 ± 0.03	2.93 ± 0.11	0.68 ± 0.11	0.47 ± 0.03
T4-EtOH	1.38 ± 0.02	2.18 ± 0.03	1.00 ± 0.01	0.49 ± 0.01
T5-EtOH	1.56 ± 0.02	2.30 ± 0.06	0.61 ± 0.09	0.59 ± 0.04

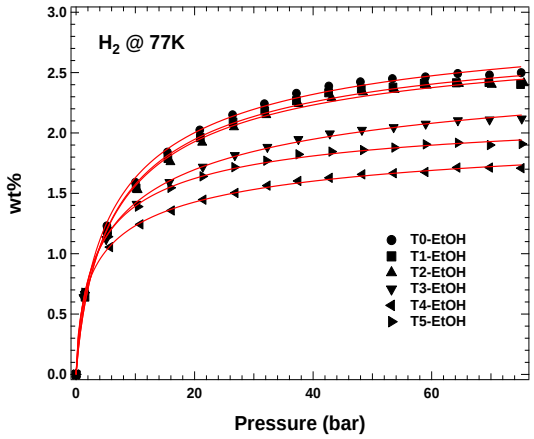

Figure 20. Comparison of H_2 PcT isotherms obtained for Tx-EtOH samples at liquid nitrogen temperature (77 K) up to 80 bar.

3.5.4 Conclusions

In order to increase the affinity toward incoming hydrogen molecules on physisorption materials, our purpose was to tailor properties by increasing surface area, to optimize the pore diameter, and the functionalization with different organic groups. Our previous study shows that the methyl functionalized material, among many other organic groups, provided the highest adsorption capacity for H_2 (2.41% at 80 bar and 77 K) [8]. Starting from these findings, in the present study we performed a systematic analysis of varying the synthesis parameters with methyl functionalized silica precursor, with the purpose to improve the adsorption capacity. The presented results indicate an effective interaction process of the H_2 molecules inside the samples structure and consequently make the Dx-EtOH and Tx-EtOH interesting materials for H_2 storage applications. The addition of the methyl

functionalized precursor in concentration ≤ 20 % compared to the simple silica precursor, results in a decrease in the skeletal density value and in the improvement of the H_2 adsorption capacity. At higher MTES concentrations ≥ 20 %, higher strength of interactions towards hydrogen molecules was evidenced. Overall, the synergic effect of surface chemistry and porosity on the efficiency of gas storage in small pores was exhibited. In comparison with other literature studies, where the obtained values for the hydrogen sorption capacity were: 2.4% at 10 bar and 77 K in activated carbon [3] or 3.3 wt.% at 298 K at a pressure up to 4.83 MPa in graphite nanofibers [4], it may be concluded that good results have been obtained with the present methyl functionalized silica samples, as well. Our further studies aim materials properties improvements for the maintaining of hydrogen storage capacity after an increased number of cycles, therefore high reversibility. A good example in this respect is the newly obtained material where a 89.5% maintain of hydrogen adsorption after 100 cycles has been observed [38].

References

[1] C. Guan, F. Su, X.S. Zhao, K. Wang, Methane storage in a template-synthesized carbon, Sep. Purif. Technol. 64 (1) (2008) 124‑126, https://doi.org/10.1016/j.seppur.2008.08.007.

[2] C.-C. Huang, H.-M. Chen, C.-H. Chen, J.-C. Huang, Effect of surface oxides on hydrogen storage of activated carbon, Sep. Purif. Technol. 70 (3) (2010) 291‑295, https://doi.org/10.1016/j.seppur.2009.10.009.

[3] C. Guan, X. Zhang, K. Wang, C. Yang, Investigation of H2 storage in a templated carbon derived from zeolite Y and PFA, Sep. Purif. Technol. 66 (3) (2009) 565‑569, https://doi.org/10.1016/j.seppur.2009.01.015.

[4] C.-W. Huang, H.-C. Wu, Y.-Y. Li, Hydrogen storage in platelet graphite nanofibers, Sep. Purif. Technol. 58 (1) (2007) 219‑223, https://doi.org/10.1016/j.seppur. 2007.07.032.

[5] C.-C. Huang, N.-W. Pu, C.-A. Wang, J.-C. Huang, Y. Sung, M.-D. Ger, Hydrogen storage in graphene decorated with Pd and Pt nano-particles using an electroless deposition technique, Sep. Purif. Technol. 82 (2011) 210‑215, https://doi.org/10. 1016/j.seppur.2011.09.020.

[6] P. Mishra, S. Mekala, F. Dreisbach, B. Mandal, S. Gumma, Adsorption of CO2, CO, CH4 and N2 on a zinc based metal organic framework, Sep. Purif. Technol. 94 (2012) 124‑130, https://doi.org/10.1016/j.seppur.2011.09.041.

[7] D. Owens, A. Han, L. Sun, Y. Mao, Synthesis of VTMS(X)-HMS-3 mesoporous ordered silica for hydrogen storage, Int. J. Hydrogen Energy 40 (6) (2015) 2736‑2741, https://doi.org/10.1016/j.ijhydene.2014.12.100.

[8] A.-M. Putz, A. Policicchio, S. Stelitano, R.G. Agostino, P. Sfîrloagă, C. Ianăşi, R.G. Agostino, C. Savii, Tailoring mesoporous silica by functionalization for gases (H2, CH4,

CO2) storage applications, Fullerenes Nanotubes Carbon Nanostruct. 26 (12) (2018) 810‑819, https://doi.org/10.1080/1536383X.2018.1502177.

[9] A. Mavrandonakis, E. Klontzas, E. Tylianakis, G.E. Froudakis, Enhancement of hydrogen adsorption in metal−organic frameworks by the incorporation of the sulfonate group and li cations. A multiscale computational study, J. Am. Chem. Soc. 131 (2009) 13410‑13414, https://doi.org/10.1021/ja9043888.

[10] G.N. Kalantzopoulos, M. Antoniou, A. Enotiadis, K. Dimos, E. Maccallini, A. Policicchio, E. Colavita, R.G. Agostino, Enhanced hydrogen and methane storage of hybrid mesoporous organosilicas, J. Mater. Chem. A 4 (23) (2016) 9275‑9285, https://doi.org/10.1039/C5TA09393G.

[11] N. Bimbo, V.P. Ting, J.E. Sharpe, T.J. Mays, Analysis of optimal conditions for adsorptive hydrogen storage in microporous solids, Colloids Surf. A 437 (2013) 113‑119, https://doi.org/10.1016/j.colsurfa.2012.11.008.

[12] U. Eberle, M. Felderhoff, F. Schuth, Chemical and physical solutions for hydrogen storage, Angew. Chem. Int. Ed. 48 (2009) 6608‑6630,, , https://doi.org/10.1002/anie.200806293.

[13] T.M. Ho, T. Howes, B.R. Bhandari, Encapsulation of gases in powder solid matrices and their applications: a review, Powder Technol. 259 (2014) 87‑108, https://doi.org/10.1016/j.powtec.2014.03.054.

[14] S.A. El-Safty, A. Shahat, Md.R. Awual, Efficient adsorbents of nanoporous aluminosilicate monoliths for organic dyes from aqueous solution, J. Colloid Interface Sci. 359 (1) (2011) 9‑18, https://doi.org/10.1016/j.jcis.2011.01.006.

[15] D. Stolten, Hydrogen and Fuel Cells: Fundamentals, Technologies and Applications, Wiley-VCH Verlag GmbH & Co. KGaA, Weinheim, 2010.

[16] S.A. El-Safty, A. Shahat, Md.R. Awual, M. Mekawy, Large three-dimensional mesocage pores tailoring silicananotubes as membrane filters: nanofiltration and permeation flux of proteins, J. Mater. Chem. 21 (2011) 5593‑5603, https://doi.org/10.1039/C0JM03269G.

[17] S.A. El-Safty, M.A. Shenashen, M. Ismael, M. Khairy, Mesocylindrical aluminosilica monolith biocaptors for size ‑ selective macromolecule cargos, Adv. Funct. Mater. 22 (14) (2012) 3013‑3021, https://doi.org/10.1002/adfm.20120039.

[18] S.A. El-Safty, M.A. Shenashen, M. Ismael, M. Khairy, Md.R. Awual, Mesoporous aluminosilica sensors for the visual removal and detection of Pd(II) and Cu(II) ions, Microporous Mesoporous Mater. 166 (2013) 195‑205, https://doi.org/10.1016/j.micromeso.2012.03.021.

[19] E. Dündar-Tekkaya, Y. Yürüm, Mesoporous MCM-41 material for hydrogen storage: a short review, Int. J. Hydrogen Energy 41 (23) (2016) 9789‑9795, https://doi.org/10.1016/j.ijhydene.2016.03.050.

[20] E. Masika, R. Mokaya, Preparation of ultrahigh surface area porous carbons templated

using zeolite 13X for enhanced hydrogen storage, Prog. Nat. Sci. Mater. Int. 23 (3) (2013) 308‑316, https://doi.org/10.1016/j.pnsc.2013.04.007.

[21] S.J. Yang, J.H. Im, H. Nishihara, H. Jung, K. Lee, T. Kyotani, C.R. Park, General relationship between hydrogen adsorption capacities at 77 and 298 K and pore characteristics of the porous adsorbents, J. Phys. Chem. C 116 (2012) 10529‑10540,, , https://doi.org/10.1021/jp302304w.

[22] N. Park, K. Choi, J. Hwang, D.W. Kim, D.O. Kim, J. Ihm, Progress on first-principlesbased materials design for hydrogen storage, PNAS 109 (2012) 19893‑19899,, , https://doi.org/10.1073/pnas.1217137109.

[23] N.S. Suraweera, A.A. Albert, J.R. Humble, C.E. Barnes, D.J. Keffer, Hydrogen adsorption and diffusion in amorphous, metal-decorated nanoporous silica, Int. J. Hydrogen Energy 39 (2014) 9241‑9253,, , https://doi.org/10.1016/j.ijhydene.2014.03.247.

[24] M. Kubo, K. Ishiyama, A. Shimojima, T. Okubo, Effect of organic groups on hydrogen adsorption properties of periodic mesoporous organosilicas, Microporous Mesoporous Mater. 147 (2012) 194‑199,, , https://doi.org/10.1016/j.micromeso.2011.06.014.

[25] F. Hoffmann, M. Cornelius, J. Morell, M. Fröba, Silica-based mesoporous organic‑inorganic hybrid materials, Angew. Chem. Int. Ed. 45 (2006) 3216‑3251,, , https://doi.org/10.1002/anie.200503075.

[26] W. Wang, J.E. Lofgreen, G.A. Ozin, Why PMO? Towards functionality and utility of periodic mesoporous organosilicas, Small 6 (2010) 2634‑2642, https://doi.org/10.1002/smll.201000617.

[27] G.N. Kalantzopoulos, A. Enotiadis, E. Maccallini, M. Antoniou, K. Dimos, A. Policicchio, E. Klontzas, E. Tylianakis, V. Binas, P.N. Trikalitis, R.G. Agostino, D. Gournis, G.E. Froudakis, Hydrogen storage in ordered and disordered phenylene bridged mesoporous organosilicas, Int. J. Hydrogen Energy 39 (5) (2014) 2104‑2114, https://doi.org/10.1016/j.ijhydene.2013.11.063.

[28] L. Almásy, A.-M. Putz, Q. Tian, G.P. Kopitsa, T.V. Khamova, R. Barabás, M. Rigó, A. Bóta, A. Wacha, M. Mirica,, B.Ţăranu, and C. Savii, hybrid mesoporous silica with controlled drug release, J. Serb. Chem. Soc. 84 (2019) 1027‑1039, https://doi.org/10.2298/JSC181109009A.

[29] R. Al-Oweini, H. El-Rassy, Synthesis and characterization by FTIR spectroscopy of silica aerogels prepared using several Si(OR)4 and R′ ′ Si(OR′)3 precursors, J. Mol. Struct. 919 (2009) 140‑145, https://doi.org/10.1016/j.molstruc.2008.08.025.

[30] M. Thommes, K. Kaneko, A.V. Neimark, J.P. Olivier, F. Rodriguez-Reinoso, J. Rouquerol, K.S.W. Sing, Physisorption of gases, with special reference to the evaluation of surface area and pore size distribution (IUPAC Technical Report), Pure Appl. Chem. 87 (9-10) (2015) 1059‑1061, https://doi.org/10.1515/pac-2014-1117.

[31] K.-A. Cychosz, M. Thommes, Progress in the physisorption characterization of nanoporous gas storage materials, Engineering 4 (4) (2018) 559‑566, https://doi.org/10.1016/j.eng.2018.06.001.

[32] A.L. Ahmad, N.N.N. Mustafa, Pore surface fractal analysis of palladium-alumina ceramic membrane using Frenkel‑Halsey‑Hill (FHH) model, J. Colloid Interface Sci. 301 (2006) 575‑584, https://doi.org/10.1016/j.jcis.2006.05.041.

[33] H.I. Meléndez-Ortiz, L.A. García-Cerda, Y. Olivares-Maldonado, G. Castruita, J.A. Mercado-Silva, Y.A. Perera-Mercado, Preparation of spherical MCM-41 molecular sieve at room temperature: influence of the synthesis conditions in the structural properties, Ceram. Int. 38 (8) (2012) 6353‑6358, https://doi.org/10.1016/j.ceramint.2012.05.007.

[34] Q. Cai, W.-Y. Lin, F.-S. Xiao, W.-Q. Pang, X.-H. Chen, B.-S. Zou, The preparation of highly ordered MCM-41 with extremely low surfactant concentration, Microporous Mesoporous Mater. 32(1-2) (1999) 1‑15,https://doi.org/10.1016/S1387-1811(99)00082-7.

[35] A.-M. Putz, K. Wang, A. Len, J. Plocek, P. Bezdicka, G.P. Kopitsa, T.V. Khamova, C. Ianăşi, L. Săcărescu, Z. Mitróová, C. Savii, M. Yan, L. Almásy, Mesoporous silica obtained with methyltriethoxysilane as co-precursor in alkaline medium, Appl. Surf. Sci. 424 (3) (2017) 275‑281, https://doi.org/10.1016/j.apsusc.2017.04.121.

[36] M.M. Rabbani, W.-T. Oh, D.-G. Nam, Synthesis and characterization of methyltriethoxysilyl-mediated mesoporous silicalites, Trans. Electr. Electron. Mater. 12 (3) (2011) 119‑122, https://doi.org/10.4313/TEEM.2011.12.3.119.

[37] A.-M. Putz, L. Almásy, A. Len, C. Ianăşi, Functionalized silica materials synthesized via co- condensation and post-grafting methods, Fullerenes Nanotubes Carbon Nanostruct. 27 (4) (2019) 323‑332, https://doi.org/10.1080/1536383X.2019. 1593154.

[38] J. Liu, H. Cheng, S. Han, H. Liu, J. Huot, Hydrogen storage properties and cycling degradation of single-phase La0.60R0.15Mg0.25Ni3.45 alloys with A2B7-type superlattice structure, Energy 192 (2020) 116617, , https://doi.org/10.1016/j.energy. 2019.116617.

3.6 CO_2 Adsorption Investigation on an Innovative Nanocomposite Material with Hierarchical Porosity

3.6.1 State of the art

Trends in global carbon dioxide (CO_2) emission in atmosphere clearly show a rapid increasing over the last decades. It can be mostly attributed to the current technologies adopted to produce power and to the automotive sector, both based on the use of fossil fuels. International Energy Agency (IEA)-World Energy Outlook (WEO) estimates CO_2 levels 90% higher than those of 1980s by 2030 [1,2]. In order to limit and reverse this trend an increasing numbers of research programs are in place with the aim to reduce CO_2 emissions in the atmosphere and provide efficient and effective process to capture and store CO_2. The former goal can be achieved by adopting more efficient technologies and renewable resources [3,4], whereas the latter can be carried out by chemisorption and adsorption of CO_2. Chemisorption of CO_2 in monoethanolamine (MEA), diethanolamine (DEA) and methyldiethanolamine (MDEA) is, however, an expensive process, limited by the severe equipment corrosion and high amount of waste produced [5,6]. Therefore, adsorption represents the current effective process for CO_2 removal. Several CO_2 adsorbents have been proposed and investigated in scientific literature, such as carbonaceous materials [7,8], polymers [9], dry alkali metal-based sorbents [10], metal-organic frameworks (MOFs) [11] and zeolites [12]. The extensive use of inorganic porous carbons as CO_2 adsorbents is limited by the high production cost due to the elevated optimal heat treatment temperatures and the additional activation costs. Moreover, they show poor selectivity and significant temperature sensitivity to CO_2 adsorption [13–15]. Dry alkali metal-based sorbents use cheap raw materials, operative temperatures range between ambient to about 500 °C, but major drawbacks are the diffusion resistance and the regeneration costs [16,17]. MOFs show very high specific surface area, tunable pore size and large accessible pore volume, but investigation is limited to laboratory-scale, long-term structural stability is questionable and the organic linkers are expensive [18–20]. Zeolites have been largely investigated as CO_2 adsorbents [21–23] due to the superior separation performance and low cost. Zeolites are, crystalline alumino-silicates characterized by a tridimensional framework of interconnected tetrahedra, comprising of aluminium, silicon and oxygen atoms that are located at corners of each tetrahedron and are shared with adjacent tetrahedral. Each tetrahedron that contains aluminum as its central atom has a deficiency of positive charge. It is balanced by the presence of exchangeable cations,

usually alkaline or alkaline-earth metals. The adsorption properties of zeolites depend on composition, structure of the framework, size and shape, purity, cationic form and molecular polarity [16]. Among zeolites, zeolite NaX, is considered a benchmark material in CO_2 capture [20–23]. Studies on CO_2 adsorption on zeolite NaX are usually focused at determining the adsorption isotherm at low-pressure ranges close to atmospheric pressure [24], whereas pure CO_2 adsorption isotherms at medium pressure ranges are less investigated. The latter can be effectively used together with the real adsorption solution theory (RAST) model for the design of a multi-component adsorption system [25].

Zeolites powders are usually shaped, using binders, in beads and pellets or supported on ceramic [26–28]. This further process, allows to prevent high pressure drop and channeling and improve mechanical properties, but affects their final cost [29]. Recently different methods were proposed to consolidate and shape zeolites [30], by mixing zeolite NaX with 20 wt.% kaolin clay and water and kneading [31], or by adding a commercial synthetic zeolite as filler (22–36 wt.%) to a geopolymer matrix formed for low temperature CO_2 capture applications [32]. Geopolymers are a new class of binders [33,34], that can be considered the amorphous analogues of the zeolites [35]. They can also find application as catalysts [36].

In this work, authors identify the proper composition field and temperature to obtain a NaX-geopolymer porous nanocomposite that shows high content and purity of the crystalline phase, a suitable extent of geopolymeric binder to guarantee good mechanical properties and an amount of water that allow the formation of mesoporosity. Microstructural and chemical characterization of the composite were provided by X-ray Diffractometry, Mercury Intrusion Porosimetry, N_2 adsorption/desorption measurements and Scanning Electron Microscopy. Pure CO_2 adsorption/desorption measurements have been also carried out at three different temperatures on monolith and commercial NaX zeolite in powder (used as reference) up to 15 bar. All the adsorption data were evaluated by Toth/Langmuir isotherm model.

3.6.2 Materials

Geopolymer-zeolites one-pot nanocomposites were prepared using metakaolin as alumino-silicate powder source. It was provided by Personal Factory S.r.l and X-ray fluorescence spectroscopy was used to determine its composition in terms of oxides. SiO_2 (42.02%wt), Al_2O_3 (53.9%wt) Fe_2O_3 (1.52%wt) and TiO_2 (1.90%wt) were found to be its mainly components. Its average particles size of 1.59 μm was calculated on a volume distribution

base. Sodium silicate solution (supplied by Condea Augusta S.P.A) was composed by SiO_2 (29.6%wt) Na_2O (13.6%wt) and water. Sodium Hydroxide (AR grade) has been purchased by Sigma Aldrich.

3.6.3 Methods

3.6.3.1 Geopolymer-Zeolites Monolith Synthesis

Several admixtures of different molar compositions within the benchmark range related to the production of NaX zeolite were tested. They are reported in terms of oxides in Table 1. Silica modulus of the activator solutions was varied in the range 0.00–0.82 (samples A90, B90 and C90) at constant Na_2O concentration to investigate the effect of the silicon content on the produced zeolitic phases. Furthermore, Na_2O concentration varied in the range 0.083–0.125 (samples A90, D90, E90) to study the effect of alkalinity at constant Silicon content in the activator solution.

Table 1. Molar composition of the admixtures and silica modulus (Ms) and Na_2O concentration of the activator solution.

	Molar composition	**SiO_2/ Na_2O (Ms)**	**Na_2O/H_2O**
A90	$1Na_2O–3.0SiO_2–1Al_2O_3–12H_2O$	0.82	0.083
B90	$1Na_2O–2.5SiO_2–1Al_2O_3–12H_2O$	0.32	0.083
C90	$1Na_2O–2.0SiO_2–1Al_2O_3–12H_2O$	0.00	0.083
D90	$1.3Na_2O–3.0SiO_2–1Al_2O_3–12H_2O$	0.63	0.108
E90	$1.5Na_2O–3.0SiO_2–1Al_2O_3–12H_2O$	0.55	0.125

Water amount was kept constant in all mixes, with a value greater than those used in the geopolymer production. The last choice was made with the dual purpose to favour the zeolites synthesis and to increase the final porosity of the monoliths.

Monolithic composites were synthesized by activating metakaolin with activator solutions of different composition to achieve the desired final composition. Firstly, the sodium hydroxide solution was obtained by dissolution of NaOH pellets in ultrapure water, with container kept sealed wherever possible to minimize contamination by atmospheric carbonation and prevent water evaporation. The solution was stirred until the NaOH pellets had dissolved and the solution became clear. Once cooled down it was poured into sodium silicate solution. The so obtained alkali activator solution was sealed, stirred and allowed to cool back down to room temperature (RT =∼25 °C). Finally, the activator solution was added to metakaolin powder and the slurry was mechanically vigorously mixed for 10

minutes. The slurries were, afterwards, rapidly casted into open and dismountable Teflon moulds in order to obtain cubic samples of dimensions 40 mm × 40 mm × 40 mm.
The moulds were then sealed from the atmosphere to prevent the moisture loss and cured for 24 h at 60 °C or 90 °C. A commercial pure NaX zeolite powder was used as reference.

3.6.3.2 Chemical and Microstructural Characterization

Identification of the crystalline phases was carried out collecting X-ray diffractograms on a Rigaku MiniFlex 600 X-ray diffractometer (Rigaku Corporation, Tokyo, Japan) with CuKα (wavelength of 1.5406 Å) radiation generated at 20 mA and 40 KV. Powdered samples have been scanned at 0.02 2θ step at a rate of 1°/minute. The Scherrer equation (Eq. (1)) has been applied to estimate the average (by volume) size of zeolite crystallites [37,38].

$$d = \frac{B\,\lambda}{\beta \cos\theta} \quad (1)$$

where d is average crystal size (nm), B is the Scherrer's constant, λ is the wavelength of the X-rays (nm), θ is the value of the Bragg angle (i.e., the angle of the peak maximum) and β is the full width at half-maximum (FWHM) of the broad peak. The crystallinity of the sample due to NaX nanozeolite was determined from the peak areas using commercial pure NaX zeolite as reference [38].
Morphology and microstructure of specimens have been examined on a scanning electron microscope (FEI model INSPECT).

3.6.3.3 BET and MIP Analysis

N_2 adsorption/desorption plots of monolith were carried out in micromeritics ASAP 2020 instruments. Before the analysis, all samples were pre-treated in vacuum condition at 200 °C for 12 h. The specific surface area was calculated using the Brunauer–Emmet–Teller method. The pore size distribution was determined with the Barret–Joyner–Halenda (BJH) method using the adsorption data, thus preventing interference of interconnectivity [39]. The micropore volume and mesopore and macropore surface area were calculated using the t-plot. Pore size distribution in the range 0.004–100 μm was analyzed by mercury intrusion porosimetry MIP. The porosity measurements were performed using a ThermoFinnigan Pascal 240 Series porosimeter (maximum pressure, 200 MPa) equipped with a low-pressure unit (140 Series) able to generate a high vacuum level (10 Pa) and operate between 100 and 400 kPa.

3.6.3.4 Mechanical Characterization

Compressive strengths have been determined on cubic specimens with dimensions of 40×40×40 mm according to UNI-EN 196-1:2005 [40]. All the values have been obtained as the average of three numbers of specimens tested.

3.6.3.5 Gas Adsorption Measurements

The CO_2 adsorption/desorption measurements have been carried out at three different temperatures: room temperature (RT =∼25 °C), low temperature (LT =∼7 °C) and high temperature (HT =∼42 °C), and in a pressure range (0÷15) bar using an optimized Sievert-type (volumetric) apparatus f-PcT for accurate and reliable gas adsorption measurements [41]. All the adsorption data were evaluated by Toth/Langmuir isotherm model with a very high accuracy. Each sample, before each measurement, was previously annealed for 12 hours at 393 K under vacuum ($P < 10^{-6}$ mbar) to eliminate the eventual fraction of water weakly bound inside the samples.

At the beginning, before starting CO_2 adsorption measurements, Helium (He) picnometry analysis was performed in order to get the best value of the sample skeletal density.

To compare the CO_2 adsorption isotherms obtained on different samples at different temperatures, as mentioned before, the Toth/Langmuir model could be used. This model allows for relatively low pressures (range 0.1–1 bar) to obtain information about the strength of interaction that occurs between the surface of the adsorbent and the adsorbed gas. So, by analyzing the 1 bar +15 bar adsorption isotherms, evaluation of the isosteric heat of adsorption according with the Clapeyron-Clausius equation (see below) could be extrapolated. The theoretical maximum storage capacity, the equilibrium constant and homogeneity grade of the pore surfaces have been evaluated analyzing the adsorption isotherms according to the Toth equation [42]:

$$wt\% = (wt\%_{max} \cdot K \cdot P) / (1 + (K \cdot P)^t)^{1/t}$$

where $wt\%_{max}$ is the asymptotic maximum storage capacity, K is the equilibrium constant and t is a parameter introduced from Toth in order to consider the homogeneity grade of the sample surface. The K constant is determined by the energetic interaction between the adsorbent and the adsorbate.

The reliability of the sample's performance in term of cyclic life was tested by submitting all samples to multiple CO_2 adsorption/desorption cycles.

3.6.4 Results and discussion

In order to obtain the NaX-nanocrystals-geopolymer monolith, two operative temperatures (60 °C and 90 °C) and several compositions were investigated. Reaction time was kept constant and equal to 24 h. Crystallization kinetic, induction period and decomposition of metastable phases are accelerated by the increasing of the process temperature. In fact, all the mixes show no formation of crystalline phases at the reaction temperature of 60 °C and after 24 h of reaction (not reported), whereas at a temperature of 90 °C crystalline phases appear (Fig. 1). The mechanism can be described as a sequence of consecutive steps: Initial dissolution of the primary mineral into aluminate and silicate monomers; formation of an amorphous aluminosilicate gel (the geopolymeric binder); its partial crystallization into zeolitic phases following a second pathway, favored by mixes composition and reaction temperature [43].

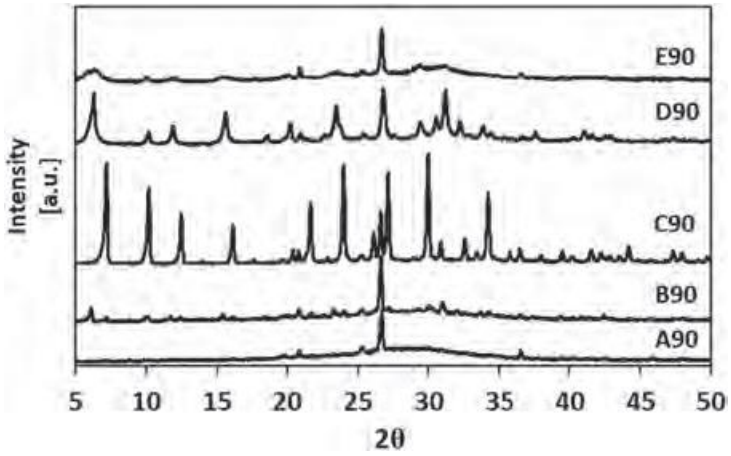

Figure 1. XRD patterns of samples obtained after 24 h of reaction at 90 °C.

The crystalline phases that were obtained are those that can be formed in the selected compositional pattern ($1–1.5Na_2O–1Al_2O_3–2–3SiO_2–12H_2O$). Pure 4A -geopolymer monolith was produced starting from mixes with Si/Al molar ratio equal to 1 and Na/Al = 1 (mixes C90) as evidenced in Figure 1. They correspond to the ratios that arise from the structural formula of the zeolite 4A based on its crystal unit cell ($Na96\ (AlO_2)96\ (SiO_2)96$). By increasing the Si/Al ratio to 1.25 (systems B) both zeolites NaX and 4A are formed and a minor extend of crystalline phases is produced. This is in agreement with several literature reports describing that these two types of zeolites are completive [44]. Further increase of Si/Al ratio up to 1.5 leads to the suppression of the crystalline phases and a pure geopolymer monolith is produced (mixes A90). The geopolymerization process resembles the zeolitization one and consists of the dissolution of metakaolin due to the hydroxide ions OH^- followed by orientation of the dissolved species, condensation and hardening of the structure due to polycondensation reactions [45]. When the activator solution consists of

just a sodium hydroxide solution, such as in system C90 (Ms =0), after the dissolution step an induction period follows, when the destroyed products start to accumulate. This promotes the formation of nuclei that evolve in zeolitic nanocrystalline phases. When waterglass is used to produce the activator solution at constant Na_2O concentration (systems B90 and A90), fast dissolution is followed by fast polycondensation reactions that limit (B90) or suppress (A90) the crystallization process with increasing Ms.

Finally, for systems with Si/Al = 1.5 (A90, D90 and E90), the increasing of alkali concentration in activator solution containing waterglass leads, at first, for the same mechanism previously explained, to the nucleation and crystallization of zeolitic phases (D90). A further increase in alkalinity (system E90) reduces the zeolite yield because it increases the SiO^{-4} solubility, thus making them unavailable for reactions.

XRD analysis of D90 sample reveals that the only zeolitic phase is zeolite NaX. Furthermore, in all the samples, traces of other crystalline phases, such as $Fe_2O_3*H_2O$, Fe_2O_3, TiO_2 and SiO_2 were detected. They are impurities of the metakaolin and behave as inert in the geopolymeric reaction process [34].

Figure 2 shows the micrographs at different magnifications, of the NaX zeolite geopolymer-monolith and a picture of the monolith. The microstructure of the composite is mainly characterized by zeolite nanocrystals glued by the geopolymeric binder to form a complex three-dimensional network of pores. Compressive strength of the D90 monoliths resulted equal to 16±0.7 MPa.

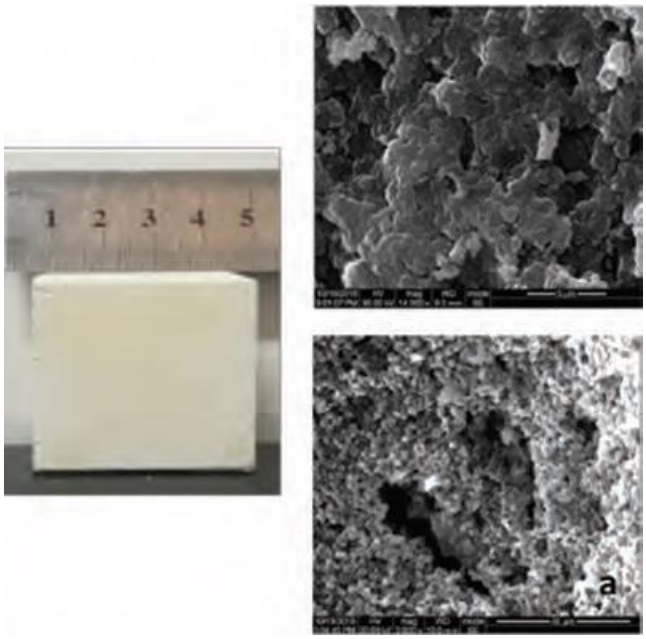

Figure 2. D90 sample, SEM analysis at different magnifications.

X-ray diffraction (XRD) patterns were carried out on D90 samples at different reaction times in order to investigate the crystallization kinetics (not shown). Induction period

ranges between 6 and 8 hours followed by a fast increase in the crystallinity of the samples. After 10 hr of reaction no further variation in XRD pattern was observed. The crystallinity of the nanocomposite in terms of NaX is about the 60% of the crystallinity of the commercial pure NaX zeolite used as reference, as determined from the peak areas [38]. The obtained result is in good agreement with the adsorption data reported in the following paragraph.

Catalytic and adsorption properties are strictly dependent on the average crystallite dimension of zeolites, because it affects intracrystalline diffusion and the external surface area, thus increasing adsorption and reaction rates. Therefore, in order to elucidate the adsorption behaviour of the monolith, the evaluation of average crystal size of the zeolite is relevant. The X-rays diffracting domain analysis has been adopted for the evaluation because it allows to differentiate the crystallite size from the size of the polycrystalline aggregate. In particular, as NaX zeolites possess cubic symmetry and consequently show highly isotropic crystal morphologies, average crystallites dimension was estimated using Scherrer's equation (Eq. (1)) from the peak width of (111) reflection plane (~6° 2θ) [38]. The average size of the NaX crystals embedded in geopolymeric matrix resulted ~34 nm, thus confirming the synthesis of nanozeolites.

In order to characterize the microstructure of the monolith, both Mercury Intrusion Porosimetry (MIP) and N_2 adsorption/desorption measurements were carried out. Pore size distribution of the monolith, measured in the range 0.004 and 100 μm through MIP is reported in Figure 3 and it can be attributed to the geopolymeric component of the monolith.

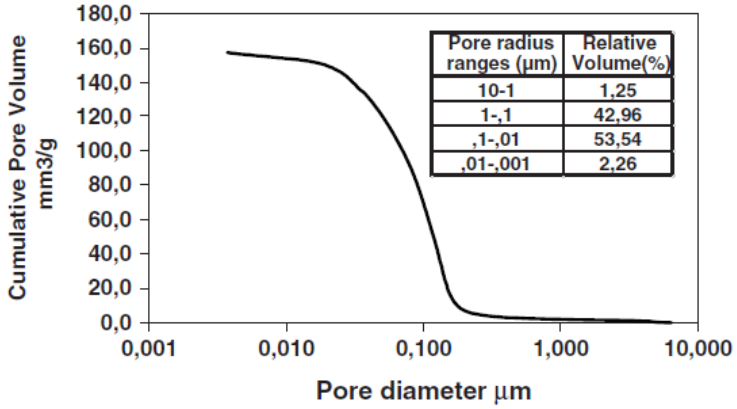

Figure 3. Total porosity and pore size distribution of sample D90 as measured by MIP.

It can be described as a monomodal distribution centered in the interval 0.01–1 μm. Other obtained properties, such as porosity and total pores volume are reported in Table 2.

It can be concluded that geopolymer porosity is mainly constituted by mesopores (20–500 A) and macropores (greater than 500 A) that are originated, respectively, by the water evaporation after unmolding and by air bubbles entrapped during the mixing process.

N_2 adsorption/desorption measurements were performed on the prepared samples to obtain information on the pores that are outside of the Hg porosimetry detection range and the main results are summarized in Table 2.

Table 2. Textural characteristic of the D90 as obtained by N_2 adsorption/desorption and MIP.

N_2 ads/des	[a] S_{BET} (m^2/g)	[b] S_{micro} (m^2/g)	[c] Mesoporous average pore size (4V/A) (Å)	[c] V_{micro} (cm^3/g)	[b] V_{meso} (cm^3/g)
	343	280	84	0.13	0.09
MIP	[d] Bulk density (g cm^{-3})	[d] Porosity by Hg (%)	[d] Total pore volume (mm^3 g^{-1})	[d] Modal pore Ø (µm)	
	1.485	23.4	157.36	0.122	

Notes: [a] BET method; [b] *t*-plot; [c] BJH method; [d] obtained by mercury intrusion porosimetry.

Application of the t-plot method shows that relevant part of the total specific surface area (S_{BET}) is made up of microporosity, thus confirming the microporous nature of the monolith. The NaX-geopolymer nanocomposite shows (Fig. 4) a H4 hysteresis loop often found with aggregated crystals of zeolites, and mesoporous zeolites [46]. In particular, the adsorption branch is a composite of Types I and II, where the pronounced uptake at low p/p_0 can be attributed to the filling of micropores, followed by multilayer physisorption and capillary condensation up to high p/p_0, where unrestricted monolayer-multilayer adsorption occurs due to presence of macropores in the pore network.

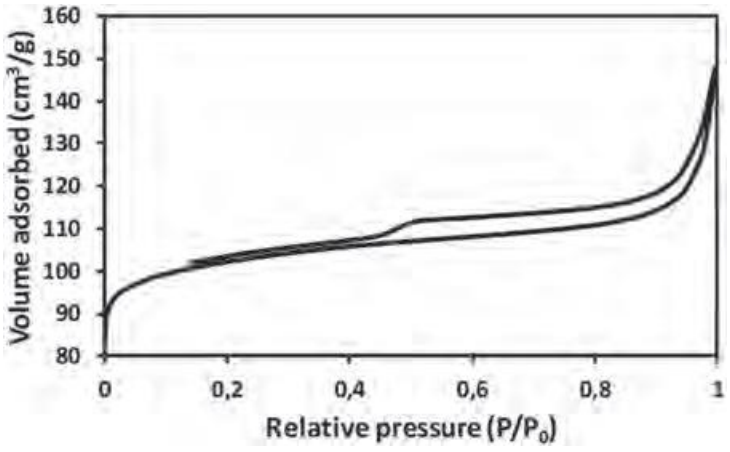

Figure 4. Nitrogen adsorption and desorption isotherm of D90 sample.

3.6.4.1 CO_2 Adsorption Measurements

The CO_2 adsorption capacity of the NaX-geopolymer monolith (D90), in terms of the Pressure-concentration-Temperature isotherms at different temperatures is reported in Figure 5. Nano-composite has a skeletal density of 2.26 ± 0.09 g/cc as measured by helium pycnometry measurements.

As expected, the sample shows a temperature dependence behaviour, with a maximum adsorption value of carbon dioxide up to P_{max} = 15 bar and an uptake that increases decreasing temperature.

In particular, CO_2 adsorption isotherms show a maximum uptake value around 21 wt% at low temperature (~7 °C) that go down to 18 wt% at high temperature (~42 °C) passing through room temperature (~25 °C) where it reached almost 19 wt% (see Fig. 7), but in no case the adsorption isotherms reach a plateau value. It is interesting to note that 76% of the maximum measured storage capacity of the composite is obtained for pressure values ≤ 2 bar.

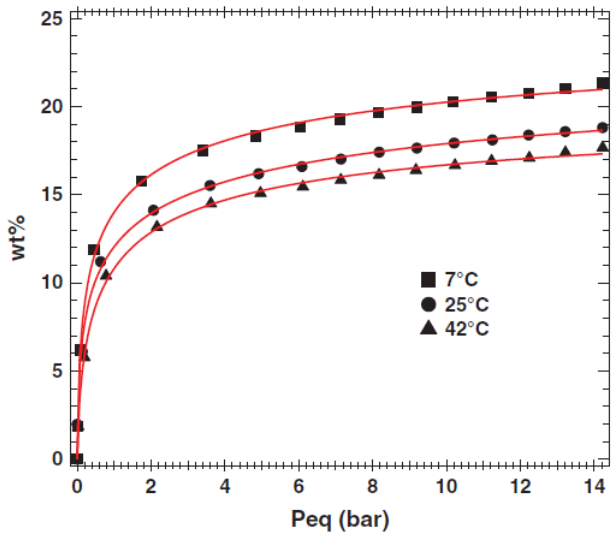

Figure 5. D90 PcT adsorption isotherms obtained with CO_2 at different temperatures up to 15 bar. Line between points is a Toth/Langmuir fitting equation. The magnitude of the error is the symbol itself.

The presence of a hysteresis (Fig. 6), and consequently the not overlapping of the adsorption and desorption isotherms, clearly indicate ta slow desorption process. The evident decrease of the maximum storage capacity for multiple cycles clearly indicate a non-totally reversible process inside the sample, at least after the first cycle (Fig. 7). In fact, the strong interaction between molecules and pristine sample surface leads to a decrease in adsorption capacity (~40%) of carbon dioxide for the cycles following the first. Variations in the isotherms trend are due to the possible passivation of adsorption sites, or occlusion of accessible volumes, by the adsorbed gas and/or bigger molecule in the incoming gas, or

poisoning and/or partially irreversibility of the adsorption process that causes the decrease in adsorption capacity.

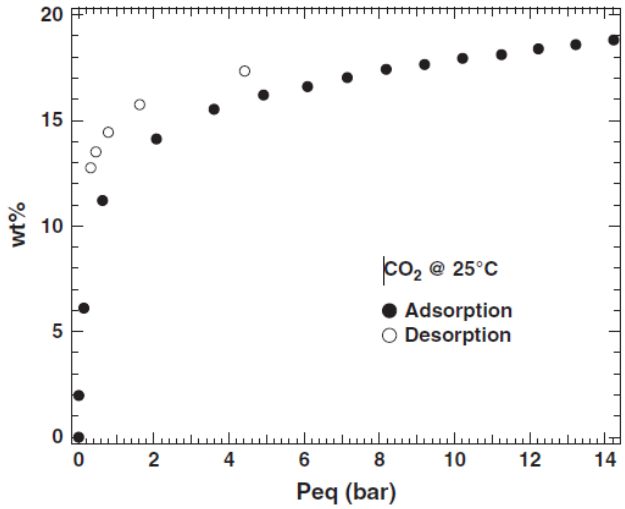

Figure 6. CO_2 PcT adsorption-desorption isotherm obtained on D90 sample at room temperature up to 15 bar. Close circle = adsorption, open circle = desorption. The magnitude of the error is the symbol itself.

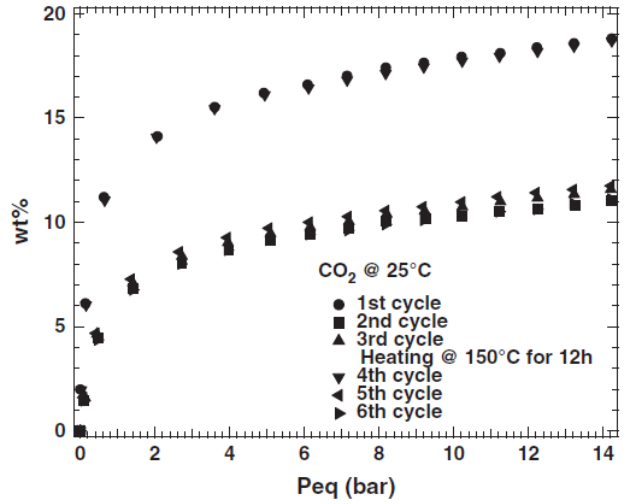

Figure 7. CO_2 adsorption isotherm cycles on D90 sample up to 15 bar at T = 298 K. The magnitude of the error is the symbol itself.

Nevertheless, at the same time, the maximum adsorption capacity of carbon dioxide by the sample can be easily restored by performing a heating treatment of the same in vacuum for about 12 hours at high temperature (150 °C). Toth analysis performed on the adsorption isotherm (Table 3), shows that the homogeneity grade of the surface is close to $t \cong 0.40$ with an interaction the between molecules and surface K that reaches a value of 19.

Table 3. Maximum CO_2 storage capacity, equilibrium constant and homogeneity grade for D90 sample obtained as Toth equation fitting parameters.

Sample	$wt\%_{max} \pm \Delta wt\%_{max}$	$K \pm \Delta K$	$t \pm \Delta t$
D90	23.93 ± 0.43	18.60 ± 2.42	0.40 ± 0.02

The extrapolated uptake value $wt\%_{max}$ = 24 highlights that at 15 bar the D90 sample it is still far enough from the adsorption plateau. It is important to remember that the theoretical limit for a completely smooth surface is t = 1. Normally we find values, for t, of about 0.4-0.5 for non-crystalline samples.

The CO_2 adsorption capacity of NaX commercial zeolite (13X_C), that is characterized by a skeletal density of 2.47 ± 0.13 g/cc, was used as reference. In Figure 8, adsorption isotherms up to 15 bar at room temperature is reported. As it is clear, the maximum adsorption uptake of carbon dioxide (CO_2) inside the sample at the higher analyzed pressure (P_{max} = 15 bar) reaches ≅ 30 wt%. The slope of the isotherm can be related to the different interaction between the gas molecules and the surface, as confirmed by Toth fit parameters.

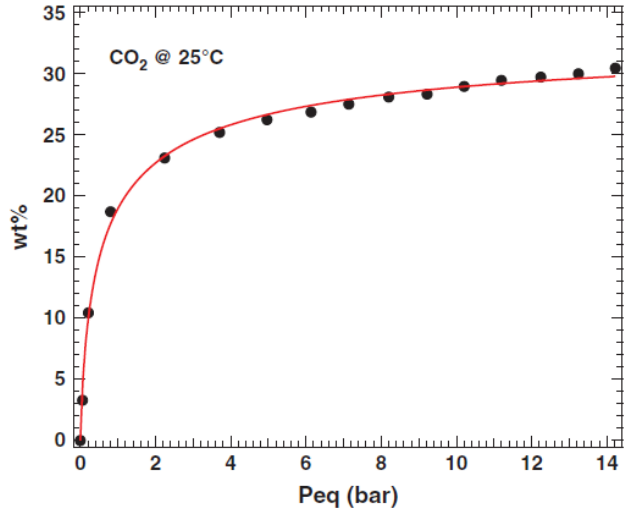

Figure 8. PcT adsorption isotherm obtained with CO_2 on 13X_C sample at $T \cong 296$ K up to 15 bar. Line between points is a Toth/Langmuir fitting equation. The magnitude of the error is the symbol itself.

From Toth analysis (see Table 4) we found that the sample shows a homogeneity grade of the surface equal to t = 0.62, with a maximum asymptotic uptake $wt\%_{max} \cong 34$, a little bit higher compared with that measured at 15 bar. The K value, related to the energetic interaction between the adsorbent and the adsorbate, as expected, is quite high confirming the ability of efficiently attracting the CO_2 molecules.

Table 4. Maximum CO_2 storage capacity, equilibrium constant and homogeneity grade for 13X_C sample obtained as Toth equation fitting parameters.

Sample	$wt\%_{max} \pm \Delta wt\%_{max}$	$K \pm \Delta K$	$t \pm \Delta t$
13X_C	33.94 ± 1.25	3.89 ± 0.80	0.62 ± 0.06

Figure 9 shows a single CO_2 adsorption-desorption process at room temperature condition. It is evident a slight hysteresis in the desorption curve (open circle) that do not perfectly overlap with the adsorption one (full circle) indicating a slow desorption process.

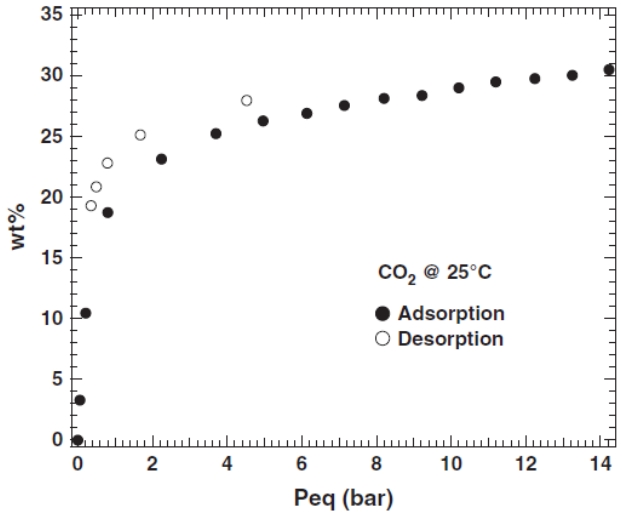

Figure 9. CO_2 PcT adsorption–desorption isotherm obtained on 13X_C sample at room temperature up to 15 bar. Close circle = adsorption, open circle = desorption. The magnitude of the error is the symbol itself.

Also, for NaX commercial zeolite, a decrease in the adsorption capacity of carbon dioxide for the cycles following the first is measured, from a value of 30 wt% down to 20 wt% (Fig. 10).

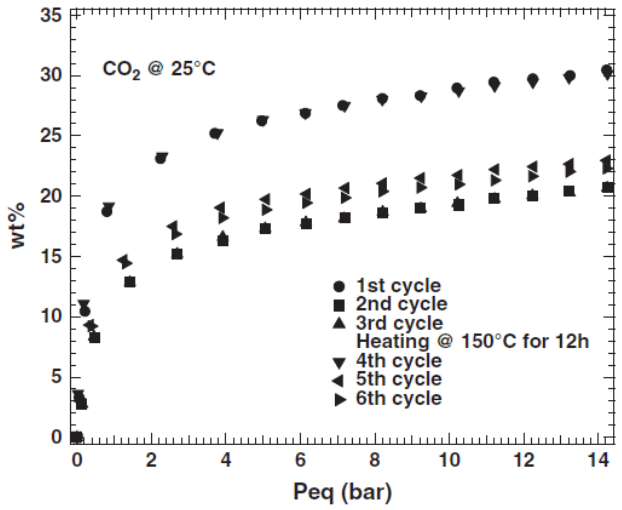

Figure 10. CO_2 adsorption isotherm cycles on 13X_C sample up to 15 bar at T ≅ 296 K. The magnitude of the error is the symbol itself.

This behavior changes for the subsequent cycles where, within the experimental error, we observe an overlapping of the different isotherms representative of the ability of the commercial NaX zeolite sample to adsorb and desorb CO_2 molecule almost reversibly without modifying its adsorption properties. The slight changes between all isotherms

following the first is related to variation of the room temperature during the single measurement. This leads to an apparent difference in the maximum uptake value.

The maximum adsorption capacity can be easily restored by performing a heating treatment of the same in vacuum for about 12 hours at high temperature (150 °C) as clearly visible in Figure 10. The first three isotherms have been acquired subsequently while the fourth has been preceded by heating at 150 °C overnight.

CO_2 adsorption isotherms comparison of NaX commercial zeolite (13X_C) and NaX/geopolymer monolith (D90) are reported in Figure 11 at room temperature condition and up to 15 bar. The two materials show a similar adsorption behavior. Furthermore, it can be easily observed that the curvature of the adsorption isotherms are different indicating, together with the relative K value, the different speed of saturation of the adsorption sites.

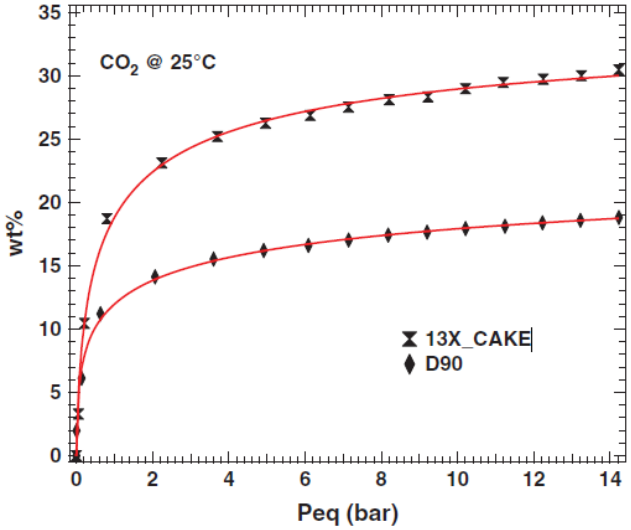

Figure 11. Comparison of CO_2 PcT isotherms obtained on 13X_C and D90 samples at room temperature (~298 K) up to 15 bar. The magnitude of the error is the symbol itself. Line between points is a Toth/Langmuir fitting equation.

The D90 sample shows a greater slope of the isotherm, also confirmed by the higher value of K compared with commercial zeolite, thus exhibiting a quicker saturation. It is a key factor for efficient CO_2 adsorption process under the operating conditions, as important as adsorption equilibria, because it affects the cycle time and the quantity of adsorbent to be used [16,47]. The behaviour can be attributed to both the presence of mesoporosity in the monolith that provides an easier and faster transport of CO_2 and the higher intracrystalline diffusion rates and external surface area due to the NaX nanocrystals [48].

Data analysis also shows that commercial pure NaX zeolite has a higher maximum storage capacity point and a t value (0.62 ± 0.06) 50% higher than D90. The monolith is, indeed, a composite consisting of a microporous phase, NaX zeolite, and the geopolymer. The latter is not only responsible of the mesoporosity and mechanical properties of the monolith, but

being an amorphous three-dimensional alumina-silicate binder, determines an increase in the heterogeneity of the surface and exhibits only moderate CO_2 adsorption capacity [49]. Furthermore, the higher decreasing in CO_2 capacity in D90 sample with respect to reference pure zeolite, after the first adsorption cycle, indicates a stronger interaction between CO_2 molecules and adsorption sites for the former adsorbents.

3.6.5 Conclusions

A NaX-geopolymer porous nanocomposite, produced using one-pot hydrothermal synthesis and starting from metakaolin and a sodium silicate solution, was tested as adsorbent for carbon dioxide. The adopted mix design and process parameters have allowed to obtain a hierarchical porosity, as measured using Mercury Intrusion Porosimetry and N_2 adsorption/desorption analyses, still preserving good mechanical properties. In particular, the monolith showed a BET surface area of around 350 m^2/g, a micropore surface area of 280 m^2/g and a mesopore volume, due to the geopolymeric binder, of 0.09 cm^3/g. Microstructure of the monolith, as obtained by SEM analysis, can be described as network of zeolite nanocrystals embedded in the porous geopolymer matrix.

The CO_2 adsorption/desorption measurements have been carried out at three different temperatures and multiple CO_2 adsorption/desorption cycles have been performed to test reliability of the samples.

As expected, the monolith shows a temperature dependence behaviour, with an uptake that increases decreasing temperature and a maximum uptake value around 21 wt% at low temperature (~280 K). The presence of a hysteresis and non-totally reversible process after the first cycle indicate a strong interaction between the gas molecules and the surface, as confirmed by Toth fit parameters. The maximum adsorption capacity can be, however, easily restored by performing a heating treatment. This is observed for both D90 and commercial NaX zeolite samples.

Furthermore, D90 shows a lower a t value, that is consistent with the presence of a heterogeneous surface produced by the concurrent presence of the crystalline phase (NaX nanocrystals) and the amorphous phase (geopolymer). Interestingly, monolith shows a higher value of K compared with commercial zeolite, thus exhibiting a quicker saturation that is a crucial factor for efficient CO_2 adsorption process. It is due to its hierarchical porosity.

In conclusion, the produced nanocomposite, that can be easily synthesized with suitable shapes, is a potential candidate for industrial CO_2 capture applications.

References

1. I. Ganesh, Renew Sust. Energ. Rev. 31, 221 (2013).

2. M. Younas, M. Sohail, L. K. Leong, M. JK Bashir, and S. Sumathi, Int. J. Environ. Sci. Technol. 13, 1839 (2016).

3. P. Frontera, A. Macario, S. Candamano, M. Barberio, F. Crea, and P. L. Antonucci, Chemical Engineering Transactions 60, 229 (2017).

4. P. Frontera, A. Macario, A. Malara, V. Modafferi, M. C. Mascolo, S. Candamano, F. Crea, and P. Antonucci, Functional Materials Letters 11, 1 (2018).

5. A. Kaithwas, M. Prasad, A. Kulshreshtha, and J. Verma, ChemEng. Res. 90, 1632 (2012).

6. C. Stewart and M. Hessami, Energ. Convers. Manage 46, 403 (2005).

7. M. Kwiatkowski, A. Policicchio, M. Seredych, and T. J. Bandosz, Carbon 98, 250 (2016).

8. A. Policicchio, D. Vuono, T. Rugiero, P. De Luca, and J. B. Nagy, Journal of CO2 Utilization 10, 30 (2015).

9. A. Policicchio, A. Meduri, C. Simari, V. Lazzaroli, S. Stelitano, R. G. Agostino, and I. Nicotera, Journal of CO2 Utilization 19, 185 (2017).

10. W. Dong, X. Chen, Y. Wu, C. Zhao, and C. L. Liu, Energy Fuel 26, 6040 (2012).

11. J. Y. Jung, F. Karadas, S. Zulfiqar, E. Deniz, S. Aparicio, M. Atilhan, C. T. Yavuz, and S. M. H., Phys. Chem. Chern. Phys. 15, 14319 (2013).

12. J. Merel, M. Clausse, and F. Meunier, Environ. Prog. 25, 327 (2006).

13. E. David and J. Kopac, J. Anal. Appl. Pyrol. 110, 322 (2014).

14. J. M. Andres, L. Orjales, A. Narros, M. M. Fuente, and M. E. Rodriguez, J. Air Waste Manage 63, 557 (2013).

15. C. H. Yu, C. H. Huang, and C. S. Tan, Aerosol Air Qual. Res. 12, 745 (2012).

16. A. Samanta, A. Zhao, G. K. H. Shimizu, P. Sarkar, and R. Gupta, Ind. Eng. Chem. Res. 51, 1438 (2011).

17. W. Dong, X. Chen, Y. Wu, C. Zhao, and C. L. Liu, Energy Fuel 26, 6040 (2012).

18. D. L. Chen, H. Shang, W. Zhu, and R. Krishna, Chem. Eng. Sci. 124, 109 (2015).

19. L. Arnold, G. Averlant, S. Marx, M. Weickert, U. Muller, J. Mertel, C. Horch, M. Peksa, and F. Stallmach, Chem. Ing. Tech. 85, 1726 (2013).

20. M. Y. Masoomi, K. C. Stylianou, A. Morsali, P. Retailleau, and D. Maspoch, Cryst. Growth Des. 14, 2092 (2014).

21. K. S. Walton, M. B. Abney, and M. D. Levan, Microporous Mesoporous Mater. 91, 78 (2006).

22. S. Cavenati, C. A. Grande, and A. E. Rodrigues, J. Chem. Eng. Data 49, 1095 (2004).

23. V. Sebastian, I. Kumakiri, R. Bredesen, and M. Menendez, J. Membr. Sci. 292, 92 (2007).

24. J. Merel, M. Clausse, and F. Meunier, Ind. Eng. Chem. Res. 47, 209 (2008).

25. F. Gholipour and M. Mofarahi, J. Supercritical Fluids 111, 47 (2016).

26. T. F. Mastropietro, E. Drioli, S. Candamano, and T. Poerio, Microporous Mesoporous Mater. 228, 141 (2016).

27. P. Frontera, S. Candamano, A. Macario, F. Crea, L. A. Scarpino, and P. L. Antonucci, Mater. Lett. 104, 72 (2013).

28. S. Candamano, P. Frontera, F. Crea, and R. Aiello, Topics in Catalysis 30–31, 369 (2004).

29. Z. Zhang, L. Li, D. He, X. Ma, C. Yan, and H. Wang, Mater. Lett. 178, 151 (2016).

30. J. Zhang, Y. He, Y. Wang, J. Mao, and X. Cui, Mater. Lett. 116, 167 (2014).

31. Z. Zhao, X. Cui, J. Ma, and R. Li, Int. J. Greenhouse Gas Control 1, 355 (2007).

32. M. Minellia, E. Papa, V. Medri, F. Micciob, P. Benito, F. Doghieri, and E. Landi, Chem. Eng. J. 341, 505 (2018).

33. L. Coppola, T. Bellezze, A. Belli, M. C. Bignozzi, F. Bolzoni, A. Brenna, M. Cabrini, S. Candamano, M. Cappai, D. Caputo, M. Carsana, L. Casnedi, R. Cioffi, O. Cocco, D. Coffetti, F. Colangelo, B. Coppola, V. Corinaldesi, F. Crea, E. Crotti, V. Daniele, S. De Gisi, F. Delogu, M. V. Diamanti, L. Di Maio, R. Di Mundo, L. Di Palma, J. Donnini, I. Farina, C. Ferone, P. Frontera, M. Gastaldi, C. Giosuè, L. Incarnato, B. Liguori, F. Lollini, S. Lorenzi, S. Manzi, O. Marino, M. Marroccoli, M. Mascolo, L. Mavilia, A. Mazzoli, F. Medici, P. Meloni, G. Merlonetti, A. Mobili, M. Notarnicola, M. Ormellese, T. Pastore, M. P. Pedeferri, A. Petrella, G. Pia, E. Redaelli, G. Roviello, P. Scarfato, G. Scoccia, G. Taglieri, A. Telesca, F. Tittarelli, F. Todaro, G. Vilardi, and F. Yang, Journal of Applied Biomaterials and Functional Materials 16, 186 (2018).

34. S. Candamano, P. De Luca, P. Frontera, and F. Crea, Environments 4, 74 (2017).

35. C. Lamuta, S. Candamano, F. Crea, and L. Pagnotta, Mater. Des.107, 57 (2016).

36. S. Candamano, P. Frontera, A. Macario, F. Crea, J. B. Nagy, and P. L. Antonucci, Chemical Engineering Research and Design 96, 78 (2015).

37. A. W. Burton, K. Ong, T. Rea, and I. Y. Chan, Microporous Mesoporous Mater. 117, 75 (2009).

38. M. Ansari, A. Aroujalian, A. Raisi, B. Dabir, and M. Fathizadeh, Advanced Powder Technology 25, 722 (2014).

39. J. C. Groen and J. Pérez-Ramírez, Appl. Catal. A 268, 121 (2004).

40. UNI-EN 196-1 2005.

41. A. Policicchio, E. Maccallini, G. N. Kalantzopoulos, U. Cataldi, S. Abate, G. Desiderio, and R. G. Agostino, Review of Scientific Instruments 84, 103907 (2013).

42. J. Toth, Journal Colloid Interface Science 225, 378 (2000).

43. J. S. J. van Deventer, J. L. Provis, P. Duxson, and G. C. Lukey, 139, 506 (2007).

44. G. Yao, J. Lei, X. Zhang, Z. Sun, and S. Zheng, Materials 11, 906 (2018).

45. F. Pacheco-Torgal, J. Castro-Gomes, and S. Jalali, Construction and Building Materials 22, 1305 (2008).

46. M. Thommes, K. Kaneko, A. V. Neimark, J. P. Olivier, F. Rodriguez-Reinoso, J. Rouquerol, and S. W. Kenneth Sing, (IUPAC Technical Report) Pure Appl. Chem. (2015).

47. C. H. Yu, C. H. Huang, and C. S. Tan, Aerosol. Air Qual. Res. 127, 45 (2012).

48. C. Chen and W. S. Ahn, CO2, Appl. Surf. Sci. 311, 107 (2014).

49. M. Minelli, V. Medri, E. Papa, F. Miccio, E. Landi, and F. Doghieri, Chem. Eng. Sci. 148, 267 (2016).

3.7 Assessment of poly(L-lactide) as an environmentally benign CO_2 capture and storage adsorbent

3.7.1 State of the art

From the Brundtland Report to the Kyoto Protocol, to the Paris Agreement and onward, international policies have been addressing environmental issues and their possible remedies, prompted by the scientific data linking climate changes to heat-trapping gases [1-3].

Among these gases carbon dioxide (CO_2) has a predominant role, an image clearly crystallized by the fact that its emissions represent an everyday topic in media coverage worldwide and no longer only a topic area debated in the scientific world [4, 5].

Two are the major strategies being evaluated to reduce CO_2 emissions. The first considers the substitution of oil-based sources and products with renewable ones [4]. The second considers the capture of CO_2 by means of either Carbon Capture and Storage (CCS) or Carbon Capture and Utilization (CCU) [5]. The difference between CCS and CCU lies in the final destination of the capture: the goal of CCS is the long-term storage of CO_2 in suitable sites; the goal of CCU is its reuse in the synthesis of commercial products [6, 7]. The direct utilization of CO_2 is also feasible and it is already employed in the food and drink industry (i.e. carbonating agent) and pharmaceutical industry (i.e. chemical intermediate), but it is restricted to high purity levels of CO_2 [6]. Normally, carbon utilization, as well as carbon storage, involves an intermediate step of CO_2 capture accomplished through many options, that can be classified according to: (a) the carbon footprint of the process (high, i.e. flue gas; medium, i.e. industrial processes; low, i.e. gas-fired power stations) [8]; (b) the stage of the process (pre-conversion, oxy-fuel combustion, post-conversion) [6]; (c) the adsorbent material involved in the capture, which are mainly membranes, chemical solvents (i.e. amines, ionic liquids) [9], and solid sorbents (i.e. activated carbons, metal organic frameworks, polymers) [10, 11].

Among the stage of the process, post-combustion capture (PCC), that refers to capturing CO_2 from flue gas after the fossil fuel has been burned, is of particular interest owing to its unique capability to retrofit with the traditional purification systems. The biggest challenge in PCC is separating CO_2 generated during combustion. Currently, the state-of-the-art technology for CO_2 separation is amine scrubbing [12] which however presents many different disadvantage such as high corrosion, substantial environmental footprints and energy cost of the process.

As an alternative, in recent years the R&D effort is focused on CO_2 capture by adsorption using solid materials [13, 14]. This process involves the chemical or physical adsorption of CO_2 on the surface of a porous material and the next desorption by either pressure swing, temperature swing, or their combination, with a lower energy consumption. This method shows a high adsorption capacity, easy recovery, high uptake efficiency under humid conditions, easy handling, and it is considered as energy-efficient alternative respect to other CO_2 capture processes [15]. In fact, the energy required for the adsorption and regeneration is low so the product can be recovered, and the adsorbent is reactivated for the next adsorption cycle. Nevertheless, it is still far from the application on a commercial scale since there is a lack of effective adsorbents [14]. Moreover, to optimize the adsorption-based CO_2 processes, we need to manage the presence of impurities, the integration of heat, and the design of the process systems. For example, specific features of adsorbent combined with the application in fixed bed processes [16] can bring a clear improvement in terms of efficiency compared to consolidated technologies. For these reasons, a key role is played by the adsorbent used, which must be capable of integrating high efficiency and ease of application into industrial systems. Therefore, the main challenge in the adsorption-based CO_2 capture is the design and synthesis of efficient adsorbents [17, 18], possibly produced through green processes or with renewable and economic materials.

A key concern for physical adsorbents is the optimization of the material to obtain the maximum adsorption capacity with the lowest energy consumption required for its regeneration. For this purpose, the principal properties are the selectivity and adsorption capacity, both dependent on the operating temperature and pressure, as well as the nature of the gas adsorbate and the adsorbent. Adsorption is defined as the enrichment of the surface adsorbent by one or more components, consequently it assumes that high surface areas and porosity can lead to higher adsorption capacities [19]. This trend has been widely reported in the literature for different gases and it is demonstrated a strict correlation between adsorption capacity and textural properties of adsorbates [20]. In detail, it is proved that a high adsorption at lower pressure is connected with the presence of micropores, according to micropore filling theory according which smaller micropores with an overlapping adsorption force cause volume filling adsorption, reaching saturated adsorption at the low-pressure. On the contrary, the adsorption at higher pressure is related to pore-filling mechanism in mesopores [21]. This behavior was found in several work on CO_2 adsorption, which reported that at low pressures, CO_2 is preferably adsorbed in micropores ($\leq$ 1 nm), while at higher pressure ($\geq$ 10 bar) adsorption occurs in mesopores. [17, 22-24].

Low temperature CO_2 adsorbents are one of the most intriguing class of solid sorbents, especially if combined with CCU strategy that does not require high pressure, leading to economic and energetic advantages [25]. In selecting a low temperature CO_2 adsorbent, parameters such as selectivity, regeneration energy and economicity play a crucial role [6]. A variety of solid physical adsorbents have been considered for CO_2 capture including microporous and mesoporous materials (MOFs, zeolites, silicas and carbon-based sorbents such as activated carbon and carbon molecular sieves), metal oxides, and hydrotalcitelike compounds, amongst others [26]. They must be cost-effective and regenerative, less sensitive to steam and offer high greater capacities and selectivities for CO_2, in order to compete with liquid amines. MOFs have unique structures, high CO_2 adsorption capacity and good selectivity, but the chemical and thermal stability limits their application in high temperature or complex environments [27]. Pure silica materials show a slight CO_2 uptake. Zeolites are synthetic products with microporous features, a highly crystalline structure and excellent thermal stability, but their adsorption capacities are always low because the surface chemistry of zeolites for binding CO_2 is less developed [28]. Porous carbons are promising for a practical application to CO_2 capture in the industry thanks to their good structural stability, recyclability and simple manufacturing process, but have less selectivity [29]. Among carbon-based materials, activated carbons (ACs) derived from biomass have become increasingly attractive due to their stability, variable porosity and eco-friendly nature. In the last year, ACs were prepared starting from natural, organic, sea and agricultural wastes, such as seaweed [30], pop-corn [31], wood [32], pine-cone [33] and others [34, 35], showing high specific surface areas (SSAs), micro-porosity and good CO_2 storage capacity. However, ACs preparation process requires chemical activating agents to enhance their porosity, a washing step to get rid of the unreacted residual chemicals and a thermal treatment to high temperatures. Besides, they are hydrophobic, which limits their applications.

Among the polymers, in literature are cited the organic compounds derived from amines (PEI) [36, 37] and more recently Porous organic polymers (POPs) [38] recognized promising materials for the capture of CO_2 due to their low density, high thermal and chemical stability, large surface area, size and structure of the tunable pores [39]. In particular, Porous coordination polymers (PCPs), are an emerging class of crystalline porous materials with wide applications, including gas adsorption and storage. This new type of polymers makes available acidic or basic active sites endowed by facile tunability and modular nature, as well as ultra-high surface area and heterogeneous nature. They show a flexible electronic and spatial structure but lower thermal stability than rigid structures in a single network; however, this problem can be overcome by interpenetration [40].

Therefore, these are complex crystalline structures with adaptable properties for the capture of CO_2 but still at an early stage of development [40]. These types of polymers (PEI, POPs, PCPs) often follow chemical functionalization procedures for their production and to obtain optimal and efficient structural features. Therefore, we are looking for adsorbents that are easy to synthesize, with low-cost and eco-sustainable materials. Among them, only a few works deal with the CO_2 adsorption on this kind of polymers and in particular on the Poly(L-lactide) (PLA). The latter is a valid candidate for both strategies to reduce CO_2 emissions. First, it is a renewable polyester, obtained from corn and commercially available (already applied in a wide range of fields, not only in temporary but also in more durable applications, from pharmaceutical to biomedical, from packaging to electronics field) which represents one of the most promising eco-friendly alternatives to Petro based plastics [41, 42]. Secondly, the study of literature data points to PLA as a possible CO_2 adsorbent, due to its CO_2-philicity [43-48]. Consequently, there is a lot of interest in deepening the interactions between CO_2 and PLA, and the modifications that such molecule gas could induce in the polymer. Up to now, the related literature is mainly focused on the effects of supercritical CO_2 on the PLA properties and so there is not enough available information related to the effects of CO_2 at conditions lower than its supercritical point [49]. Properties of PLA depend on its component isomers, processing temperature, annealing time and molecular weight (*Mw*) [50]. In particular, the PLA lactides are formed by the condensation of two molecules of lactic acid, so three types of lactides can be obtained: *dd*-lactide, *ld*-lactide (PDLA) and *ll*-lactide (PLLA). The *l:d* ratio of the monomers has large impact on the material properties through its effect on transition temperature and crystallization, which increases with the increase in the percentage of *l*-lactic.

The stereochemistry and thermal history have direct influence on PLA crystallinity, and therefore, on its properties in general. PLA crystals can grow in 5 structures named α, α', β, γ and *Sc* forms. They are characterized by different helix conformations and cell symmetries, which develop upon different thermal and/or mechanical treatments [51]. The α form, formed at crystallization temperatures above 393 K , has a 10^3 helices packed in an orthorhombic unit cell, while α'-form, formed at crystallization temperatures below 373 K, has similar 10^3 helical conformation and crystal system as those of the α-form, but with a looser lateral chain packing. The β form develops upon mechanical stretching of the more stable α form, and the γ form was obtained by epitaxial crystallization of PLA on hexamethylbenzene. Besides the homocrystallization of PLLA or PDLA, the two types of enantiomeric chains can co-crystallize together into a new structure, termed as "stereocomplex". Consequently, the crystallinity influences many polymer properties including hardness, modulus, tensile strength, stiffness, crease and melting points [51].

At this regard, several authors, using a quartz crystal microbalance, studied the influence of the thermal history of a polymer film in the gas sorption and concluded that the polymer film thermal history only has significant impact in gas sorption for pressures higher than 2MPa [52-54].

At the same time, Smith et al. [49] studied the sorption and the diffusion properties of CO_2 at high pressure and the changes induced by physisoprtion on the PLA films. They proved a good CO_2 adsorption capacity of PLA film with a small hysteresis cycle and the modification inducted by CO_2 pressure on the PLA film. In particular, they reported on none chemical changes but on a broadening of PLA chains caused by CO_2 physisorption at high pressure.

In all cases, the studies carried out have been performed on PLA films, while no studies have been carried out to evaluate the properties of adsorption and diffusion of CO_2 of the PLA as its morphology changes.

The aim of this work is to fill this literature lack with a deeper investigation of PLA adsorption properties and their relationship with structural/morphological properties. In particular, the present paper reports the results of research activity focused on: gaseous CO_2, low pressure (0-15 bar), low operative temperature (303 K), mild preparation/regenerative energy (303 K and 333 K), morphology (powder, flakes and pellets).

3.7.2 Materials and Methods

3.7.2.1 General information

Poly(L-lactide) (Mw = 50,000 Da, pellets) was purchased from Galatea Biotech Srl. All solvents were purchased from Sigma-Aldrich. Helium (99.999% purity), nitrogen (99.998% purity) and carbon dioxide (99.998% purity) used for adsorption/desorption tests were purchased from Pirossigeno snc.

3.7.2.2 Preparation of PLA samples

Poly(L-lactide) (PLA) is a commercial polymer supplied mainly as pellets. In order to obtain and evaluate a morphology that is most suitable for CO_2 adsorption, other two typologies of PLA samples were prepared for a total of three morphologies: pellets, powder and “flakes” (**Errore. L'origine riferimento non è stata trovata.**).

Table 1. Specific parameters distinguishing the three PLA samples investigated for CO_2 adsorption.

Sample	Morphology	Preparation	Mass (g)	Skeletal density (g/cm^3)
cPLA	pellets	as received	0.62	1.23
			0.52	1.20
pPLA	powder	xylenes recrystallization	0.16	1.27
			0.17	1.23
fPLA	flakes	DCM/EtOH precipitation	0.08	1.46
			0.07	1.48

Commercial poly(L-lactide) pellets (cPLA) were used as received (

Figure ***2***).

Poly(L-lactide) powder (pPLA) was obtained by recrystallization of commercial pellets from a xylenes solution. In detail, the cPLA is dissolved in the minimum volume of hot (> 413 K) solvent to form a saturated solution for 2h, then the solution was allowed to cool and the resulting crystals were washed with n-pentane to get rid of the xylenes solutions, collected by filtration and dried in vacuo (

Figure ***2***).

Poly(L-lactide) flakes (fPLA) were obtained following a procedure based on a methodology developed by Cao et al. [55]. Commercial pellets (50 g) were dissolved in dichloromethane (DCM, 30 mL) and were precipitated it again as flakes by addition of ethanol (EtOH) drops while stirring. After the precipitation was complete, the flakes were dried in vacuum (

Figure ***2***).

Figure 2. Poly(L-lactide) samples.

3.7.3 Characterization of the PLA samples

Scanning electron images were recorded using a Quanta FEG 400 (FEI) scanning electron microscope (SEM). All images were acquired by using an electron beam in the energetic range 5÷15 keV providing the typical morphology of the samples deposited on carbon tape. X-Ray Diffraction (XRD) data were collected on a Philips PW 1830 diffractometer using Cu Ka (40 kV, 40 mA) filtered radiation. The measurements were obtained in reflection mode placing the sample powder/fibers on the special homemade sample holder. All measurements have been done at room temperature (RT) and the patterns were recorded in the 2-theta (2θ) range from 2° to 45°, in steps of 0.02° and counting time 1 s per step. The effect related to the sample stage has been considered.

Textural properties of the PLA samples were carried out by physical adsorption of N_2 at 77 K using a Micromeritics ASAP 2460 apparatus, manufactured by Micromeritics Instrument Corp. (USA). Before each adsorption measurements, each sample was dried overnight under vacuum ($P < 0.01$ mbar) at 333 K. The specific surface area (SSA) was calculated according to the Brunauer-Emmett-Teller (BET) method [56] within relative pressure range of 0.05÷0.3. The total pore volume V_{tot} was calculated from the N_2 uptake at relative pressure $P/P_0 = 0.995$ and the pore size distributions (PSD) was calculated by Density Functional Theory (DFT) considering cylinder-shaped pores [57-59].

The CO_2 adsorption/desorption measurements were performed at room temperature (~303 K) and in the pressure range 0÷15 bar, using an optimized Sievert type volumetric apparatus f-PcT for accurate and reliable gas adsorption measurements [60]. Before the CO_2 adsorption/desorption experiments, helium (He) pycnometry analysis [60, 61] was performed on each sample to evaluate skeletal density. Reliability of PLA samples performance in terms of cyclic life was tested by subjecting all samples to multiple CO_2 adsorption/desorption cycles.

3.7.4 Results and Discussion

3.7.4.1 SEM characterization

Samples cPLA, pPLA and fPLA were characterized by SEM in order to evaluate the morphological difference of the prepared samples (Figure 3).

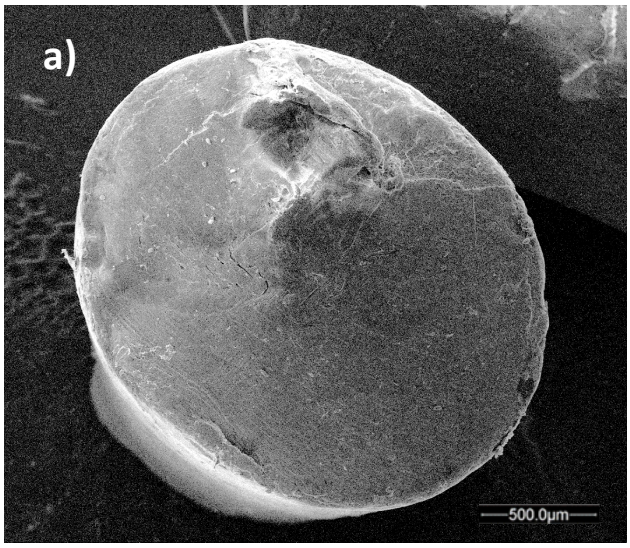
a)
500.0µm

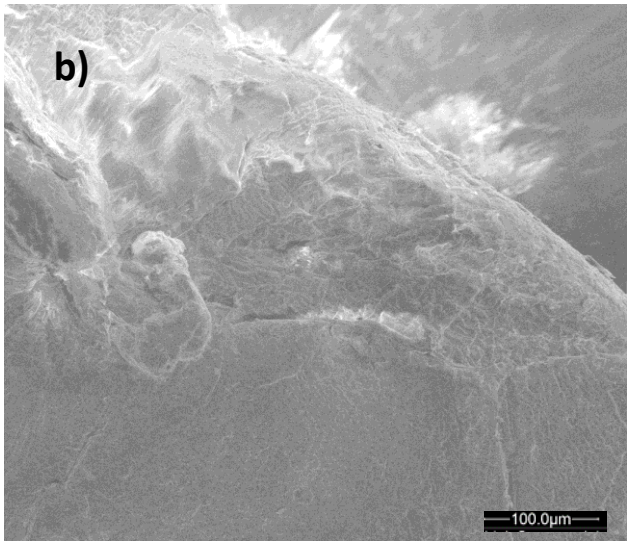
b)
100.0µm

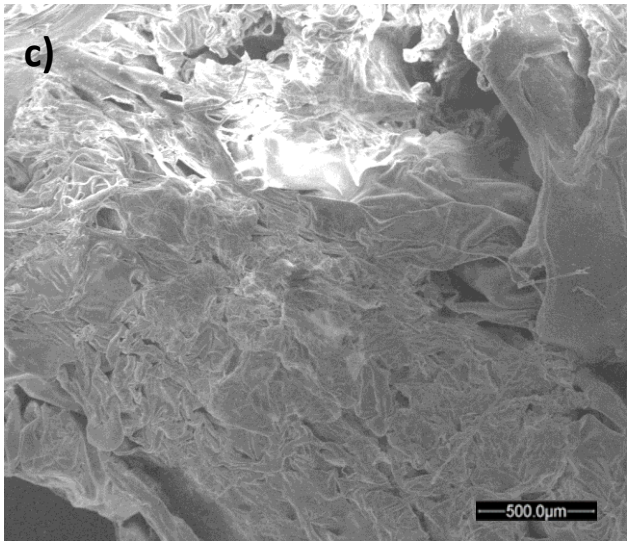
c)
500.0µm

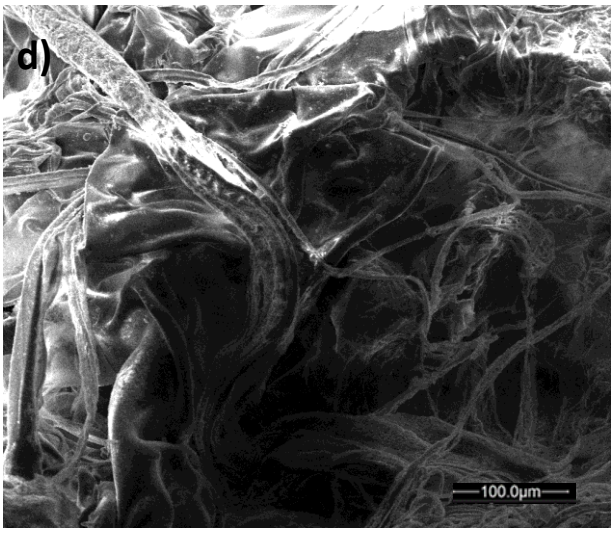
d)
100.0µm

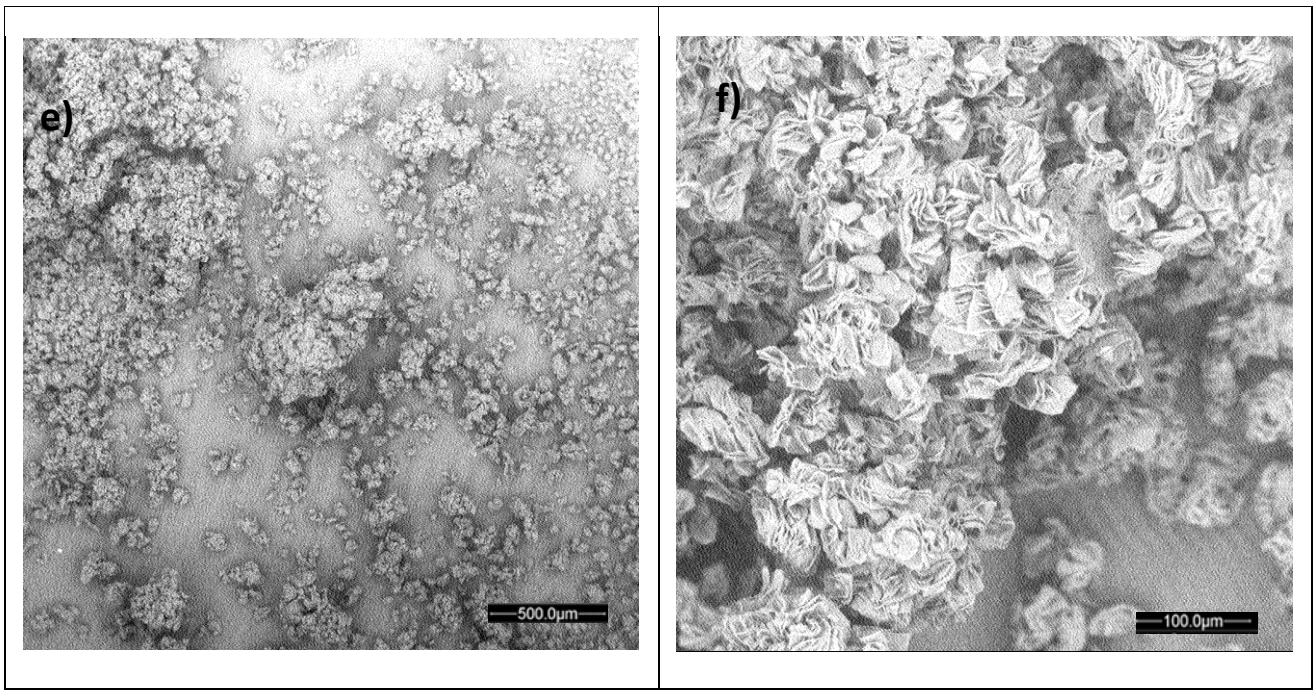

Figure 3. SEM images with different magnification of: (a, b) **cPLA**; (c, d) **fPLA**; (e, f) **pPLA**.

An analysis of the acquired SEM images gives an excellent overview of the range of mesostructures present in each sample and allow a clear distinction among the morphologies of the different samples. In Figure 3a and 2b, the SEM image of *cPLA*, it is possible to see the uniform, compact surface of the commercial pellet on the microscale, with few fracture patterns. In Figure 3c and 2d, the *fPLA* sample clearly shows a disordered complex 3D structure made out of interwaving ribbons and filaments.

The typical transverse dimension of these elongated structures is ranging from few microns to hundreds of microns while their length is on the millimeter scale. On the contrary, looking at the *pPLA* in Figure 3e and 2f, it is interesting to appreciate how the xylenes-induced recrystallization has brought a dramatic change in the shown structure: we do not find any elongated ribbon but more fragmented grains with several slit-like crevices. The microscale 3D network shows granular aggregates differing in shape and diameter (up to 10 µm ca.).

3.7.4.2 XRD characterization

The results of XRD analysis (Figure 4) show that all samples exhibit a semi-crystalline nature as reported by Almeida et al. [62] on commercial PLLA. No signatures of new crystalline phases are present for the fPLA and cPLA.

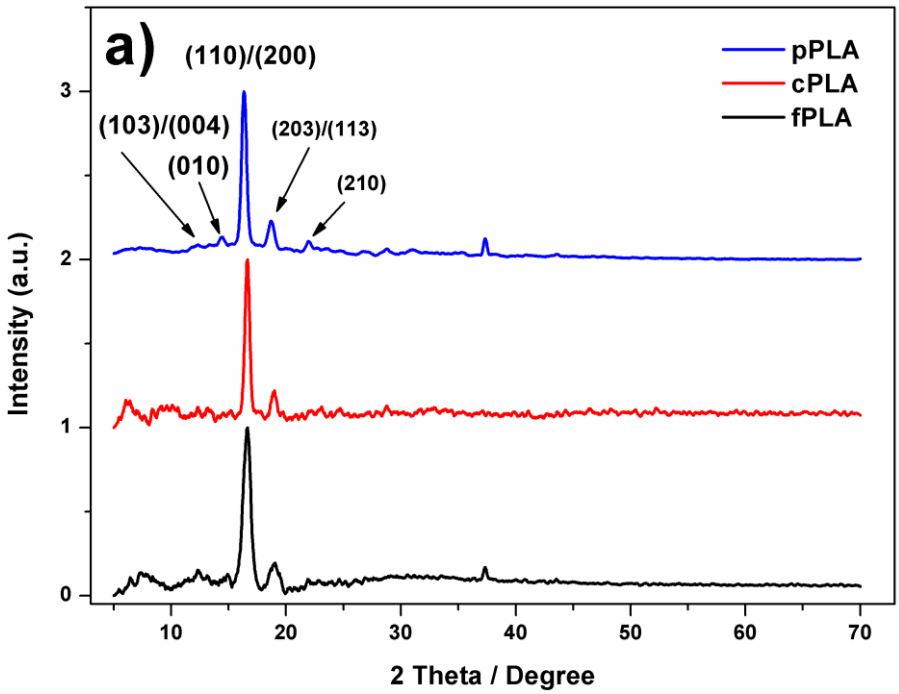

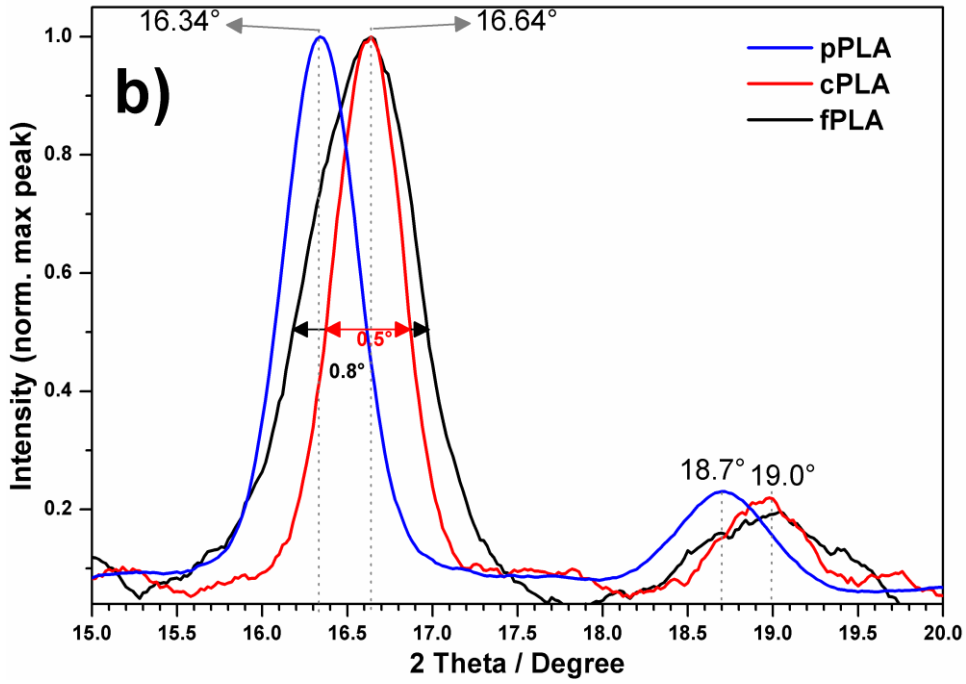

Figure 4. X-ray diffraction patterns of cPLA, pPLA and fPLA samples. 2θ region of: (a) 5÷40°; (b) 15÷20°.

In the diffractograms of **Figure 4**Figure 4a two main peaks appear at 16.64° and 19.0° corresponding to the reflections from the (110) and/or (200) planes and (203) planes, respectively [63]. The average distance between crystalline planes, as estimated from the

most prominent peak of the diffractogram by the use of the Bragg equation, is 5.34 Å and the 4.67 Å, respectively (see Table 2).

The only exception is represented by the pPLA sample, whose diffractogram shows slightly shifted values for these peaks (Figure 4b). The shift toward lower angles (16.34° and 18.7°) is reflected in a slightly higher distance between (110)/(200) and (203) crystalline planes (5.42 Å and 4.74 Å, respectively). Besides, the pPLA spectrum shows two less intense peaks at 14.5° and 22°, respectively, which can be associated with (010) and (210) planes. So, the most intense peaks of cPLA and fPLA can be indexed to the disordered pseudoorthorhombic α' structure, while the pPLA diffractogram can be ascribed to pseudoorthorhombic α structure with left-handed 10/3 helices chain conformation. This difference is probably due to the sample preparation method (xylene recrystallization), which involves heating the sample to a temperature higher than 413 K producing what is referred to as "α'- α crystal transition" [63, 64].

An analysis of the full width at half maximum (FWHM) data (see Table 2) points out a higher value for the flake morphology (0.8°) with respect to the others (0.5°). By means of the Scherrer equation [65], we find that the average crystalline grain dimension for the flakes sample is as low as 100 Å, more than a third lower with regard to the commercial and powder samples (161 Å in both cases).

Table 2. X-ray diffraction characterization data.

Sample	**2θ (°)**	**d (Å)[a]**	**2θ (°)**	**d (Å)[a]**	**FWHM (°)[b]**	**grain size (Å)[c]**
cPLA	16.64	5.34	19.0	4.67	0.5	161
pPLA	16.34	5.42	18.7	4.74	0.5	161
fPLA	16.64	5.34	19.0	4.67	0.8	100

[a]*Distance between crystalline planes;*
[b]*Full width at half maximum of the 2θ peak at 16.64°;*
[c]*Average dimensions of the crystalline grain, calculated according to the Scherrer equation [65].*

3.7.4.3 Porosimetry characterization

To link morphological properties to the structural ones, cPLA, pPLA and fPLA samples were analyzed by porosimetry via physical adsorption of N_2 at 77 K. Adsorption isotherms (Figure 5) were obtained by measuring the amount of N_2 adsorbed across a wide range of

relative pressures at a constant temperature.

The isotherm curve of commercial sample cPLA (Figure 5- blue line) shows negligible adsorption in all the range of pressure investigated. On the other hand, the nitrogen gas sorption isotherms for the pPLA (Figure 5- red curve) and fPLA (Figure 5- black curve) samples have a similar trend, that is of type II according to the IUPAC classification [66]. In the 0-900 mbar pressure range, the pPLA and fPLA isotherms show a continuous increase by increasing the pressure, which usually indicates an adsorption on the outer surface structures. For relative pressure above 900 mbar, a rapid increase in the nitrogen adsorption is observed by increasing the pressure. This data, together with the H3 hysteresis loops in the P/P_0 range 600 – 1000 mbar may indicate in part a capillary condensation taking place in mesopores. The fPLA sample shows a wider hysteresis cycle indicating the presence of pores with different shape and dimension and therefore of an uneven morphology. This agrees with the XRD analysis which identifies for this sample a more disordered form and with SEM images showing a non-uniform morphology.

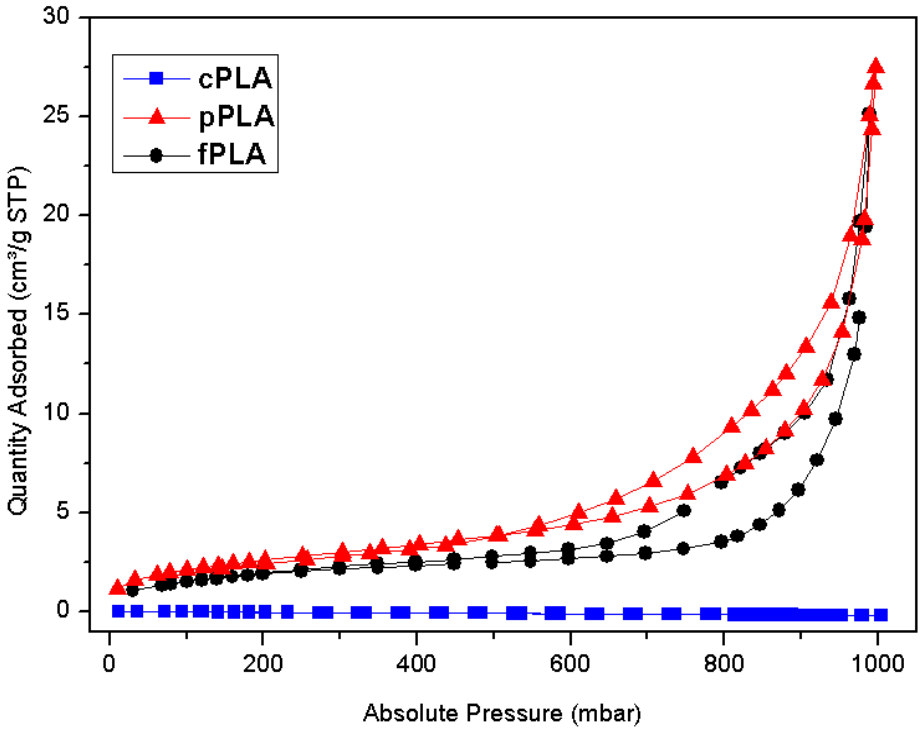

Figure 5. N_2 adsorption–desorption isotherms at 77 K.

The analysis of N_2 adsorption isotherm allowed to quantify the textural parameters of all sample as reported in Table 3.

Table 3. N_2 adsorption/desorption isotherms data for PLA samples.

Sample	S_{BET} (m^2/g) [a]	V_T (cm^3/g) [b]
cPLA	-	-
pPLA	9.7	0.040
fPLA	7.2	0.030

[a] *S_{BET}: specific surface area computed using BET equation in the relative pressure range of 0.05–0.3.*
[b] *V_T: total pore volume estimated at a relative pressure P/P_0 = 0.99.*

As a result of the adsorption measurement, the sample cPLA shows no appreciable SSA, while the other two samples (pPLA and fPLA) have a low surface value (9.7 and 7.2 m^2/g, respectively) compatible with that reported in literature for poly(L-lactide) with different morphologies [67]. The pore size distribution for pPLA and fPLA were calculated by using the density functional theory (DFT) with slit-shape pores (Figure 6).

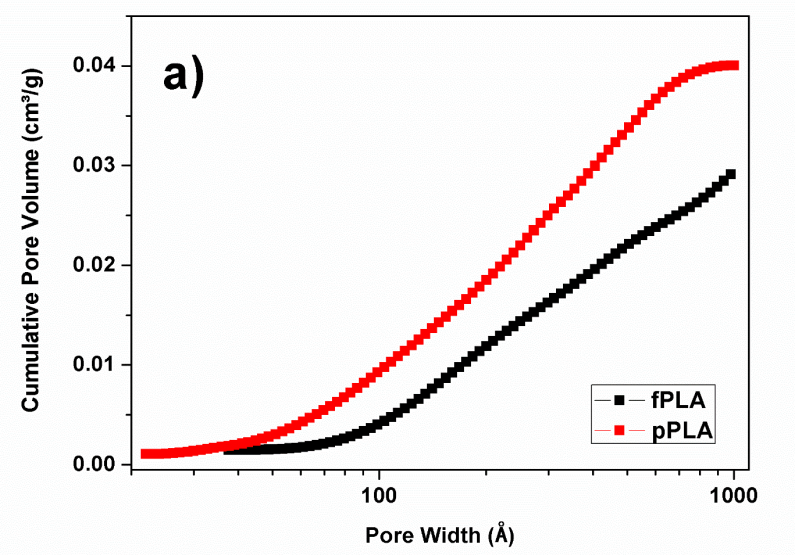

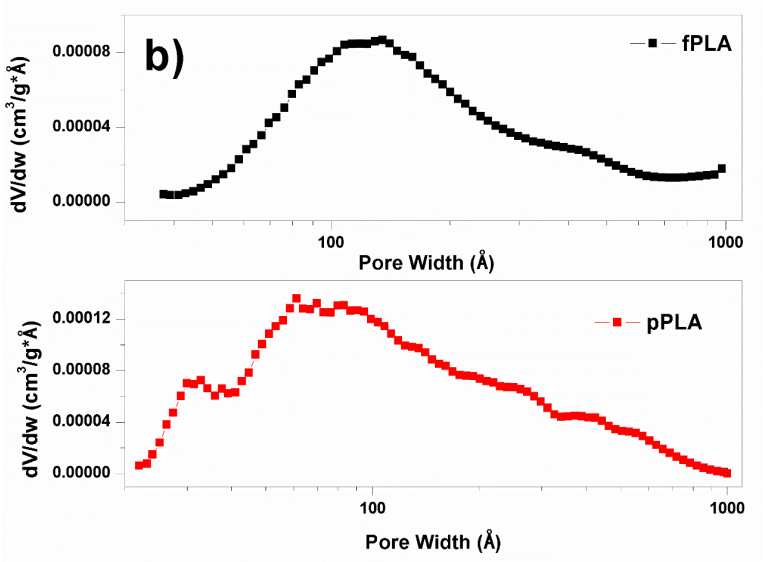

Figure 6. Pore size distribution: (a) cumulative pore volume; (b) pore distribution.

The analysis of cumulative volume (Figure 6a) clearly indicates that both samples are mainly characterized by mesopores up to 500 Å that occupy 80% of the total pore volume for both fPLA and pPLA samples i.e. of 0.022 over 0.030 and 0.034 over 0.040 cm^3/g, respectively.

By comparing the cumulative volume curves, it is possible to see a similar trend, but different maximum values. More in detail, the PSD charts (Figure 6b) shows a band which start in the low region of the mesoporosity, centered around 100 Å, and extend throughout the mesoporous region. The porosity is therefore homogenous and concentrated in the meso and macro pore region.

3.7.4.4 CO_2 adsorption/desorption measurements

The CO_2 adsorption/desorption properties of the PLA samples, carried out at 303 K and in the pressure range 0÷15 bar, were investigated in two different pre-treatment conditions. In particular, we evaluated the differences between samples outgassed overnight in vacuum at 303 K (Figure 7) and 333 K (Figure 8). For each temperature, the samples were subjected to multiple cycles, with and without thermal treatment in between (Figure S5 and S6).

Each cycle consists of adsorption-desorption step which provides information on the interactions between the adsorbate and the polymer. In fact, a reduction of the adsorption capacity could be expected between the first and second adsorption cycle, but if this persists after the thermal treatment, it is indicative of a strong interaction between adsorbent and

adsorbate with consequent chemical modification, otherwise it indicates that only low energy interactions or physical changes occurred during adsorption.

Besides, the presence adsorption-desorption cycle of a hysteresis loop between adsorption/desorption isotherms is indicative of a modification of the polymer. Thus, to obtain more information on the interaction between PLA and CO_2, the sorption isotherm was determined involving two adsorption/desorption cycles before thermal treatment and one more cycle after it (Figure 7). All adsorption isotherms reported in Figure 6 and 7, do not show any adsorption at low pressure, but it increases at around 10 bar. This can be ascribed, according to literature [17, 22-24], to presence of mesoporous structure.

Looking at the CO_2 isotherms curves for the samples treated at 303 K (Figure 7) it is easy to note that for all the analyzed samples the CO_2 maximum adsorption capacity increases almost linearly by increasing the gas pressure. Comparing the maximum storage value at 15 bar of the first cycle (Table 4 and Figure S1a), the fPLA sample shows a maximum adsorption value of 7.8 wt%, far higher than values recorded for both cPLA and pPLA (2.0 wt% and 3.8 wt%, respectively).

The sorbed quantity was rather high than the values reported in the literature for PLA films under similar pressure and temperature conditions [45, 47, 52]. In the same conditions (15 bar and RT), Rocca-Smith et al. [49] reported, in fact, an adsorbed quantity of CO_2 equal to 4%, which is similar to the adsorption capacity of cPLA and pPLA, while it is half of that recorded for the fPLA sample.

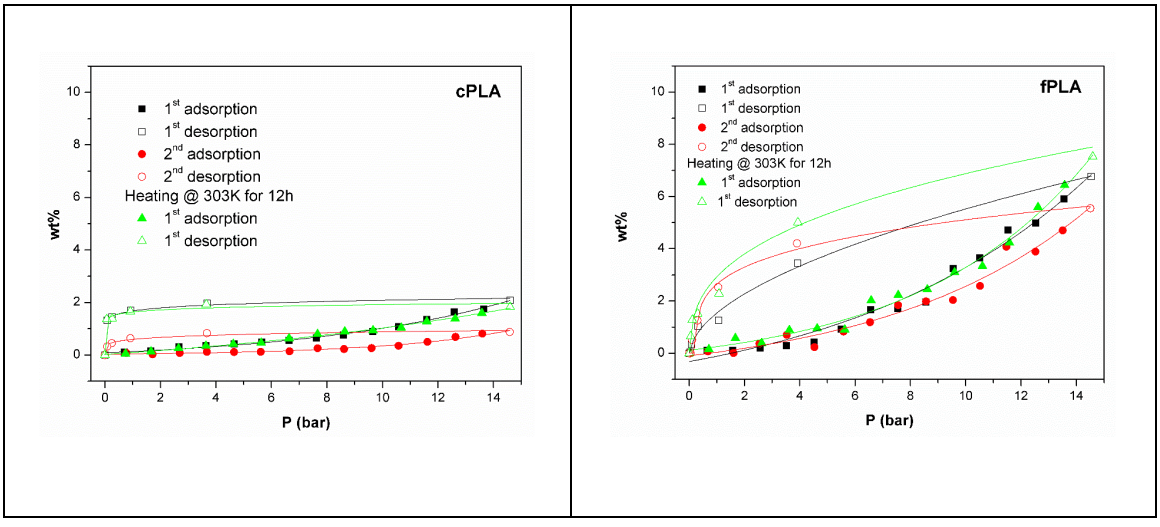

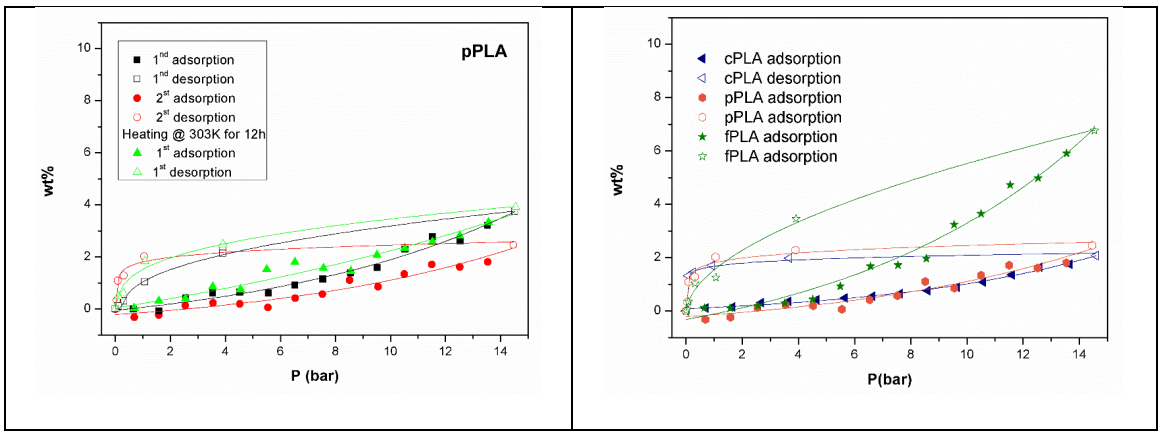

Figure 7. CO_2 adsorption-desorption isotherms after thermal treatment at 303 K for 12 h on: (a) **cPLA**, (b) **pPLA**, (c) **fPla. (d**) Comparison between first adsorption-desorption cycle of every sample. All experiments were carried out at 303 K and up to 15 bar. The magnitude of the error is 0.1 wt% (symbol). Solid line between points it is just a guide for the eyes.

The highest absorption of fPLA can be attributed to the morphology and crystalline structure of the sample. In fact, crystal changes give rise to intrinsic structural characteristics that influence the physical properties of polymer materials. For example, the α'-form of PLA with looser chain packing and structural disorder, leads to lower barrier property. The barrier property depends on the diffusivity that is related to the crystalline structure and it is higher for the amorphous phase thus leading to a higher adsorption [51, 68, 69]. In this case, the samples fPLA and cPLA show a phase α' with respect to that α of the pPLA sample. Moreover, the sample fPLA has a more heterogeneous surface which presumably involves a greater number of adsorption sites with respect to the cPLA and the pPLA thus favoring the increase of the adsorption capacity.

Looking at Figures 6, the shape of the desorption isotherms has a non-linear behavior with the amounts of sorbed CO_2. The sorbed quantity remains higher than those of the first absorption and a meaningful desorption takes place only below 1 bar leading to a large hysteresis phenomenon in the PLA. At the end of the desorption process, the system returns to the initial condition, consequently there is no phenomenon of entrapment and the molecules of CO_2 have been retained only physically, without chemisorption. The behavior of the second adsorption/desorption was strictly analogous to the first, except for a reduction in the maximum storage capacity with consequent reduction in the amplitude of the hysteresis which is restored after the regeneration of the sample at 303 K in vacuum overnight (see Table 4). The same analysis was performed on the PLA samples pre-treated at 333 K as reported in Figure 8. It is evident such as the fPLA shows the highest adsorption capacity of 16 wt% (3.64 mmol/g) at 15 bar. These values are comparable with several adsorption materials [35], but they are lower than majority ACs which present a range of adsorption capacity between 2 and 5 mmol/g at 1 bar [30, 31]. In any case, it should be

noted that the value found is associated with a material that has a SSA of 7.2 m^2/g and a pore volume of 0.03 cm^3/g against the 3000 m^2/g and 0.5-2 cm^3/g of the ACs, respectively. Also in this case, most of the previous observations still hold: (a) the CO_2 maximum adsorption value increases by increasing the gas pressure; (b) it decreases in the second cycle; (c) it is easily restored with appropriate thermal treatment; (d) the morphology of the flakes is better than the other morphologies showing a greater capacity of adsorption (Table 4 and Figure S2d); (e) a hysteresis cycle between first and second sorption/desorption cycle indicative of a physical modification of the polymer.

It is important to highlight how increasing the pretreatment temperature from 303 K to 333 K, while not affecting significatively the behaviour and maximum storage capacity of the cPLA and pPLA samples, has beneficial effects on the fPLA adsorption (storage capacity increases up to 16 wt%).

This effect can presumably be attributed to a better compromise between morphology and degassing temperature. For a better comprehension of the effect of CO_2 on the sample, XRD spectra and SEM images were acquired also after gas exposure (see Figure S3 and S4) not highlighting any evident difference compared with the pristine ones.

Going deeper in this direction, we can compare the volume occupied by the condensed CO_2 at the maximum pressure (15 bar) with the total pore volume we got from the BET analysis for the probed samples. Considering the fPLA sample thermally treated at 303 K, we have a maximum adsorption of 8wt% or 1.8 mmol CO_2/gPLA. The liquid CO_2 has a molar density of 24.3 mmol/cm^3 therefore the adsorbed CO_2 occupy 0.074 cm^3/gPLA which is more than double compared to that of the pores measured with N_2. An even stronger evidence of this phenomenon is evident after the annealing at 333 K of the fPLA sample where the adsorbed CO_2 volume is four times higher than that of the pores seen by the N_2. This is an initial strong hint to suppose a sorption mechanism different from the physical adsorption that is strongly related to the extension of the specific surface area and the cumulative pore volume.

On the other hand, the other two samples show similar adsorption in spite of their completely different apparent cumulative pore volume. All these evidences can be rationalized by considering the absorption of CO_2 in the PLA polymeric matrix. It has been measured that the pristine powders of PLA samples can absorb large quantities of CO_2. The measured uptake is compatible with our data and goes up to 25 wt% at 250 bar and 313 K [45]. Beside to this “solid state”-like absorption, it has been recorded a moderate increase of the polymer matrix volume.

The latter phenomenon, known as swelling, is limited if compared to other polymers as PEO where it is four-time larger [45]. The accessible volume in the PLA matrix, due to

methyl groups, accommodates the CO_2 molecules that are bonded through the Lewis acid-base interaction with the carbonyl groups. CO_2 absorption, in turn, weakens the chain-chain interaction bringing an increase of the polymer volume. Limitation to the volume increase is given by the presence of PLA crystallites that blocks a further expansion of the volume [45].

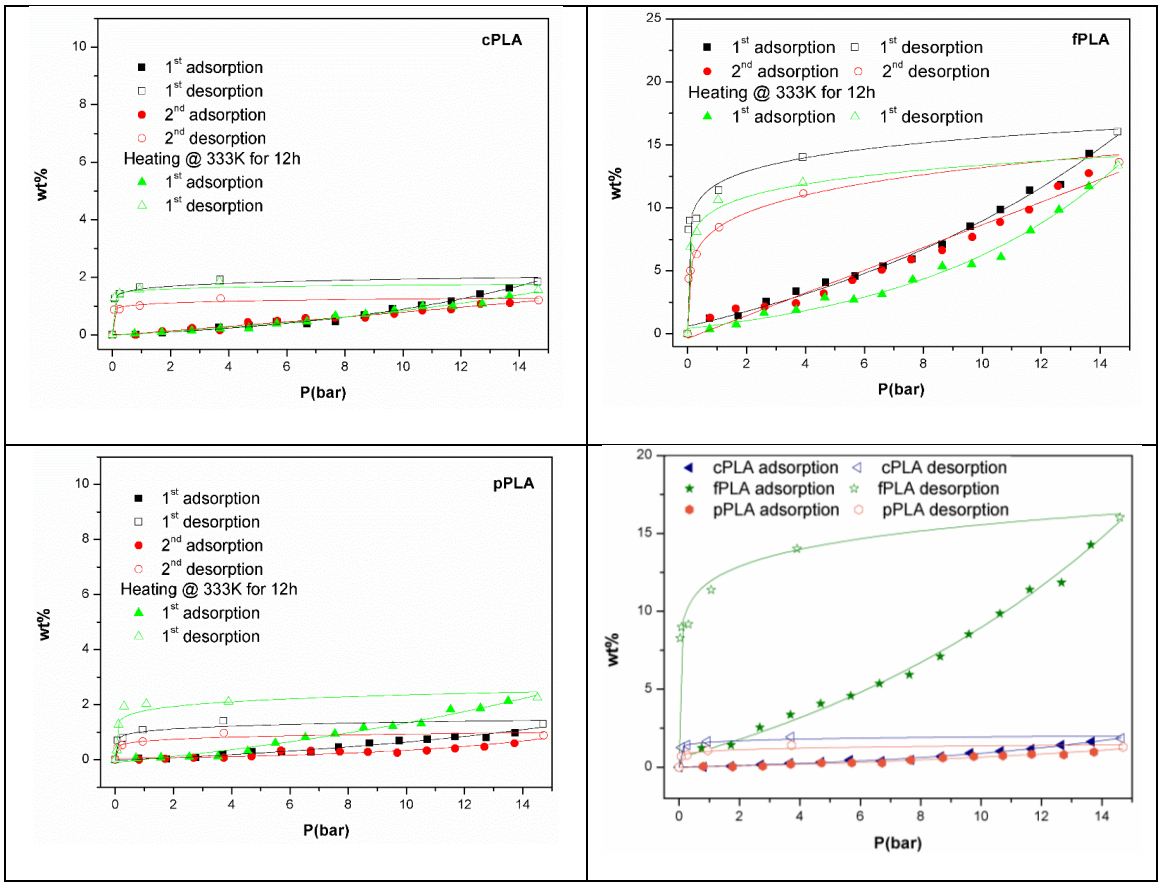

Figure 8. CO_2 adsorption isotherms after thermal treatment at 333 K for 12 h on: (a) cPLA, (b) pPLA, (c) fPLA. (d) Comparison between first adsorption-desorption cycle of every sample. All experiments were carried out at 303 K and up to 15 bar. The magnitude of the error is 0.1 wt%. Solid line between points it is just a guide for the eyes.

Table 4. CO_2 maximum storage capacity at 15 bar for all the PLA samples in both pre-treatment conditions.

Sample	303 K annealing			333 K annealing		
	1st cycle (wt%)	2nd cycle (wt%)	After regen. (wt%)	1st cycle (wt%)	2nd cycle (wt%)	After regen. (wt%)
cPLA	2.1	1.0	1.8	1.8	0.9	1.6
pPLA	3.7	2.5	2.9	3.2	2.4	3.2
fPLA	7.0	4.9	7.6	16.0	11.8	13.7

Bearing this in mind, we can ascribe the measured sorption of both pPLA and cPLA samples to the CO_2 solution into their polymeric matrices with a minor effect of the heat treatment. Concerning this samples, our data point out a larger CO_2 absorption in pPLA probably due to the presence of the induced porosity. As a matter of fact, pPLA samples show a mesoporous structure even though the crystallite dimension remains similar to cPLA. A larger lattice parameter is also measured and, thus, a larger interstitial volume is expected.

On the other hand, the fPLA samples has both a more disordered form and a larger mesoporosity with respect to cPLA and pPLA. These features are linked to larger CO_2 sorption and greater sensitivity to the annealing process. The maximum sorbed quantity is close to 15% at 303 K and 15 bar for the sample annealed to 333 K. This value is reached at 50 bar in commercial PLA [45]. Thus, we are in presence of a larger sorption capacity due to both a greater chain mobility due to a plastilization effect [70], and a lower limitation to the swelling effect being smaller the crystallites. Furthermore, the increased mesoporosity allows easier accessibility of the fPLA bulk. The changes in the polymer matrix structure are also the basis for greater sensitivity to thermal treatments: the low glass transition temperature in PLA can be decreased by the presence of CO_2 [45] in combination with a more amorphous starting configuration.

Finally, the observation of a large hysteresis loop in all the measured samples, corroborates the interpretation of the data. The thermal annealing at 333 K induces changes in the structure of the fPLA creating microporosity. Evidence of that microporosity is a more marked hysteresis for the fPLA compared to the other samples in the CO_2 isotherm of Figure 7 (d). The greater distancing between the adsorption and desorption curves is correlated to the micropores filling, which determines a phenomenon of CO_2 solution (similar to capillary condensation). This phenomenon is prevalent respect to physisorption given the increase of CO_2 uptake compared to the isotherm at 303 K. On the other hand, the morphological characteristics of the fPLA make it more sensitive to temperature and therefore to porosity modifications. This is partially evident in pPLA sample, too. In fact, in case this alternative sorption process would take place, a more reversible isotherm is expected while we are in presence of an H4-type loop [66] where the adsorption/desorption branches separation is associated with the filling of micropores.

3.7.5 Conclusions

PLA is the most widely used commercial bio-based plastic. It can be produced from many carbon raw materials through a wide range of low CO_2 emissions technologies, which with appropriate modifications can further reduce the CO_2 footprint [71]. In addition to low carbon production, PLA has a wide range of applications, in which its properties have improved the functionality of the product leading to a CO_2 emission reduction. In the end, PLA offers a wide range of end-of-life options that contribute to the circular economy and therefore to the reduction of CO_2 emissions. In the CO_2 adsorption sector, several adsorbent materials are no environmentally friendly or produced by no-green processes.

Addressing the problem of CO_2 capture through the use of no environmentally friendly materials seems to be a contradiction. Therefore, the PLA study was born from the interest in verifying whether this completely biocompatible and extremely easy to synthesize polymer, in addition to these advantages, had potential properties for the capture of CO_2, such as to be a possible alternative to other certainly effective materials but with environmental or energy disadvantages in their production.

In order to evaluate the PLA adsorption capacity, for which it is necessary a porous structure, its morphology was modified using a green process. The method used to modify the PLA morphology don't use thermal or chemical activation processes, contrary to several adsorption materials.

So, the present paper reports the investigation of PLA carbon capture properties at relatively bland conditions of pressure and temperature. Three PLA samples were prepared, differing in morphology (commercial pellet cPLA, powder pPLA, flakes fPLA). In order to get a deep understanding of our system, we performed analysis using different techniques to correlate the structural and morphological features with the adsorption/desorption ones on both mesoscopic and nanoscopic scales. We performed systematic characterizations of PLA structures by SEM, XRD and adsorption/desorption capacity of N_2 and CO_2 by using the volumetric technique. Carbon dioxide isotherms indicated that: (1) all samples adsorb CO_2; (2) there is an effect of the sample morphology on CO_2 adsorption: flakes sample adsorbs at least twice the CO_2 wt% adsorbed by other morphologies; (3) there is a detrimental effect of cyclic life; (4) regeneration in vacuum restores maximum adsorption capacity; (5) increasing the pretreatment temperature from 303 to 333 K influences mostly flakes morphology with a major beneficial effect on the fPLA; (6) the best results were obtained with the flake sample fPLA pretreated at 333 K and exposed to CO_2 at 15 bar (16 wt%). So, the better performance of fPLA sample respect to CO_2 adsorption can be attributed to its more disordered crystalline structure (pseudo-orthorhombic α' structure) and larger porosity despite its moderate SSA. Besides, these textural and crystalline properties are the origin for higher sensitivity to thermal treatments

of fPLA respect to other samples. At higher temperature, there are some effects, such as a reduction of the chain-chain interaction and an increase in the chain mobility, which produce a plasticization effect increasing the porosity and thus, the CO_2 sorbed. Consequently, starting more disordered and porous structure favored these effects.

Overall, CO_2 adsorption analysis shows that the analyzed poly(L-lactide) based materials are not extremely stable toward gas capture and storage but, at the same time, show values comparable with other adsorbents, with more green production process, and that appropriate choices in morphology and regeneration may play an important role and lead to important results. In fact, the fPLA sample could represent an interesting starting point for the synthesis of CO_2 eco-friendly adsorbing solutions.

3.7.6 Supporting Information

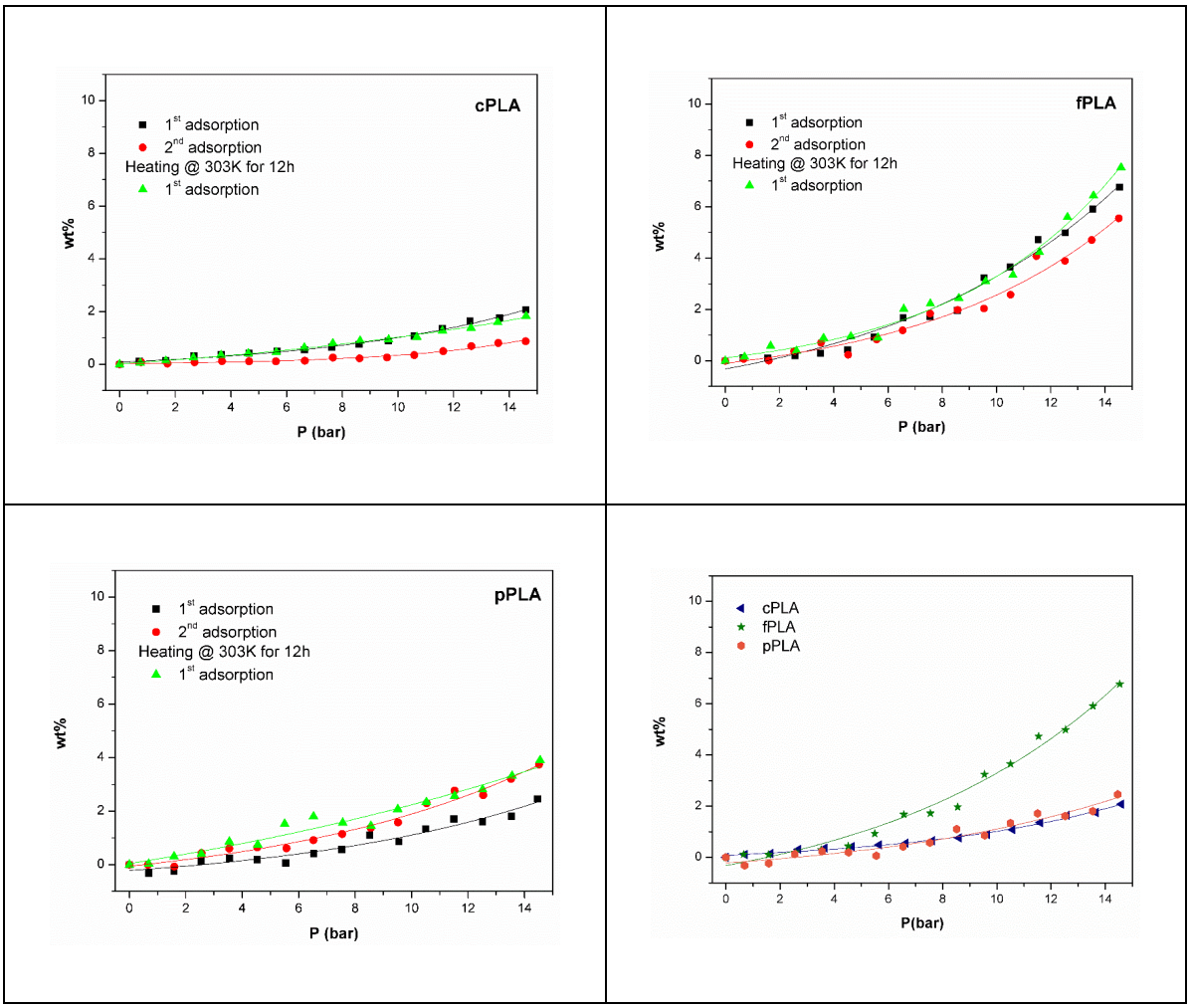

Figure S1. CO_2 adsorption isotherms after thermal treatment at 303 K for 12h on: (a) **cPLA**, (b) **pPLA**, (c) **fPLA**. (d) Comparison between first adsorption-desorption cycle of every sample. All experiments were carried out at 303 K and up to 15 bar. The magnitude of the error is 0.1 w% (symbol). Solid line between points it is just a guide for the eyes.

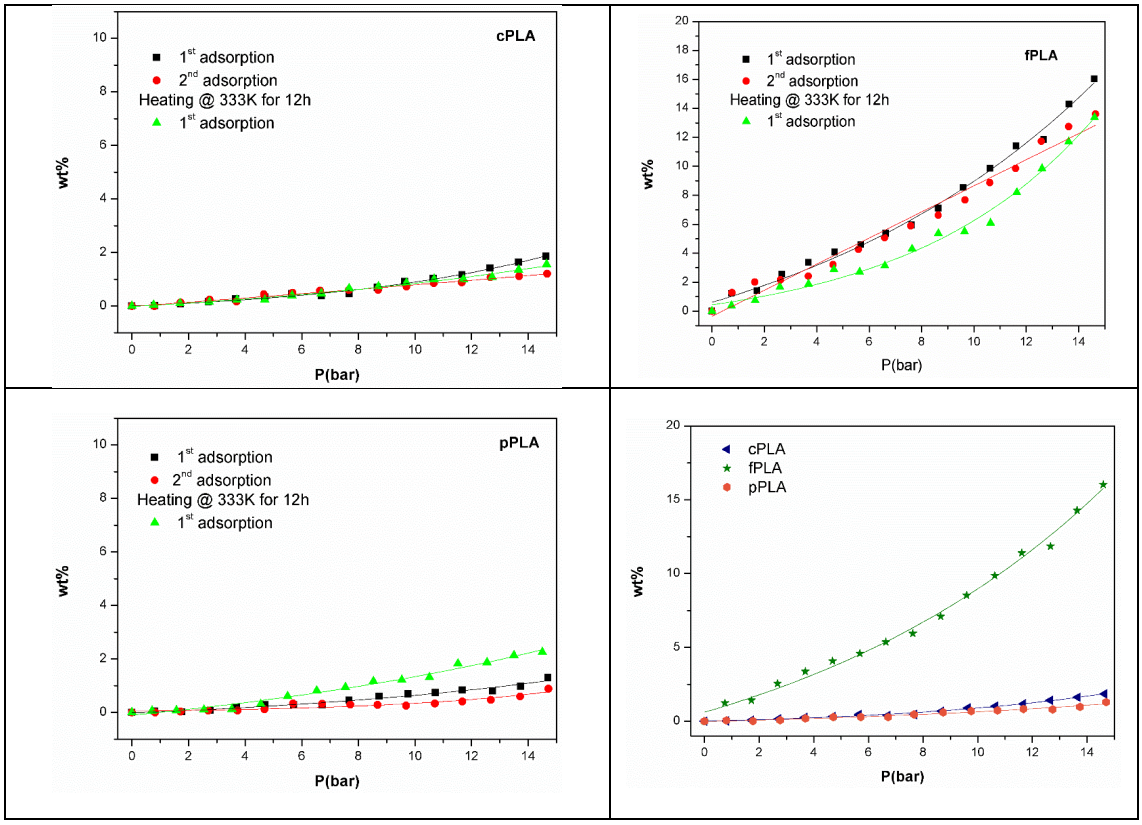

Figure S2. CO_2 adsorption isotherms after thermal treatment at 333 K for 12 h on: (a) **cPLA**, (b) **pPLA**, (c) **fPLA**. (d) Comparison between first adsorption-desorption cycle of every sample. All experiments were carried out at 303 K and up to 15 bar. The magnitude of the error is 0.1 w% (symbol). Solid line between points it is just a guide for the eyes.

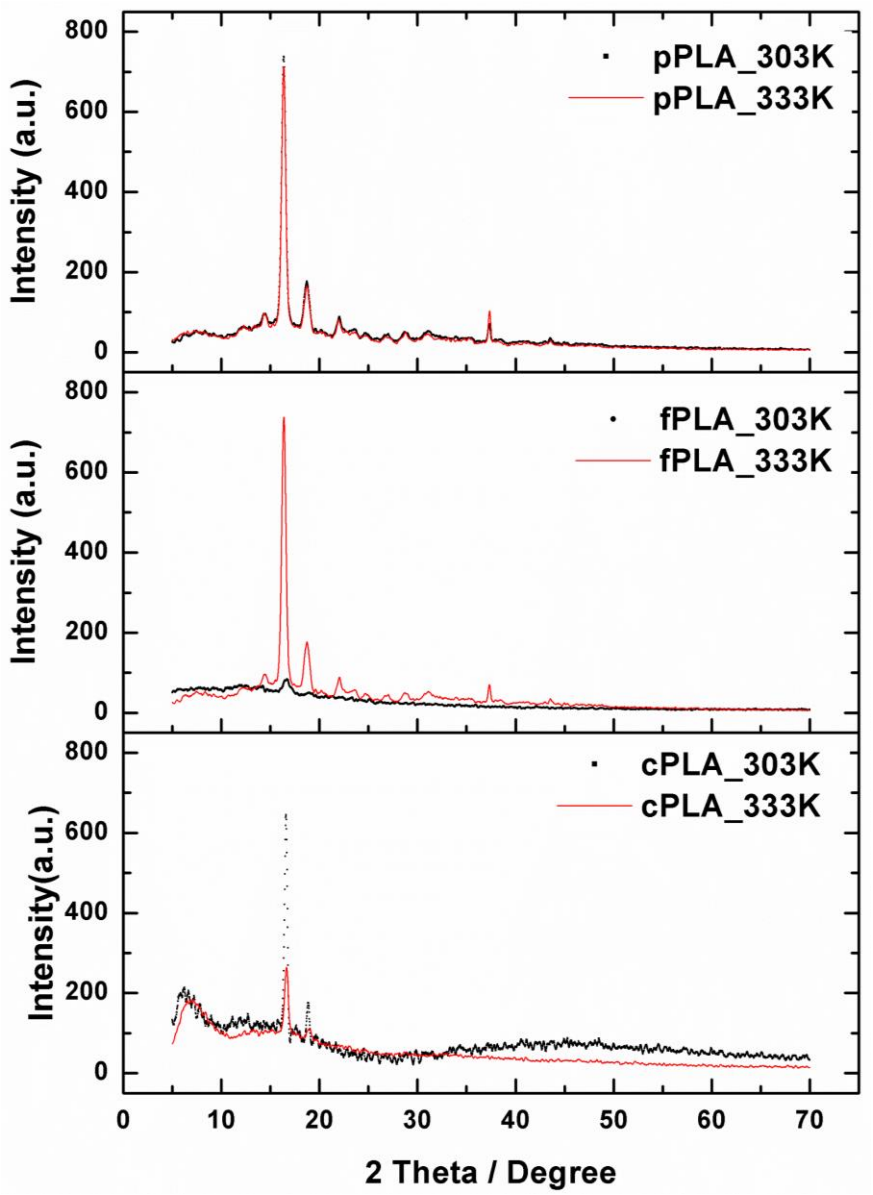

Figure S3. XRD spectra of all samples before degas at 303 K and 333 K

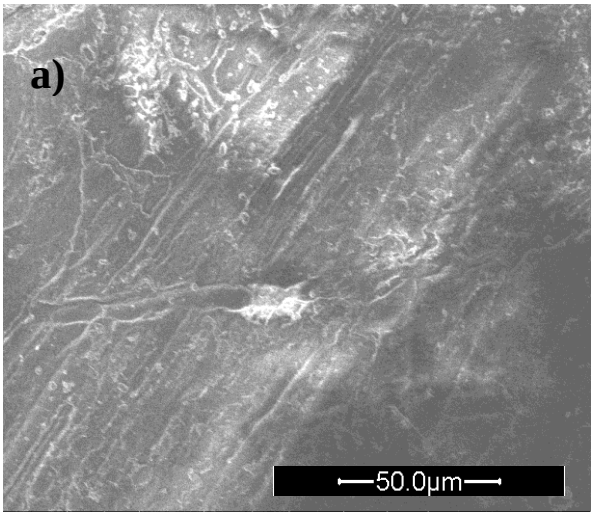

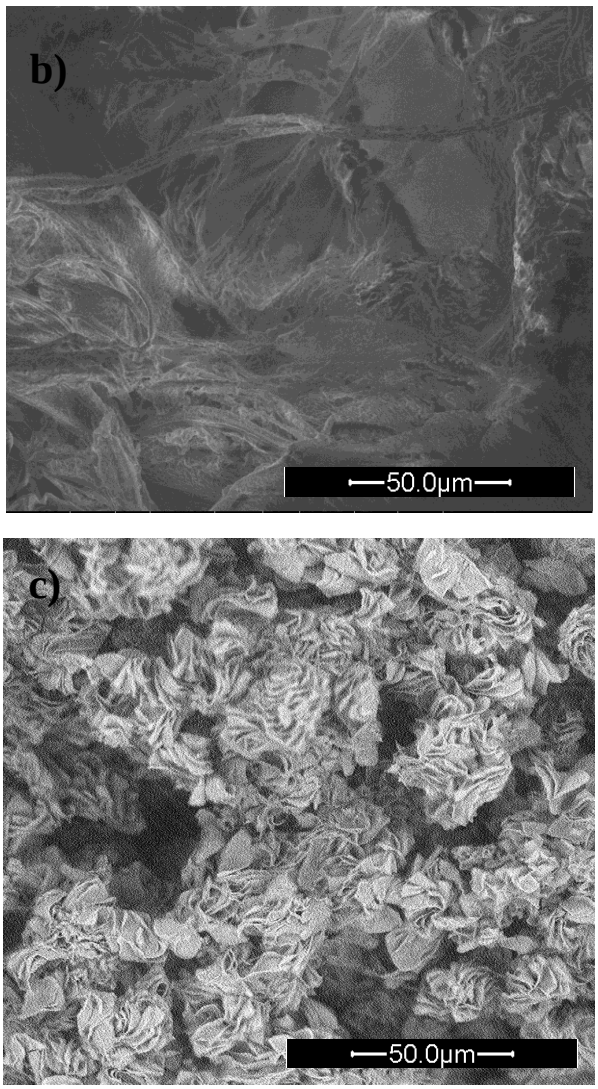

Figure S4. SEM images of a) cPLA; b) fPla; c) pPla.

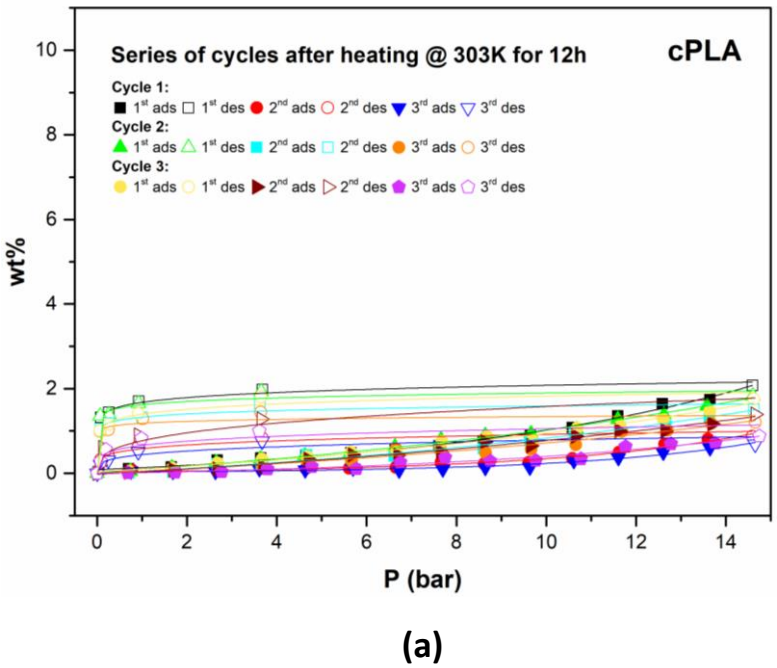

(a)

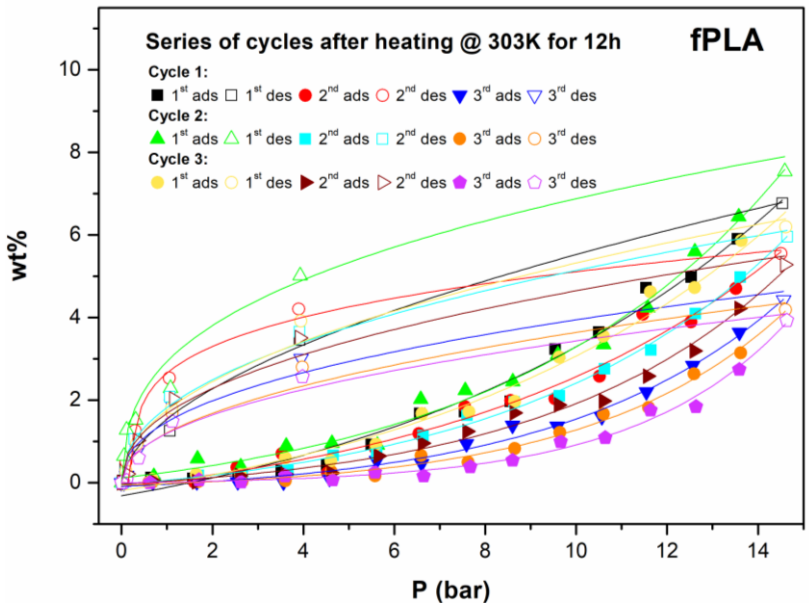

(b)

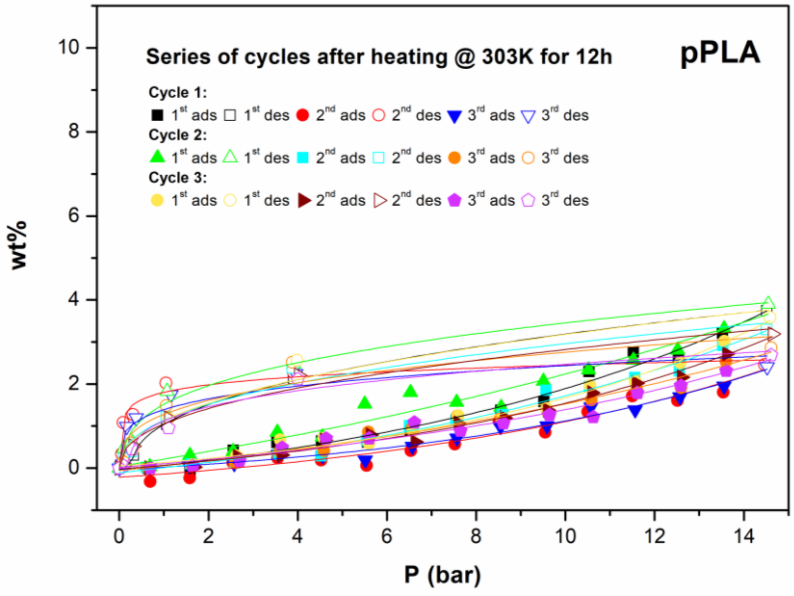

(c)

Figure S5. *Carbon dioxide multiple adsorption/desorption isotherms cycles in a) cPLA; b) fPla and c) pPla up to 15 bar at room temperature after regeneration at 303 K for12 h.*

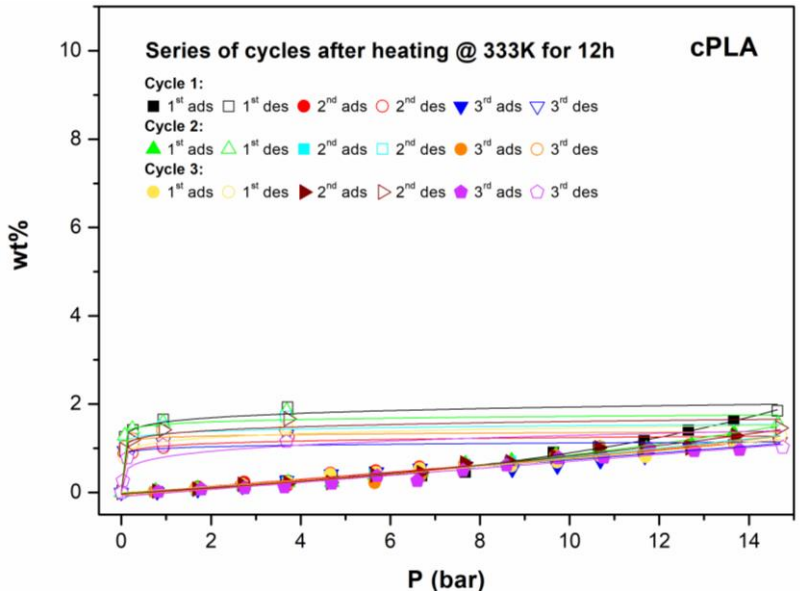

(a)

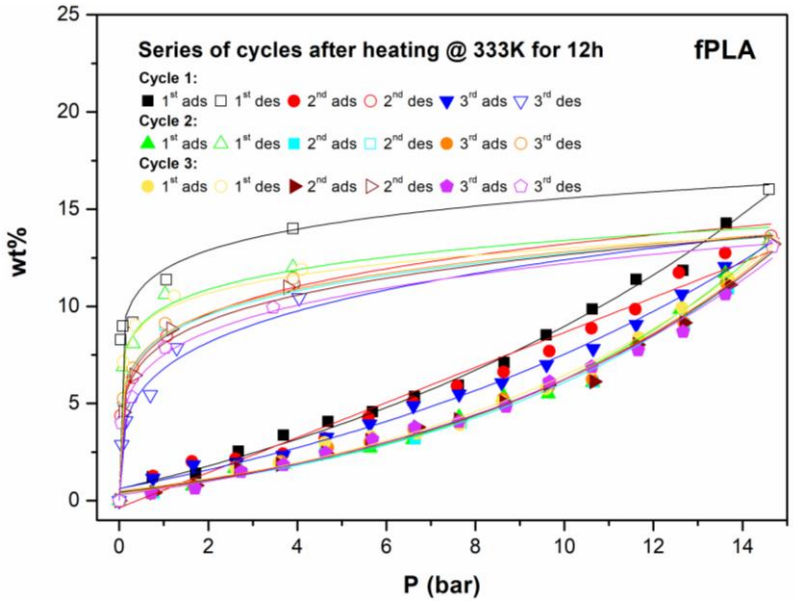

(b)

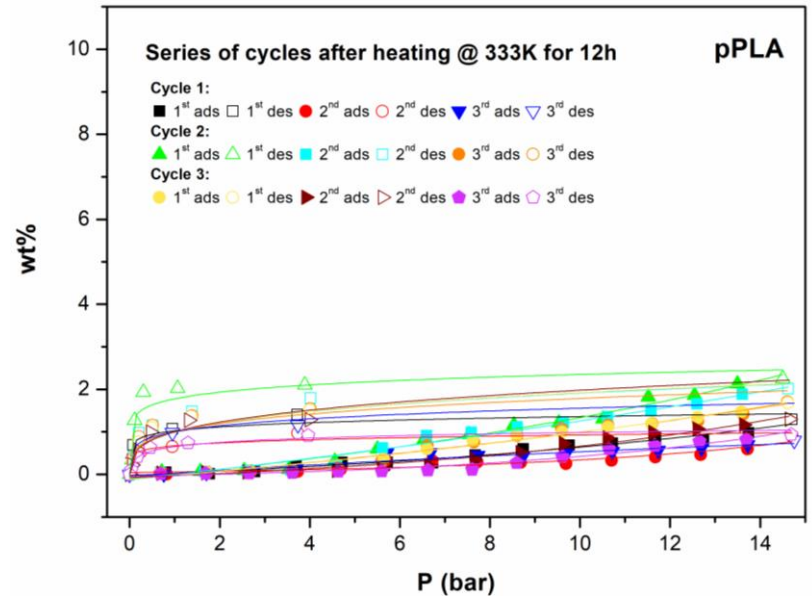

(c)

Figure S6. Carbon dioxide multiple adsorption/desorption isotherms cycles in a) cPLA; b) fPla and c) pPla up to 15 bar at room temperature after regeneration at 333 K for12 h.

References

1. Cassia, R., et al., Climate Change and the Impact of Greenhouse Gasses: CO(2) and NO, Friends and Foes of Plant Oxidative Stress. Frontiers in plant science, 2018. **9**: p. 273-273.

2. Hathaway, J. and E.W. Maibach, Health Implications of Climate Change: a Review of the Literature About the Perception of the Public and Health Professionals. Current Environmental Health Reports, 2018. **5**(1): p. 197-204.

3. Essl, F., et al., Climate change, carbon market instruments, and biodiversity: focusing on synergies and avoiding pitfalls. WIREs Climate Change, 2018. **9**(1): p. e486.

4. Boot-Handford, M.E., et al., Carbon capture and storage update. Energy & Environmental Science, 2014. **7**(1): p. 130-189.

5. Markewitz, P., et al., Worldwide innovations in the development of carbon capture technologies and the utilization of CO2. Energy & Environmental Science, 2012. **5**(6): p. 7281-7305.

6. Cuéllar-Franca, R.M. and A. Azapagic, Carbon capture, storage and utilisation technologies: A critical analysis and comparison of their life cycle environmental impacts. Journal of CO2 Utilization, 2015. **9**: p. 82-102.

7. Armstrong;, P.S.E.A.Q.K., Carbon Dioxide Utilisation: Closing the Carbon Cycle. 1st Edition ed. 2015: Elsevier. 336.

8. Maitland, G.C., Carbon Capture and Storage: concluding remarks. Faraday Discussions, 2016. **192**(0): p. 581-599.

9. Zeng, S., et al., Ionic-Liquid-Based CO2 Capture Systems: Structure, Interaction and Process. Chemical Reviews, 2017. **117**(14): p. 9625-9673.

10. Yu, J., et al., CO2 Capture and Separations Using MOFs: Computational and Experimental Studies. Chemical Reviews, 2017. **117**(14): p. 9674-9754.

11. Policicchio, A., et al., Assessment of commercial poly(ε-caprolactone) as a renewable candidate for carbon capture and utilization. Journal of CO2 Utilization, 2017. **19**: p. 185-193.

12. Dutcher, B., M. Fan, and A.G. Russell, Amine-Based CO2 Capture Technology Development from the Beginning of 2013—A Review. ACS Applied Materials & Interfaces, 2015. **7**(4): p. 2137-2148.

13. Lee, S.-Y. and S.-J. Park, A review on solid adsorbents for carbon dioxide capture. Journal of Industrial and Engineering Chemistry, 2015. **23**: p. 1-11.

14. Wang, Q., et al., CO2 capture by solid adsorbents and their applications: current status and new trends. Energy & Environmental Science, 2011. **4**(1): p. 42-55.

15. Sayari, A., Y. Belmabkhout, and R. Serna-Guerrero, Flue gas treatment via CO2 adsorption. Chemical Engineering Journal, 2011. **171**(3): p. 760-774.

16. Zanco, S.E., et al., Addressing the Criticalities for the Deployment of Adsorption-based CO2 Capture Processes. Energy Procedia, 2017. **114**: p. 2497-2505.

17. Zhao, H., et al., Carbon-based adsorbents for post-combustion capture: a review. Greenhouse Gases: Science and Technology, 2018. **8**(1): p. 11-36.

18. Wang, Y., et al., A Review of Post-combustion CO2 Capture Technologies from Coal-fired Power Plants. Energy Procedia, 2017. **114**: p. 650-665.

19. Minuto, F.D., et al., Liquid-like hydrogen in the micropores of commercial activated carbons. International Journal of Hydrogen Energy, 2015. **40**(42): p. 14562-14572.

20. Policicchio, A., et al., Activated carbon and metal organic framework as adsorbent for low-pressure methane storage applications: an overview. Journal of Porous Materials, 2017. **24**(4): p. 905-922.

21. Jean Rouquerol, F.R., Philip Llewellyn, Guillaume Maurin, Kenneth Sing,, Adsorption by Powders and Porous Solids. 2nd ed. Principles, Methodology and Applications.

22. Casco, M.E., et al., Effect of the porous structure in carbon materials for CO2 capture at atmospheric and high-pressure. Carbon, 2014. **67**: p. 230-235.

23. Hu, X., et al., CO2-Filling Capacity and Selectivity of Carbon Nanopores: Synthesis, Texture, and Pore-Size Distribution from Quenched-Solid Density Functional Theory (QSDFT). Environmental Science & Technology, 2011. **45**(16): p. 7068-7074.

24. Huang, K., et al., Significantly increasing porosity of mesoporous carbon by NaNH2 activation for enhanced CO2 adsorption. Microporous and Mesoporous Materials, 2016. **230**: p. 100-108.

25. Joos, L., et al., Cutting the cost of carbon capture: a case for carbon capture and utilization. Faraday Discussions, 2016. **192**(0): p. 391-414.

26. D'Alessandro, D.M., B. Smit, and J.R. Long, Carbon Dioxide Capture: Prospects for New Materials. Angewandte Chemie International Edition, 2010. **49**(35): p. 6058-6082.

27. Liu, Y., Z.U. Wang, and H.-C. Zhou, Recent advances in carbon dioxide capture with metal-organic frameworks. Greenhouse Gases: Science and Technology, 2012. **2**(4): p. 239-259.

28. Megías-Sayago, C., et al., CO2 Adsorption Capacities in Zeolites and Layered Double Hydroxide Materials. Frontiers in Chemistry, 2019. **7**(551).

29. Lu, A.-H., G.-P. Hao, and X.-Q. Zhang, Porous Carbons for Carbon Dioxide Capture, in Porous Materials for Carbon Dioxide Capture, A.-H. Lu and S. Dai, Editors. 2014, Springer Berlin Heidelberg: Berlin, Heidelberg. p. 15-77.

30. Balahmar, N., A.S. Al-Jumialy, and R. Mokaya, Biomass to porous carbon in one step: directly activated biomass for high performance CO2 storage. Journal of Materials Chemistry A, 2017. **5**(24): p. 12330-12339.

31. Liang, T., et al., Popcorn-Derived Porous Carbon for Energy Storage and CO2 Capture. Langmuir, 2016. **32**(32): p. 8042-8049.

32. Hirst, E.A., A. Taylor, and R. Mokaya, A simple flash carbonization route for conversion of biomass to porous carbons with high CO2 storage capacity. Journal of Materials Chemistry A, 2018. **6**(26): p. 12393-12403.

33. Li, K., et al., Pine cone shell-based activated carbon used for CO2 adsorption. Journal of Materials Chemistry A, 2016. **4**(14): p. 5223-5234.

34. Ochedi, F.O., Y. Liu, and Y.G. Adewuyi, State-of-the-art review on capture of CO2 using adsorbents prepared from waste materials. Process Safety and Environmental Protection, 2020. **139**: p. 1-25.

35. Pardakhti, M., et al., Trends in Solid Adsorbent Materials Development for CO2 Capture. ACS Applied Materials & Interfaces, 2019. **11**(38): p. 34533-34559.

36. Goeppert, A., et al., Carbon Dioxide Capture from the Air Using a Polyamine Based Regenerable Solid Adsorbent. Journal of the American Chemical Society, 2011. **133**(50): p. 20164-20167.

37. Lu, W., et al., Carbon Dioxide Capture from Air Using Amine-Grafted Porous Polymer Networks. The Journal of Physical Chemistry C, 2013. **117**(8): p. 4057-4061.

38. Sung, S. and M.P. Suh, Highly efficient carbon dioxide capture with a porous organic polymer impregnated with polyethylenimine. Journal of Materials Chemistry A, 2014. **2**(33): p. 13245-13249.

39. Wang, W., M. Zhou, and D. Yuan, Carbon dioxide capture in amorphous porous organic polymers. Journal of Materials Chemistry A, 2017. **5**(4): p. 1334-1347.

40. Wu, P., et al., Carbon dioxide capture and efficient fixation in a dynamic porous coordination polymer. Nature Communications, 2019. **10**(1): p. 4362.

41. Vilela, C., et al., The quest for sustainable polyesters – insights into the future. Polymer Chemistry, 2014. **5**(9): p. 3119-3141.

42. Nagarajan, V., A.K. Mohanty, and M. Misra, Perspective on Polylactic Acid (PLA) based Sustainable Materials for Durable Applications: Focus on Toughness and Heat Resistance. ACS Sustainable Chemistry & Engineering, 2016. **4**(6): p. 2899-2916.

43. Pini, R., et al., Sorption and Swelling of Poly(D,L-lactic acid) and Poly(lactic-co-glycolic acid) in Supercritical CO2. Macromolecular Symposia, 2007. **259**(1): p. 197-202.

44. Nalawade, S.P., et al., Investigation of the interaction of CO2 with poly (L-lactide), poly(DL-lactide) and poly(ε-caprolactone) using FTIR spectroscopy. Journal of Applied Polymer Science, 2008. **109**(5): p. 3376-3381.

45. Champeau, M., et al., In situ FTIR micro-spectroscopy to investigate polymeric fibers under supercritical carbon dioxide: CO2 sorption and swelling measurements. The Journal of Supercritical Fluids, 2014. **90**: p. 44-52.

46. Komatsuka, T., A. Kusakabe, and K. Nagai, Characterization and gas transport properties of poly(lactic acid) blend membranes. Desalination, 2008. **234**(1): p. 212-220.

47. Oliveira, N.S., et al., Gas solubility of carbon dioxide in poly(lactic acid) at high pressures: Thermal treatment effect. Journal of Polymer Science Part B: Polymer Physics, 2007. **45**(5): p. 616-625.

48. Mahmood, S.H., M. Keshtkar, and C.B. Park, Determination of carbon dioxide solubility in polylactide acid with accurate PVT properties. The Journal of Chemical Thermodynamics, 2014. **70**: p. 13-23.

49. Rocca-Smith, J.R., et al., How high pressure CO2 impacts PLA film properties. Express Polymer Letters, 2017. **11**(4): p. 320 - 333.

50. Farah, S., D.G. Anderson, and R. Langer, Physical and mechanical properties of PLA, and their functions in widespread applications — A comprehensive review. Advanced Drug Delivery Reviews, 2016. **107**: p. 367-392.

51. Liu, G., X. Zhang, and D. Wang, Tailoring Crystallization: Towards High-Performance Poly(lactic acid). Advanced Materials, 2014. **26**(40): p. 6905-6911.

52. Oliveira, N.S., et al., Carbon dioxide, ethylene and water vapor sorption in poly(lactic acid). Fluid Phase Equilibria, 2006. **250**(1): p. 116-124.

53. Oliveira, N.S., et al., Gas solubility of carbon dioxide in poly(lactic acid) at high pressures. Journal of Polymer Science Part B: Polymer Physics, 2006. **44**(6): p. 1010-1019.

54. Aionicesei, E., M. Škerget, and Ž. Knez, Measurement of CO2 solubility and diffusivity in poly(l-lactide) and poly(d,l-lactide-co-glycolide) by magnetic suspension balance. The Journal of Supercritical Fluids, 2008. **47**(2): p. 296-301.

55. Cao, Y., J. Feng, and P. Wu, Preparation of organically dispersible graphene nanosheet powders through a lyophilization method and their poly(lactic acid) composites. Carbon, 2010. **48**(13): p. 3834-3839.

56. Brunauer, S., P.H. Emmett, and E. Teller, Adsorption of Gases in Multimolecular Layers. Journal of the American Chemical Society, 1938. **60**(2): p. 309-319.

57. Seaton, N.A., J.P.R.B. Walton, and N. quirke, A new analysis method for the determination of the pore size distribution of porous carbons from nitrogen adsorption measurements. Carbon, 1989. **27**(6): p. 853-861.

58. Hillmyer;, M.S.S.N.R.C.M.A., Porous Polymers. 2011, NJ, USA.

59. Germain, J., et al., High Surface Area Nanoporous Polymers for Reversible Hydrogen Storage. Chemistry of Materials, 2006. **18**(18): p. 4430-4435.

60. Policicchio, A., et al., Volumetric apparatus for hydrogen adsorption and diffusion measurements: Sources of systematic error and impact of their experimental resolutions. Review of Scientific Instruments, 2013. **84**(10): p. 103907.

61. Kondo, S., T. Ishikawa, and I. Abe, Adsorption Science. Li Guoxi, Trans., 2005: p. 182-188.

62. dos Santos Almeida, A., et al., Development of hybrid nanocomposites based on PLLA and low-field NMR characterization. Polymer Testing, 2012. **31**(2): p. 267-275.

63. Kawai, T., et al., Crystallization and Melting Behavior of Poly (l-lactic Acid). Macromolecules, 2007. **40**(26): p. 9463-9469.

64. Li, J., et al., Crystalline structures and crystallization behaviors of poly(l-lactide) in poly(l-lactide)/graphene nanosheet composites. Polymer Chemistry, 2015. **6**(21): p. 3988-4002.

65. Patterson, A.L., The Scherrer Formula for X-Ray Particle Size Determination. Physical Review, 1939. **56**(10): p. 978-982.

66. Kenneth S. W. Sing, D.H.E., R. A. W. Haul, L. Moscou, Robert A. Pierotti, Jean Rouquerol, Teresa Siemieniewska,, Reporting Physisorption Data for Gas/Solid Systems, in Handbook of Heterogeneous Catalysis. 2008. p. 1217-1230.

67. Michàlek;, J.S.R.H.N.K.M.M.M.J.M.L.S.K.A.Z.J., Morphological Characterization of Nanofibers: Methods and Application in Practice. Journal of Nanomaterials, 2012. **2012**: p. 14.

68. Casco, M.E., et al., CO2 adsorption on crystalline graphitic nanostructures. Journal of CO2 Utilization, 2014. **5**: p. 60-65.

69. Compañ, V., et al., On the crystallinity effect on the gas sorption in semicrystalline linear low density polyethylene (LLDPE). Journal of Polymer Science Part B: Polymer Physics, 2007. **45**(14): p. 1798-1807.

70. Kazarian, S.G., et al., In Situ Spectroscopy of Polymers Subjected to Supercritical CO2: Plasticization and Dye Impregnation. Applied Spectroscopy, 1997. **51**(4): p. 491-494.

71. Morão, A. and F. de Bie, Life Cycle Impact Assessment of Polylactic Acid (PLA) Produced from Sugarcane in Thailand. Journal of Polymers and the Environment, 2019. **27**(11): p. 2523-2539.

4. Appendix

4.1 Activated carbons from amorphous cellulose

4.1.1 Introduction

Activated Carbons (ACs) are porous materials extensively studied since the eighteenth century and, nowadays, they are used in a broad range of industrial and domestic applications [1]. The great popularity of these materials originates from their relatively cheap value to be used for general-purpose adsorbents. Indeed, many ACs show high SSA, and it is not so difficult to produce materials with values around ~1000 m^2g^{-1} and porosity range between micropore to mesopore, depending on the manufacturing process.

ACs are produced form a wide variety of raw organic materials; many of these precursors have a natural origin, such as coals, lignite, bituminous mineral coals, anthracite, wooden and vegetable materials, bones, and also organic and agricultural wastes [2]. They can exist in various forms including powders, granules, cylindrical extrudates, spherical beads, polymers and fibers, and are usually produced from two main processes: the physical or chemical activation [3].

The charred structure reflects the precursor structure. Chars are defined graphitic if they are made of long-range ordered parallel planes of graphene organized in a three-dimensional structure; all the other, which are not graphitic, have a high disordered and twisted network of parallel layer planes. Pore formation occurs in part during the carbonization process due to the interstices forming between the aromatic sheets [1], while is mainly the activation process that develops the pore structure, improving their accessibility, and determining the pore width and the total pore volume.

In both types of activation, some forms of the chemical attack are involved. In chemical activation, the raw material is impregnated with a reagent such as KOH or phosphoric acid, and undergoes a heat treatment; whereas, in physical activation, the carbonized precursor is heated in a mildly reactive atmosphere like CO_2 or steam [4,5]. Therefore, the structure of the resulting ACs is disordered and mostly amorphous made of hexagonal arrangements of hybridized sp^2 carbon atoms which often present sp^3 defects, and are terminated by hydrogen atoms or oxygen complexes. Nevertheless, from the theoretical and computational approaches for MS or DFT calculation, ACs are usually modelled digitally

as slit-like pores with parallel, homogeneous walls and graphene layers [6,7,8]. ACs with very narrow porosity are generally referred as carbon molecular sieves (CMS), differentiating between those presenting an assembly of interconnected ultramicropores, and those ink-bottle shaped, which show pores of different sizes with a molecular-sized entrance [9,10]. They can have high SSA with porosity mainly in micropore range, providing large adsorption capacity and selective diffusivity which appears to be the best for many applications such as removal of impurities from gases and liquids, gas separation and gas storage [11].

For these reasons, it is important to investigate how porosity formation occurs in the synthesis processes of precursor materials by trying to understand the influence and relevance of the different key parameters during the process. The goal is to manage these parameters to have a tunable porosity according to gaseous species, combined with the use of biocompatible and low-cost precursors.

4.1.2 Experimental section

This section is devoted to a description of the synthesis and characterization of high active surface carbon materials. The starting material chosen for the production of ACs is amorphous cellulose, while the activation method used is the physical one.

4.1.2.1 Samples preparation

The choice fell on amorphous cellulose because it belongs to the family of natural polymers being a polysaccharide consisting of unbranched chains of glucose molecules (from hundreds of thousands of units). The cellulose monomer formula is $C_6H_{10}O_5$ with molecular weight equal to 162.14 g/mol. The bond between the individual molecules of glucose is of the type β $(1 \rightarrow 4)$ glycosidic. In addition to having a good percentage of carbon, it is also economic and biocompatible. The linear chains are linked together by hydrogen bonds that tend to arrange them in parallel forming agglomerates ranked (fibers) to form microcrystals difficult to dissolve.

The raw material is amorphous cellulose Gel Blot paper purchased from sigmaaldrich.com. The reason for that choice is the high purity of this paper-like sheets (see Fig. 1).

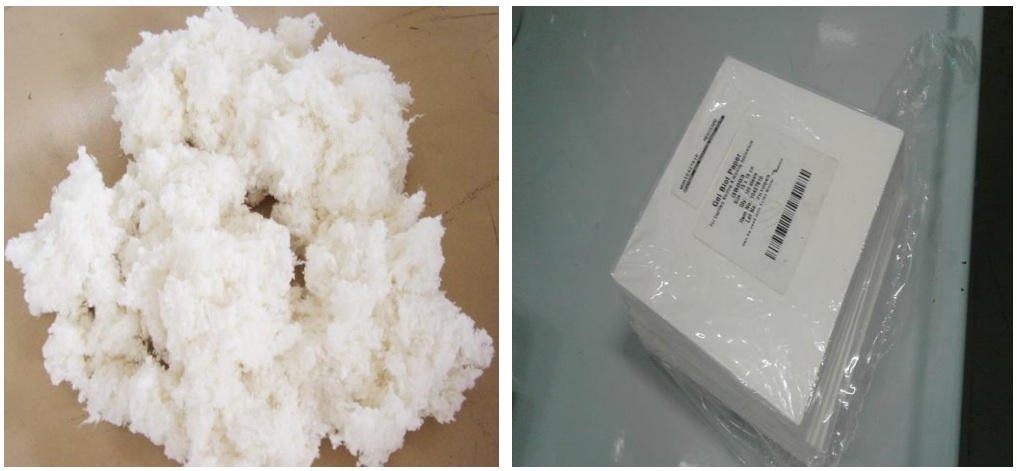

Figure 1. Image on the left is highly pure cotton linters used to produce Gel plot paper. On the right the Gel plot papers.

Therefore, in this work, we have produced ACs from amorphous cellulose to get an optimized adsorbent material for high capacity of hydrogen storage.

To enhance the capacity of hydrogen storage by activated carbon, we have chosen to vary parametrically the variables in the so-called physical activation process i.e., in the method of preparing pellet of raw material; the carbonization time and temperature; the activation time; the activation temperature.

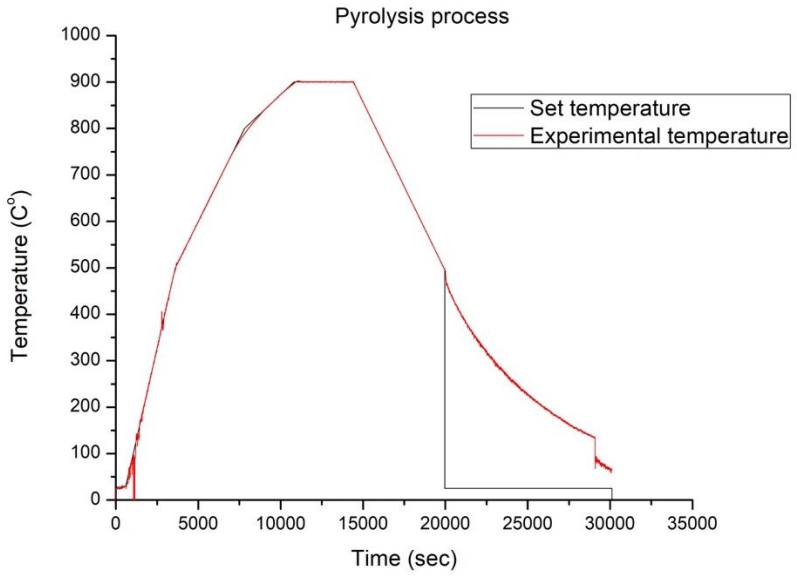

Figure 2. A typical temperature plot of a pyrolysis procedure.

In general, the procedure to obtain physical AC involves 5 steps (see fig. 2 as an example):

A. INITIAL STEP. A **pellet** of the raw material is put in a metallic pipe and an **inert gas** is inserted with constant **flux**. The sample temperature is then raised with a **constant rate** to the **carbonization temperature**.

B. CARBONIZATION. The sample is kept under a constant **flux** for a certain **time lapse (Carbonization time)** while the **carbonization temperature** is varied.

C. SECOND STEP. The temperature is raised to the **activation temperature** with a constant **rate** while the **gas species**, as well as its **flux**, can be changed or kept.

D. ACTIVATION. The sample is kept under a constant **flux** for at the **activation temperature (T_{act})** for a certain **time lapse (Activation time t_{act})**.

E. COOLING. The sample temperature is decreased at a **constant rate** leaving a constant flux of the activation gas on.

Then, the synthesis parameter (in bold in the previous page) are:

1- **Carbonization condition**: the gases used in the carbonization step are carbon dioxide or nitrogen;

2- **Pellet preparation**: two methods of preparing the pristine cellulose pellet were used:

a. Pellet from cutting cellulose paper: in this procedure, the cellulose paper was cut into small pieces (around 2 mm in length) and then compressed by using high pressure (up to 0.5 GPa) to produce cylindrical pellet. Samples obtained by this method in this work labelled by **APAC**.

b. Pellet prepared from cellulose flake: cellulose paper immersed in distilled water and steered in order to increase the homogeneity of the cellulose matter. The samples in this approach labelled by **AFPAC** samples (flake cellulose).

3- **Activation temperature**: activation process is the second part of the pyrolysis process running at a higher temperature; the activation temperature varied from 850 °C to 950 °C.

4- **Activation time**: the extension of time at which the sample is kept is called activation time. This parameter is varied between 30 min to 90 min in order to find the optimal condition for a suitable porosity is developed.

The first part of the laboratory work regarded the optimization of the carbonization step. An APAC pellet was prepared and the pyrolysis parameters were varied as in the following Table 1 (see **bold** values) while the activation temperature (900 °C) and time (60 min) were kept constant.

In particular, we tested the effects of changing the carbonization gas from nitrogen (normally used in this procedure) and CO_2.

Sample	Time (min)	Temp. (°C)	Flow (Nl/min)	Gas	Temp. Rate (°C/min)
APAC1	0	25	0	-	0
	10	**30**	**0.5**	**N_2**	**0.5**
	67	**700**	**0.5**	**N_2**	**10**
	20	**800**	**0.5**	**N_2**	**5**
	0.1	800	0	-	0
	20	900	0.5	CO_2	5
	60	900	0.5	CO_2	0
	175	25	0.5	$C0_2$	- 5
APAC2					
	0	23	-	-	-
	10	30	0.5	CO_2	0.50
	50	500	0.5	CO_2	9.4
	100	**900**	**0.5**	**CO_2**	**4**
	60	900	0.5	CO_2	-
	210	25	0.5	CO_2	- 4.17
APAC3					
	0	26.8	-	-	-
	10	**30**	**0.5**	**CO_2**	**0.32**
	50	**500**	**0.5**	**CO_2**	**9.4**
	70	**800**	**0.5**	**CO_2**	**4.3**
	50	**900**	**0.5**	**CO_2**	**2**
	60	900	0.5	CO_2	-
	200	25	0.5	CO_2	- 4.4

Table 1. APAC samples pyrolysis parameters.

Following this procedure, we obtained three samples that were analyzed to extract their porosity features such as BET surface area and total pore volume by means of the ASAP apparatus. The results are shown in the following Table 2:

Sample	**BET surface area (m^2/g)**	**Total pore volume (cm^3/g)**
APAC1	908.1 ± 1.5	0.35
APAC2	882.1 ± 1.4	0.32
APAC3	1499 ± 4.0	0.65

Table 2. APAC samples textural results.

From the reported values, it is clear that the parameters' values used in that APAC3 preparation were by far the best having both the highest SSA and pore volume. Therefore, the carbonization process for the upcoming samples fixed to be similar to sample APAC3.

APAC3 samples. Successively, in order to depict the effects of the activation time, three samples were produced by changing the sole activation time. The following Table 3 reports the pyrolysis parameters for the produced samples. Samples' name reports the activation temperature and time.

Sample	Step	Time (min)	Temp. (°C)	Flow (Nl/min)	Gas	Temp. Rate (°C/min)
APAC3_900C_45min	0	0	26.8	-	-	-
	1	10	30	0.5	CO_2	0.32
	2	50	500	0.5	CO_2	9.4
	3	70	800	0.5	CO_2	4.3
	4	50	900	0.5	CO_2	2
	5	**45**	**900**	**0.5**	$\boldsymbol{CO_2}$	-
	6	200	25	0.5	CO_2	- 4.4
APAC3_900C_60min	0	0	26.8	-	-	-
	1	10	30	0.5	CO_2	0.32
	2	50	500	0.5	CO_2	9.4
	3	70	800	0.5	CO_2	4.3
	4	50	900	0.5	CO_2	2
	5	**60**	**900**	**0.5**	$\boldsymbol{CO_2}$	-
	6	200	25	0.5	CO_2	- 4.4
APAC3_900C_75min	0	0	26.8	-	-	-
	1	10	30	0.5	CO_2	0.32
	2	50	500	0.5	CO_2	9.4
	3	70	800	0.5	CO_2	4.3
	4	50	900	0.5	CO_2	2
	5	**75**	**900**	**0.5**	$\boldsymbol{CO_2}$	-
	6	200	25	0.5	CO_2	- 4.4

Table 3. APAC3 pyrolysis parameters.

The activated carbon yield for APAC samples at a fixed temperature (900 °C) is changing with the activation time as reported in the following table and graph:

Sample	Activated carbon yield %	Raw material Loss %
APAC3_900C_45min	10.39	89.61
APAC3_900C_60min	9.22	90.78
APAC3_900C_75min	9.02	90.98

Table 4. Activated carbon yield for APAC3 samples.

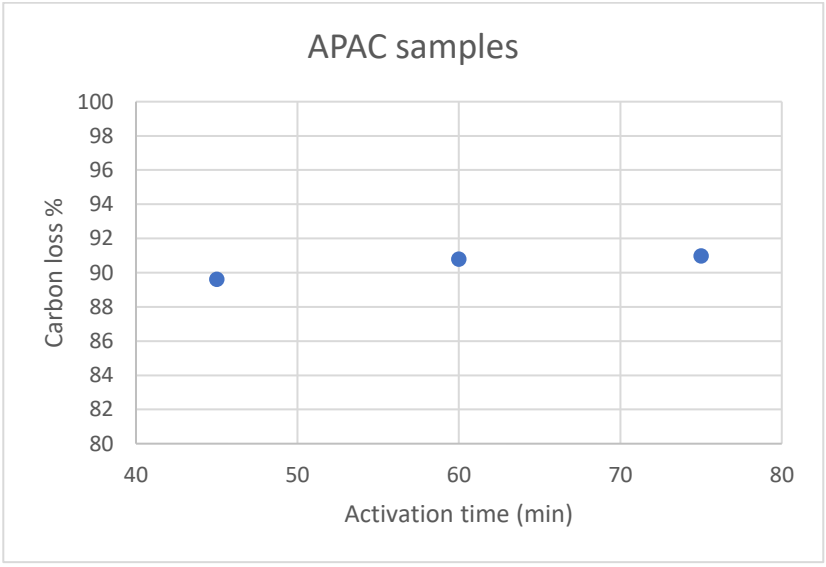

Figure 3. Carbon mass loss versus activation holding time for APAC samples.

A longer activation time did not result in a great variation of the initial raw material mass loss and, thus, the obtained activated carbon is quite stable for a large variation of activation time.

AFPAC Samples. A third series of sample was produced by changing the pellet preparation procedure i.e. by producing the samples from cellulose flakes (AFPAC samples). The activation time and the activation temperature were also parametrically changed. The following table reports the used parameters and the relative samples labelling.

Sample	Step	Time (min)	Temp. (°C)	Flow (Nl/min)	Gas	Temp. Rate (°C/min)
AFPAC_900C_30min	0	0	26.8	-	-	-
	1	10	30	0.5	CO_2	0.32
	2	50	500	0.5	CO_2	9.4
	3	70	800	0.5	CO_2	4.3
	4	50	900	0.5	CO_2	2
	5	**30**	**900**	**0.5**	$\boldsymbol{CO_2}$	**-**
	6	200	25	0.5	CO_2	- 4.4
	Step	Time	Temp.	Flow	Gas	Temp. Rate
AFPAC_900C_45min	0	0	26.8	-	-	-
	1	10	30	0.5	CO_2	0.32
	2	50	500	0.5	CO_2	9.4
	3	70	800	0.5	CO_2	4.3
	4	50	900	0.5	CO_2	2
	5	**45**	**900**	**0.5**	$\boldsymbol{CO_2}$	**-**
	6	200	25	0.5	CO_2	- 4.4
	Step	Time	Temp.	Flow	Gas	Temp. Rate
AFPAC_900C_60min	0	0	26.8	-	-	-
	1	10	30	0.5	CO_2	0.32
	2	50	500	0.5	CO_2	9.4
	3	70	800	0.5	CO_2	4.3
	4	50	900	0.5	CO_2	2
	5	**60**	**900**	**0.5**	$\boldsymbol{CO_2}$	**-**
	6	200	25	0.5	CO_2	- 4.4
	Step	Time	Temp.	Flow	Gas	Temp. Rate
AFPAC_900C_75min	0	0	26.8	-	-	-
	1	10	30	0.5	CO_2	0.32
	2	50	500	0.5	CO_2	9.4
	3	70	800	0.5	CO_2	4.3
	4	50	900	0.5	CO_2	2
	5	**75**	**900**	**0.5**	$\boldsymbol{CO_2}$	**-**
	6	200	25	0.5	CO_2	- 4.4
	Step	Time	Temp.	Flow	Gas	Temp. Rate
AFPAC_900C_90min	0	0	26.8	-	-	-
	1	10	30	0.5	CO_2	0.32
	2	50	500	0.5	CO_2	9.4
	3	70	800	0.5	CO_2	4.3
	4	50	900	0.5	CO_2	2
	5	**90**	**900**	**0.5**	$\boldsymbol{CO_2}$	**-**
	6	200	25	0.5	CO_2	- 4.4
	Step	Time	Temp.	Flow	Gas	Temp. Rate
AFPAC_850C_60min	0	0	26.8	-	-	-
	1	10	30	0.5	CO_2	0.32
	2	50	500	0.5	CO_2	9.4
	3	70	800	0.5	CO_2	4.3

	4	50	850	0.5	CO_2	2
	5	**60**	**850**	**0.5**	$\boldsymbol{CO_2}$	-
	6	200	25	0.5	CO_2	- 4.4
	Step	Time	Temp.	Flow	Gas	Temp. Rate
AFPAC_950C_60min	0	0	26.8	-	-	-
	1	10	30	0.5	CO_2	0.32
	2	50	500	0.5	CO_2	9.4
	3	70	800	0.5	CO_2	4.3
	4	50	950	0.5	CO_2	2
	5	**60**	**950**	**0.5**	$\boldsymbol{CO_2}$	-
	6	200	25	0.5	CO_2	- 4.4

Table 5. AFPAC pyrolysis parameters.

The activated carbon yield and loss of the AFPAC samples after an activation time at 60 min at varying activation temperature are reported in the following table. Here we note a larger change in the carbon yield having a very low value (< 4%) for the higher temperature.

Sample	Activated carbon yield %	Carbon Loss %
AFPAC_850C_60min	14.83	85.17
AFPAC_900C_60min	8.90	91.10
AFPAC_950C_60min	3.73	96.27

Table 6. Activated carbon yield for AFPAC samples.

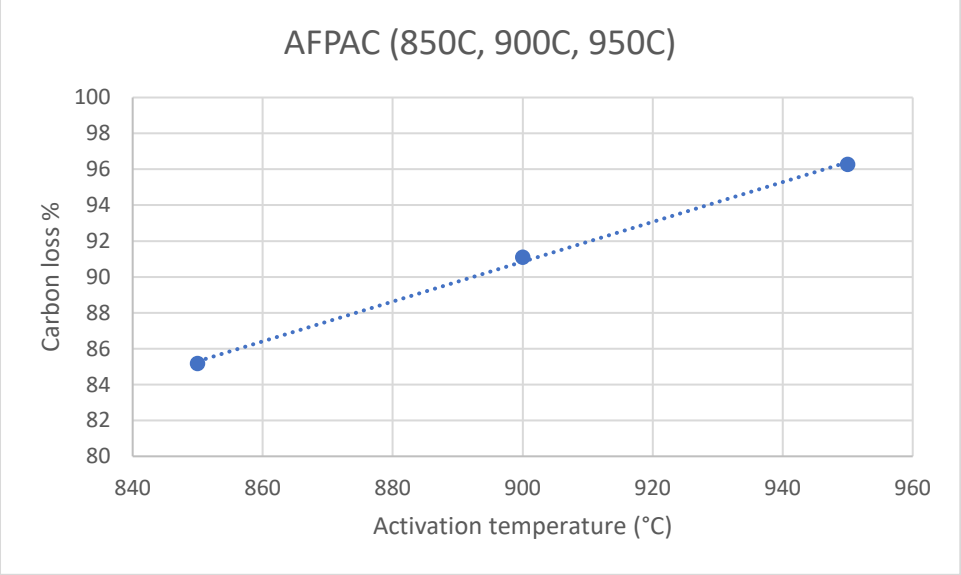

Figure 4. Raw material mass loss versus activation temperature for AFPAC samples with a fixed activation time t_{act} = 60 min.

The following table and figure show that the activation time, at a fixed temperature of 900°C, is less critical in the mass reduction of the carbon yield.

Sample	Activated carbon yield %	Carbon Loss %
AFPAC_900C_30min	12.74	87.26
AFPAC_900C_45min	13.43	86.57
AFPAC_900C_60min	8.90	91.10
AFPAC_900C_75min	10.08	89.92
AFPAC_900C_90min	8.92	91.08

Table 6. Activated carbon yield for AFPAC_900 °C samples.

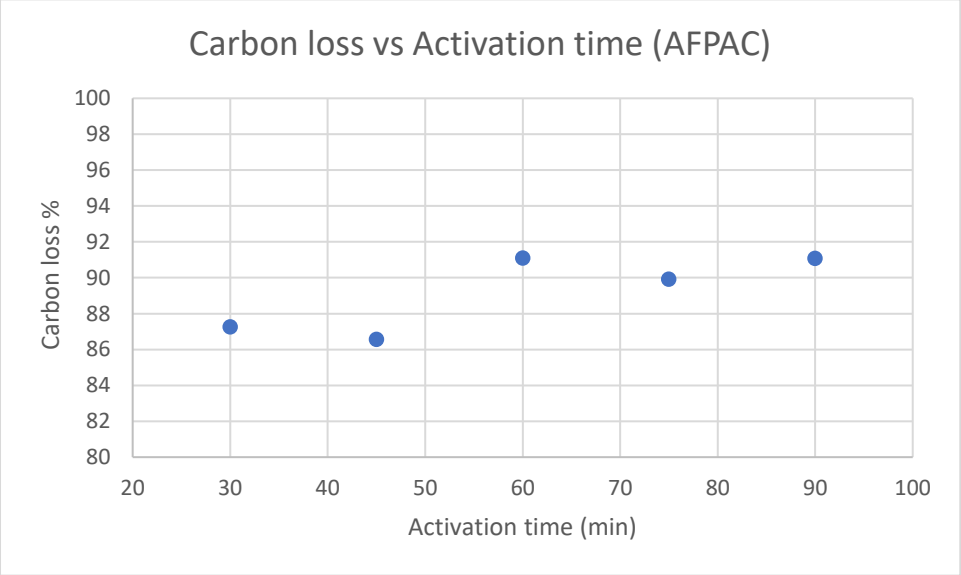

Figure 5. Carbon mass loss versus activation time for AFPAC samples holding the activation temperature to 900 °C.

4.1.2.2 Results

4.1.2.2.1 Porosity analysis

Nitrogen adsorption isotherm. The evaluation of the BET specific surface area (SSA) and porosity (pore size distribution – PSD; pore volume) of the activated carbon samples was performed by applying the BET theoretical model and the Non-Linear DFT to the data collected by means of the ASAP micromeritics 2460. The preparation procedure of samples before the data acquisition is performed by a thermal treatment of the sample held at 200°C in vacuum in order to remove the potential contaminations.

The N_2 adsorption isotherms acquired at 77 K on the APAC 3 samples are reported in the following figure.

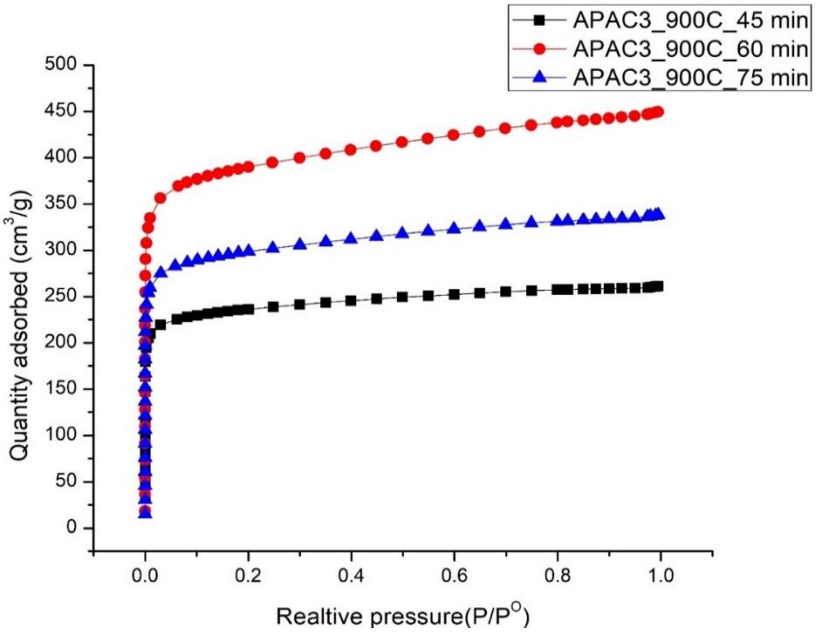

Figure 6. Nitrogen adsorption isotherm for APAC3 samples prepared by cutting cellulose paper method with fixed activation temperature (900 °C) and different time (APAC3_900C_45min, APAC3_900C_60min, APAC3_900C_75min).

The adsorption isotherms are of Type Ia according to the IUPAC classification which indicate adsorption of molecule on the micropore surface. The initial slope rises steeply at low pressure and it reaches a plateau at high relative pressures and is fully reversible (Sing et al. 1985). At a first glance, we can note that the shape of the knee of the adsorption isotherm at very low relative pressure is referred to existence of narrow microporosity and a homogeneous PSD. Similar results are obtained for the AFPAC samples: the overall shapes of the N_2 adsorption isotherms are very similar with meaningful differences in terms of total adsorbed N_2 quantity and slightly different plateau shape.

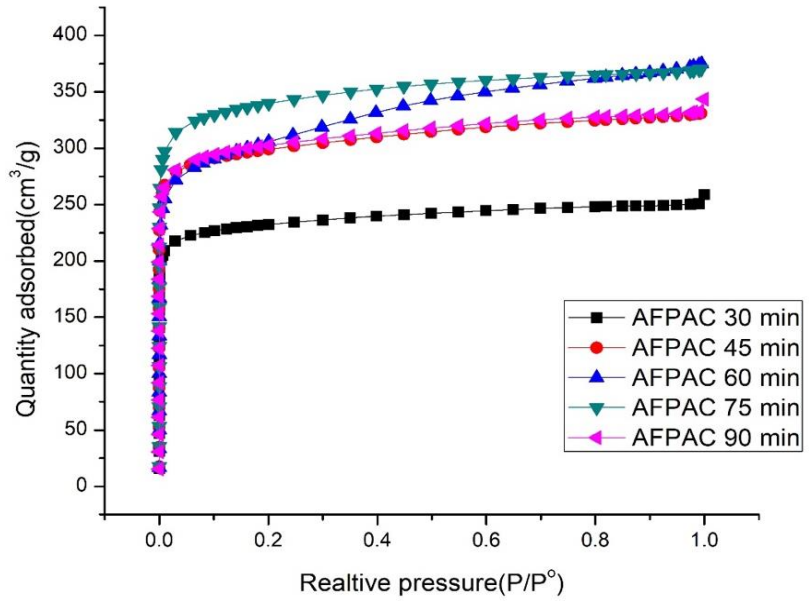

Figure 7. Nitrogen adsorption isotherms for AFPAC samples prepared by flake cellulose method with fixed activation temperature (900 °C) and different time (AFPAC_900C_30min, AFPAC_900C_45min, AFPAC_900C_60min, AFPAC_900C_75min, AFPAC_900C_90min).

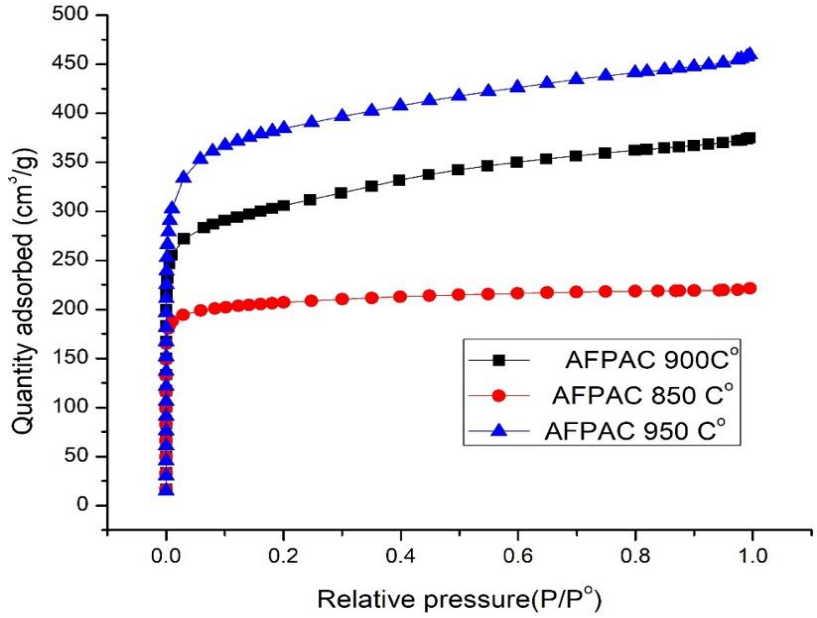

Figure 8. Nitrogen adsorption isotherms for AFPAC samples prepared by flake cellulose method with fixed activation time (60 min) and different temperature (AFPAC_850C_60min, AFPAC_900C_60min, AFPAC_950C_60min).

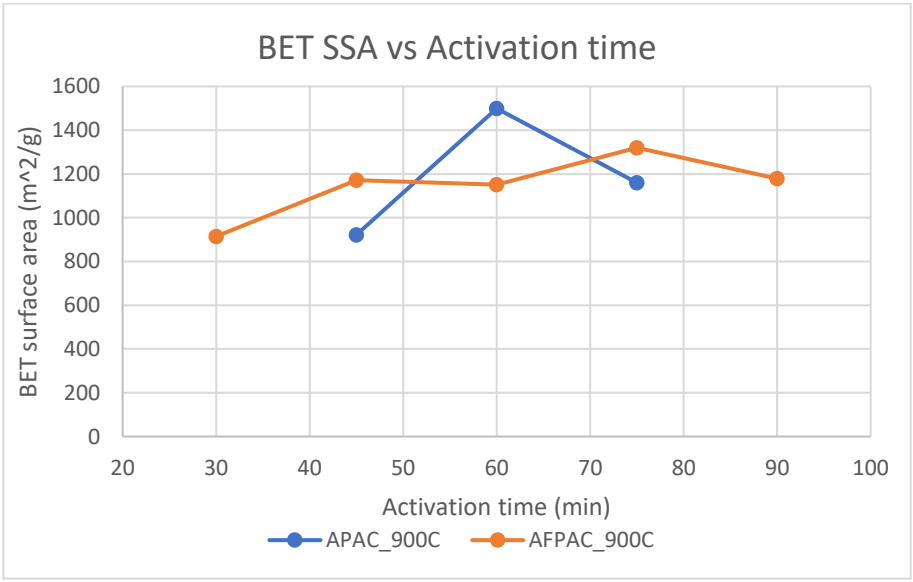

Figure 9. BET specific surface area of activated carbon samples from cellulose pellet with different preparation method in dependence of the activation time. Activation temperature is 900 °C for all the reported samples.

Specific surface area. The calculated BET specific surface area -SSA- values for the samples prepared at 900 °C are shown in the figure 9. The SSA varied from a maximum of 1499 m^2/g for the APAC_900C_60min sample to a minimum of 914 m^2/g of the AFPAC_900C_30min sample. In average, the SSA does not depend on the preparation procedure showing the all samples similar values. These BET areas values are close to

those reported in literature. In fact, the BET SSA of the commercial activated carbons are in the range of 600-1500 m^2/g.

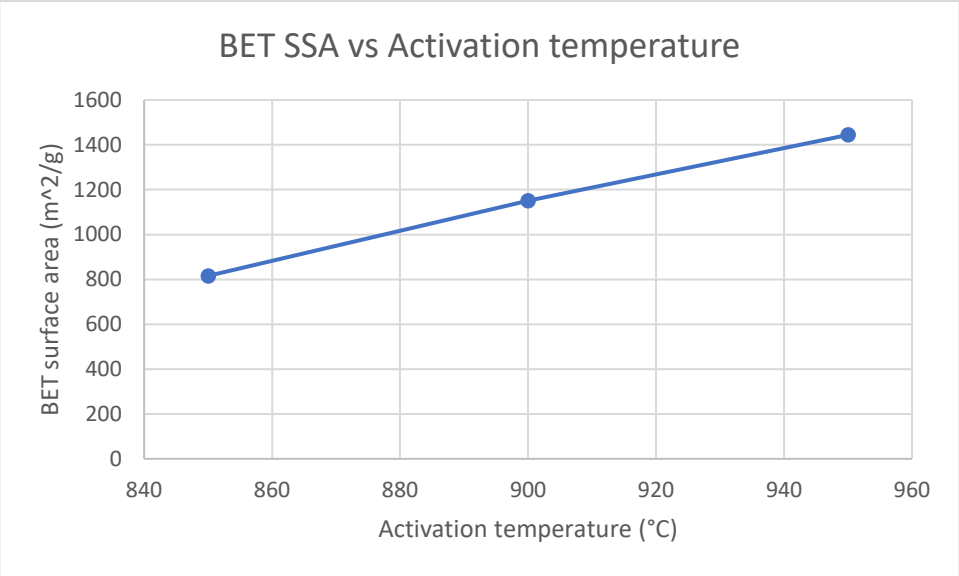

Figure 10. Specific surface area of AFPAC samples as function of activation temperature (the activation time fixed at 60 min).

A strong dependence on the activation temperature was recorded for the AFPAC sample where a quite linear correlation between BET surface area and activation temperature is found. The maximum observed SSA is for AFPAC 950C sample with 1444 m^2/g.

Pore Size Distribution: an evaluation of the pore size distributions (PSD) were obtained using the latest version of SAIEUS software (www.nldft.com - Micromeritics, GA). This software uses a new series of NLDFT models for the characterization of porous carbons. These new models are based upon the leading work of Jacek Jagiello and James Olivier and employ NLDFT techniques for 2-D finite geometry of pores to calculate the PSD of materials from adsorption isotherms [12-14].

The adsorption isotherm data were interpolated by using the Origin software into 50 equidistant measurements points. Thus, the interpolated adsorbed data were uploaded into SAIEUS software for the PSD evaluation and the calculation of the cumulative pore volume. SAIEUS software offer many geometrical models for the NLDFT calculation in such a way that it is possible to select the proper model based on the adsorption system. In this work two geometrical models were used for fitting to experimental data: the Carbon-N2-77, NLDFT Standard Slit pore model and the Carbon-N2-77, 2D-NLDFT Heterogeneous Surface model [15,16].

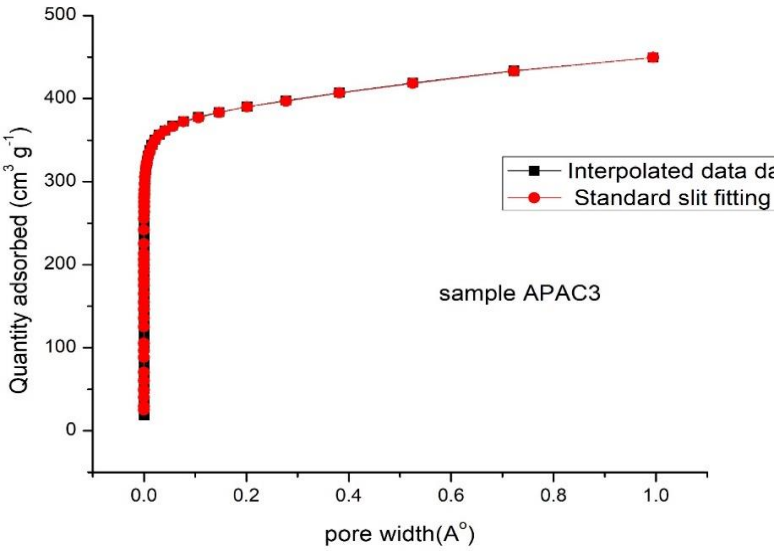

Figure 11. A typical result of the fitting procedure on the acquired data for the APAC3 sample. The isotherm curve fitting is performed by using NLDFT-standard slit model.

In order to compare the two models, the standard deviation of the fitted curve from the isotherm data is calculated. As it is clear from the data reported in the following table for the APAC3 samples, the heterogenous surface model describes the data more accurately.

Sample	**Standard deviation**	
	Standard slit	**Heterogenous surface**
APAC3_900C_45min	3.23	**2.94**
APAC3_900C_60min	3.56	**1.75**
APAC3_900C_75min	2.45	**1.29**

Table 7. Standard deviation of PSD calculated with Standard slit-Heterogeneous surface models for the APAC samples.

On the other hand, the AFPAC samples show a different behavior. They are described at low activation temperature and/or activation time by the Slit pore model while at increasing temperature and/or time, where the mass loss is higher, the heterogeneous surface model is more adequate in describing the pore surface geometry.

Sample	**Standard deviation**	
	Standard slit	**Heterogenous surface**
AFPAC_900C_30min	**1.66**	3.05
AFPAC_900C_45min	**1.84**	2.80
AFPAC_900C_60min	3.47	**2.91**
AFPAC_900C_75min	2.44	**1.17**
AFPAC_900C_90min	3.41	**2.66**
AFPAC_850C_60min	**6.31**	9.59

AFPAC_950C_60min	5.26	**0.86**

Table 8. Standard deviation of PSD calculated with Standard slit-Heterogeneous surface models for the AFPAC samples. The results in bold are referred to the model with a lower standard deviation.

By keeping these results in mind, we compare the evolution of the calculated PSD for the probed samples. The figure 12 shows the PSD values for the APAC3 samples prepared at 900 °C at increasing activation time. We can note that their main features are all located below 20 Å conforming the microporous nature of these sample. Furthermore, the main peak is located, without any dependence on the activation time, below 7 Å giving us the way to classify as ultra-microporous the APAC3 samples.

A final note concerns the position of the maxima: they do not shift changing just in amplitude. This has to be related to the fact that the heterogeneous surface model has the best fit for all the APAC3 samples. In other words, the morphology of the pore surface is independent from the activation time.

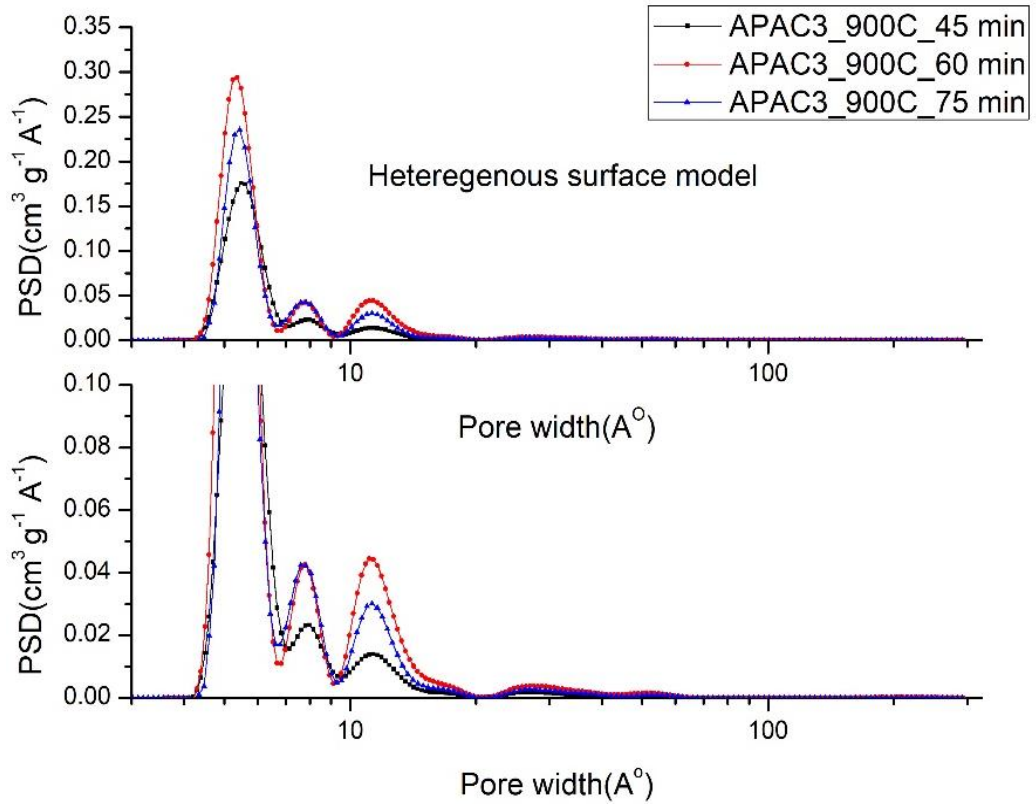

Figure 12. APAC3 samples: Pore size distribution by 2D-NLDFT Heterogeneous surface model.

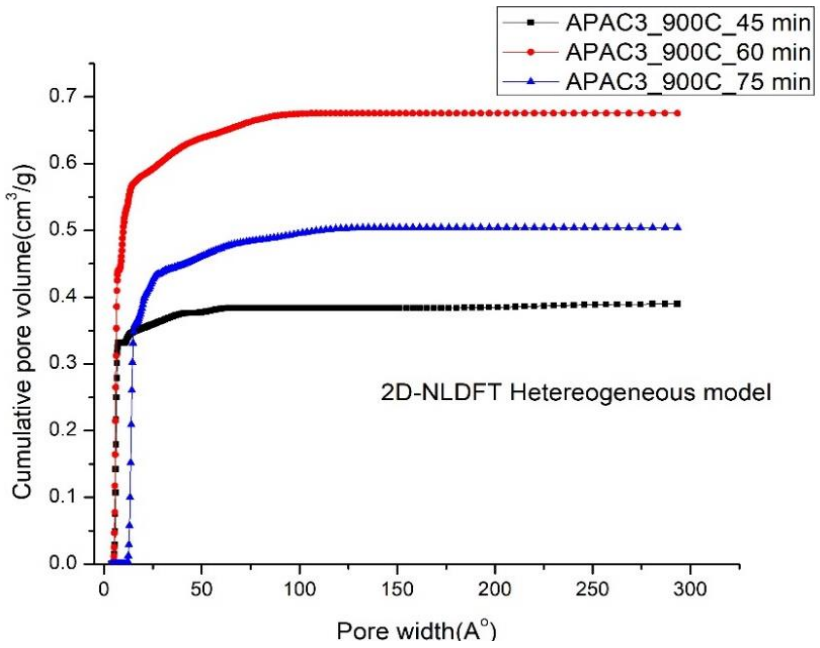

Figure 13. APAC3 samples: Cumulative pore volume by 2D-NLDFT Heterogeneous surface model.

From the same model we can derive that the larger total pore volume is observed in APAC3_900C_60min, 0.68 cm^3/g, with a corresponding average pore width of 5.86 Å. The smaller total pore volume in sample APAC3_900C_45min is 0.39 cm^3/g associated with average pore width of 5.99 Å. The AFPAC samples were analyzed in a similar way and the results are summarized in the following graphs and tables.

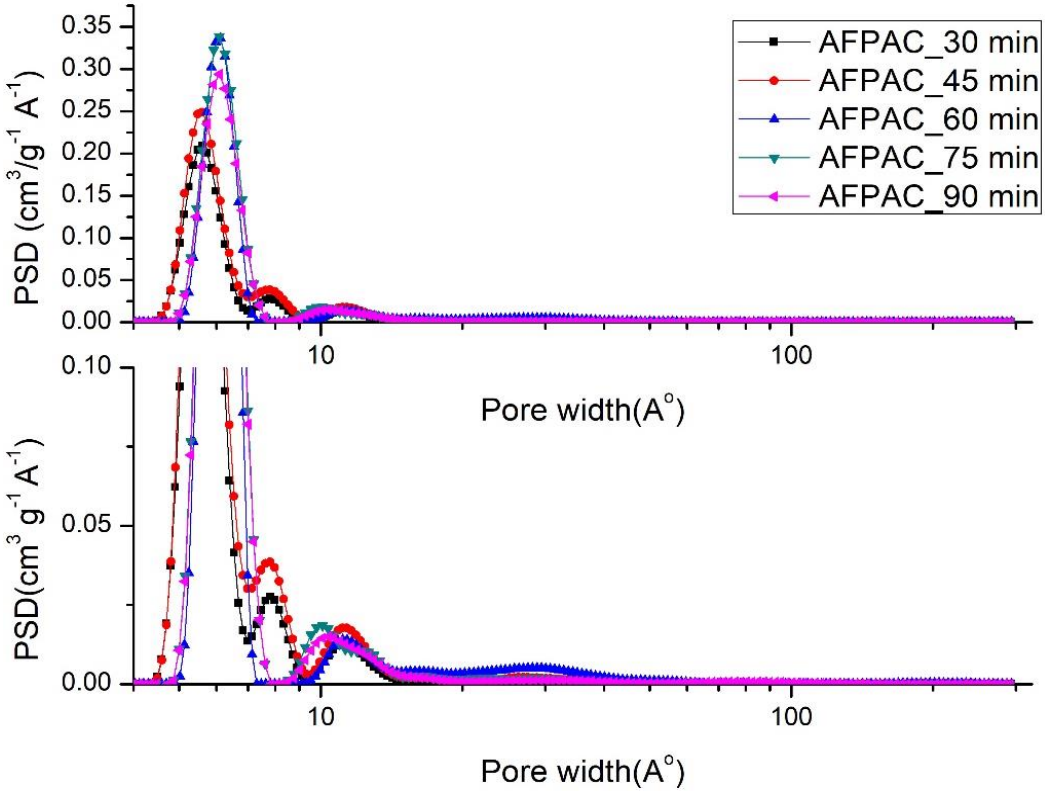

Figure 14. AFPAC samples with a fixed activation temperature (900 °C) and variable activation time: Pore size distribution by the NLDFT Standard Slit pore model (30, 45 min samples) and 2D-NLDFT Heterogeneous surface model (60, 75, 90 min samples).

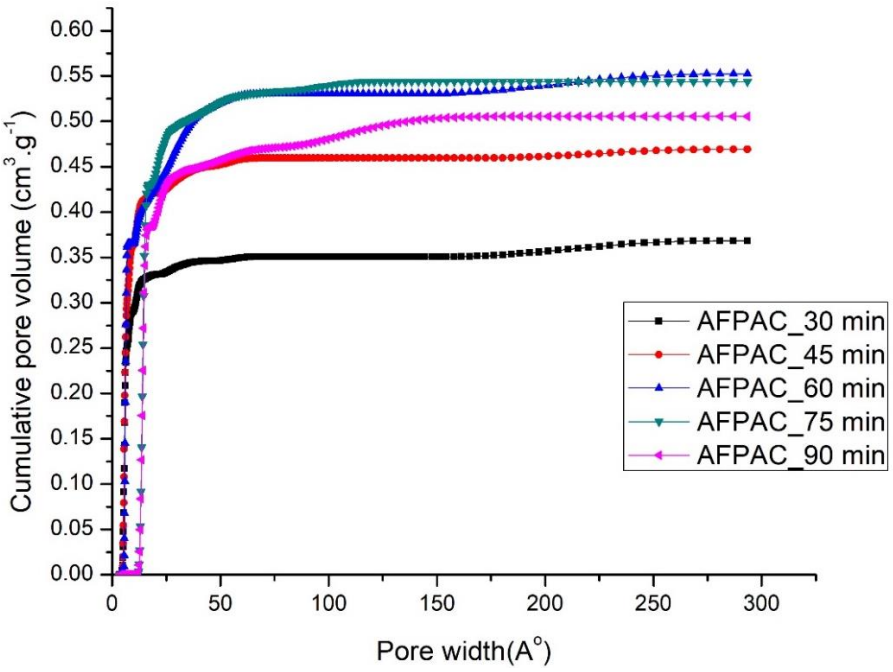

Figure 15. AFPAC samples with a fixed activation temperature (900°C) and variable activation time: Cumulative pore volume by the NLDFT Standard Slit pore model (30, 45 min samples) and 2D-NLDFT Heterogeneous surface model (60, 75, 90 min samples).

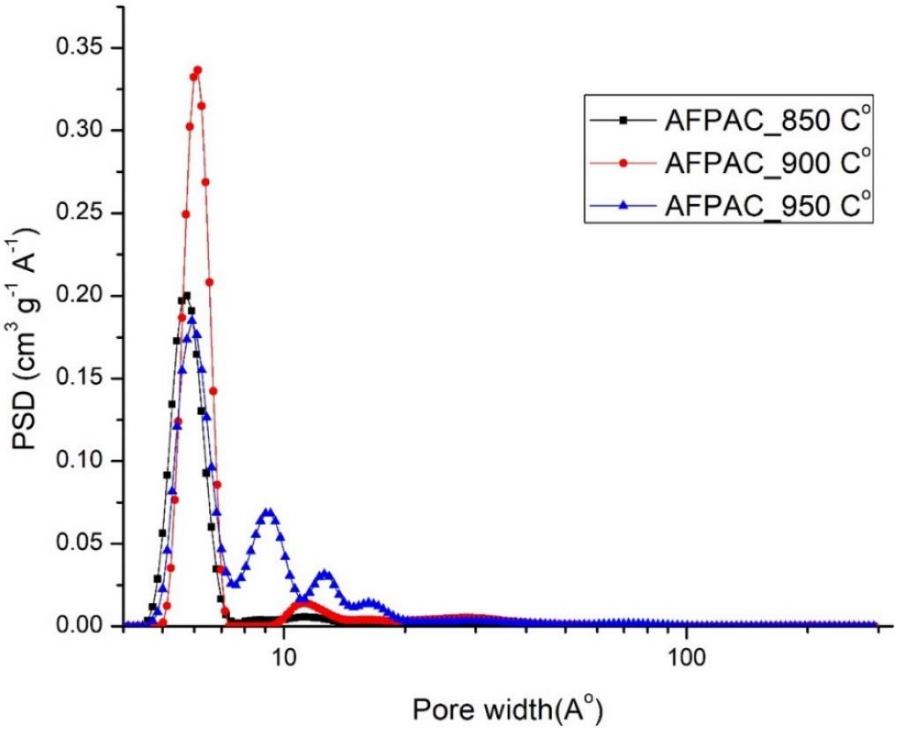

Figure 16. AFPAC samples with a variable activation temperature and fixed activation time (60 min): Pore size distribution by the NLDFT Standard Slit pore model (850°C sample) and 2D-NLDFT Heterogeneous surface model (900°C/950°C min samples).

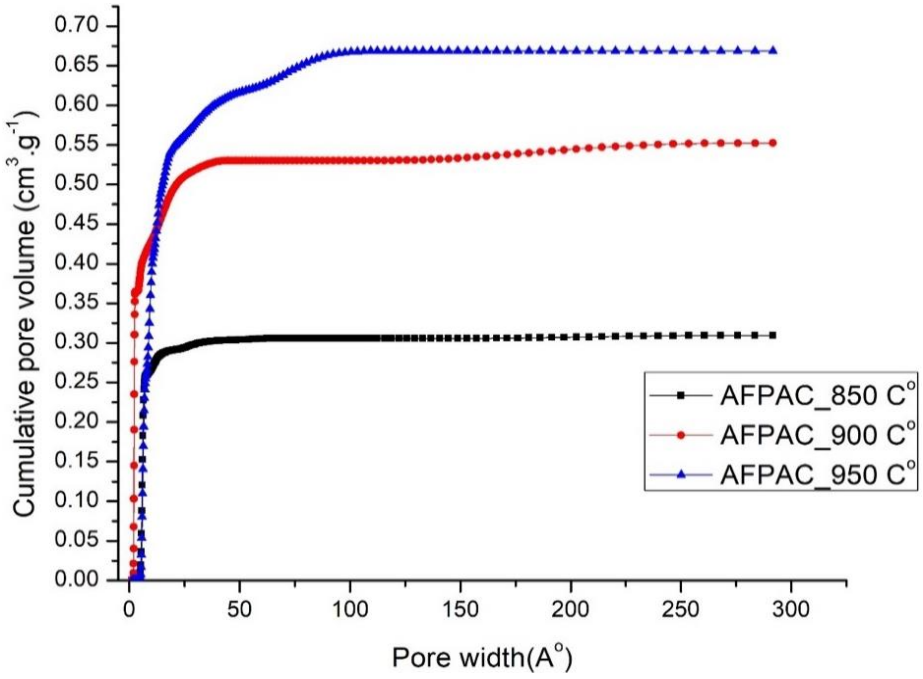

Figure 17. AFPAC samples with a variable activation temperature and fixed activation time (60 min): Cumulative pore volume by the NLDFT Standard Slit pore model (850 °C sample) and 2D-NLDFT Heterogeneous surface model (900 °C / 950 °C min samples).

Samples	**NLDFT total pore volume (cm^3/g)**		**NLDFT average pore width (A°)**		**BET area (m^2/g)**
	Slit	Hetero	Slit	Hetero	
APAC3_900C_45min	0.37	**0.39**	5.48	**5.99**	921 ± 2
APAC3_900C_60min	0.65	**0.68**	5.36	**5.86**	1499 ± 4
APAC3_900C_75min	0.49	**0.50**	5.44	**5.92**	1160 ± 2
Samples	**NLDFT total pore volume (cm^3/g)**		**NLDFT average pore width (A°)**		**BET area (m^2/g)**
	Slit	Hetero	Slit	Hetero	
AFPAC_900C_30min	**0.368**	0.386	**5.60**	6.12	914 ± 1
AFPAC_900C_45min	**0.469**	0.489	**5.60**	6.12	1172 ± 2
AFPAC_900C_60min	0.536	**0.552**	5.60	**6.12**	1150 ± 2
AFPAC_900C_75min	0.527	**0.544**	5.44	**6.09**	1319 ± 2
AFPAC_900C_90min	0.491	**0.505**	5.44	**5.44**	1179 ± 2
AFPAC_850C_60min	**0.309**	0.330	**5.75**	6.09	815 ± 1
AFPAC_950C_60min	0.654	**0.669**	5.44	**5.92**	1444 ± 4

Table 9. Pore Size Distribution obtained by SAIEUS software. The results in bold are referred to the model with a lower standard deviation.

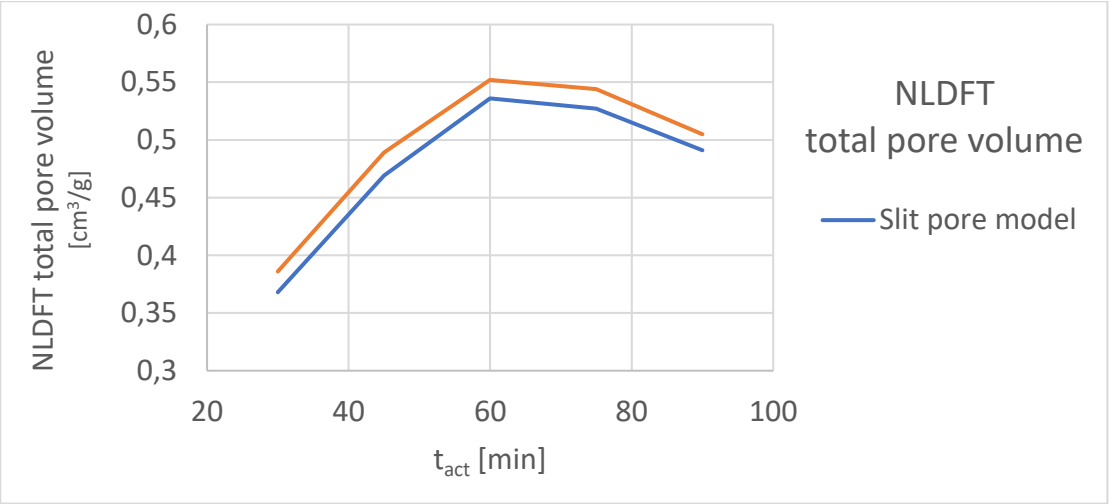

Figure 18. Dependence of the total pore volume on the activation time for AFPAC samples produced at 900°C as calculated by means of the two used NLDFT models.

In order to better describe the samples, we should distinguish between the total pore volume (see table above) and the microporous one. The total pore volume is the sum of micropores and mesopores and macropores contribution while the micropore volume is limited to volume of pore with diameter less than 2 nm. The micropore volume is conventionally measured by the volume of the adsorbed gas, which completely fills the micropores, expressed in terms of bulk liquid at atmospheric pressure and at the temperature of measurement [17]. The following tables report the micropore volume values for all the samples investigated.

Samples	**Micropore volume (cm^3/g)**
	Heterogeneous surface model
APAC3_900C_45 min	0.35
APAC3_900C_60 min	0.58
APAC3_900C_75 min	0.44

Table 10. Micropore volume for APAC3 samples.

Sample	**Micropore volume (cm^3/g)**	
	Slit pore model	Heterogeneous surface model
AFPAC_900C_30min	**0.33**	0.36
AFPAC_900C_45 min	**0.42**	0.44
AFPAC_900C_60 min	0.41	**0.43**
AFPAC_900C_75 min	0.48	**0.50**
AFPAC_900C_90 min	0.43	**0.45**
AFPAC_850C_60 min	**0.29**	0.32
AFPAC_950C_60 min	0.53	**0.55**

Table 11. Micropore volume for AFPAC samples.

A better clue on the microporous structure of the probed samples can be gained by comparing the microporous volume with SSA values estimated by the BET method. The following plot resumes the correlation for all the samples as evaluated with both the used models. As we can clearly see, there is a exact linear correlation between the two values. Therefore, we can deduce two outputs:

1) the nature of the samples can be described as purely microporous as all the sample surface is related to the microporous volume. In fact, only in this case a linear relation can held between SSA and micropore volume.

2) the N_2 adsorption process is exactly described by the IUPAC type I isotherm, the so called “micropore filling” one.

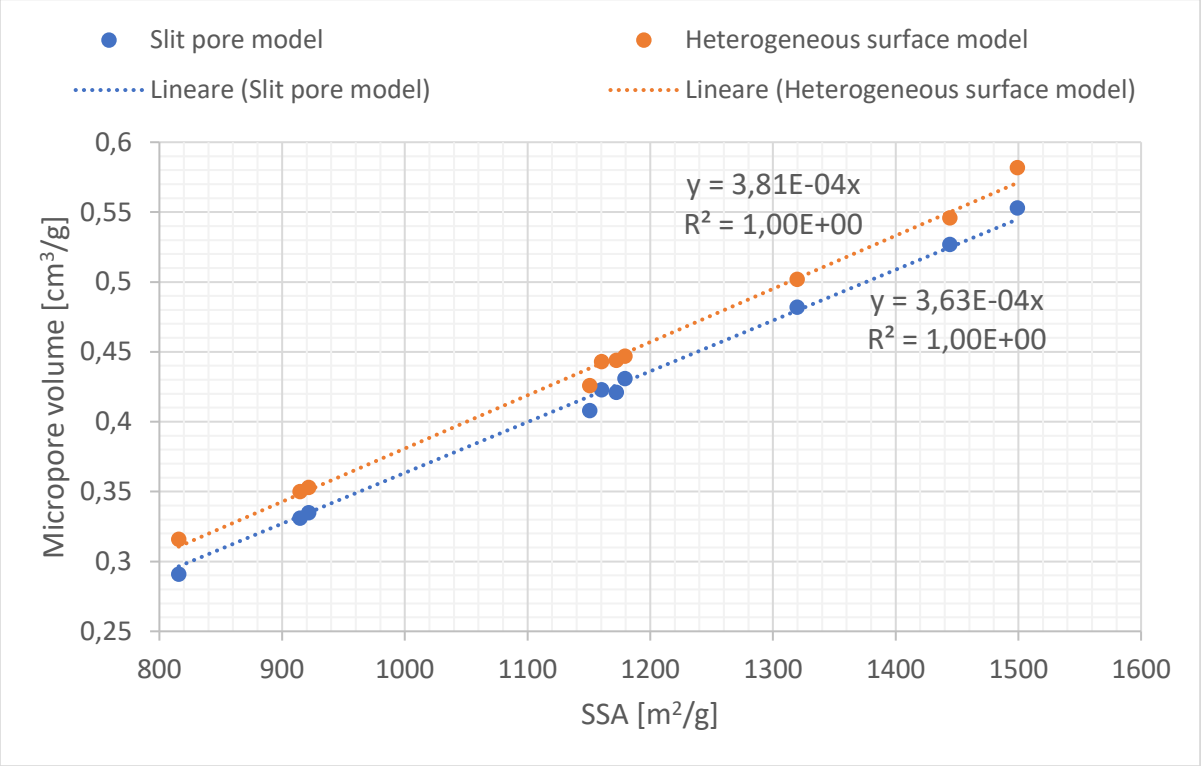

Figure 19. Micropore volume correlation with SSA for all the produced samples. Micropore volume is calculated by means of the two used NLDFT models while the SSA is recovered by the BET method.

4.1.2.2.2 SEM investigation

A direct inspection of the sample morphology in the 100 nm - 100 µm range can be gained by electron microscopy. By means of an electron beam of 15 keV, we collected the secondary electron images from APAC3_900C_60min and AFPAC_900C_60min samples. At low magnification, the fiber structure of the starting material can be easily recognized from both the surfaces. Each individual fiber is 10-20 µm wide and up to 1 mm

long. The fact that interlaced structure of the pellet is maintained after the pyrolysis process is consistent with the solid nature of the pyrolyzed pellet which does not easily shatter.

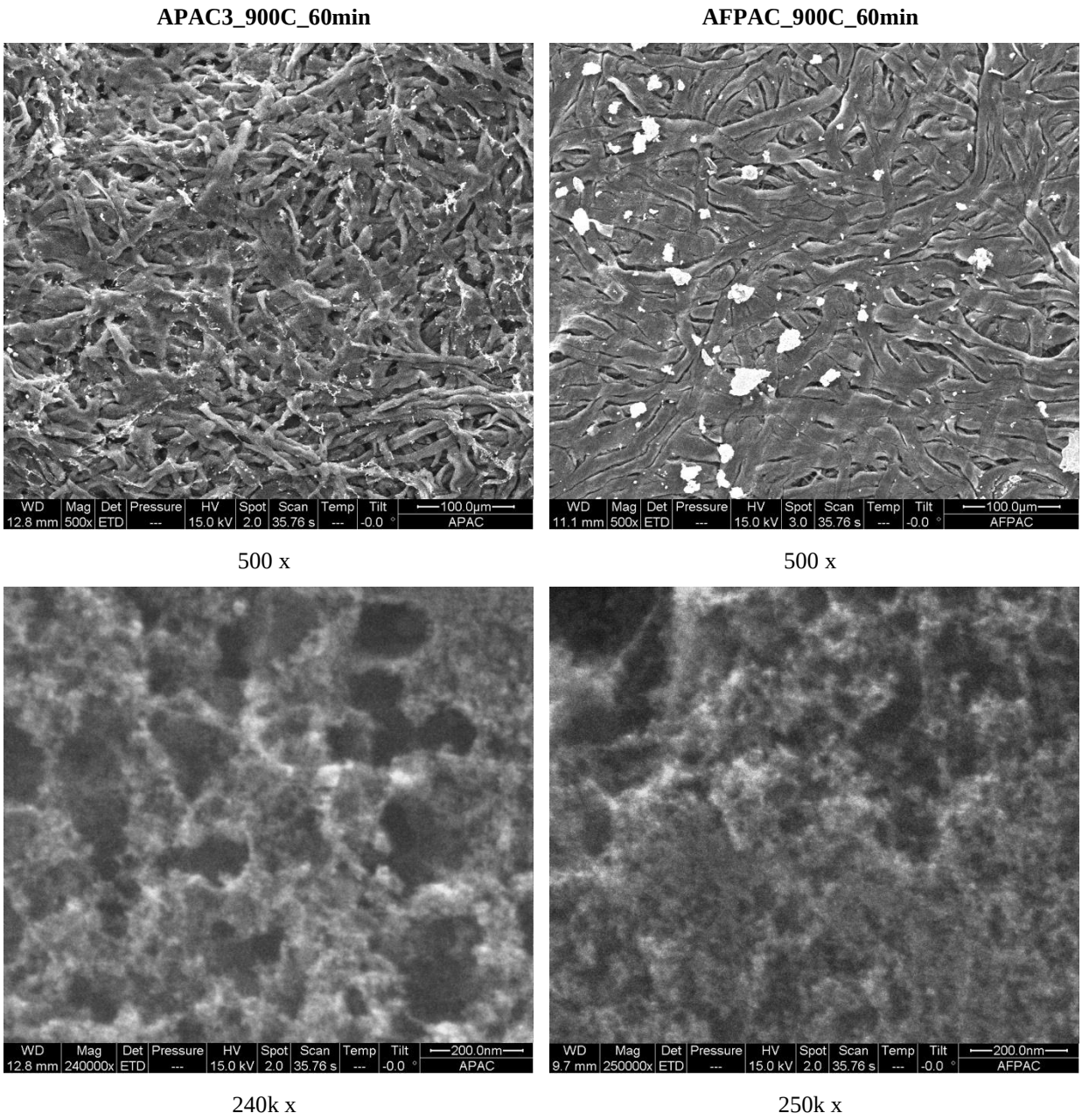

Figure 20. SEM images recorded at 15 keV primary beam. High magnification images are shown in the lower panel.

The mesoscopic structure of the sample is unveiled at the highest magnification allowed by the used SEM apparatus: 240k x. In the lower panel of the previous image, we can appreciate some differences and similarities between the two samples in terms of mesoporosity. In fact, the granular structure of the samples, both in terms of voids and of skeletal structure, shows typical dimensions ranging from few nm to hundreds of nm. With this respect, the APAC3 sample shows slightly larger voids with an average dimension of 48 nm and an apparent porosity is 35% as evaluated by means of ImageJ toolkit, while the AFPAC sample has an average void dimension of 43 nm with a porosity of 36%.

4.1.2.2.3 Hydrogen adsorption

The hydrogen adsorption on the AC samples was evaluated at 77 K and up to 1 bar by means of the ASAP micromeritics 2460 apparatus. All the samples were thermally treated (200 °C) in vacuum overnight before the adsorption cycle measurement.

A typical H_2 adsorption isotherm is depicted in the following figure. For all probed samples, its main features are:

a. A steep increase of the adsorbed H_2 molecules at very low pressures (1 wt% is obtained at only 100 mbar in the present case).
b. A gentle curvature at slightly higher pressures indicating that the sub-monolayer regime, where the linear Henry law is valid, is over.
c. A nearly linear increase for pressures approaching 1 bar which is expected when the simple Langmuir model is not valid. In this case, in fact, a horizontal plateau is expected indicating the formation of a monolayer.

As previously described, the Töth model is used in these cases where the physisorption process does not proceed with a layer-by-layer growth on the condensed film.

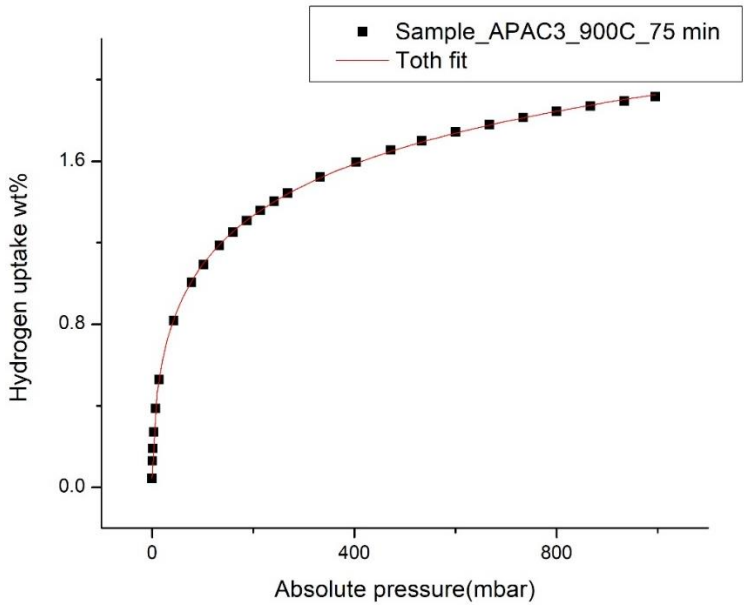

Figure 21. H_2 adsorption isotherm experimental data (squares) collected at 77 K and Töth fitting curve (line) for the APAC3_900C_75min sample.

In the following, we report the full corpus of the acquired data concerning the H_2 adsorption at 77 K. For each adsorption isotherm, the fitting Töth curve is used reported as a continuos line whereas the sata are reported as dots whose dimension are representative of the evaluation error.

We can note that all the measured curves are very nicely reproduced by the 3-parameter fitting curve giving us a strong confidence on the possibility to interpret the parameters as representative of the observed adsorption process.

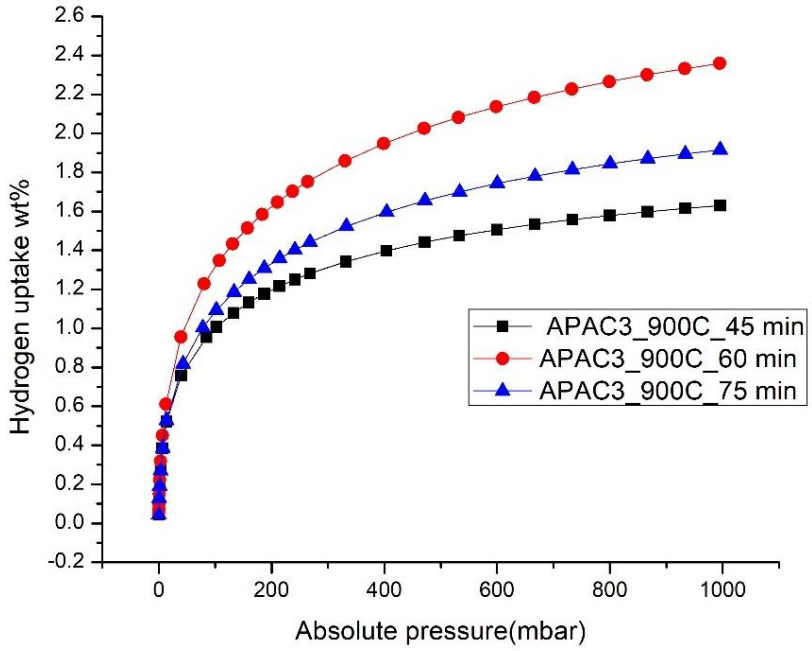

Figure 22. H_2 adsorption isotherm experimental data (markers) collected at 77K and the relative Töth fitting curve (lines) for the APAC3 samples.

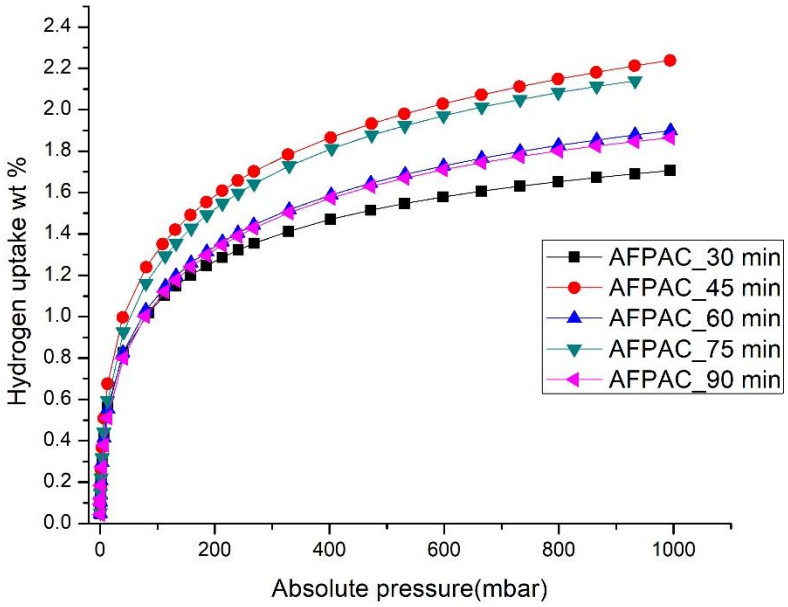

Figure 23. H_2 adsorption isotherm experimental data (markers) collected at 77 K and the relative Töth fitting curve (lines) for the AFPAC samples.

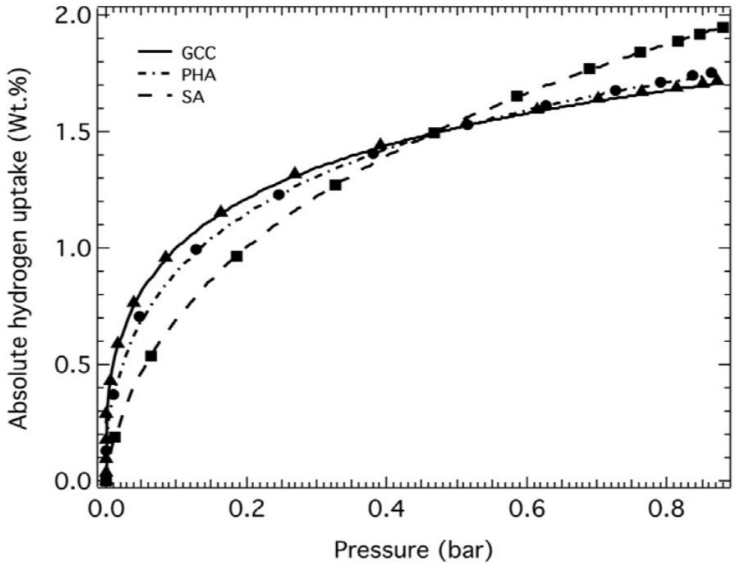

Figure 24. H_2 adsoprtion isotherms, acquired in the same conditions of the measured samples, on three commercial activated carbon samples whose SSA surface is close the the AFPAC samples.

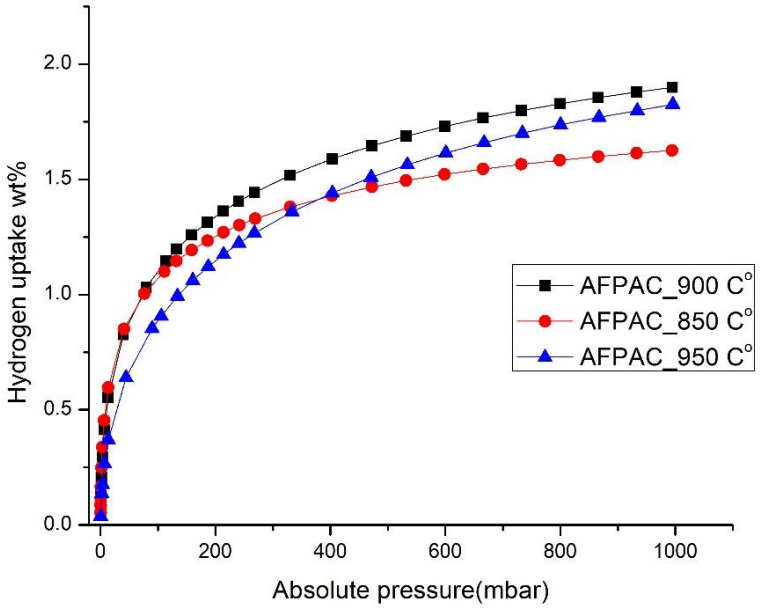

Figure 25. H_2 adsorption isotherm experimental data (markers) collected at 77 K and the relative Töth fitting curve (lines) for the AFPAC samples obtained at different activation temperatures.

The main features of the measured isotherms are reported in the following tables.

Sample	Hydrogen uptake @ 1 bar (wt%)	Surface H_2 density (molec/nm^2)	Toth fit parameters		
			$Wt_{max}\% \pm \Delta\, Wt_{max}\%$	$K \pm \Delta K$	$t \pm \Delta t$
APAC3_900C_45min	1.63	5,3	3.07±0.04	0.34±0.02	0.28±0.03
APAC3_900C_60min	2.36	4,7	5.55±0.10	0.20±0.01	0.26±0.04
APAC3_900C_75min	1.92	5,0	4.28±0.08	0.21±0.01	0.27±0.04

Table 12. Hydrogen adsorption isotherm data and Töth fit parameters for APAC3 samples.

Sample	Hydrogen uptake @ 1 bar (wt%)	Surface H_2 density (molec/nm^2)	Toth fit parameters		
			$Wt_{max}\% \pm \Delta Wt_{max}\%$	$K \pm \Delta K$	$t \pm \Delta t$
AFPAC_900C_30min	1.71	5.6	3.12±0.03	0.42±0.01	0.28±0.03
AFPAC_900C_45min	2.24	5.7	5.12±0.05	0.47±0.02	0.24±0.02
AFPAC_900C_60min	1.90	5.0	4.30±0.06	0.34±0.01	0.25±0.03
AFPAC_900C_75min	2.16	4.9	4.67±0.08	0.23±0.01	0.27±0.04
AFPAC_900C_90min	1.86	4.7	3.73±0.08	0.18±0.01	0.29±0.05
AFPAC_850C_60min	1.63	6.0	2.66±0.02	0.55±0.02	0.29±0.02
AFPAC_950C_60min	1.82	3.8	5.56±0.23	0.067±0.005	0.26±0.07

Table 13. Hydrogen adsorption isotherm data and Töth fit parameters for AFPAC samples.

The hydrogen uptake at 1 bar is divided by the SSA in order to get the surface density of the H_2 molecules in terms of g/m^2. This parameter helps us to evaluate the effectiveness of the sorption process in dependence of the pore morphology. Another way to represent this data is to represent them as H_2 molecules per nm^2 (see third column). The following figures show how this values changes with the different samples together with a similar calculation relative to the asymptotic adsorption value as extracted from the $Wt\%_{max}$ parameter of the Töth fitting curve.

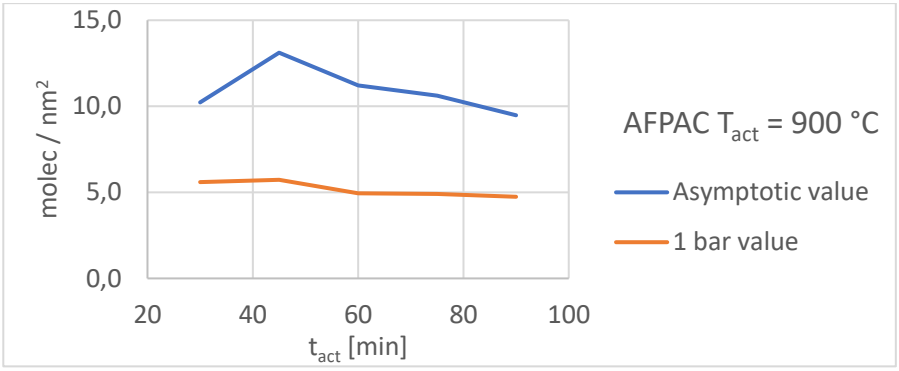

Figure 26. Molecular H_2 surface density for the AFPAC samples obtained at 900 °C activation temperatures and different activation time.

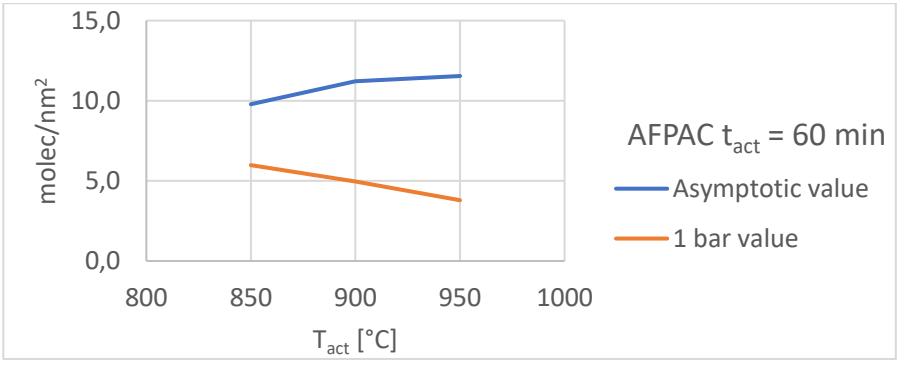

Figure 27. Molecular H_2 surface density for the AFPAC samples obtained at different activation temperatures and a fixed activation time (60 min).

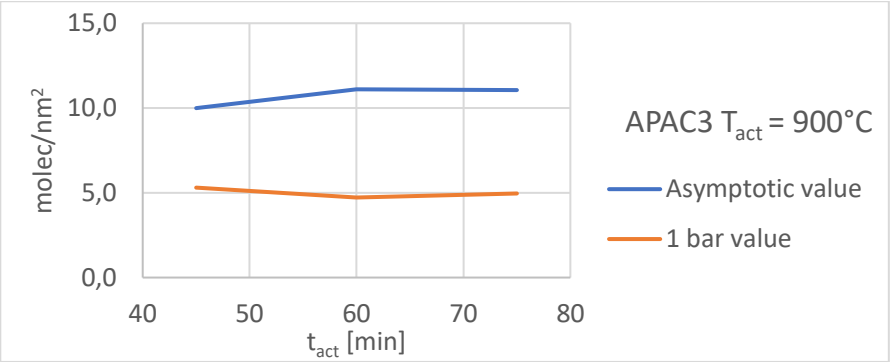

Figure 28. Molecular H_2 surface density for the APAC3 samples obtained at 900 °C activation temperatures and different activation time.

It is interesting to note that the adsorption at 1 bar reaches values very close to the ideal monolayer coverage. The latter is the condition in which the steric occupation of the surface by H_2 molecules forming a layer with the liquid H_2 density is achieved. In this case, we could expect 7 H_2 molecules per nm^2. Our values are varying between 3.8 and 6.0 molecules per nm^2 giving a direct hint on the most effective surfaces at 1 bar and 77 K. The AFPAC samples produced with a small activation time or at lower temperature have surface densities close to the maximum i.e. at 80-85% of 1 ML equivalent coverage. On the other hand, at high activation temperatures the pore surface become very less effective having densities close to 4 molecules per nm^2.

For higher pressures, the extrapolated asymptotic adsorption value is given by the surface densities calculated from the $Wt\%_{max}$ parameter of the Töth fitting curve.

Surprisingly, this values are beyond the ideal ML regime reaching for the AFPAC_900C_45min sample a value (13.1 molec/nm^2) very close to a double equivalent layer.

This beaviuor was already recorded for activated samples with an high fraction of micropores [18-19] where a density close to the liquid phase was measured in ultra-micropores whose typical dimension was 7 Å.

A closer look to the trends of the Töth curve parameters is giving us further details (see following figures).

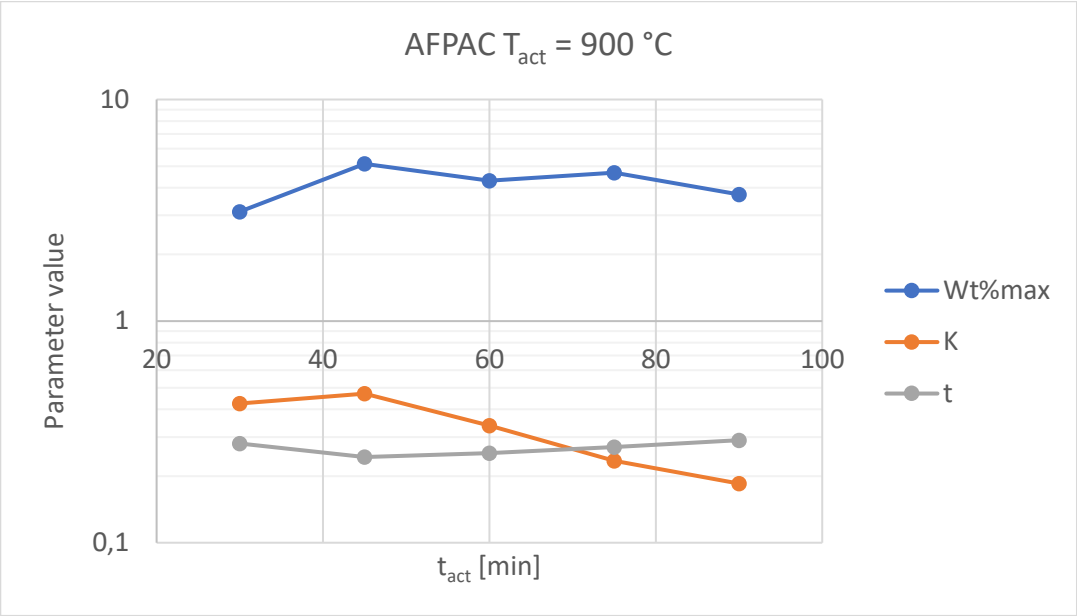

Figure 29. Töth curve parameters for the AFPAC samples obtained at 900°C activation temperatures and different activation time.

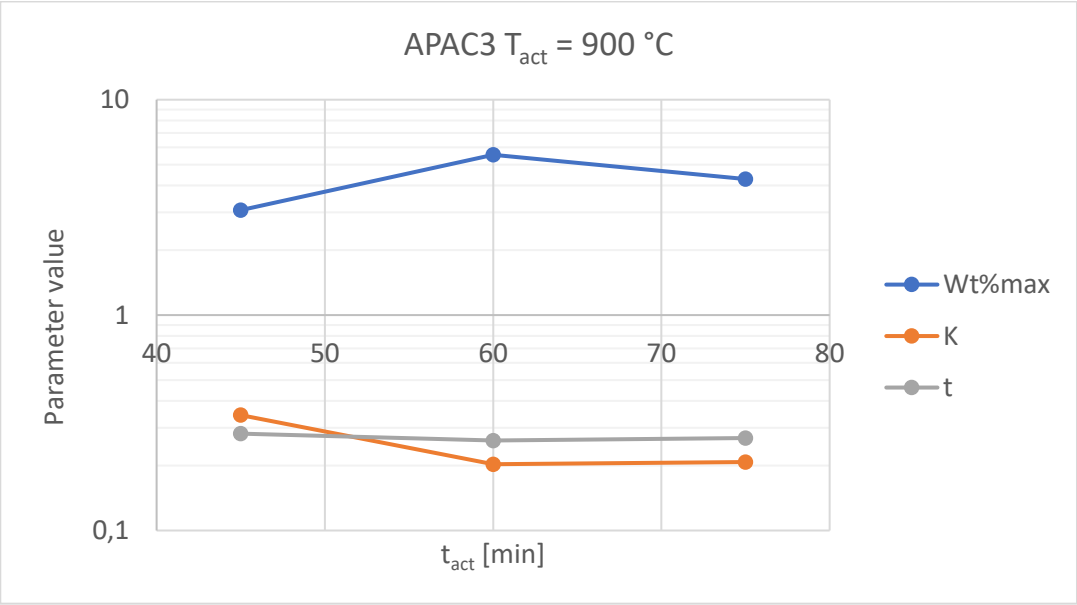

Figure 30. Töth curve parameters for the APAC3 samples obtained at 900 °C activation temperatures and different activation time.

As a first point, the equilibrium constant K is strictly related to the observed H_2 surface density at 1 bar and 77 K. Also in this case, the highest value is recorded for the AFPAC_900C_45min sample and it decrease with the activation time.

The t parameter values are nearly constant and similar for both the sample series. The average value, 0.27, has to be interpreted as and indication fo a very heterogeneous surface.

This is corroboratong the resul given by the NLDFT results which showed a better fitting fot this kind of surface model.

Another important observation comes from the comparison of the adsorption and desorption curves. For all the probed samples, there is no evidence of hysteresis or H_2 trapping as reported in similar samples [18-19].

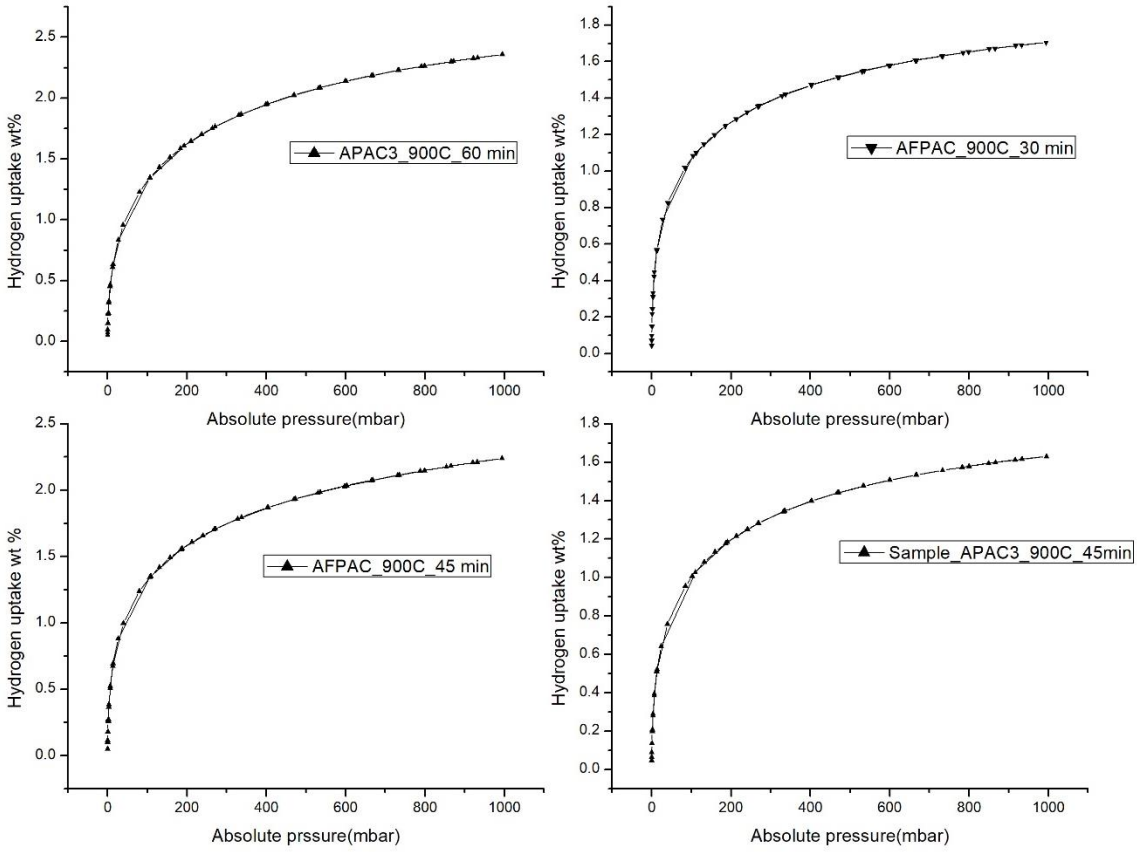

Figure 31. Experimental data for hydrogen adsorption-desorption curves at 77 K and up to 1 bar.

4.1.2.3 Impregnation with copper

In order to synthesize and to tune SSA and pore's size and shapes, as suggested by the literature, we performed a metal impregnation [20,21]. It has in fact been shown that this method allows changing the width of pores of ACs, increasing or decreasing the volume of the micropores [22,23]. Therefore, to evaluate the effects of metallic, particularly copper (Cu), impregnation at different concentrations of amorphous cellulose was performed. Subsequently, we have synthesized activated carbon samples to obtain homogeneous microporosity and high SSA and in view to maximize their hydrogen adsorption capacity.

So, starting from flakes amorphous cellulose (as it lends itself better to the impregnation process in solution), three samples were synthesized as follow, step 1: in a solution of 100 ml of distilled water have been added three different concentrations of copper gluconate (1, 2 and 5%) in which two grams of flakes amorphous cellulose were immersed; the compound mechanically was stirred for 24 hours at a temperature of 40 °C to carry out slow evaporation of the solvent. Step 2: the obtained materials were placed in a vacuum apparatus for about 5/6 hours in order to eliminate residual moisture. Step 3: The dry materials were placed in a hydraulic machine and a pressure of 5000 kg/cm^2 was loaded on them for 5 minutes. After the compression, the dry material was in the form of cylindrical pellets.

The samples are subsequently subjected to a heat treatment (pyrolysis/activation process) deciding to set, on the basis of the previous experimentation, the following parameters: CO_2 flow of 0.5 Nl/min, activation temperature of 1173 K and activation time of 60 min (see Table 14). The samples obtained, AFPAC_Cu1% (with 1%), AFPAC_Cu2% (with 2%) and AFPAC_Cu5% (with 5%), were compared with the non-impregnated reference sample, AFPAC (with 0%).

Table 14. AFPAC and AFPAC_Cu1/2/5% synthesis parameters.

Sample	Amorphous cellulose mass [g]	Copper gluconate mass [g]	Impregnated pellet mass [g]	Activated pellet mass [g]	Burn-off [wt%]	Synthesis parameters	
						Temperature [K]	Time [min]
AFPAC	1,98	-	-	0,18	91,1	1173	60
AFPAC_Cu1%	2,05	0,08	2,07	0,16	92,1	1173	60
AFPAC_Cu2%	2,05	0,16	2,09	0,16	92,5	1173	60
AFPAC_Cu5%	2,05	0,39	2,28	0,19	91,5	1173	60

4.1.2.3.1 Sample characterization

Nitrogen adsorption isotherms and pore size distribution (PSD) are presented in Figure 32. The parameters of the pore structure such as pore volumes and specific surface area (SSA) calculated from the isotherms are collected in Table 15.

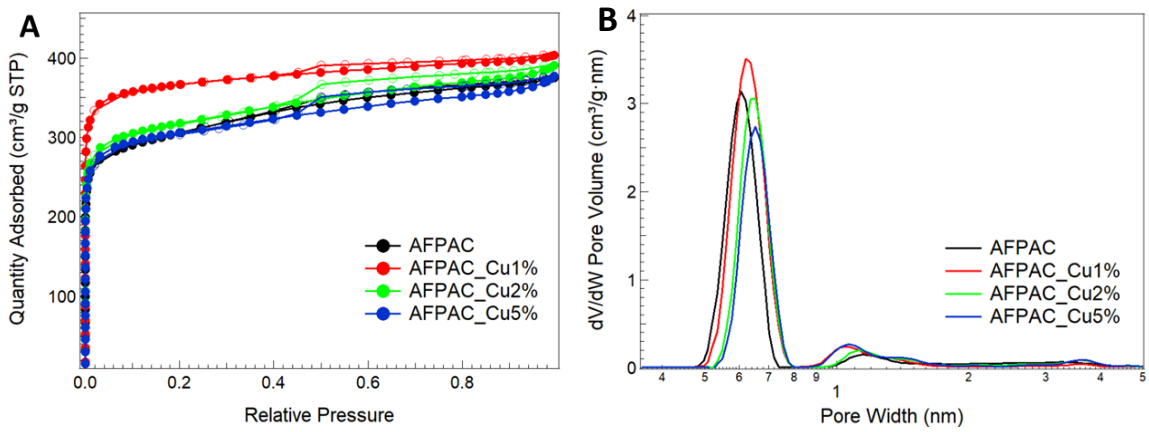

Figure 32. A) Nitrogen adsorption isotherms and B) Pore size distributions of the samples tested.

Looking at the values reported in Table 15 below, it is noteworthy that the impregnation of the amorphous cellulose with Cu particles, even in a very small amount, leads to a changing in the sample's structural parameters. In particular, the addition of 1% of Cu within the raw material allows to obtain an increase of S_{BET} of almost 25% in the synthetized activated carbon sample. In contrast, a decrease compared to AFPAC_Cu1% is observed by adding more percentage of Cu, in particular we obtained S_{BET} values of 1215 m^2/g and 1172 m^2/g for the AFPAC_Cu2% and AFPAC_Cu5% respectively.

Table 15. Samples textural properties calculated from the adsorption isotherms.

Sample	**S_{BET}**	**$V_{<0.7nm}$**	**$_{0.7nm}<V_{<2nm}$**	**V_{mic}**	**V_{mes}**	**V_T**	**V_{mic}/V_T**
	[m^2/g]	[cm^3/g]	[cm^3/g]	[cm^3/g]	[cm^3/g]	[cm^3/g]	[%]
AFPAC	1151	0.36	0.07	0.43	0.13	0.56	77
AFPAC_Cu1%	1441	0.41	0.12	0.53	0.05	0.58	91
AFPAC_Cu2%	1215	0.31	0.12	0.43	0.13	0.56	77
AFPAC_Cu5%	1172	0.27	0.15	0.42	0.12	0.54	78

The AFPAC_Cu1% has a porosity very different from the other samples since even if the total pore volume (V_T) is almost the same, the microporosity (V_{mic}) it is clearly greater. In fact, in the AFPAC_Cu1% sample the microporous structure is predominant (around 91% of its total pore volume) although some mesoporosity (V_{mes}) exists as is possible to note by the slightly increase of the N_2 adsorption isotherms (see Figure 32A). In particular is present a higher fraction of ultramicropores (d < 0.7 nm) that represents 77.4% of the sample's microporosity. This kind of pores are those expected to be the most effective in

the gas adsorption processes. The other two impregnated samples (2 and 5%) instead show no improvement in structural features compared to the non-impregnated sample (AFPAC). The SEM images of AFPAC and the impregnated samples (AFPAC_Cu1/2/5%) are shown in Figure 33A, B, C, D respectively, with a magnification of 100000X (500 nm scale).

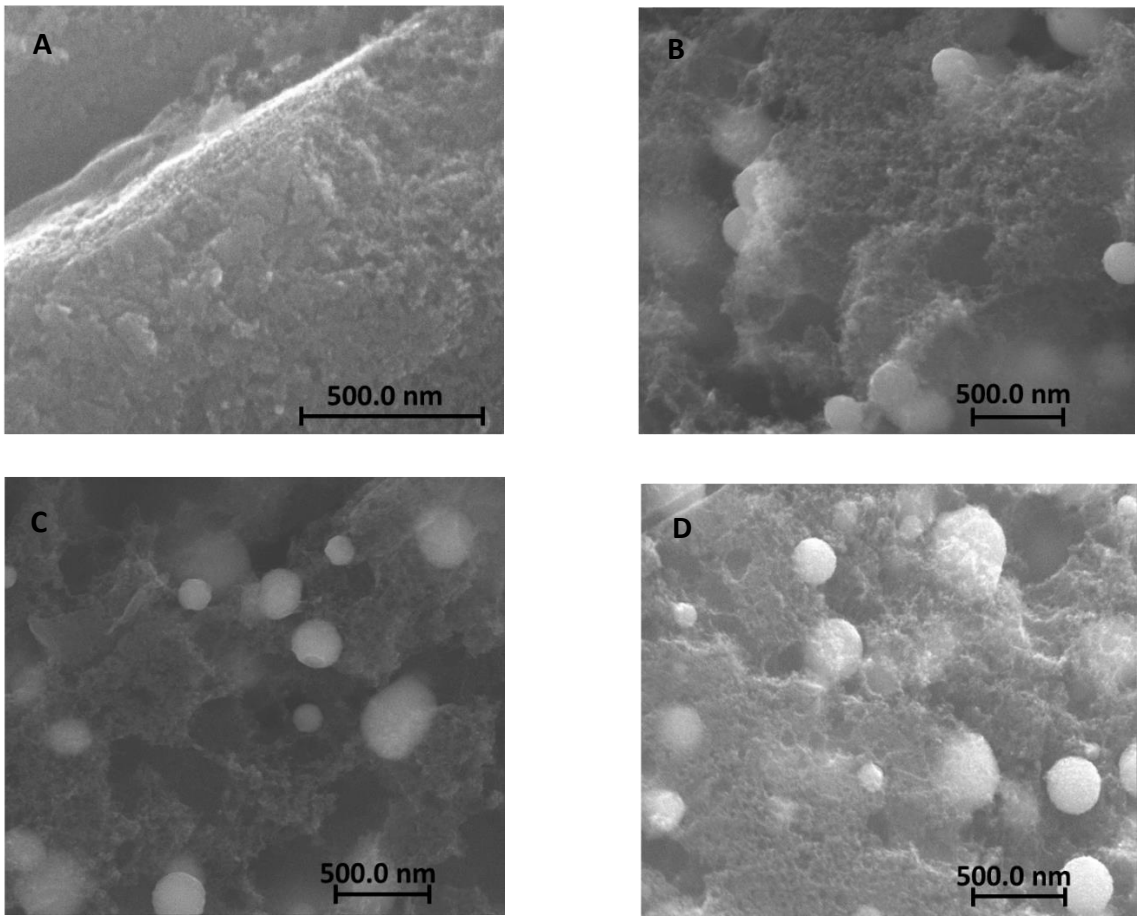

Figure 33. SEM images of the A) AFPAC, B) AFPAC_Cu1%, C) AFPAC_Cu2% and D) AFPAC_Cu5% samples with 500 nm scale.

Looking Figure 33 the increasing amount of Cu within the different samples it is evident, where is possible to see as the metal particles are incorporated into the porous carbon matrix uniformly extended over the whole area. As expected, the AFPAC sample shows its porous structure without presence of any Cu particle (Figure 33A). From SEM analysis we can assert that all AFPAC and AFPAC_Cu1/2/5% samples show a uniform porosity and, as also confirmed by BET/PSD measurements/analysis, typical dimensions of the hollow structures (average pore size) around few nanometers.

Figure 34A shows the H_2 adsorption/desorption isotherms measured on the AFPAC samples at room temperature condition (≅ 298 K) and up to pressure of 80 bar. The amount of H_2 adsorbed is below 0.5 wt% in line with many other materials tested in the same

conditions [24,25]. As we expect, the best adsorption (0.35 wt%) is recorded by the sample impregnated at 1% (AFPAC_Cu1%), thanks to its higher ultramicroporosity.

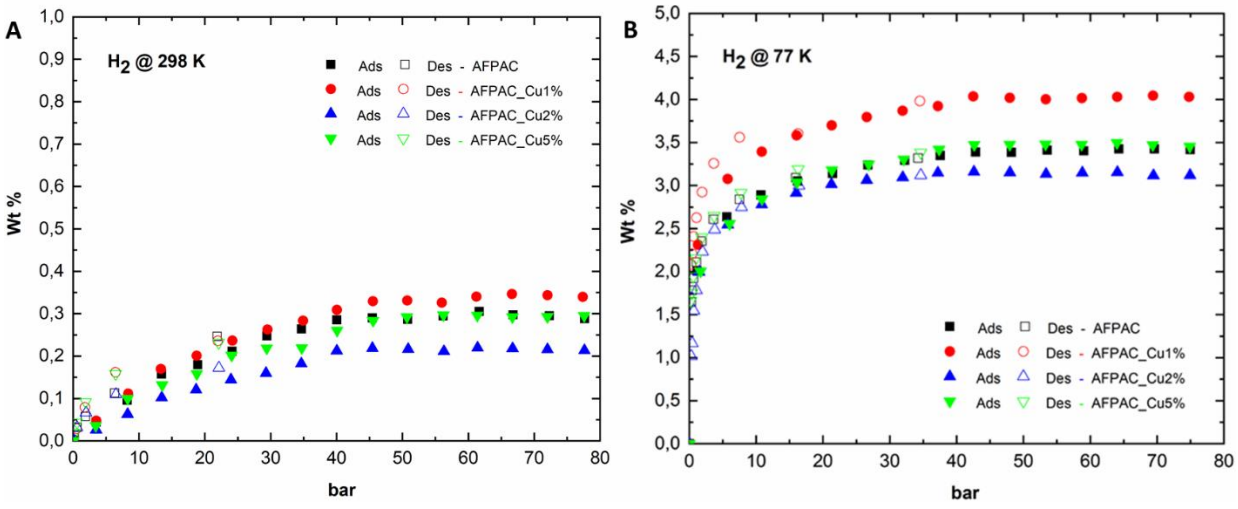

Figure 34. Hydrogen adsorption/desorption isotherms up to 80 bar for the AFPAC and impregnated samples at A) 298 K and B) 77 K.

At liquid nitrogen temperature (Fig. 34B) the adsorption capacity increase as expected for all samples, leading to uptake value between 3 and 4 wt% at the maximum analyzed pressure. Also, in this case, the best adsorption capacity (4.1 wt%) occurs for the AFPAC_Cu1% sample, which is higher than the value indicated by the empirical relation known as "Chahine rule" [25,26] predicting the adsorption of around ~1 wt% H_2 for each 500 m^2g^{-1} of SSA. In particular, for the sample impregnated at Cu1% a ~ 11% increase in the amount of H_2 adsorbed compared to AFPAC sample was found. This behavior can be linked to its highest microporosity and, particularly, to the highest volume in the ultramicroporous region (d < 0.7 nm) in which the gas-surface interactions are stronger [27-29]. Increase in the percentage of Cu impregnation lead to a deterioration of the performances with an amount of adsorbed H_2 similar, or even worst, to that of pure AFPAC.

Finally, a preliminary survey on the chemical composition of the samples was investigated by X-ray Photoelectron Spectroscopy (XPS) technique. Figure 35 shows the survey scans of the AFPAC samples before and after impregnation, while the atomic composition data are reported in Table 16. All the expected elements are observed and there is no indication of presence of any kind of contaminant. C is the main constituent of the samples, while the O signature represents a small component. After impregnation, the Cu component arises in the survey scans. Although the atomic percentage of Cu is comparable for the AFPAC 1% and AFPAC 2% samples, the atomic percentages of copper indicate that the impregnation step is more efficient as the Cu concentration increases.

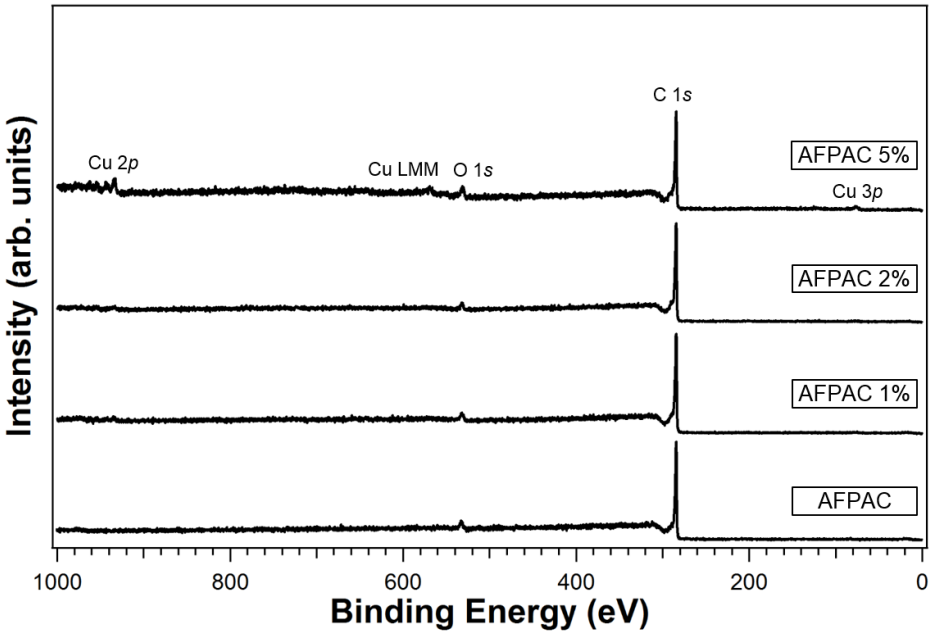

Figure 35. Survey scan XPS spectra of AFPAC samples before and after impregnation steps.

Table 16. Stoichiometric analysis from XPS data.

Sample	C	O	Cu
AFPAC	96.3	3.7	-
AFPAC 1%	95.2	4.2	0.6
AFPAC 2%	95.9	3.7	0.4
AFPAC 5%	92.4	5.9	1.7

4.1.3 Conclusion remarks

We have reported the preparation of activated carbon samples and their characterization for H_2 adsorption. The samples were prepared by using as starting raw material the amorphous cellulose and adopting a pyrolysis method. By varying the pyrolysis parameters, samples of different porosity and H_2 affinity were obtained.

As a first result, we obtain samples with a very high degree of microporosity and, furthermore, the larger part of the pores has diameter lower than 1 nm having an average value between 5 and 6 Å. This ultra-microporous samples show high SSA values as evaluated by the BET method reaching 1500 m^2/g as a maximum value.

The activated carbon obtained from flakes has the better morphological features in terms of extension of the specific surface area and microporosity.

The reported morphology strongly influences the H_2 adsorption properties. The adsorbed H_2 molecules quantities at 1 bar and 77 K reach values very close to the ideal monolayer coverage in which H_2 molecules form a single layer with the liquid H_2 density on the surface. The observation of a maximum value of 6.0 molecules per nm^2 with respect to the ideal ML value of 7 molecules per nm^2 gives a direct hint on the high effectiveness of the sample surfaces at 1 bar and 77 K. The AFPAC samples produced with a small activation time or at lower temperature have surface densities close to the maximum i.e. at 80-85% of 1 ML equivalent coverage. On the other hand, at high activation temperatures the pore surface become very less effective having densities close to 4 molecules per nm^2.

The surface densities calculated from the $Wt\%_{max}$ parameter of the Töth fitting curve tell us that the extrapolated asymptotic adsorption values for higher pressures are beyond the ideal ML regime reaching for the AFPAC_900C_45min sample a value (13.1 molec/nm^2) very close to a double equivalent layer. A similar behaviour was already recorded for activated samples with a high fraction of micropores where a density close to the liquid phase was measured in ultra-micropores whose typical dimension was 7 Å.

Regarding the copper-impregnated samples, we can state that only the AFPAC_Cu1% sample showed a substantial improvement in structural properties compared to the non-impregnated sample, in terms of an increase in SSA (+ 25%) and an improvement in porosity with a greater development of microporosity (+ 23%). While the structural features are not improved for the impregnated samples with higher concentration (2 and 5%). This is confirmed by the hydrogen adsorption characterization, where the highest storage capacities (at both tested temperatures, 298 and 77 K) are shown by the sample with 1% copper percentage, while reducing with increasing concentration.

Finally, we can say that the adopted procedures for the production of super / ultramicroporous samples from amorphous cellulose gave encouraging results in terms of usefulness in H_2 storage application, highlighting what the key parameters may be in activation processes or in sample preparation methods.

References

1. Sing KSW. Adsorption by Active Carbons. Adsorpt. by Powders Porous Solids, Elsevier; 2014, p. 321–91. doi:10.1016/B978-0-08-097035-6.00010-3.

2. Xia Y, Yang Z, Zhu Y. Porous carbon-based materials for hydrogen storage: advancement and challenges. J Mater Chem A 2013;1:9365. doi:10.1039/c3ta10583k.

3. Ho TM, Howes T, Bhandari BR. Encapsulation of gases in powder solid matrices and their applications: A review. Powder Technol 2014; 259:87-108. doi:10.1016/j.powtec.2014.03.054.

4. Kunowsky M, Suárez-García F, Linares-Solano Á. Adsorbent density impact on gas storage capacities. Microporous Mesoporous Mater 2013; 173:47–52. doi:10.1016/j.micromeso.2013.02.010.

5. Ravikovitch P, Vishnyakov a, Russo R, Neimark A. Unified Approach to Pore Size Characterization of Microporous Carbonaceous Materials from N2,Ar,and CO2 Adsorption Isotherms. Langmuir 2000;16:2311–20.

6. Oh H, Gennett T, Atanassov P, Kurttepeli M, Bals S, Hurst KE, et al. Hydrogen adsorption properties of platinum decorated hierarchically structured templated carbons. Microporous Mesoporous Mater 2013;177:66-74.doi:10.1016/j.micromes.2013.04.020.

7. Beckner M, Dailly A. Adsorption Enthalpy Calculations of Hydrogen Adsorption at Ambient Temperature and Pressures Exceeding 300 bar. Am J Anal Chem 2013;04:8–16. doi:10.4236/ajac.2013.410A3002.

8. Schlapbach L, Züttel a. Hydrogen-storage materials for mobile applications. Nature 2001;414:353–8. doi:10.1038/35104634.

9. Langmuir I. THE CONSTITUTION AND FUNDAMENTAL PROPERTIES OF SOLIDS AND LIQUIDS. II. LIQUIDS. 1. J Am Chem Soc 1917;39:1848–906. doi:10.1021/ja02254a006.

10. Thomas KM. Hydrogen adsorption and storage on porous materials. Catal Today 2007;120:389–98. doi:10.1016/j.cattod.2006.09.015.

11. Chang F, Zhou J, Chen P, Chen Y, Jia H, Saad SMI, et al. Microporous and mesoporous materials for gas storage and separation: A review. Asia-Pacific J Chem Eng 2013;8:618–26. doi:10.1002/apj.1717.

12. Pore Size Heterogeneity and the Carbon Slit Pore: A Density Functional Theory Model; Lastoskie, Gubbins, and Quirke; Langmuir 1993,9, pp. 2693-2702.

13. Determination of Pore Size Distribution from Density Functional Theoretic Models of Adsorption and Condensation within Porous Solids; Olivier and Conklin; Presented at the International Symposium on the Effects of Surface Heterogeneity in Adsorption and Catalysis on Solids; Kazimier Dolny, Poland, July 1992.

14. Determination of Pore Size Distribution from Density Functional Theory: A Comparison of Nitrogen and Argon Results. In Characterization of Porous Solids; Olivier, Conklin, and Szombathely; Proceedings of the IUPAC Symposium (COPS III); Elsevier Press: Marselle, France, 1993.

15. J. Jagiello and J. P. Olivier, 2D-NLDFT Adsorption Models for Carbon Slit-Shaped Pores with Surface Energetical Heterogeneity and Geometrical Corrugation. Carbon (2013) 55, 70-80.

16. J. Jagiello and J. P. Olivier, Carbon Slit Pore Model Incorporating Surface Energetical Heterogeneity and Geometrical Corrugation. Adsorption (2013) 19, 777-783.

17. http://old.iupac.org/reports/2001/colloid_2001/manual_of_s_and_t/node17.html.

18. Francesco Demetrio Minuto, Alfonso Policicchio, Alfredo Aloise, Raffaele Giuseppe Agostino, Liquid-like hydrogen in the micropores of commercial activated carbons., International Journal of Hydrogen Energy 07/2015, DOI:10.1016/j.ijhydene.2015.07.029.

19. Francesco Demetrio Minuto, Rafael Balderas, Alfonso Policicchio, Michael Hirscher, Raffaele G. Agostino, Assessment methodology of promising porous materials for near ambient temperature hydrogen storage applications, International Journal of Hydrogen Energy, Volume 43, Issue 31, 2018, Pages 14550-14556DOI: 10.1016/j.ijhydene.2018.06.004.

20. Bhatnagar A, Hogland W, Marques M, Sillanpää M. An overview of the modification methods of activated carbon for its water treatment applications. Chem Eng J 2013;219:499–511. https://doi.org/10.1016/j.cej.2012.12.038.

21. Shafeeyan MS, Daud WMAW, Houshmand A, Shamiri A. A review on surface modification of activated carbon for carbon dioxide adsorption. J Anal Appl Pyrolysis 2010;89:143–51. https://doi.org/10.1016/j.jaap.2010.07.006.

22. Haro M, Ruiz B, Andrade M, Mestre AS, Parra JB, Carvalho AP, et al. Dual role of copper on the reactivity of activated carbons from coal and lignocellulosic precursors. Microporous Mesoporous Mater 2012. https://doi.org/10.1016/j.microm.2011.07.005.

23. Bradley RH. Surface studies of Cu/Cr/Ag impregnated microporous carbons. Appl Surf Sci 1995;90:271–6. https://doi.org/10.1016/0169-4332(95)00167-0.

24. Thomas KM. Hydrogen adsorption and storage on porous materials. Catal Today 2007;120:389–98. doi:10.1016/j.cattod.2006.09.015.

25. Gross KJ, Carrington KR, Berkeley C, Purewal J, Company FM, Dantzer P, et al. Recommended Best Practices for the Characterization of Storage Properties of Hydrogen Storage Materials. H2 Technol Consult LLC 2012;Hydrogen S:579.

26. Panella B, Hirscher M, Roth S. Hydrogen adsorption in different carbon nanostructures. Carbon N Y 2005;43:2209–14. doi:10.1016/j.carbon.2005.03.037.

27. Gogotsi Y, Portet C, Osswald S, Simmons JM, Yildirim T, Laudisio G, et al. Importance of pore size in high-pressure hydrogen storage by porous carbons. Int J Hydrogen Energy 2009;34:6314–9. doi:10.1016/j.ijhydene.2009.05.073.

28. Wróbel-Iwaniec I, Díez N, Gryglewicz G. Chitosan-based highly activated carbons for hydrogen storage. Int J Hydrogen Energy 2015; 40:5788-96. doi:10.1016/j.ijhydene.2015.03.034.

29. Zhao W, Fierro V, Zlotea C, Aylon E, Izquierdo MT, Latroche M, et al. Activated carbons with appropriate micropore size distribution for hydrogen adsorption. Int J Hydrogen Energy 2011;36:5431–4. doi:10.1016/j.ijhydene.2010.12.137.

5. Conclusions

The activity research was performed in order to develop, characterize and compare a different kind of porous nanostructured materials. In particular, various preparation methods were studied and tested based on the selected material type, and the processes and key parameters for the porosity development were analyzed in detail. Finally, the gas adsorption properties for energy applications were verified and evaluated.

To carry out these activities, various investigation techniques were used, such as scanning electron microscopy (SEM) and transmission electron microscopy (TEM), X-ray diffraction (XRD), X-ray analysis energy dispersion (EDX), Fourier transform infrared spectroscopy (FTIR), Sievert-type volumetric techniques.

In the following, was resumed the main findings for each analyzed system and a general note on the entire PhD work.

- ✓ ***Activated Carbons (ACs) samples from Pinecones (Pinus pinea).***

  Pinecones, a common biomass waste, has an interesting composition in terms of cellulose and lignin content that makes them excellent precursors in various activated carbon production processes. The synthesized, nanostructured, activated carbon materials show textural properties, a high specific surface area (up to 1173 m^2/g), and a large volume of micropores, which are all features that make them suitable for various applications ranging from the gas adsorption to energy storage. For this purpose, activated carbon samples from pinecones were prepared using chemical activation with different KOH/precursor ratio to evaluate their hydrogen adsorption capacity at liquid nitrogen temperatures (77 K) at pressures of up to 80 bar and methane adsorption properties at room temperature (≅ 298 K) and pressure up to 35 bar using for both gases a volumetric Sievert-type apparatus.

  A complete and detailed characterization of the synthesized activated carbon samples was obtained using nitrogen adsorption/desorption measurements at liquid nitrogen temperature (77 K), for the textural properties' analysis, by scanning electron microscopy and X-ray diffraction for topography and long-range order estimation, and by wavelength dispersive spectrometry for chemical composition, respectively. All the adsorption data were analyzed by the Tóth isotherm model.

  The results showed that chemical activation induced the formation of an optimal pore size distribution for hydrogen adsorption centered at about 0.5 nm and the proportion of micropore volume was higher than 50%, which resulted in an

adsorption capacity of 5.5 wt% at 77 K and 80 bar; this was an increase of as much as 150% relative to the one predicted by the Chahine rule. At the same time, the probed activated carbon samples show both higher methane storage values for pressures up to 35 bar (the maximum value reached is 15 wt%) and totally reversible methane uptake up to many cycles without any treatment in between indication of very stable properties.

Therefore, the experimental work showed could represent a good alternative method to the gas storage through the use of eco-compatible nanostructured materials.

- ✓ ***Activated Carbons (ACs) samples from Posidonia Oceanica and Wood chips.***

  The goal of this experimentation has been to investigate the feasibility to use a local biomass (Posidonia Oceanica and Wood chips), as a raw precursor, to the production of activated carbons (AC) with a high surface area and remarkable hydrogen (H_2) adsorption properties.

  Biomasses (particle size of 0.3-0.4 mm) were pyrolyzed at 600 °C with a heating rate of 5 °C/min under an argon atmosphere. The biochar obtained from the carbonization step was chemically activated with KOH. The activation methodology induces a considerable improvement of the properties of the porous carbon in terms of carbon content (from 58 to 69 wt% to 93-96 wt%), surface area (from 41 to 425 m^2/g to 2810-2835 m^2/g) and H_2 adsorption in cryogenic condition (from 0.1 wt% to over 5 wt%).

- ✓ ***Activated Carbon Fibers (ACFs) samples from commercial Kevlar®.***

  This study reports the development of activated carbon fibers prepared from commercial Kevlar® through an innovative pyrolysis method, consisting of carbonization in inert ambient and subsequent physical activation in oxidizing atmosphere, using a unique apparatus. Varying three key parameters, time (range 60-240 min), temperature (range 1023-1123 K) and gas-flow (0.3/0.9/1.2 Nl/min of CO_2), the correlation between the activation procedure and the resulting samples structure was evaluated. The best results in terms of microporosity and gas adsorption properties have been obtained by reducing the activation time. Furthermore, the purpose has been to optimize the characteristics in terms of Specific Surface Area, Total Pore Volume and optimal Pore Size Distribution. The method made it possible to develop an adsorbent material with a high fraction of micropores up to 94% of the total pore volume, straddling the supermicroporosity

(0.7-2 nm) and ultramicroporosity (<0.7 nm) region. Such textural properties have resulted in high gases storage capacities, tested at different temperatures (280, 298, 314 K), with maximum uptake of 46 wt% for CO_2 and almost 10 wt% for CH_4. All produced samples were characterized by helium picnometry to estimate skeletal density, Scanning Electron Microscopy to obtain morphological information, porosimetry to know structural properties. The adsorption behaviour was tested using a Sievert-type apparatus in the pressure range of 0-15 bar for CO_2 and 0-40 bar for CH_4.

- ✓ ***Ordered Mesoporous Silica.***

  H_2 adsorption properties of ordered mesoporous silica prepared with different ratios of functionalized precursors have been studied. Silica particles were synthesized by sol-gel method, with tetradecyltrimethyl ammonium bromide (C14) or dodecyl trimethyl ammonium bromide (C12) as structure directing agents, and tetraethoxysilane (TEOS) and methyltriethoxysilane (MTES), by varying the molar ratio of the two precursors. The porosity and microstructure of the materials in function of the MTES/TEOS ratio were evaluated by using nitrogen adsorption and X-ray diffraction and showed that the samples contained amorphous and ordered porous domains. Stable porous structure able to hold H_2 molecule and give them back when required has been obtained. The higher hydrogen adsorption capacities measured at 77 K were obtained for the samples synthesized with reduced amount of MTES, followed by the samples with no MTES, with both C12 and C14 directing agents. Increased amount of MTES precursor led to lowering of the adsorption capacity. The increase of the adsorption capacity already below 20 bar, observed for all samples, could be an advantage for practical application since a lower pressure is preferable. The study revealed the influence of the synthesis parameters to the hydrogen sorption performance and serves as guidance for applications as hydrogen adsorptive materials.

- ✓ ***NaX nanozeolite-geopolymermonolith.***

  A NaX nanozeolite-geopolymermonolith, with hierarchical porosity, has been produced by a one-pot hydrothermal synthesis using metakaolin as alluminosilicate source and a sodium silicate solution as activator. Its final composition, reported in terms of oxides, is $1.3–Na_2O–3.0SiO_2–1Al_2O_3–12H_2O$.

  Its microstructural and chemical features and CO_2 adsorption performance have been investigated. The microstructure of the composite is characterized by NaX

zeolite nanocrystals glued by the geopolymeric binder to form a complex three-dimensional network of pores. Overall porosity resulted ~23.5%, whereas compressive strength is 16 ± 0.7 MPa. Monolith showed BET surface area of 350 m^2/g, a micropore surface area of 280 m^2/g and a mesopore volume, due to the geopolymeric binder, of 0.09 cm^3/g. Its CO_2 adsorption capacity has been measured at the temperatures of 7, 25 and 42 °C up to 15 bar using an optimized Sievert-type (volumetric) apparatus. All the adsorption data were evaluated by Toth/Langmuir isotherm model and commercial pure NaX zeolite was used as reference. CO_2 adsorption isotherms show a maximum uptake value around 21 wt% at (~7 °C) that decrease to 18 wt% at high temperature (~42 °C) passing through 19 wt% at room temperature (~25 °C). The homogeneity grade of the surface, as obtained using Toth analysis performed on the adsorption isotherm, is close to $t \cong 0.40$, lower than the 0.61 obtained for pure commercial NaX zeolite, as a consequence of the binder formation. Monolith exhibits a notably higher K values and quicker saturation with respect to reference that can be ascribed to the presence of mesoporosity that provides an easier and faster transport of CO_2 in the NaX nanozeolite framework. The produced composite is a potential solid adsorbent candidate in industrial process.

- ✓ ***Poly(L-lactide) (PLA).***

  In selecting a low temperature Carbon capture and storage - CCS adsorbent, parameters such as selectivity, regeneration energy, and economicity play a crucial role. Poly(L-lactide) (PLA) is one of the most promising materials in science and engineering, not only because it is a green polymer progressively replacing petrobased plastics, but also for its carbon dioxide (CO_2)-philic nature that makes it a suitable candidate for greenhouse gas capture and climate change mitigation. Literature data point to PLA as a valid CCS candidate, although no direct gaseous CO_2 adsorption investigation or with mild preparation/regenerative energy was reported. In the experimental work performed, a deeper investigation of the adsorption/desorption properties of PLA in presence of gaseous CO_2 at room temperature was undertaken by means of a home-made Sievert-type apparatus. The effects of pressure (0–15 bar), morphology (commercial pellets, powder, and flakes), and regenerative energy (303 and 333 K) were investigated. PLA samples were also characterized by helium picnometry to obtain skeletal density and by XRD and SEM to obtain morphological and structural information. Results show that PLA represents a valid and ecological alternative among the materials for the

capture of CO_2. The PLA absorption capacity reaches 16 wt% at 15 bar and 303 K, and is closely linked to the thermal treatment, morphology, and crystalline structure of the material.

- ✓ ***Activated Carbons (ACs) from commercial amorphous cellulose.***

  Different preparation methods of activated carbon samples from amorphous cellulose were carried out to verifying their H_2 adsorption properties. Particular attention has been given to variation the pyrolysis parameters, obtaining samples of different porosity and H_2 affinity, with high SSA (up to 1500 m^2/g) and micropores fraction (especially ultramicroporosity). In this way, it was possible to correlate the morphology/structure of the samples and the hydrogen adsorption capacity, highlighting the formation of a single layer with the liquid H_2 density on the surface. Values of 6.0 molecules per nm^2 at 1 bar and 77 K demonstrate the adsorption effectiveness of some samples produced with a small activation time or at a lower temperature than the others.

  Among the samples of activated carbon metal-doped, preliminary studies have shown that benefits are obtained in the formation of porosity with low concentrations of copper (1%), while no improvement occurs by increasing the concentration of the impregnation. This is confirmed by the best adsorption capacity (4.1 wt%) occurs for the AFPAC_Cu1% sample (measured at 77 K and 80 bar), which is also higher than the value indicated by the empirical relation known as “Chahine rule”. These promising results suggest further investigations about this preparation method, in order to better understand the triggered mechanisms and the role of metal nanoparticles also extending the study to other types of metals.

Finally, it can conclude that the various methods of synthesis and preparation of porous nanostructures for gas adsorption are shown interesting and promising. The research work focused on the study of the mechanisms of porosity formation in the various materials trying to optimize the key parameters of the processes, in particular, in the physical activation process in activated carbon. In this way, an attempt was made to produce nanostructures with a tunable and more homogeneous porosity as possible in order to favor the physisorption processes of gases of energy interest. All the systems studied have shown for the various gaseous species investigated, in addition to high storage capacities, cycling and highly reversible processes, thus attributing to them an application potential in various technological solutions.

The outlook of this research work is to contribute in general at improvement of gas storage performances and, in particular, upon achievement the 6 wt% DOE (Department of Energy - USA) target for hydrogen storage. This would represent the definitive consolidation of hydrogen as a green energy carrier, fundamental for the eco-sustainability transition of the transports and energy systems.